

University of Southampton Research Repository ePrints Soton

Copyright © and Moral Rights for this thesis are retained by the author and/or other copyright owners. A copy can be downloaded for personal non-commercial research or study, without prior permission or charge. This thesis cannot be reproduced or quoted extensively from without first obtaining permission in writing from the copyright holder/s. The content must not be changed in any way or sold commercially in any format or medium without the formal permission of the copyright holders.

When referring to this work, full bibliographic details including the author, title, awarding institution and date of the thesis must be given e.g.

AUTHOR (year of submission) "Full thesis title", University of Southampton, name of the University School or Department, PhD Thesis, pagination

UNIVERSITY OF SOUTHAMPTON

Faculty of Engineering and the Environment

Institute of Sound and Vibration Research

**Nonlinear Vibration Isolators with Asymmetric
Stiffness**

by

Ali Abolfathi

Thesis for the degree of Doctor of Philosophy

September 2012

UNIVERSITY OF SOUTHAMPTON

ABSTRACT

Faculty of Engineering and the Environment
Institute of Sound and Vibration Research

Doctor of Philosophy

NONLINEAR VIBRATION ISOLATORS WITH ASYMMETRIC STIFFNESS

by Ali Abolfathi

A vibration source is commonly coupled to a receiving structure by a vibration isolator. A key trade-off in the choice of vibration isolator is the requirement for a wide frequency range of isolation without excessive static deflection. This compromise can, in principle, be circumvented by employing a softening nonlinear isolator that presents a high stiffness to the weight of the isolated mass but a low tangent stiffness in the vicinity of the equilibrium position. The first part of this thesis is concerned with the static response of a number of elements that are expected to exhibit such a nonlinear stiffness characteristic. A mechanism with geometrical nonlinearity is studied first and found to offer some benefits compared with a similar one reported in the literature. Beams are commonly employed as linear springs and their suitability as nonlinear isolators is considered here. It is shown that the stiffness of a simply supported beam loaded transversely at its centre is of a hardening type in contrast to what is reported in the literature. Post-buckled beams are also investigated as candidates for nonlinear springs of vibration isolators although the sudden change in stiffness at the buckling point is unfavourable. Curved beams and beams with eccentric loading are investigated as alternatives to a straight axially loaded post-buckled beam. Static analyses are presented which show that curvature or eccentricity in loading can be incorporated to smooth the force-deflection curves. A commercially available rubber isolation mount is also studied as an example of an axially loaded curved element and its force-deflection characteristic measured. The hypothesis that it can be modelled by a curved beam is found not to hold. The inter-variability observed between samples is evaluated which illustrates the potential for mistune of nonlinear mounts in general.

Nonlinear stiffness gives rise to the possibility of asymmetry about the equilibrium position, either as an inherent characteristic of the isolator or as a result of a mistuned added mass or static preload. A nonlinear isolator with asymmetric stiffness is modelled as a Duffing oscillator. The force transmissibility of the oscillator is obtained analytically using the Harmonic Balance Method from which the performance of the isolator is evaluated quantitatively as a function of both static load and mistuned mass. A study is presented for the case of a nonlinear isolator comprised of a curved beam. The high stiffness of the beam in extension causes impulsive behaviour in the transmitted force which is alleviated by the inclusion of a linear spring placed in series. It is shown that this combination significantly outperforms a linear isolator with the same static deflection.

Table of Contents

Abstract.....	i
List of Figures.....	vii
List of tables.....	xvii
Declaration of authorship.....	Error! Bookmark not defined.
Acknowledgments.....	xxi
List of symbols and abbreviations	xxiii
1 Introduction.....	1
1.1 Vibration isolation	2
1.2 Motivation for research.....	4
1.3 Nonlinear vibration isolators.....	6
1.3.1 Negative stiffness mechanism.....	6
1.3.2 Magnet springs.....	9
1.3.3 Beams as nonlinear springs.....	10
1.3.4 Viscoelastic vibration isolation mounts	17
1.4 Dynamic response of nonlinear vibration isolators.....	18
1.5 Thesis objectives.....	20
1.6 Contributions of the thesis	20
1.7 Thesis outline.....	21
2 Quasi-Zero-Stiffness (QZS) mechanisms	25
2.1 Introduction.....	25
2.2 A snap-through lever mechanism	26
2.3 Experiment on a snap-through mechanism.....	32
2.4 A Quasi-Zero-Stiffness mechanism.....	39
2.5 A QZS system with preload.....	43
2.6 Comparison between two QZS mechanisms.....	46
2.7 Conclusions.....	50

3	Beams as nonlinear springs	53
3.1	Introduction	53
3.2	Principal theory of a straight beam's deformation	55
3.2.1	Deflection of a beam due to a pure bending moment	56
3.2.2	Effect of rotation.....	61
3.3	The static stiffness characteristics of a simply supported beam loaded at its centre ...	63
3.3.1	Exact solution	64
3.3.2	An approximate solution	67
3.3.3	Discussion.....	72
3.3.4	Accuracy of the approximate solution.....	73
3.4	Buckling and post-buckling of beam.....	80
3.4.1	Buckling analysis of beams (Euler Buckling)	80
3.4.2	A post-buckled straight beam	82
3.5	Beam loaded eccentrically.....	89
3.6	Curved beams	91
3.7	Dynamic and static stiffness of beams.....	95
3.8	Internal resonances	97
3.8.1	Resonances of rod isolator.....	98
3.8.2	Case study, isolating a one kg mass with curved beams	102
3.9	Conclusions	108
4	Bubble mounts.....	111
4.1	Introduction	111
4.2	Force-deflection characteristics.....	112
4.3	Modelling the bubble mount with curved beams	116
4.4	Variability in the properties of bubble mounts.....	120
4.5	Conclusions	125
5	Force transmissibility of an asymmetric Duffing oscillator	127
5.1	Introduction	127
5.2	Equations of motion for forced response of a Duffing oscillator	128
5.3	Example of a QZS nonlinear isolator modelled by a cubic nonlinearity.....	129

5.4	Effect of static preload on the dynamic response of nonlinear vibration isolator with cubic stiffness.....	133
5.4.1	Forced response.....	133
5.4.2	Force transmissibility.....	138
5.5	Effect of a mistuned mass on a nonlinear isolator with cubic stiffness.....	144
5.5.1	Forced response.....	145
5.5.2	Force transmissibility.....	148
5.6	The effect of the linear term on the performance of a nonlinear vibration isolator ...	151
5.7	Conclusions.....	155
6	Dynamic response of a curved beam isolator.....	159
6.1	Introduction.....	159
6.2	Modelling of a curved beam isolator.....	160
6.3	Forced response of a curved beam isolator.....	164
6.4	Curved beam isolator loaded statically.....	171
6.5	Force transmissibility of a curved beam isolator.....	174
6.6	Transmitted force in the time domain.....	178
6.7	Conclusions.....	184
7	Concluding remarks and future works.....	187
7.1	Recommendations for future work.....	191
	Appendix A. Accuracy of solutions.....	195
	References.....	203

List of Figures

Figure 1-1: a) A force excited single degree of freedom system, b) transmitted force to the base	2
Figure 1-2: Magnitude of transmissibility of a viscously damped linear single degree of freedom system	3
Figure 1-3: Natural frequency as a function of static deflection for a linear single degree of freedom system	5
Figure 1-4: Schematic of a force-displacement curve of a nonlinear isolator, black line: force-deflection, dashed line: corresponding linear spring, red line: tangent to the curve at the statically loaded position.....	5
Figure 1-5: Quasi-Zero-stiffness mechanism, arrow: force excitation, double headed arrow: possible movement of base [9].....	7
Figure 1-6: Schematic geometry of a pair of torsion sprung crank arm [14].....	8
Figure 1-7: The principle of magnetic anti-spring systems, a) magnets at the equilibrium position, b) magnets moved with respect to each other in the vertical direction, F_0 : magnetic force, F_y : vertical component of magnetic force, d: distance between magnets [18]	9
Figure 1-8: A simple structure for mounting and constraining Euler springs [22]	11
Figure 1-9: A schematic diagram of a negative torsional stiffness mechanism, the base link (0), movable connecting link (1), an insertion (2), and elements of elastic link (1') [26].....	12
Figure 1-10: Cross-sectional view of GAS experimental test rig, (A) stressed blade, (B) link wire, (C) load disk, (D) angular movement of the blade base, (E) radial movement of the blade base, (F) anti-tilt tower, (G) anti-tilt centring wires, (H) suspension wire (or rod), (I) load [19] 13	
Figure 1-11: Schematic view of the Monolithic geometric anti-spring mechanism [28]	14
Figure 2-1: a) The lever mechanism shown at an arbitrary position, b) free body diagram of the right lever, c) Free body diagram of hinge.....	27
Figure 2-2: Non-dimensional force-displacement curves for the mechanism of Figure 2-1 ($\beta=0.5$).....	29

Figure 2-3: Non-dimensional stiffness of the mechanism as a function of non-dimensional displacement ($\beta=0.5$).....	30
Figure 2-4: The negative stiffness displacement range as a function of initial angle.....	31
Figure 2-5: The experimental rig.....	33
Figure 2-6: Schematic diagram of Bonello's rig a) un-deformed b) deformed [66].....	34
Figure 2-7: The non-dimensional force-displacement for different values of initial angle with linearisations shown around the unloaded positions	35
Figure 2-8: FRFs for $2b = 64mm$ ($\theta_0 = 53^\circ$), solid line: first accelerometer, dashed lines: second accelerometer, a) Accelerance (hammer test), b) Transmissibility (shaker with random excitation, 100 averages).....	36
Figure 2-9: Natural frequency variation as a function of separation of cantilevers.....	37
Figure 2-10: Damping ratio ζ for different separation of cantilevers	38
Figure 2-11: a) The QZS mechanism shown at an arbitrary position, b) free body diagram of the right lever, c) free body diagram of hinge	39
Figure 2-12: The non-dimensional force-displacement of the QZS mechanism for different initial angles and of the vertical spring alone	42
Figure 2-13: Non-dimensional stiffness as a function of non-dimensional displacement for different initial angles.....	42
Figure 2-14: The pre-loaded vertical spring, a) unloaded vertical spring, b) preloaded vertical spring, c) the position of preloaded vertical spring regarding snap-through mechanism.....	43
Figure 2-15: The preloaded QZS mechanism ($\beta=0.5$, $\gamma=2$, and $\theta_0=30^\circ$).....	45
Figure 2-16: QZS mechanisms, a) Oblique spring mechanism, b) lever mechanism	46
Figure 2-17: Non-dimensional force as a function of non-dimensional displacement, black lines: QZS oblique spring mechanism, cyan line: QZS lever mechanism	48
Figure 2-18: Non-dimensional stiffness as a function of non-dimensional displacement, black lines: oblique spring mechanism, cyan lines: lever mechanism.....	49
Figure 3-1: a) Deflection of an initial straight beam due to pure bending moment, b) Sign convention for curvature.....	55

Figure 3-2: Simply supported beam loaded by bending moment, a) deflected beam, b) small section of beam of length ds	57
Figure 3-3: Non-dimensional bending moment as a function of non-dimensional lateral displacement of the tip, curves: shape of the deflected beam	59
Figure 3-4: Comparison of the analytical results with the results obtained from ANSYS for the axial displacement of the tip of the beam and the transverse displacement at the centre of the beam	60
Figure 3-5: Cross stiffness as a function of deflection	61
Figure 3-6: Relationship between the angle and the displacement in the x direction	62
Figure 3-7: Simply supported beam loaded at the centre, a) schematic of the beam, b) a small section of the beam	64
Figure 3-8: Non-dimensional force as a function of non-dimensional transverse displacement	71
Figure 3-9: The bending moment in a simply supported beam loaded at the centre	73
Figure 3-10: Deflected shape of the beam for different values of load, solid lines (-): exact shape, dotted lines (...): shape given by a Sine function	74
Figure 3-11: Normalised mean square error between the actual and approximate shapes of the beam	75
Figure 3-12: Slope of transverse displacement, solid lines (-): exact solution, dotted lines (...): approximate solution	75
Figure 3-13: Mean Square Error of slope normalised by the area under the curve	76
Figure 3-14: Second derivative of the transverse displacement, solid lines (-): exact solution, dotted lines (...): sine function	77
Figure 3-15: Mean Square Error of the second derivative normalised by the area under the curve	78
Figure 3-16: Relationship between the distance between the beam supports, its length and the transverse displacement	79
Figure 3-17: Simply supported column, a) unloaded, b) buckled, c) free body diagram	81
Figure 3-18: Simply supported beam under axial load, a) unloaded, b) buckled, c) free body diagram	83

Figure 3-19: Non-dimensional force-displacement of inextensible buckled beam	87
Figure 3-20: Schematic diagram of force-deflection before and after buckling.....	88
Figure 3-21: Simply supported beam under axial eccentric load, a) unloaded, b) loaded, c) free body diagram.....	90
Figure 3-22: Non-dimensional force-displacement of inextensible beam loaded eccentrically..	91
Figure 3-23: Curve beam, a) unloaded, b) loaded, c) free body diagram.....	92
Figure 3-24: Non-dimensional force-displacement of an inextensible curved beam	94
Figure 3-25: Non-dimensional force-displacement of inextensible curved beam.....	94
Figure 3-26: Non-dimensional tangent stiffness of inextensible curved beams.....	95
Figure 3-27: Minimum tangent stiffness and its corresponding static stiffness of the straight beam loaded eccentrically (solid line: minimum tangent stiffness, dashed line: corresponding static stiffness).....	96
Figure 3-28: Minimum tangent stiffness and corresponding static stiffness for a curved beam as a function of angle of curvature (solid line: minimum tangent stiffness, dashed line: corresponding static stiffness).....	97
Figure 3-29: a) Schematic diagram of a distributed parameter isolator, b) free body diagram...	98
Figure 3-30: Non-dimensional impedances of a rod ($Z_{22}/\sqrt{k_L m}$) and mass ($Z_m/\sqrt{k_L m}$) alongside non-dimensional natural frequencies of the rod for $\mu=0.1$ (dash-dotted line: fixed-fixed boundary condition, dotted line: fixed-free boundary condition).....	101
Figure 3-31: Schematic diagram of a vibration isolator with curved beams as springs	102
Figure 3-32: Lowest natural frequency of curve beam sized to achieve 1 Hz fundamental frequency, +: in-plane flexure mode of analytical solution [76], *: finite element model of unloaded curve beam bounded both ends, dots: finite element model of statically loaded curve beam bounded both ends, o: finite element model of curve beam supporting mass at one end simply supported	106
Figure 3-33: Mode shape of curved beam with initial angle equal to 5 degree.....	107
Figure 3-34: Force transmissibility of curved beam isolator of initial curvature angle α equal to 5 degree and damping ratio equal to 0.5% obtained by finite element method.....	108
Figure 4-1: Bubble mount	111

Figure 4-2: Force-deflection of different sizes of bubble mount (Tech Products Corporation)	113
Figure 4-3: Bubble mount test rig, a) connecting the load cell directly to the bubble mount by a rod, b) loaded bubble mount, c) a disk installed to resemble contact with the isolated mass, d) loaded bubble mount with a disk on the top	114
Figure 4-4: Force-deflection of bubble mount loaded quasi-statically , a) displacement applied directly through rod, b) disk added between rod and bubble mount	115
Figure 4-5: Average force-displacement graph obtained by averaging the loading and unloading curves	115
Figure 4-6: Cross section of bubble mount (Tech Products Corporation)	116
Figure 4-7: Mean square error as a function of length and initial curvature angle for fixed buckling load	117
Figure 4-8: Mean square error as a function of curvature angle and buckling load for fixed length	118
Figure 4-9: Force-displacement of the bubble mount and optimized curved beams	119
Figure 4-10: Force-displacement of bubble mount and optimized curved beams. (Data up to the minimum tangent stiffness point is considered and length is chosen to match physical dimension of bubble mount)	120
Figure 4-11: Force-displacement of ten nominally identical bubble mounts, last cycle of loading is considered	121
Figure 4-12: Variation of tangent stiffness and corresponding static stiffness in percentage from their mean values for different bubble mounts	123
Figure 4-13: Minimum Tangent stiffness as a function of static stiffness for each bubble mount (circles) alongside best linear fit (solid line)	124
Figure 4-14: a) Displacement due to optimal load normalised by average displacement, b) Tangent stiffness of optimally loaded bubble mount, normalised by averaged minimum tangent stiffness	125
Figure 5-1: QZS mechanism with oblique springs as nonlinear vibration isolator, loaded statically at the zero stiffness position	130
Figure 5-2: Schematic of force-deflection curve for a nonlinear spring with cubic nonlinearity, dashed line: tangent to the curve at the statically loaded position	132

Figure 5-3: a) Magnitude of FRC of the harmonic term, b) phase angle of FRC for different values of static preload, $\gamma=0.0783$, $\zeta=0.025$, and $f_1=0.1$, solid lines: stable branch, dotted lines: unstable branch, dots: time domain solutions, dashed line: locus of $A_1|_{\phi=-90^\circ}$ 137

Figure 5-4: FRC of bias amplitude for $\gamma=0.0783$, $\zeta=0.025$, and $f_1=0.1$, solid lines: stable branch, dotted lines: unstable branch, dots: time domain solutions, dashed line: locus of $A_0|_{\phi=-90^\circ}$... 138

Figure 5-5: Transmissibility as a function of non-dimensional frequency Ω for $\gamma=0.0783$, $\zeta=0.025$, and $f_1=0.1$, solid lines: stable solution, dotted lines: unstable solutions, dots: time domain solutions, dashed line: locus of transmissibility at which phase angle is -90° 140

Figure 5-6: Transmissibility as a function of non-dimensional frequency Ω for $\gamma=0.0783$, $\zeta=0.025$, and $f_1=0.1$, solid lines: stable solution, dotted lines: unstable solutions, dashed line: transmissibility of equivalent linear isolators, dashed-dot line: locus of peaks..... 141

Figure 5-7: Transmissibility as a function of non-dimensional frequency Ω for $\gamma=2.606$, $\zeta=0.025$, and $f_1=0.1$, solid lines: stable solution, dotted lines: unstable solutions, dashed-dot line: locus of peaks, Grey lines: transmissibility curves for $\gamma=0.0783$ 142

Figure 5-8: Isolation frequency as a function of static load, circles: peak frequency dominant, dots: transmissibility less than one, lines: isolation frequency of equivalent linear isolator with stiffness equal to tangent stiffness, (solid line: $\gamma=0.0783$, dashed line: $\gamma=2.606$), dotted line: isolation frequency of linear isolator with the same static deflection due to the mass..... 143

Figure 5-9: FRC of bias amplitude for $\gamma=0.0783$, $\zeta=0.025$, and $f_1=0.1$, solid lines: stable branch, dotted lines: unstable branch, dots: time domain solutions 146

Figure 5-10: FRCs of harmonic amplitude for $\gamma=0.0783$, $\zeta=0.025$, and $f_1=0.1$, solid lines: stable branch, dotted lines: unstable branch, dots: time domain solutions, dashed line: locus of $A_1|_{\phi=-90^\circ}$ 147

Figure 5-11: FRC of harmonic amplitude for $\gamma=0.0783$, $\zeta=0.025$, and $f_1=0.1$, solid lines: stable branch, dotted lines: unstable branch, dashed line: locus of $A_1|_{\phi=-90^\circ}$ 148

Figure 5-12: Transmissibility as a function of non-dimensional frequency Ω for $\gamma=0.0783$, $\zeta=0.025$, and $f_1=0.1$, solid lines: stable solution, dotted lines: unstable solutions, dots: time domain solutions..... 149

Figure 5-13: Isolation frequency as a function of mass ratio, circles: peak frequency dominant, dots: transmissibility less than one, lines: isolation frequency of equivalent linear isolator with stiffness equal to tangent stiffness, (solid line: $\gamma=0.0783$, dotted line: $\gamma=2.606$), dashed line: isolation frequency of linear isolator 150

Figure 5-14: FRC of bias amplitude for $\gamma=0.0783$, $\zeta=0.025$, $f_0=0.5$ and $f_1=0.1$, solid lines: stable branch, dotted lines: unstable branch, dots: time domain solutions	152
Figure 5-15: FRC of harmonic term of response for $\gamma=0.0783$, $\zeta=0.025$, $f_0=0.5$ and $f_1=0.1$, solid lines: stable branch, dotted lines: unstable branch, dots: time domain solutions, dashed line: locus of $A_1 _{\phi=-90^\circ}$	153
Figure 5-16: Transmissibility as a function of non-dimensional frequency Ω for different linear stiffness and $\gamma=0.0783$, $\zeta=0.025$, $f_0=0.5$, and $f_1=0.1$, solid lines: stable solution, dotted lines: unstable solutions, dots: time domain solutions, dashed line: locus of transmissibility at which phase angle is -90°	154
Figure 5-17: Isolation frequency as a function of static preload for $\gamma=0.0783$, $\zeta=0.025$, and $f_1=0.1$, circles: peak frequency dominant, dots: transmissibility less than one, lines: isolation frequency of equivalent linear isolator with stiffness equal to tangent stiffness, dotted line: isolation frequency of linear isolator	155
Figure 6-1: a) Schematic view of the curved beam isolator, b) Model of the curved beam isolator with additional linear spring to overcome convergence problems in the numerical simulation (it is also used in section 6.6 to improve the performance of the isolator.).....	161
Figure 6-2: Non-dimensional force-deflection curve for curved beam isolator and polynomial third order fit for different initial angles and $k_c=100$, (Dashed line: exact solution of chapter 3, solid line: Range that data is fitted to, dotted line: Fitted third order polynomial).....	163
Figure 6-3: Harmonic term of forced response A_1 and bias term of forced response A_0 for curved beam isolator loaded to its minimum tangent stiffness position, $f_1=0.01$, $k_c=100$, and $\zeta=0.025$, approximate solutions from the HBM are obtained by using coefficients given in Table 6-1 (solid line: approximate results, dots: accurate solution from the time domain simulation)	166
Figure 6-4: Harmonic term of forced response A_1 for curved beam isolator for $f_1=0.1$, $k_c=100$, and $\zeta=0.25$, (solid line: HBM results stable branch, dotted line: HBM results unstable branch, dots: time domain simulation).....	167
Figure 6-5: Harmonic term of forced response A_1 for curved beam isolator for $f_1=0.1$, $k_c=100$, $\zeta=0.25$, and $\alpha=2^\circ$, (black solid line: HBM results stable branch, black dotted line: HBM results unstable branch, ($\kappa=0.08$, $\gamma=0.0143$, $f_0=-0.019$), grey line: fitted line to the time domain data, dots: time domain simulation).....	168
Figure 6-6: Curved beam isolator oscillation time history (exact time domain solution) for $\alpha=2^\circ$, $f_1=0.1$, $\zeta=0.025$, and $k_c=100$, dashed line: applied harmonic force	169

Figure 6-7: waterfall spectrum of forced response for curved beam isolator for $f_1=0.1$, $k_c=100$, $\zeta=0.25$, and $\alpha=2^\circ$ 170

Figure 6-8: Bias term of forced response A_0 for the curved beam isolator for $f_1=0.1$, $k_c=100$, and $\zeta=0.25$, (The coefficient for approximate Duffing oscillator is given in Table 6-1, solid line: Approximate model, stable branch, dotted line: approximate model, unstable branch, dots: exact model)..... 171

Figure 6-9: Harmonic term of forced response for curved beam isolator with initial curvature angle $\alpha=2^\circ$ for different static loads f_s , $f_1=0.1$, $k_c=100$, and $\zeta=0.025$, (solid line: approximate model, stable branch, dotted line: approximate model, unstable branch, dots: exact model) ... 173

Figure 6-10: Bias of forced response for the curved beam isolator with initial curvature angle of 2° for different static , $f_1=0.1$, $k_c=100$, and $\zeta=0.025$, (solid line: approximate model, stable branch, dotted line: approximate model, unstable branch, dots: exact model)..... 174

Figure 6-11: Transmissibility as a function of non-dimensional frequency Ω for the curved beam isolator with three different initial angles α , for $\zeta=0.025$ and $f_1=0.01$, $k_c=100$, solid lines: approximate solution (coefficients for Duffing oscillator model is given in Table 6-1), dots: results of exact model..... 175

Figure 6-12: Transmissibility as a function of non-dimensional frequency Ω for the curve beam isolator with three different initial angles α , for $\zeta=0.025$, $f_1=0.1$, $f_s=0$, and $k_c=100$,(Parameters for approximate solution from Table 6-1) solid lines: approximate solution stable branch, dotted lines: approximate solution unstable branch, dots: results of exact model of the time domain simulation 176

Figure 6-13: Force transmissibility for curved beam isolator with initial curvature angle $\alpha=2^\circ$ for different static preloads f_s , $f_1=0.1$, $k_c=100$, and $\zeta=0.025$, parameters for approximate Duffing oscillator are given in Table 6-2 (solid line: approximate results stable branch, dotted line: approximate results unstable branch, dots: exact results of the time domain simulation)..... 177

Figure 6-14: Force transmissibility for curved beam isolator with initial curvature angle $\alpha=2^\circ$,(isolators are normalised with the total static deflection and dynamic load, f_1 , is adjusted to have the equivalent dynamic force of $f_1=0.1$), for different static preloads f_s , $k_c=100$, and $\zeta=0.025$, (solid line: approximate results stable branch, dotted line: approximate results unstable branch, dots: exact results of the time domain simulation) 177

Figure 6-15: Time history of transmitted force through curved beam isolator for excitation frequency of 0.58 for $\alpha=2^\circ$, $f_1=0.1$, $\zeta=0.025$, $f_s=0$, and $k_c=100$ 178

Figure 6-16: Total Harmonic Distortion (THD) of harmonic term of forced response A_1 in per cent as a function of non-dimensional frequency for $f_1=0.1$, $\zeta=0.025$, $f_s=0$, $k_c=100$, (solid line: increasing frequency, dashed line decreasing frequency) 179

Figure 6-17: Total Harmonic Distortion (THD) of force transmissibility in per cent as a function of non-dimensional frequency for $f_1=0.1$, $\zeta=0.025$, $f_s=0$, $k_c=100$, (solid line: increasing frequency, dashed line decreasing frequency)	180
Figure 6-18: Non-dimensional force-deflection curve of the curved beam isolator for initial curvature angle $\alpha=2^\circ$	181
Figure 6-19: Harmonic term of forced response A_1 for curved beam isolator for $\alpha=2^\circ$, $f_1=0.05$, $f_s=0$ and $\zeta=0.25$, (Approximate Duffing model of Table 6-3; solid line: approximate solution stable branch, dotted line: approximate solution unstable branch, dots: time domain simulation)	182
Figure 6-20: Transmissibility as a function of non-dimensional frequency Ω for the curved beam isolator with two different linear springs stiffness k_c , for $\zeta=0.025$, $f_1=0.1$, $f_s=0$, (Approximate Duffing model of Table 6-3; solid line: approximate solution stable branch, dotted line: approximate solution unstable branch, dotted-dashed line: linear isolator with the same static deflection due to the isolated mass)	183
Figure 6-21: Steady state time history of the transmitted force of the curved beam isolator at non-dimensional frequency $\Omega = 0.68$ for $k_c = 1$, $\zeta = 0.025$, $f_1 = 0.1$, and $f_s = 0$	184
Figure A-1: Phase portrait of nonlinear vibration isolator for $\zeta = 0.025$, $\gamma = 0.0783$, $f_1 = 0.1$, and $f_0 = 0.01$	196
Figure A-2: Total harmonic distortion as a function of non-dimensional frequency for $\zeta = 0.025$, $\gamma = 0.0783$, $f_1 = 0.1$, and $f_0 = 0.01$	197
Figure A-3: Phase portrait of nonlinear vibration isolator for decreasing frequency, $\zeta = 0.025$, $\gamma = 0.0783$, $f_1 = 0.1$, and $f_0 = 0.01$	197
Figure A-4: Total harmonic distortion as a function of non-dimensional frequency for $\zeta = 0.025$, $\gamma = 0.0783$, $f_1 = 0.1$, and $f_0 = 0.2$	198
Figure A-5: Phase portrait of nonlinear vibration isolator for increasing frequency, $\zeta = 0.025$, $\gamma = 0.0783$, $f_1 = 0.1$, and $f_0 = 0.2$	199
Figure A-6: Time history of nonlinear vibration isolator for different non-dimensional frequencies, $\zeta = 0.025$, $\gamma = 0.0783$, $f_1 = 0.1$, and $f_0 = 0.2$	199
Figure A-7: Total harmonic distortion as a function of non-dimensional frequency for $\zeta = 0.025$, $\gamma = 0.0783$, $f_1 = 0.1$, and $f_0 = 0.5$	200
Figure A-8: Total harmonic distortion as a function of non-dimensional frequency for $\zeta = 0.025$, $\gamma = 0.0783$, $f_1 = 0.1$, and $f_0 = 0.95$	201

List of tables

Table 3-1: Dimensions of curved beam for different curvature angle	103
Table 4-1: Initial values of length of curved beam and buckling load for different curvature angles	117
Table 4-2: Correlation matrix for force-deflection of bubble mounts	122
Table 6-1: Coefficients of the fit of the form $ax^3 + bx^2 + cx = 0$ to the force-deflection of the curved beam isolator about its minimum tangent stiffness position and transformed polynomial of the form $z^3 + \kappa z = f_0'$, ($z=x+\delta$)	164
Table 6-2: Coefficients of the Duffing oscillator model $(\ddot{x} + 2\zeta\dot{x} + \kappa x + \gamma x^3 = f_1 \cos(\Omega t) + f_0)$ of the curved beam isolator with initial curvature angle α of 2° , $k_c=100$	172
Table 6-3: Coefficient of the Duffing oscillator model $(\ddot{x} + 2\zeta\dot{x} + \kappa x + \gamma x^3 = f_1 \cos(\Omega t) + f_0)$ of the curved beam isolator with initial curvature angle α of 2°	181

Declaration of authorship

I, Ali Abolfathi, declare that the thesis entitled “Nonlinear vibration isolators with asymmetric stiffness” and the work presented in the thesis are both my own, and have been generated by me as the result of my own original research. I confirm that:

- this work was done wholly or mainly while in candidature for a research degree at this University;
- where any part of this thesis has previously been submitted for a degree or any other qualification at this University or any other institution, this has been clearly stated;
- where I have consulted the published work of others, this is always clearly attributed;
- where I have quoted from the work of others, the source is always given. With the exception of such quotations, this thesis is entirely my own work;
- I have acknowledged all main sources of help;
- where the thesis is based on work done by myself jointly with others, I have made clear exactly what was done by others and what I have contributed myself;
- parts of this work have been published as:
 1. Abolfathi, A., Brennan, M.J. and Waters, T.P. (2010) *Large deflection of a simply supported beam*. Southampton, GB, University of Southampton, 28pp. (ISVR Technical Memorandum, 988).
 2. Abolfathi, A., Waters, T.P. and Brennan, M.J. (2011) *Passive vibration isolation using axially loaded curved beams*. In, ICSV18: 18th International Congress on Sound and Vibration, Rio de Janeiro, BR, 10 - 14 July 2011.

Signed:

Date:

Acknowledgments

I am indebted and heartily thankful to my supervisors Dr Tim Waters and Professor Michael Brennan for their excellent guidance, care and patience. They have provided encouragement and support in many different ways. I owe my understanding of the subject to them. I would like to make a special mention of Mike's help and supervision after he left ISVR.

I would also like to show my gratitude to my review panel: Dr Neil Ferguson, Professor Brian Mace and later, Dr Emiliano Rustighi. Their comments and criticisms during the review sessions were certainly beneficial to both me and the work presented in this thesis. I would also like to thank all ISVR technical and administrative staff who have supported me so well during this period. I gratefully acknowledge the financial support from ISVR, through the Lord Rayleigh scholarship.

I would like to thank all my friends at ISVR who made my experience here pleasant and also were great help when required. I would like to mention David Herron for his willingness to go out of Southampton and his passion for walking. I am also grateful to him for proof-reading most of this thesis and for being constantly there to help. There are also my other friends without who the experience of Southampton would not be so delightful.

However, my study would not be possible without help and support from my family. I am deeply grateful to my parents whose unlimited support and encouragement allowed me to continue my studies. I am much obliged to my wife Anahita for her unwavering understanding, for her selfless love throughout, and her encouragement and companionship during the preparation of this thesis.

List of symbols and abbreviations

FEM	Finite Element Method
FRC	Frequency Response Curve
FRF	Frequency Response Function
HBM	Harmonic Balance Method
HSLDS	High-Static-Low-Dynamic-Stiffness
QZS	Quasi-Zero-Stiffness
SDOF	Single Degree Of Freedom
THD	Total Harmonic Distortion
\wedge	Denotes non-dimensional quantity
\cdot	Differentiation with respect to time
$'$	Differentiation with respect to non-dimensional time
A_0	Bias term of response
A_1	Amplitude of harmonic term of response
a	Lever length
c	Damping coefficient or constant of integration
e	Eccentricity
E	Elastic moduli
f_0	Normalised static force
f_1	Amplitude of normalised harmonic load
f_e	Force at equilibrium position
F_n	Reaction force
F_r, F_l	Levers' reaction force (right and left)
f_s	Static load
F_s	Spring force
f_{t0}	Static transmitted force
f_{t1}	Harmonic transmitted force
f_t	Transmitted force
F_t	Magnitude of transmitted force

h	Height of lever mechanism
I	Second moment of area
k	Stiffness coefficient
k_c	Stiffness of cantilever beam
k_l	Linear stiffness
k_s	Static stiffness
L	Length of a beam
m	Mass
P	Applied force on a beam
P_E	Euler buckling load
r	Frequency ratio ω_n/ω
s	Distance along deflected beam
t	Thickness
T_1	Force transmissibility
u	Displacement of a beam's tip
w	Transverse displacement
x	Axial displacement
x_e	Displacement at equilibrium position
y	Transverse displacement
Z	Impedance
α	Curvature angle
β	Geometrical ratio
γ	Stiffness ratio or cubic normalised stiffness
δ	Static deflection
ε	Strain
ζ	Damping ratio
θ	Angle between the lever and normal line
θ_0	Initial angle between the lever and normal line
κ	Linear normalised stiffness
μ	Mass ratio
ρ	Radius of curvature
τ	Normalised time

φ	Angle of reaction force
ϕ	Phase of response
ϕ_t	Phase of transmissibility
ω_n	Natural frequency
Ω	Normalised frequency

1 Introduction

Vibration is an important consideration in many mechanical systems. In some cases, vibration is necessary for the system to perform its function, such as vibrating conveyors. However, in the majority of cases, it is unwanted and possibly harmful, particularly when the vibration affects people or sensitive equipment. The levels of vibrations that are considered to be acceptable today are lower than they were in the past. In addition, advances in technology, especially in materials and manufacturing engineering, have led to the development of components and systems that are more prone to vibration than those they replace. This is due to reduction in mass and/or an increase in the velocity at which the system is operated. An example of this is Rolls-Royce Trent XWB jet engine, where a 15% module weight reduction was achieved relative to the previous engine. These mean there is a great and continuing interest in vibration control.

One of the methods to control vibration is to isolate the receiver from its source. The devices used to achieve this are called vibration isolators. While most mechanical systems are designed to operate in their linear range, there are some systems where nonlinearity may be desirable with regard to the performance of the system. The purpose of this thesis is to investigate the possible advantages of implementing a nonlinear vibration isolator and the methods to achieve such nonlinear characteristics.

An introduction to vibration isolation is given in section 1.1. The motivation for doing this research work is addressed in section 1.2. A review on the previous attempts to build isolators with low natural frequency is presented in section 1.3 and their nonlinear dynamic response is presented in section 1.4. The objectives of the thesis are listed in section 1.5 and the contributions in section 1.6. The thesis contents are presented in the final section of this chapter.

1.1 Vibration isolation

According to Rivin [1]: “vibration isolation is one of the vibration control techniques whereby the source of vibration excitation and the object to be protected are separated by an auxiliary system comprising special devices called vibration isolators or vibration isolation mounts”. The purpose of an isolator may differ depending on the situation. It may isolate rotating machinery from transmitting its vibration to its surroundings or protect a precise piece of equipment from unwanted vibration. Despite different purposes, the same principles apply in each case. The concept can be best described by a single degree of freedom system [2]. For a linear system, the displacement transmissibility for a base excited system is the same as force transmissibility for a force excited system. It is therefore sufficient at this stage to consider only a force excited system. Note that for nonlinear systems, such as those investigated in chapter 5 and 6, the transmitted force and transmitted displacement are not the same.

A single degree of freedom system is shown in Figure 1-1. A harmonic force, f , is applied to the mass and the motion of the mass is defined by x . The base is assumed to be rigid without any displacement. The equation of motion for the system is given in the following equation,

$$m\ddot{x} + c\dot{x} + kx = f \quad (1-1)$$

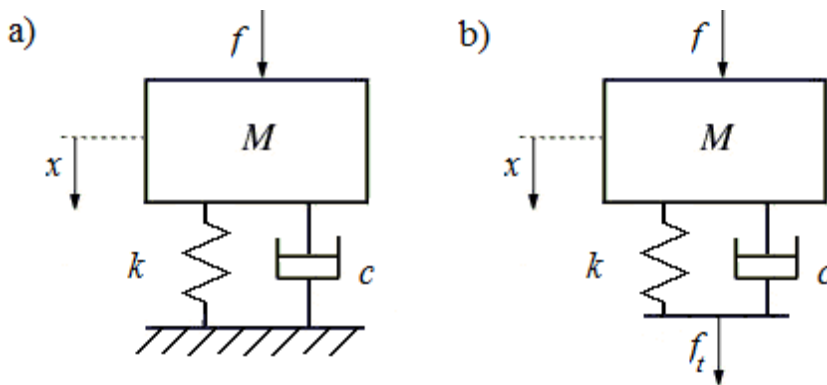


Figure 1-1: a) A force excited single degree of freedom system, b) transmitted force to the base

If the harmonic force is described by the function $f(t) = Fe^{i\omega t}$, the steady state response will be $x(t) = Xe^{i\omega t}$ and the transmitted force to the base will be $f_t(t) = F_t e^{i\omega t}$, where i is the imaginary number. X and F_t in these equations have complex values. The ratio F_t/F is called forced transmissibility and this can be derived for the above system as follows,

$$\frac{F_t}{F} = \frac{1 + 2i\zeta r}{1 - r^2 + 2i\zeta r} \quad (1-2)$$

where ζ is the damping ratio and r is the frequency ratio defined as ω/ω_n , and

$$\omega_n = \sqrt{k/m} \quad (1-3)$$

is the natural frequency.

The modulus of transmissibility for different values of damping ratio is shown in Figure 1-2. There is a peak for every curve at about the natural frequency of the system. A transmissibility value of less than unity means that the transmitted force is smaller than the applied force, so that there is some vibration isolation effect between the base and the mass. All of the transmissibility curves cross the line of unit transmissibility at the same point where the frequency ratio is $\sqrt{2}$. This frequency is referred to here as the isolation frequency.

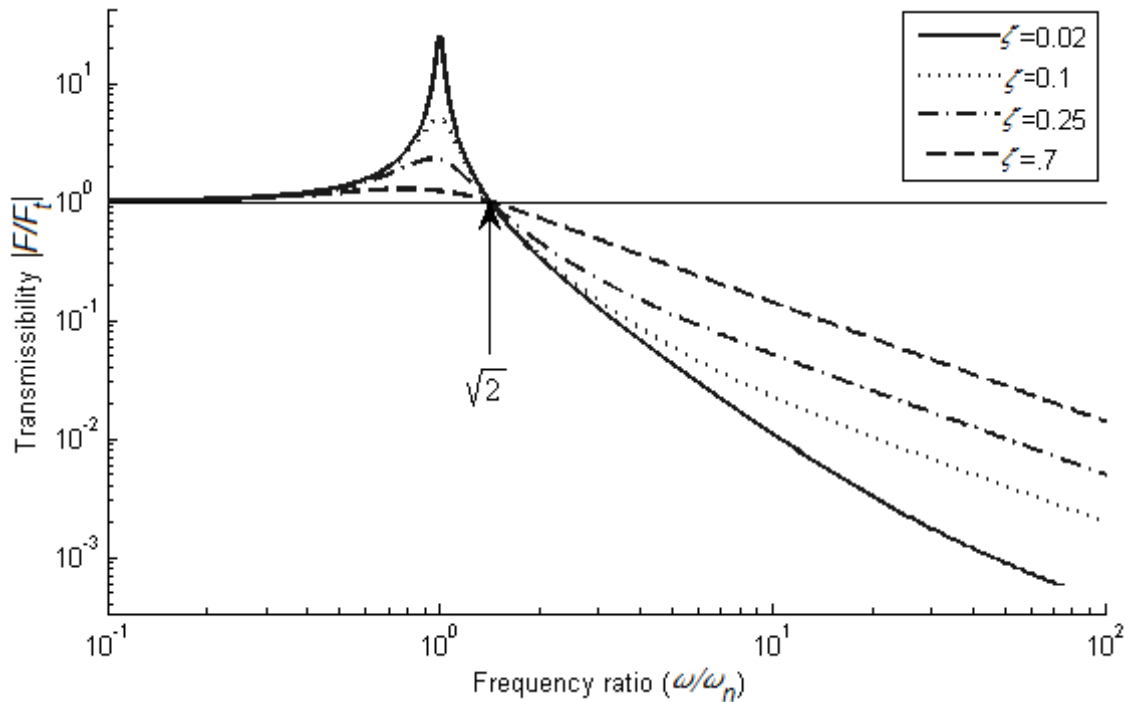


Figure 1-2: Magnitude of transmissibility of a viscously damped linear single degree of freedom system

1.2 Motivation for research

It is clear from the preceding section that in order to have effective vibration isolation over a wide range of excitation frequencies, it is necessary to have a low natural frequency. Since, it is not usually desirable to increase the mass, reducing stiffness of the spring is usually the preferred way to achieve this practically. A reduction in stiffness of the spring (or an increase in the mass) will result in greater static deflection of the system which, for a mass-spring mechanism, is given by Hooke's law,

$$\delta k = mg \quad (1-4)$$

where δ is the static deflection. If the stiffness of the spring is substituted from equation (1-4) into equation (1-3) one obtains expression for the natural frequency,

$$\omega_n = \sqrt{\frac{g}{\delta}} \quad (1-5)$$

The natural frequency as a function of static deflection is shown in Figure 1-3 and is seen to decrease by increasing static deflection. This confirms that in order to achieve vibration isolation at low frequencies, a large static deflection must be accommodated, which may be not possible in practice, e.g. a static displacement of 248 mm is required to achieve a natural frequency of 1 Hz.

This limitation can be overcome by using a spring with a nonlinear force displacement characteristic. A typical force-displacement curve for a nonlinear isolator is shown in Figure 1-4. The slope of the force-deflection curve at any point of interest is called "*tangent stiffness*" here which is also referred to as "dynamic stiffness" in some literature (e.g. [3-8]). It can be used as an equivalent stiffness in calculating the natural frequency assuming that the amplitude of oscillation is small enough and it is oscillating about that point. The tangent line is shown in red in the graph at a position marked x_e at which the tangent stiffness is minimum. The isolator can be loaded to this position statically for example, by the weight of the supported mass. The nonlinear isolator may be compared with a linear isolator with the same static deflection due to the mass. The force-deflection of such an isolator is shown by a dashed line in

Figure 1-4. The slope of this line is called “*static stiffness*” here which is considered as a parameter of the nonlinear isolator. It can be seen that the tangent stiffness is much lower than the static stiffness in this particular case.

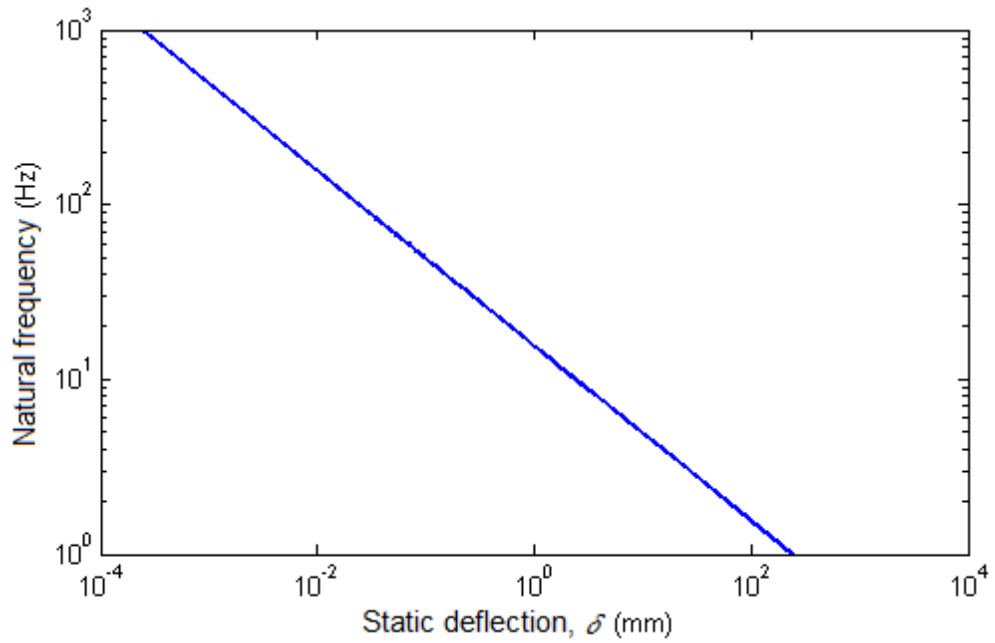


Figure 1-3: Natural frequency as a function of static deflection for a linear single degree of freedom system

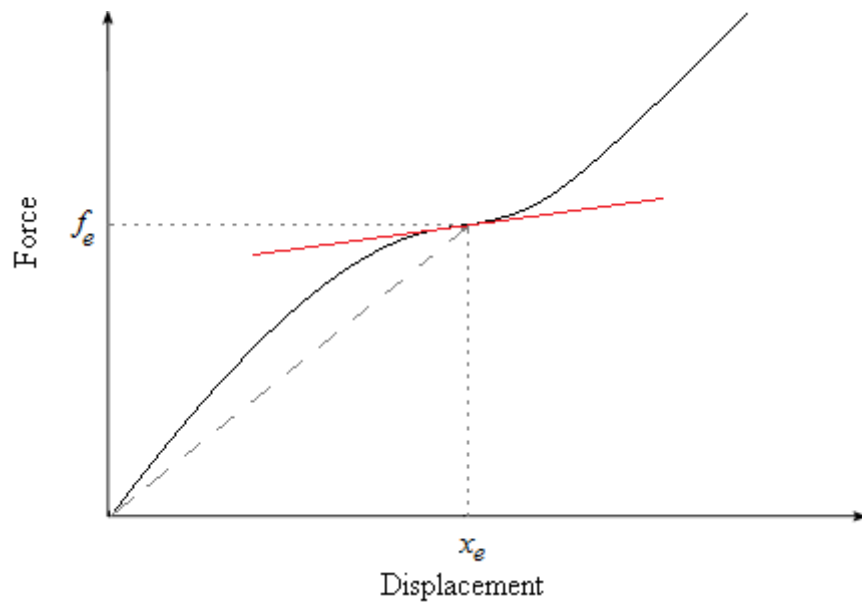


Figure 1-4: Schematic of a force-displacement curve of a nonlinear isolator, black line: force-deflection, dashed line: corresponding linear spring, red line: tangent to the curve at the statically loaded position

The large static stiffness keeps the static deflection within an acceptable range and the low tangent stiffness allows a low natural frequency when loaded, providing the amplitude of vibration is small. Such isolation mounts are referred to in some literature as “*High-Static-Low-Dynamic-Stiffness*” (*HSLDS*) devices (e.g. [6, 7])

There are several different approaches by which a force-displacement characteristic of the shape shown in Figure 1-4 can be achieved practically. Three of these are considered in this thesis: mechanisms, axially loaded buckled beams and a rubber mount.

1.3 Nonlinear vibration isolators

The literature reports a considerable number of studies on nonlinear vibration isolators. Ibrahim [8] published a comprehensive review on nonlinear passive vibration isolators. This covers a wide range of mechanisms and mounts. Some of these isolators are reviewed here in five different groups, in accordance with the thesis content. The sub-sections are named based on the distinguishing feature of the vibration isolator, but in some cases it may be possible to categorise them in more than one group. Nonlinear isolators that incorporate a mechanism with negative stiffness intervals are studied in the first sub-section. The second group uses magnets as the elements that provide negative stiffness. The third group are those that include beams as nonlinear springs. The last group is dedicated to viscoelastic isolators.

1.3.1 Negative stiffness mechanism

A desirable stiffness characteristic for nonlinear vibration isolators can be achieved by the addition of a mechanism with negative stiffness to a linear spring. Negative stiffness occurs when the restoring force becomes smaller as the displacement becomes larger. The system becomes unstable in this region and, when loaded “snaps through” to a range with positive stiffness. Different systems can possess negative stiffness. Previous studies on mechanisms which employ linear springs and a special linkage to achieve negative stiffness are addressed together in this section.

Alabuzhev et al. [9] presented different nonlinear vibration protection systems with Quasi-Zero-Stiffness (QZS) in their research monograph. The term QZS refers to systems that have zero tangent stiffness while loaded statically. Schematic diagrams of various QZS mechanisms are shown in Figure 1-5. They comprise of a load bearing elastic element with positive stiffness which is the vertical spring in the mechanisms shown in Figure 1-5. The addition of other springs through special mechanisms shown in the figure provides negative stiffness which adds to the stiffness of the vertical spring. Alabuzhev et al. studied these mechanisms statically and also obtained the dynamic response of a nonlinear oscillator with nonlinear restoring force of polynomial type as a general model for nonlinear isolators. The monograph ends with methods to design such isolators. However, they did not refer to nonlinear dynamics of the isolators in the last section on the design and only static force bearing capacity is considered at that stage.

Please refer to the mentioned reference.

Figure 1-5: Quasi-Zero-stiffness mechanism, arrow: force excitation, double headed arrow: possible movement of base [9]

Platus [10-12] introduced a negative stiffness mechanism and combined it with a linear spring to isolate sub-Hertz vibration. A snap-through mechanism was used to reduce the vertical stiffness while a column-beam arrangement was used to isolate horizontal movement. Commercial vibration isolators for vibration-sensitive instruments were built based on his work. Natural frequencies as low as 0.5 Hz were achieved for their vibration isolators. Ahn [13] investigated the performance of this vibration isolator by calculating the fundamental frequency of the isolator and used this to suggest design guidelines for nonlinear isolators.

Winterflood and Blair [14] introduced a long period vertical vibration isolator which is called a torsion crank linkage. This comprises of a mass hung on two crank arms which are held in place by a torsional spring (torsion rod) at the pivot end, as shown in Figure 1-6. The crank arm acts as an inverse pendulum which has negative stiffness. The angle ϕ defines the position at which the torsion spring is unloaded. The mass can move vertically up and down. The angle α is the statically loaded position. The mechanism geometry can be defined by three lengths r , l , and x , which are the crank-arm length, the supporting link length, and the offset distance respectively. They used the mechanism to accomplish low tangent stiffness in the vicinity of the working point. However, the mechanism attains negative stiffness in part of its displacement range by increasing the initial angle further which should be avoided.

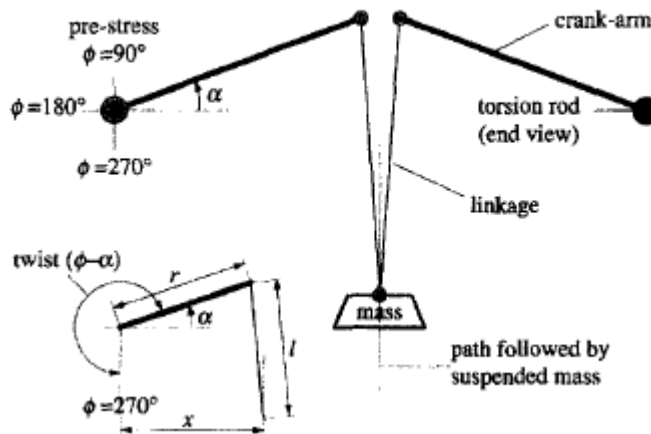


Figure 1-6: Schematic geometry of a pair of torsion sprung crank arm [14]

Carrella et al. [5] built a test rig to show the effect of negative stiffness on the free vibration of an oscillator. The mechanism consists of a horizontal beam that is hinged at one end with two coil springs attached to the middle to form a single degree of freedom rotational system. They showed that the frequency can be reduced by a factor of 4 when correction springs are attached through a lever to the beam.

Park and Luu [15] studied four different negative stiffness mechanisms and compared their performance in reducing the natural frequency of an isolator experimentally. They obtained the force-deflection equations for the mechanisms statically. They used them to set the parameters of the mechanisms to achieve the lowest possible natural frequency. The natural frequency was

obtained by measurements. They did not analyse the nonlinear dynamics of the mechanism or consider nonlinear effects in the measurements.

Carrella et al. analysed a QZS mechanism statically and optimized it to have the widest low stiffness displacement range in reference [3]. The force transmissibility of this mechanism is investigated in reference [16] by modelling it with a Duffing oscillator. They showed analytically that the nonlinear mechanism outperforms the linear system with equal static deflection. Kovacic et al. [17] analysed the forced response of the same mechanism loaded by static and dynamic loads simultaneously.

1.3.2 Magnet springs

The second group that can be used to achieve nonlinear characteristics are those implementing magnets. The principle of a magnetic anti-spring system is described in Figure 1-7. As magnets move with respect to each other in the vertical direction a vertical component of force appears. This vertical component opposes the movement and provides negative stiffness. Beccaria et al. [18] implemented magnets as anti-springs in an isolator proposed for the VIRGO gravitational wave detector. They showed that the vertical resonance of the isolator chain can reduce from 7 Hz to 2 Hz by the addition of magnets to the original isolator.

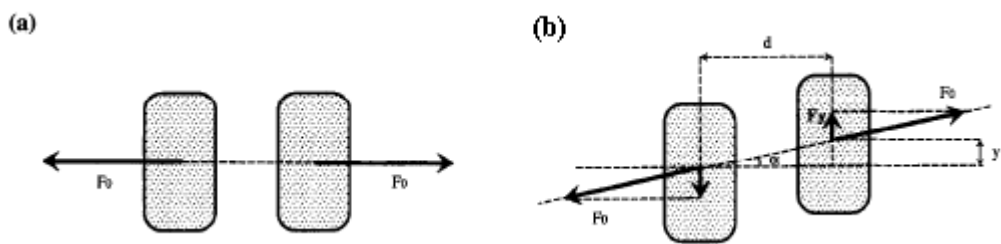


Figure 1-7: The principle of magnetic anti-spring systems, a) magnets at the equilibrium position, b) magnets moved with respect to each other in the vertical direction, F_0 : magnetic force, F_y : vertical component of magnetic force, d : distance between magnets [18]

The performance of magnetic anti-springs depends strongly on the horizontal separation between them. Winterflood and Blair [14] and Bertolini et al. [19] pointed out some

disadvantages of magnetic anti-springs such as difficulties in achieving a wide displacement range of stiffness neutralization and their strong dependency on temperature.

Carrella et al. [7] built a rig by adding magnets to a linear mass and spring, and studied the effect of nonlinear stiffness on transmissibility. The linear vibration isolator comprised of two vertical coil springs between which an isolated mass was mounted. Magnets were placed at the other ends of the springs and the isolated mass was itself a magnet. The magnets were arranged in such a way to attract each other and so form a negative stiffness that counteracts the positive stiffness of the spring. The resulting mechanism possessed low tangent stiffness around the static equilibrium point. The natural frequency reduced from 14 Hz to 7 Hz as a result of the addition of the magnets.

1.3.3 Beams as nonlinear springs

Beams that undergo large deformation exhibits nonlinear force-deflection thus potentially can be used as nonlinear spring for a vibration isolator. The tangent stiffness of a beam that is loaded axially in compression is reducing, which makes them a candidate to be used in nonlinear vibration isolators and different implementations of them are studied in the following sub-section. It is suggested beams loaded transversely have a softening characteristics [20] i.e. tangent stiffness becomes lower, thus suitable for nonlinear vibration isolation. A literature review on the force-deflection of beams going under large deformation and loaded transversely is presented in the sub-section 1.3.3.2.

1.3.3.1 Axially loaded buckled beams

The nonlinear force-deflection characteristics of axially loaded buckled beams make them a suitable candidate for use as spring elements of a vibration isolator directly or through some mechanisms. First, the mechanisms that incorporate buckled beams are reviewed here. These mechanisms can possess negative stiffness in part of their displacement range and can also be categorised in the negative stiffness mechanisms group which was reviewed in sub-section 1.3.1.

Another advantage of using buckled beams is to increase internal resonances of the isolator. The large static deflection in linear springs used to achieve a low natural frequency necessitates a

large mass of elastic material which in turn supports low frequency internal modes of the spring. This limitation can be overcome by using a column spring in its Euler buckled mode. The working range of the column spring can be adjusted to start just after buckling. As a result, the spring element is used for its dynamic working range, not for the static deflection which results in higher internal resonance frequencies and better isolation performance.

A column spring in its Euler buckling mode is used as a stiffness element in a high performance vibration isolator by Winterflood et al. [21, 22]. The mathematical analysis and experimental implementation of the Euler spring in the isolator are presented in reference [23]. It is argued that the mass of a Euler column may be (1/250)th of the mass of its linear spring equivalent, which makes the internal resonances occur at higher frequencies.

In reference [22], they proposed a pivoted lever mechanism to constrain the movement of Euler springs, which is shown in Figure 1-8. They showed that negative stiffness can be achieved through the beam that buckles to the side at which the pivot is situated, while the one that buckles away from the pivot has a positive spring rate. By combining the stiffness of these two springs a very low tangent stiffness is achievable. However, the resulting stiffness is significantly nonlinear and it is not so easy to achieve a very low stiffness by this method.

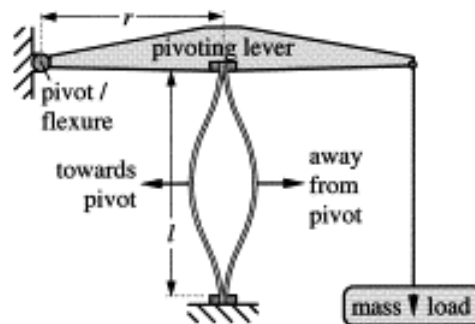


Figure 1-8: A simple structure for mounting and constraining Euler springs [22]

Lee et al. [24, 25] presented a negative torsional stiffness mechanism, shown in Figure 1-9. It comprised of a number of longitudinally compressed thin plates which are marked with (1') in Figure 1-9. They used the finite element method (FEM) to optimise the negative stiffness torsional element in order to achieve the required negative stiffness range with the smallest possible size.

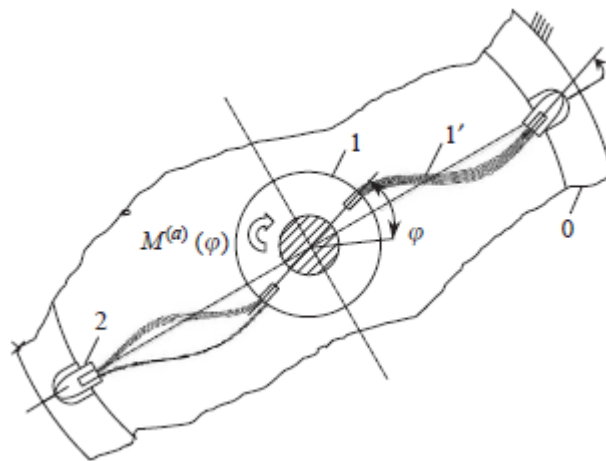


Figure 1-9: A schematic diagram of a negative torsional stiffness mechanism, the base link (0), movable connecting link (1), an insertion (2), and elements of elastic link (1') [26]

Lee and Goverdovskiy [27] studied the possibility of incorporating a negative stiffness element into a conventional passive vibration isolator used in the passenger seats of vehicles. They compared the performance of different isolators in the low frequency bands and concluded that the performance of the traditional vibration isolators is not ideal for that purpose. They introduced a nonlinear elastic element with variable torsion negative stiffness (TNS) to control the stiffness of the isolator. It is possible to add this element to any existing vibration protection mechanism and optimise its parameters to achieve the desired level of vibration protection. The experimental results of a combined nonlinear isolator with the original isolators of a land vehicle and a helicopter are presented. Results were obtained through laboratory tests as well as field tests which were matched with theoretical predictions. They did not consider the nonlinear dynamics of the isolator in either their tests or analysis.

The chaotic vibration of the same mechanism with negative stiffness elements is addressed in [26]. The Lyapunov largest exponent and Poincare map of phase trajectories were used to study stability. It is shown that although the negative stiffness elements have a tendency towards chaotic vibration, they cannot destabilize the motion of a combined mechanism.

Bertolini et al. [19] introduced a mechanism based on the torsion crank linkage. They replaced crank arms with tapered width cantilever beams (A in Figure 1-10) and used a disc (C in Figure 1-10) to connect link wires to the mass. A cross-sectional view of the experimental test rig they built is shown in Figure 1-10. The rig is made adjustable by the initial angle of the blades (defined by 'D' in the figure) and the blades' position (defined by 'E' in the figure). The

movement of disc ‘C’ changes the wire inclination, which affects the vertical component of the wire tension and provides negative stiffness in the mechanism. The test results agree very well with the analytical results, and the mechanism was shown to be capable of achieving natural frequencies down to 0.25 Hz. This mechanism is referred to as geometric anti-spring (GAS).

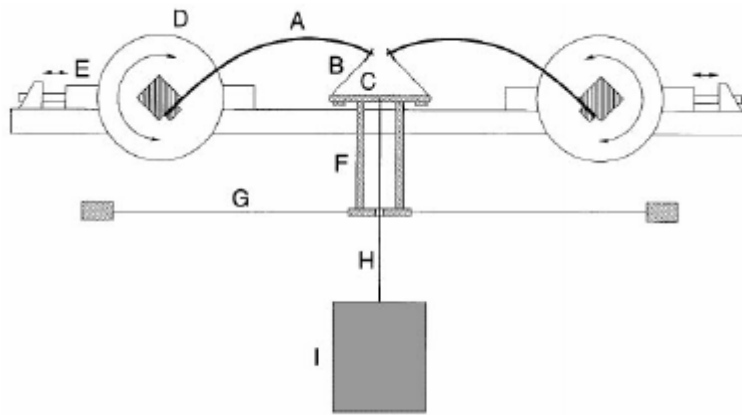


Figure 1-10: Cross-sectional view of GAS experimental test rig, (A) stressed blade, (B) link wire, (C) load disk, (D) angular movement of the blade base, (E) radial movement of the blade base, (F) anti-tilt tower, (G) anti-tilt centring wires, (H) suspension wire (or rod), (I) load [19]

The geometric anti-spring concept [19] was further developed into the monolithic geometric anti-spring (MGAS) to improve the GAS system performance significantly [28]. A schematic view of the MGAS mechanism is shown in Figure 1-11. The main advantage of this mechanism over the GAS is its simplicity. Fewer mechanical parts results in fewer unwanted natural frequencies which can reduce the performance of the isolators. The triangular shaped blade base is clamped and simulates a cantilever beam. The external force is applied to the centre where the vertices of the blades are joined. The symmetry causes the horizontal components of the force to cancel out and the mechanism can be treated as a single degree of freedom system. Depending on the load and separation of the clamps, the mechanism can become unstable under the applied load which is due to negative stiffness in parts of its displacement range.

The geometry of the mechanism can be chosen in such a way as to minimize the natural frequency. They concluded that nonlinearity is not a major problem for the application they considered, namely a vertical passive seismic noise attenuator conceived for ground-based gravitational wave interferometers. They also studied the thermal stability of the mechanism. It

is possible to reduce the sensitivity of the mechanism to temperature variations, but it is difficult and probably requires trial and error adjustments. They did not report any experimental work.

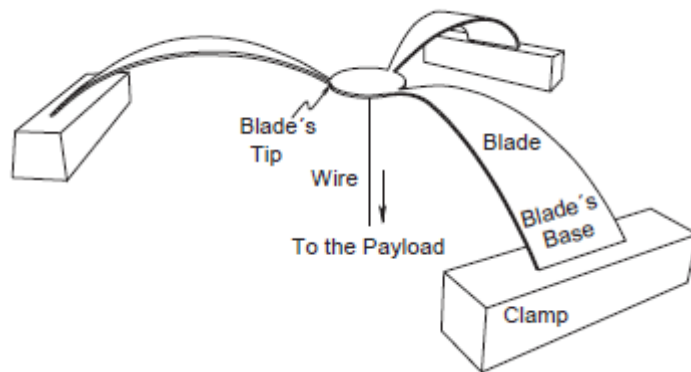


Figure 1-11: Schematic view of the Monolithic geometric anti-spring mechanism [28]

Virgin and Davis [29] studied the buckled beam to be implemented directly as a vibration isolator. They used an approximate second order solution to find the force-deflection characteristics and stiffness of a buckled simply supported straight beam. An experimental rig was used to validate their results. They measured transmissibility across the mount. They showed that a lower level of transmissibility is achievable by implementing buckled beams as vibration isolators compared to a linear one. A linear isolator would need a static deflection four times the one they measured to achieve the same natural frequency.

Shoup [30] used a pair of initially straight strips that were clamped in a semi-circular shape to form a nonlinear shock and vibration isolation mount. It was claimed that the low tangent stiffness provides vibration isolation from very low frequencies, while hardening springs can prevent excessive deformation due to shock inputs. He obtained the force-deflection curve for the strip pair and used the Ritz averaging method to obtain the dynamic response. He showed that the response is of a hardening type. Shoup and Simmonds [31] introduced an adjustable version of the vibration and shock isolation mount comprised of clamped strips. They obtained the force-deflection curve for different distances between the load and clamp. A design routine based on maximum bending stress of the strips was also proposed.

Plaut et al. [32] considered a buckled fixed-fixed beam as a vibration isolator. They obtained non-dimensional governing differential equations and considered harmonic base excitation.

They considered a solution comprised of a static equilibrium part and a dynamic part. These were solved numerically. Displacement transmissibility was obtained for different static loads and beam dimensions. It was shown that a wide frequency range of isolation is achievable by implementing buckled beams.

Plaut et al. developed their model to a two degree of freedom system in [33]. They considered an asymmetric bar to be supported by two buckled columns or two pairs of pre-bent columns bonded by a viscoelastic filler. The transmissibility of the centre of mass was obtained for a low range of frequencies. They showed that asymmetry introduces an additional peak between the first and second mode compared to the symmetrical model. El-Kafrawy et al. [34] considered the same bar isolated with only straight buckled columns. They compared two cases of allowing horizontal movement of the bar and preventing horizontal movement of the bar, concluding that good isolation is achievable in both cases. Jeffers et al. [35] continued the previous work and considered a three-dimensional model. They isolated a plate with four pairs of pre-bent columns bonded with viscoelastic material. They considered a symmetric and asymmetric plate, solving for the response numerically. They showed that the isolation method is effective for a wide range of excitation frequencies. El-kafrawy et al. [36] considered the same configuration, but only considered a straight buckled column. Here again, they compared two cases of allowing lateral movement of the plate and preventing it.

1.3.3.2 Beams loaded transversely undergoing large deformation

The large deformation of beams must be investigated in order to assess their suitability as spring elements of nonlinear vibration isolators. Large deflection of a simply supported beam, loaded centrally, seems to be a simple example to which large deflection theory can apply. However, it is revealed that there is some misinterpretation in the literature about its nonlinear characteristics, which is addressed in chapter 3.

The problem of large deformation of beams has attracted a lot of attention and some different methods have been suggested to solve this problem. Frisch-Fay [37] has cited most of the work up to its publication date in his book “Flexible bars”. Bishop and Drucker [38] presented an analytical solution for the large deflection of a cantilever beam loaded at its tip in terms of elliptical integrals. Conway [39] found a solution for the large deflection of a simply supported beam. He considered the distance between the supports to be fixed without considering axial

stresses. By these assumptions, this is the case of a beam that can slide on the supports and the length of the beam between supports is variable which is not his definition of the case. The problem was solved for two cases of the vertical reaction at the supports and for a perpendicular reaction force with friction. Gospodnetic [40] considered a thin elastic beam deflected by three symmetrically arranged knife-edged supports. In the absence of friction, he considered that the supports exert forces normal to the deflected beam and are situated at fixed distances from each other while the beam could slide. He also found the solution in terms of elliptical integrals. The ratio of the maximum deflection obtained from the nonlinear theory and the linear theory as a function of applied force was plotted. It was claimed to be different from the analogous diagram given in reference [39].

Sundara Raja Iyengar and Lakshmana Rao [41] studied the same problem as the one in reference [39] and considered a uniformly distributed load in addition to the concentrated load. They used a power series expansion for the angle along the beam length to find the solution for the problem.

Wang et al. [42] used a numerical method to find the large deflection of a cantilever loaded along its length and a simply-supported beam loaded partially along its length or by a concentrated load. He used the finite difference method to find a solution for the bending differential equation along the length of the beam and compared the results with experimental results. Wang [43] introduced a different numerical method based on integrating along the horizontal axis for a cantilever beam loaded at its end and for a simply supported beam subject to a non-symmetrical load. In reference [44] equations for a cantilever and a simply supported beam with a distributed load were integrated to obtain the relationship between the angle along the beam, the projection in the axial direction and the load. Numerical methods were then implemented to solve the problem and deflections were calculated using numerical integration.

Beléndez [45] restated the analytical solution for a cantilever beam loaded at its tip using an elliptical integral and compared the results of analytical and numerical solutions with experimental results.

Thomsen [20] studied vibration of a simply-supported beam under a harmonic concentrated force at its midpoint. He considered simply-supported beams with moveable and immovable supports. The Galerkin method was used. The effect of shortening of the projection length in the

axial direction was not considered, which resulted in the erroneous conclusion that a simply supported beam with movable supports acts as a softening system.

1.3.4 Viscoelastic vibration isolation mounts

Rubber is widely utilized in vibration isolation mounts. It has been shown that the stiffness and loss factor of rubber materials depend on the temperature and frequency of oscillation [46, 47]. McCallion and Davies [48] studied the effect of temperature, frequency and also amplitude of oscillation on the mechanical properties of rubber under compressive loading. The variation in stiffness, hysteresis energy absorbed in a cycle, and resilience are shown in their paper through experimental data. They have also tried to develop expressions to model the dynamic behaviour of a rubber-like material.

Shaska et al. [49] investigated characteristics of a butyl rubber isolator loaded in shear and the potential advantage over linear isolators. They obtained the effective shear modulus and effective loss factor as a function of excitation amplitude. They showed that the transmissibility of the nonlinear isolator is less than the linear isolator when the excitation frequency exceeds a particular frequency, where this frequency depends on temperature and excitation amplitude.

The nonlinear characteristics of rubber due to pre-stress is addressed by Harris and Stevenson [50]. In the design of engine mounts, a primary and secondary stiffness are usually considered based on geometry change. The tangent stiffness is assumed larger than static stiffness with a correction factor in the range of 1.2-1.4 [51, 52].

Geometrical nonlinearities can be used to achieve a low tangent stiffness for a statically loaded rubber mount. Richards and Singh [53] proposed a method to characterize the nonlinear properties of stiffness of rubber based on force-deflection measurements. They tested three different types of mounts. One of which had geometrical nonlinearities and a reduced dynamic stiffness at the loaded position. Kim and Singh [54] developed a method to identify the multi-dimensional frequency-dependent transfer stiffness over a wide frequency range. The effect of preload, temperature and amplitude of oscillation is not considered in their study. They tested their method on the same mounts as the previous study. Zhang and Richards [55] proposed a

parameter identification method for rubber isolator mounts where the Maxwell model is used to represent the isolator mounts. The method is tested on three vibration isolation mounts. It is shown that the model with two Maxwell elements can accurately represent the measured static and dynamic characteristics of rubber isolator mounts.

1.4 Dynamic response of nonlinear vibration isolators

Linearization of the force-deflection relation can be used to investigate a system with nonlinear stiffness. This approach has been adopted by many researchers to study nonlinear vibration isolators. However, it is only valid for small oscillations about the working position and does not address the nonlinear dynamics of oscillators. There are also reports on measured dynamic response spectra for different excitation types in which nonlinear dynamics of the isolators is not discussed. (For example refer to references [14, 18, 21, 22, 27, 32-36, 50])

Methods of analysing the nonlinear dynamics are well established [56, 57]. Kirk [58] investigated the response of vibration isolators with nonlinear stiffness under random excitation. Ravindra and Mallik [59] studied the performance of nonlinear isolators under harmonic excitation. They considered both stiffness and damping nonlinearities, with a symmetric and asymmetric restoring force. They used the Harmonic Balance Method (HBM) to obtain the response. It is concluded that a vibration isolator with softening stiffness outperforms one with a hardening stiffness. The effect of damping was also investigated in their work. It was shown that the nonlinear isolator with asymmetric stiffness does not isolate base excitation satisfactorily for the parameters they chose in their studies. Their analysis was limited to some specific values for the parameters of the system and they did not explore all nonlinear dynamic features of such isolators.

Carrella et al. [16] studied the dynamic response of a quasi-zero stiffness isolator by using an approximation based on a model that consisted of a Duffing oscillator without a linear stiffness term. The HBM was used to obtain the response of the system at the excitation frequency. The force transmissibility of the isolator was obtained and it was concluded that the nonlinear isolator offers a performance advantage over a linear one provided that the system parameters are chosen appropriately and the excitation amplitude is limited. Kovacic et al. [17] considered

the effect of static load on the same isolator and investigated period doubling bifurcation and its development to chaotic motion. It was shown that improvement of static characteristics can be achieved in this case by incorporating a nonlinear softening spring in the vibration isolator; however this can lead to period-doubling bifurcations for such a nonlinear vibration isolator under static and dynamic excitation simultaneously.

The force transmissibility of a nonlinear isolator is compared to its displacement transmissibility in reference [6]. The isolator is tuned in such a way that its minimum stiffness is greater than zero and it is modelled by a Duffing oscillator with hardening nonlinearities. It is shown that, unlike a linear isolator, the force and displacement transmissibility are not the same. The performance of the same nonlinear isolator which is tuned in a way that potential energy of the system has a double-well is investigated by Lu et al. [60] under random excitation. It is shown that an isolation region occurs between the two troughs of the transmissibility plot. These troughs can be shifted by applying a harmonic control load.

A nonlinear isolator with cubic stiffness and damping nonlinearities is studied by Milovanovic et al. [61]. They compared the performance of the nonlinear isolator with cubic viscous damping and linear damping in displacement transmissibility. The stiffness of both isolators is considered to be comprised of linear and cubic stiffness terms. They showed that a finite value of damping is required for a given nonlinear stiffness to achieve a bounded response for a base excited system. Although the system with cubic damping has a better displacement isolation performance in the resonance region, the transmissibility at high frequencies is much higher compared to the isolator with a linear damper.

A vibration isolator system for a vehicle seat is proposed by Le and Ahn [62]. They used a negative stiffness mechanism to reduce the tangent stiffness of a vehicle seat isolator. They used the HBM to obtain the dynamic response at the excitation frequency. The advantage of the isolator over conventional isolators was demonstrated through measurements of steady state and transient response to harmonic excitation and also random excitation.

1.5 Thesis objectives

The literature review has shown that there is interest in both academia and industry to improve the performance of isolation mounts by using nonlinear stiffness elements. Much of the previous work on this subject has been on the static characteristics, or on the linearised dynamics of nonlinear isolators; few references have addressed the nonlinear dynamics of such mounts. In particular, the dynamic response of a nonlinear isolator with asymmetric stiffness has not been investigated thoroughly in previous work. The asymmetry can be an inherent characteristic of the mount or can be due to mistuned loading. This thesis addresses this issue with the following objectives:

- To establish the static characteristics of a nonlinear isolator with low tangent stiffness consisting of a QZS mechanism. The design of a test rig based on this mechanism is also considered.
- To consider whether a beam can be used as a nonlinear stiffness element in an isolator.
- To determine whether a commercially available rubber mount can be modelled by a curved- beam model.
- To determine the force transmissibility of a nonlinear isolator with asymmetric stiffness and to investigate its effectiveness.
- To quantify the performance of a nonlinear isolator comprised of curved beams as spring elements in suppressing the transmitted force, and to determine if it can be modelled as a Duffing oscillator.

1.6 Contributions of the thesis

The contributions of the thesis are:

1. It is shown that a mechanism with low tangent stiffness is easily adjustable for different static preloads. A detailed comparison between this mechanism and a similar one with low tangent stiffness is presented and the benefit of each one as a nonlinear isolator is highlighted.

2. It has been found that a simply supported beam loaded transversely in the middle acts as a hardening spring for large deformations, contrary to claims made in the literature.
3. The minimum tangent stiffness and its corresponding static stiffness are obtained as functions of initial curvature angle of curved beams, and the eccentricity of the loading for straight beams. The stiffness graphs are proposed as a measure of isolation performance for mounts with them as their spring elements. It has been found that an order of magnitude reduction in the tangent stiffness compared to a linear isolator with the same static deflection can be achieved.
4. It was determined that a bell-shape commercially-available rubber isolation mount cannot be adequately modelled by a curved beam. The variability in stiffness characteristics between nominally identical mounts was also measured and quantified which demonstrates the requirement of considering the nonlinear effect of variation of loading on performance of nonlinear isolators.
5. The effects of static preload and incorrect values for the supported mass, as sources of asymmetry in stiffness, on the force transmissibility of a model for such nonlinear isolation based on a Duffing oscillator model have been established. It has been shown that a nonlinear isolator outperforms a linear one for a relatively wide range of static preload or incorrect values for the supported mass, i.e. a degree of robustness for its use has been established.
6. The effectiveness of a vibration isolator comprised of curved beams as its spring elements is established dynamically. However, it has also been found that the time history of the transmitted force exhibits periodic impulse-like behaviour, which is attributed to the existence of a high range of values for the asymmetric stiffness. Implementing a linear spring in series with the curved beam is suggested as a method to overcome this problem and this alternative is compared with using a linear spring alone.

1.7 Thesis outline

A ‘snap-through mechanism’ that possesses a negative stiffness region is analysed in chapter 2. It is added to a vertical spring to form a QZS mechanism. Its parameters are optimised to obtain the widest displacement range for which low stiffness occurs. It is compared with another QZS

mechanism that was formed of oblique springs in addition to the vertical one. Measurements made on a snap-through mechanism are presented at the end of the chapter.

Large deformation of beams is studied in the chapter 3. The principal theory is presented and this is followed by an investigation of the large deformation of a simply supported beam loaded transversely. An approximate solution is obtained for the beam's force-deflection characteristics and the results are compared with those obtained by using the finite element method. The buckling and post-buckling of an axially loaded beam is studied in section 3.4. The reduction in the tangent stiffness of the beam at buckling makes the post-buckled beam a candidate for the spring element of nonlinear vibration isolators. The beam loaded eccentrically and curved beams are also studied as alternatives to the post-buckled beam in order to improve its characteristics for isolation purposes. A case study is presented at the end of the chapter in which the effect of higher order resonances of the curved beam on vibration isolation performance is evaluated.

A commercially available rubber isolation mount, called a *bubble mount*, is studied in chapter 4. Measurements for the force-deflection characteristics of the mount are presented and the possibility of modelling the bubble mount as a curved beam is investigated. The variability in characteristics of these bubble mounts is also addressed through measuring the force-deflection curve for a set of nominally identical mounts.

The nonlinear dynamics of vibration isolators with asymmetric stiffness is studied in chapter 5. Differential equations for the forced response of the Duffing oscillator are presented. A QZS mechanism is reintroduced as an example of an isolator that can be modelled by the Duffing equation. The effect of static preload on the nonlinear dynamics of a Duffing oscillator with purely cubic stiffness is then investigated. The forced response is obtained, followed by force transmissibility. The effect of mistuned mass on the dynamic response is addressed in section 5.5 by considering its forced response and the isolation frequency as a function of mistuned mass. The effect of an additional linear stiffness term on a Duffing oscillator dynamic response is addressed in section 5.6.

The dynamic response of a vibration isolator that is comprised of curved beams is investigated in chapter 6. A model of the curved beam isolator is presented in section 6.2. The forced response of the curved beam isolator for different initial curvature angles is obtained in section

6.3 followed by a study of the effect of static preload. The force transmissibility of the isolator is obtained and is used to evaluate the performance of the isolator in the next section. The transmitted force in the time domain is addressed in the section 6.7.

The thesis closes with conclusions and suggestions for future work in chapter 7.

2 Quasi-Zero-Stiffness (QZS) mechanisms

2.1 Introduction

Quasi-Zero-Stiffness (QZS) mechanisms are so called because they can be tuned to possess zero tangent stiffness for infinitesimally small displacements in the vicinity of the statically loaded position. One method of achieving such a characteristic is to implement mechanisms with snap-through instability [63, 64] in parallel with the main load bearing elastic elements. The instability in these mechanisms is due to the existence of a displacement range where stiffness is negative. By loading these mechanisms, they perform like a softening spring up to a point after which there is a negative stiffness range. By increasing load further, they snap through an unstable equilibrium point to the other stable arrangement. By adding such a mechanism to a vibration isolator mount, the isolator keeps its static load bearing capability but with reduced tangent stiffness when statically loaded.

There are several mechanisms that possess snap-through instability and these are referred to here as “snap-through mechanisms”. The static behaviour of a snap-through mechanism is studied here. A QZS mechanism is formed by adding this mechanism to a linear spring and adjusting the mechanism parameters. The QZS mechanism is studied statically as well and the range at which the stiffness is less than the stiffness of the vertical spring is obtained. It is shown that the mechanism could easily be tuned for different loads by making the vertical spring position adjustable.

The QZS mechanism that is the subject of this chapter is compared with a similar mechanism that has previously been investigated by Carrella et al.[3]. The force and stiffness equations are stated using consistent notation and the variation of force and stiffness as a function of displacement for the two mechanisms are compared. The source of difference between the two mechanisms is also identified.

A test rig that is similar to one of the snap-through mechanisms exists in the ISVR. It was introduced as a tuneable vibration absorber by Bonello et al. [65]. The model of the snap through mechanism is used to predict the behaviour of the test rig. It has been tested to confirm the theory presented here, and to find the possible practical difficulties in the design of such a test rig. A hammer test and also a shaker test with base excitation were used to conduct the measurements.

The aim of this chapter is to evaluate statically the possibility of utilising a QZS mechanism as a nonlinear vibration isolator and to establish the dependency of its characteristics on the mechanism parameters. To achieve these, the snap-through mechanism is introduced in section 2.2. The QZS mechanism has been studied in section 2.4. The effect of preload on the QZS mechanism is investigated in the next section. Two QZS mechanisms are compared in section 2.6. The test rig is introduced, modelled and test results are presented in section 2.3. The chapter finishes with conclusions.

2.2 A snap-through lever mechanism

A mechanism is investigated in this section that possesses negative stiffness over a finite displacement range. The mechanism is comprised of two levers that are hinged at one end and sliding at the other end. The levers are further connected by a lateral spring. The mechanism is shown in Figure 2-1 (a). It is similar to one of the mechanisms that was studied in reference [9] and also a mechanism studied by Bonello et al. [66]. The position of the lateral spring of the mechanism studied here is different, which introduced a geometrical coefficient in the equations that is described later in this section. A static force F is applied vertically at the hinge, and the displacement x of the same point is measured in the vertical direction. The free body diagram of the hinge is shown in Figure 2-1 (c) where F_l and F_r are the reaction of the left and right levers

respectively and F is the applied force. In Figure 2-1 (b), the free body diagram of the right lever is illustrated. F_s is the spring force and F_n is the surface reaction force. The forces acting on the hinge, the applied force F and the levers' reactions, must be in equilibrium (Figure 2-1 (c)) such that,

$$F = F_r \sin \varphi + F_l \sin \varphi = 2F_r \sin \varphi \quad (2-1)$$

since, by symmetry, $F_l = F_r$. From Figure 2-1 (b), the lever reaction can be derived as a function of the spring force F_s ,

$$F_r \cos \varphi = F_s \quad (2-2)$$

By substituting F_r from equation (2-2) into equation (2-1), the following expression can be obtained for the applied force, F .

$$F = 2F_s \tan \varphi \quad (2-3)$$

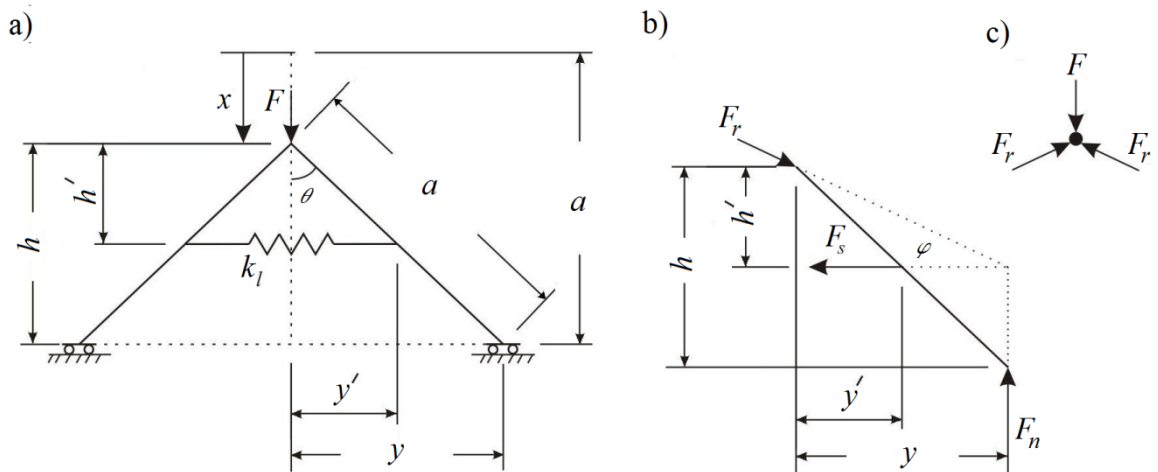


Figure 2-1: a) The lever mechanism shown at an arbitrary position, b) free body diagram of the right lever, c) Free body diagram of hinge

Let the values of y , x and θ when the spring is unstretched be y_0 , x_0 , and θ_0 . Also, define the parameter β as h'/h or equivalently y'/y which determines the vertical position of the lateral spring. Then the following equations can be derived for $\tan \varphi$ and F_s .

$$\tan \varphi = \frac{h'}{y} = \beta \frac{h}{y} \quad (2-4)$$

$$F_s = k_l(2y' - 2y'_0) = 2k\beta(y - y_0) \quad (2-5)$$

Substituting for F_s and $\tan \varphi$ from equations (2-4) and (2-5), equation (2-3) can be rewritten as:

$$F = 4k_l\beta^2 h \left(1 - \frac{y_0}{y}\right) \quad (2-6)$$

The length h can be obtained in terms of x and a , the lever length,

$$h = a - x \quad (2-7)$$

The distance of the movable support from centre, y can also be obtained in terms of x , and a :

$$y = \sqrt{2ax - x^2} \quad (2-8)$$

The initial position of movable support, y_0 , can be obtained as a function of unloaded angle θ_0 , and the length of the lever, a ,

$$y_0 = a \sin \theta_0 \quad (2-9)$$

The applied force, F , can be derived in terms of x by substituting equations (2-7), (2-8), and (2-9) into equation (2-6):

$$F = 4k_l\beta^2(a - x) \left(1 - \frac{a \sin \theta_0}{\sqrt{2ax - x^2}}\right) \quad (2-10)$$

The above equation can be non-dimensionalised by dividing throughout by ak_l and defining non-dimensional displacement \hat{x} equal to x/a , so that,

$$\frac{F}{ak_l} = 4\beta^2(1 - \hat{x}) \left(1 - \frac{\sin \theta_0}{\sqrt{2\hat{x} - \hat{x}^2}} \right) \quad (2-11)$$

The non-dimensional force as a function of non-dimensional displacement is shown in Figure 2-2. The graphs are plotted for different values of initial angles. Despite different initial angles, all the curves meet each other at the non-dimensional displacement equal to one where the mechanism is horizontal and the levers' reactions have no vertical component. There is an unstable equilibrium position at the horizontal position. The curves are anti-symmetric about the unstable equilibrium position. By loading the mechanism, the force increases to its maximum where the tangent stiffness is equal to zero and after this point it snaps through the horizontal position. The tangent stiffness is negative from this point to the local minimum point where the tangent stiffness is zero again. The negative tangent stiffness causes an unstable displacement range. By increasing the initial angle, the maximum force before snap-through occurs decreases and the displacement range at which the stiffness is negative becomes smaller.

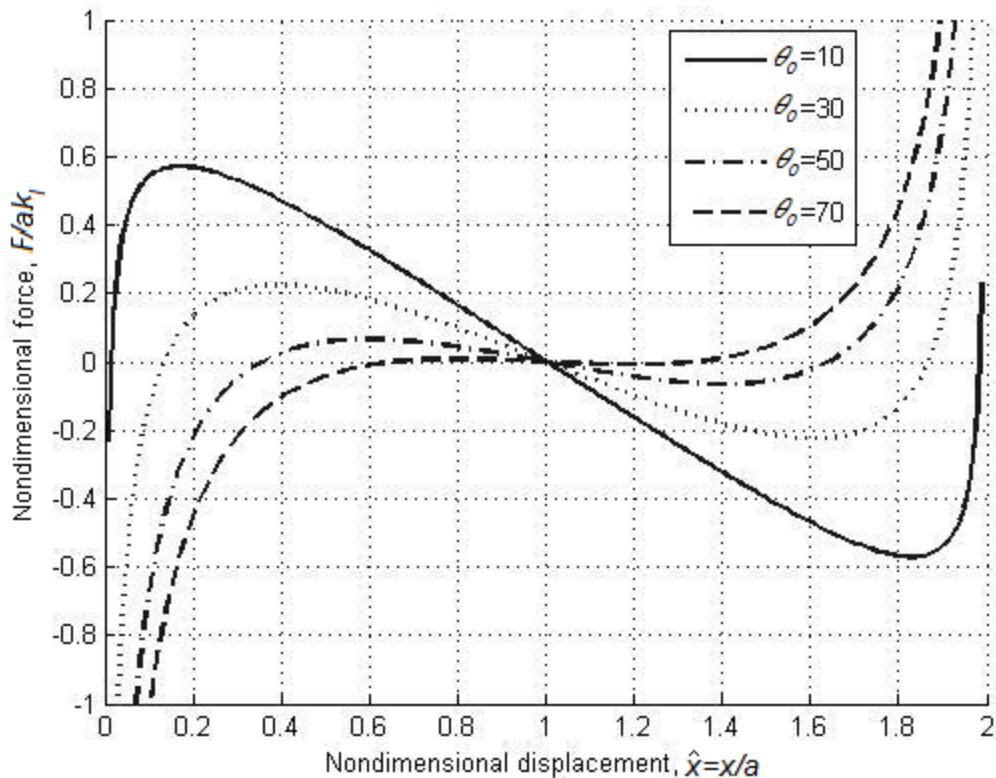


Figure 2-2: Non-dimensional force-displacement curves for the mechanism of Figure 2-1 ($\beta=0.5$)

The tangent stiffness can be obtained by differentiating the force-deflection relation governed by equation (2-10). In non-dimensional terms,

$$\hat{K} = 4\beta^2 \left[\frac{\sin \theta_0}{(2\hat{x} - \hat{x}^2)^{\frac{3}{2}}} - 1 \right] \quad (2-12)$$

where the non-dimensional stiffness is defined as $\hat{K} = K/k_l$. The non-dimensional stiffness as a function of non-dimensional displacement is shown in Figure 2-3. The stiffness is symmetrical about the unstable equilibrium position, i.e. $\hat{x} = 1$. The displacement range at which stiffness is negative and the absolute value of the stiffness both decrease by increasing initial angle. By differentiating the stiffness with respect to the displacement and setting it equal to zero, it is revealed that the stiffness is minimum when the levers are in the horizontal position.

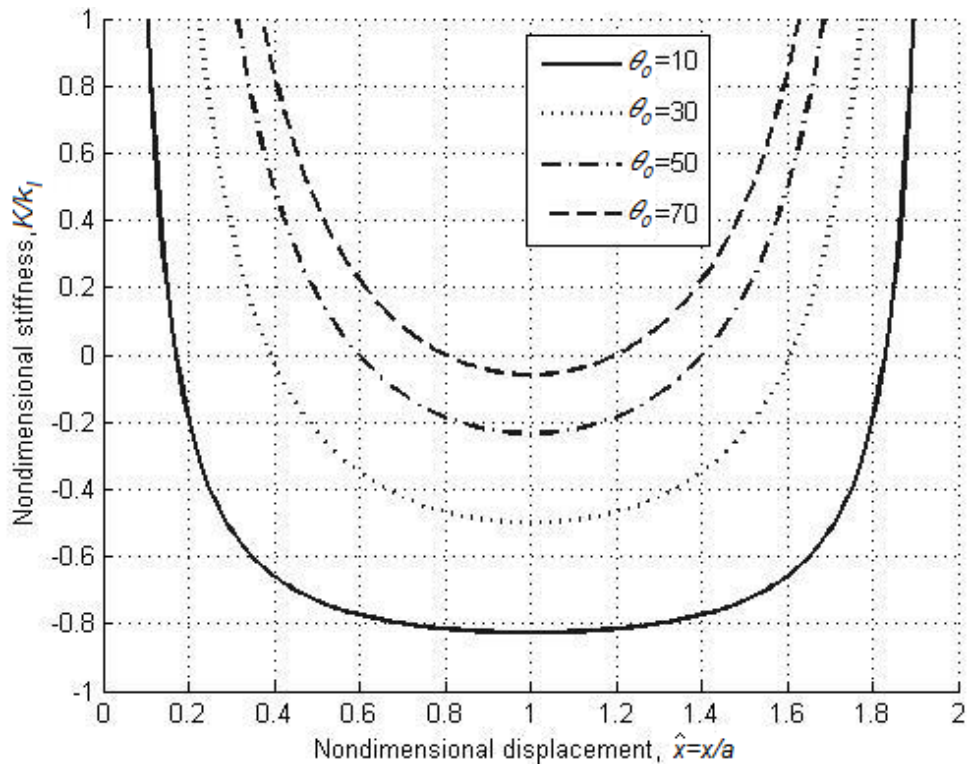


Figure 2-3: Non-dimensional stiffness of the mechanism as a function of non-dimensional displacement ($\beta=0.5$)

By substituting non-dimensional displacement equal to one in equation (2-12), the minimum stiffness is found to be,

$$\frac{K_{min}}{k_l} = 4\beta^2(\sin \theta_0 - 1) \quad (2-13)$$

The displacement interval at which the stiffness is negative can be found by finding the positions at which the stiffness is zero,

$$\hat{x}|_{K=0} = 1 \mp \sqrt{1 - (\sin \theta_0)^{2/3}} \quad (2-14)$$

The displacement range at which the stiffness is negative is shown in Figure 2-4 and is defined by the hatched area. It is symmetric about the line passing through the non-dimensional displacement equal to unity where the mechanism is horizontal. The displacement range at which the stiffness is negative becomes smaller as the initial angle increases. The negative stiffness range extends to the entire displacement range as the initial angle approaches zero.

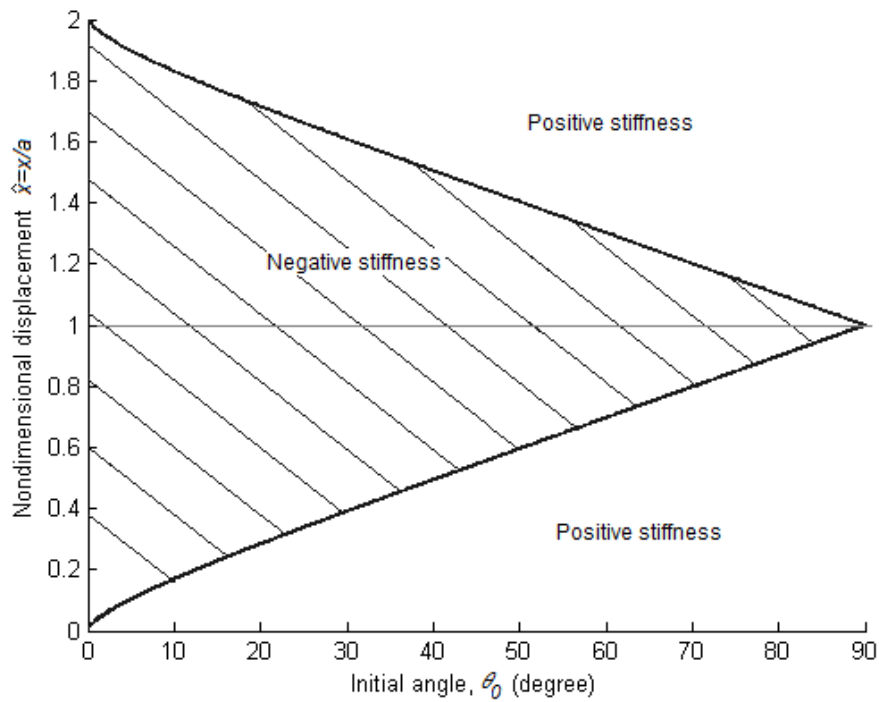


Figure 2-4: The negative stiffness displacement range as a function of initial angle

2.3 Experiment on a snap-through mechanism

A mechanism similar to the snap-through lever mechanism but based on the click mechanism of an insect flight motor [67] was studied by Bonello et al. [65, 66], for which a demonstrator test rig was built and tested at ISVR [66].

The stiffness of the rig is adjustable and it was originally used as an adjustable tuned vibration absorber. Bonello et al. [66] measured the natural frequencies for different distances between the levers and its response for different excitation amplitudes. By keeping the mass of the absorber constant, the variation in natural frequencies is due to changes in the rig stiffness. The capability of changing the natural frequency enables it to adapt to a different working frequency and perform over a range of excitation frequencies. Some measurements have been performed on the rig here to identify the possible practical difficulties in conducting experiments on such mechanisms and to provide an illustration of a similar mechanism with strong nonlinearity.

In studying the snap-through mechanism in section 2.2 the focus was on the snap-through behaviour relating to the displacement range at which the stiffness is negative. The stiffness was calculated at the unstable equilibrium position which is used later in this chapter to form a QZS isolator. However, it is not possible to measure the rig property at its unstable equilibrium position. Therefore, the tests are conducted without applying any load on the rig. The equivalent weight of the rig considering its stiffness is negligible and so the rig could be assumed to be at its initial unloaded position.

The rig is shown in Figure 2-5. It comprises two vertically orientated cantilevers which play the lateral spring role in the mechanism. The restoring force is generated due to outward bending of the cantilevers. Two levers are hinged by small bearings to the free end of the cantilevers. The other ends of the levers are hinged together where two small mass are attached to the mechanism. By applying a downward force to the top joint, the joint moves down and the angle between the levers gets wider. An adjusting bolt at the bottom of the rig can be used to change the distance between the cantilevers which changes the stiffness.

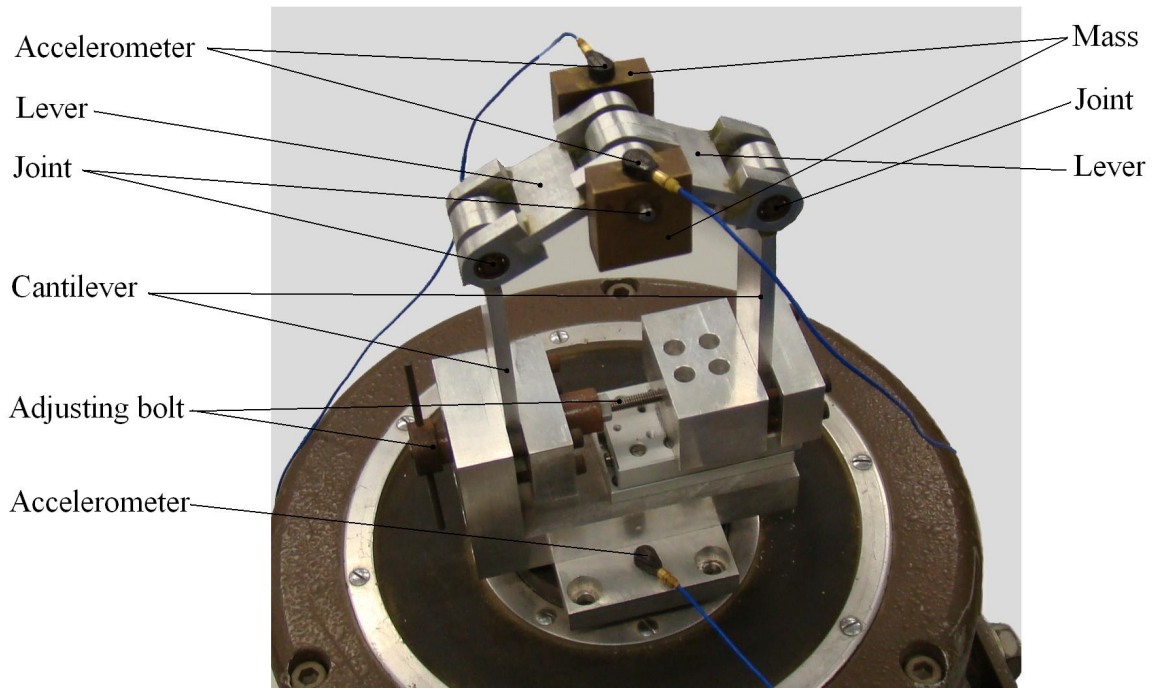


Figure 2-5: The experimental rig

A schematic diagram of the undeformed rig is shown in Figure 2-6 (a). It differs slightly from the snap-through mechanism of section 2.2. The horizontal component of the cantilevers' reaction replicates the lateral spring force in the snap-through mechanism. Equation (2-5) can be rewritten for the rig,

$$F_s = k_c(y - y_0) \quad (2-15)$$

where F_s is the horizontal component of the cantilevers' force, y is half of the distance between the two cantilevers' tips, k_c is the stiffness of the cantilever at its tip due to horizontal loading, and y_0 is this distance at the unloaded condition. The cantilevers are connected to the end of the levers, thus, parameter β which defines the position of the lateral spring in equation (2-5) is equal to unity.

Replacing the above equation with the lateral spring force in equation (2-11), the applied force F can be derived for the rig,

$$\frac{F}{ak_c} = 2(1 - \hat{x}) \left(1 - \frac{\sin \theta_0}{\sqrt{2\hat{x} - \hat{x}^2}} \right) \quad (2-16)$$

where \hat{x} is the non-dimensional displacement and is equal to x/a . The non-dimensional stiffness corresponding to equation (2-12) can be similarly obtained, and is given by,

$$\frac{K}{k_c} = 2 \left[\frac{\sin \theta_0}{(2\hat{x} - \hat{x}^2)^{\frac{3}{2}}} - 1 \right] \quad (2-17)$$

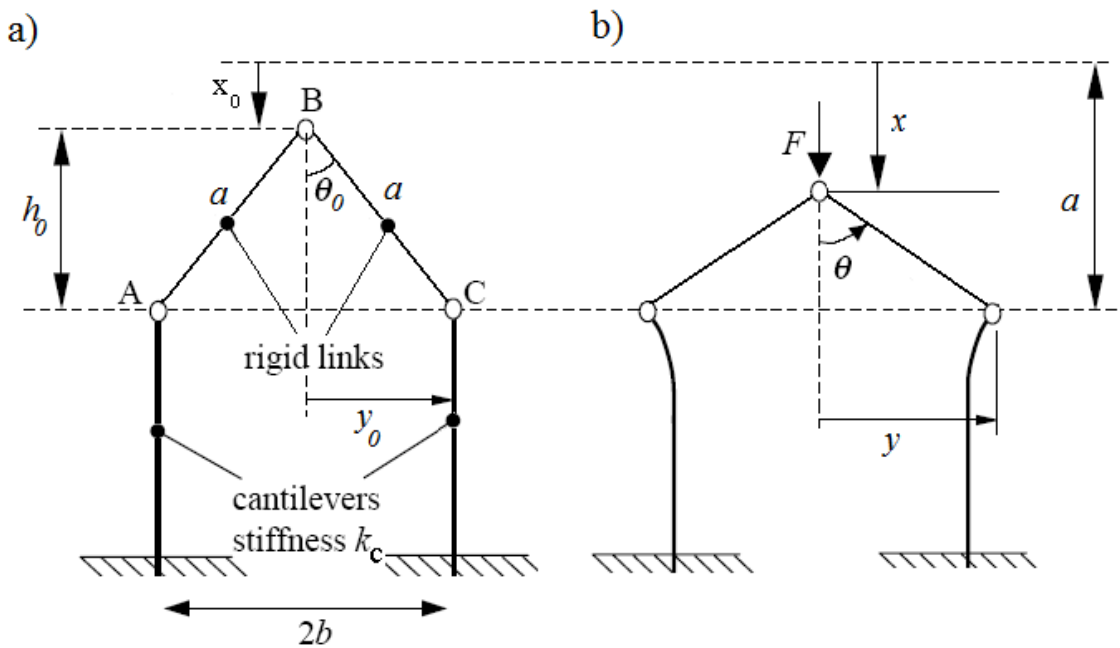


Figure 2-6: Schematic diagram of Bonello's rig a) un-deformed b) deformed [66]

The predicted force versus displacement is plotted in Figure 2-7. This graph is plotted using equation (2-16). To plot the force-displacement in dimensional form, the stiffness of the rig is calculated by measuring the cantilevers' dimensions. The calculated stiffness is 222 kN/m. The lever length is 40 mm. The force is calculated for three different distances between the levers which is stated on the graph with corresponding initial angles. For small vibration, the force displacement function can be considered as linearized around the static equilibrium position. The dashed lines represent the linearized force-displacements at the unloaded position and the slope of these lines defines the tangent stiffness.

It is apparent from this figure that the slopes of these dashed lines (stiffness) decrease with increase in initial angle. The stiffness can be calculated from equation (2-17) at each

equilibrium position. The consequence of changing stiffness is variation in natural frequency which can be observed in practice by measuring FRFs.

Although the test rig is nonlinear, the high stiffness of the cantilevers makes it very difficult to oscillate it with large enough amplitude to obtain nonlinear behaviour. By keeping the amplitude of excitation small, it was ensured that the measurements were done in a linear manner. The coherence between excitation and response was also checked to make sure the results were linear.

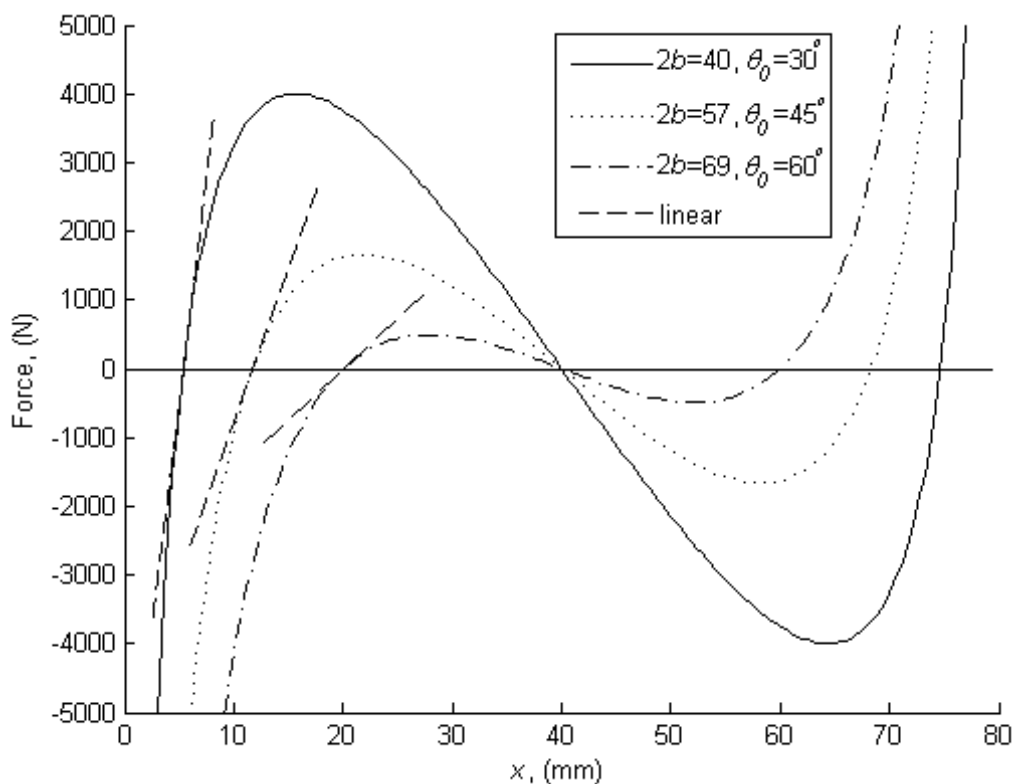


Figure 2-7: The non-dimensional force-displacement for different values of initial angle with linearisations shown around the unloaded positions

Experiments were conducted to measure the natural frequency for different distances between the cantilevers. The first set of data was acquired by doing a hammer test and measuring the acceleration. Two accelerometers were situated on top of the two small masses. The lever was hit on the top, where the levers are hinged, by an instrumented hammer. The results of the hammer test for the two measured accelerances are shown in Figure 2-8 (a). The distance between the cantilevers was 64 mm which corresponds to an initial angle of 53° . There is a

dominant peak at the about 140 Hz and the two accelerances match well up to 200 Hz. The accelerances of the rig are converging at high frequencies to 20 dB (ref. $1\text{ms}^{-2}/\text{N}$) from which the equivalent mass of the rig is estimated to be about 100 g.

The transmissibility frequency response was measured by applying a random signal to the base by a shaker and recording the base acceleration by a third accelerometer connected to the base. The transmissibility for the same distances between levers is shown in Figure 2-8 (b). It can be seen that there is a dominant peak at the same frequency of about 140 Hz and the results from two accelerometers are almost the same up to 200 Hz. There are damped resonances at 270 Hz and 250 Hz for first and second accelerometer respectively. These are additional modes of the rig which have not been identified.

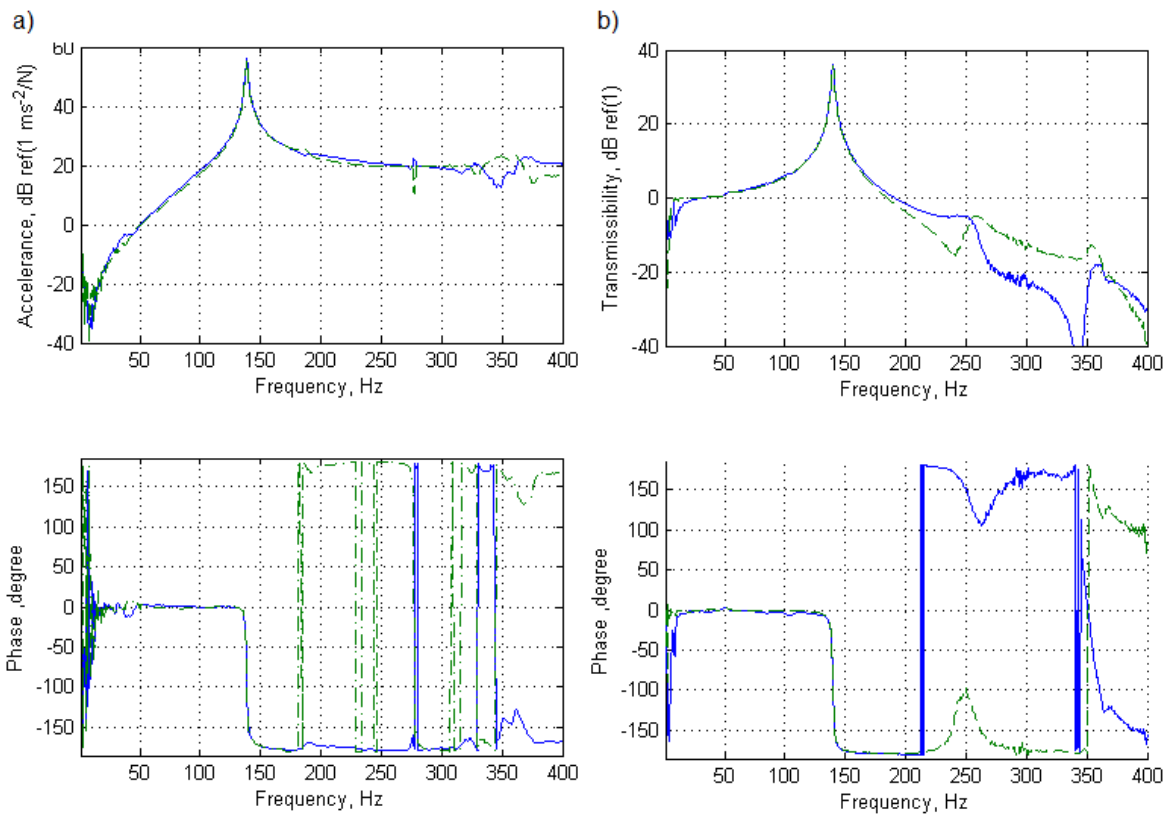


Figure 2-8: FRFs for $2b = 64\text{mm}$ ($\theta_0 = 53^\circ$), solid line: first accelerometer, dashed lines: second accelerometer, a) Accelerance (hammer test), b) Transmissibility (shaker with random excitation, 100 averages)

The tests were repeated for different distances between the cantilevers and the natural frequency was estimated from FRFs in each case. These estimated natural frequencies from both hammer

and base excitation by shaker are plotted as a function of distance between cantilevers in Figure 2-9 alongside the predicted results using theoretical equations where the stiffness of the cantilevers is calculated by measuring its dimensions. These natural frequencies are denoted as the first set of predicted results in the graph. There is considerable discrepancy between this prediction and the measured data.

The second set of predicted results is calculated by estimating the rig's stiffness from the natural frequency for the position where the cantilevers are 64mm apart. This estimation agrees with the experimental results. The stiffness of the cantilevers estimated by this method is 64 kN/m which is about 30 per cent of the calculated stiffness by considering the cantilevers' dimensions. The non-perfect fixed boundary condition at the ends of the cantilevers and the backlash and stiffness of the bearings could be reasons for this disagreement.

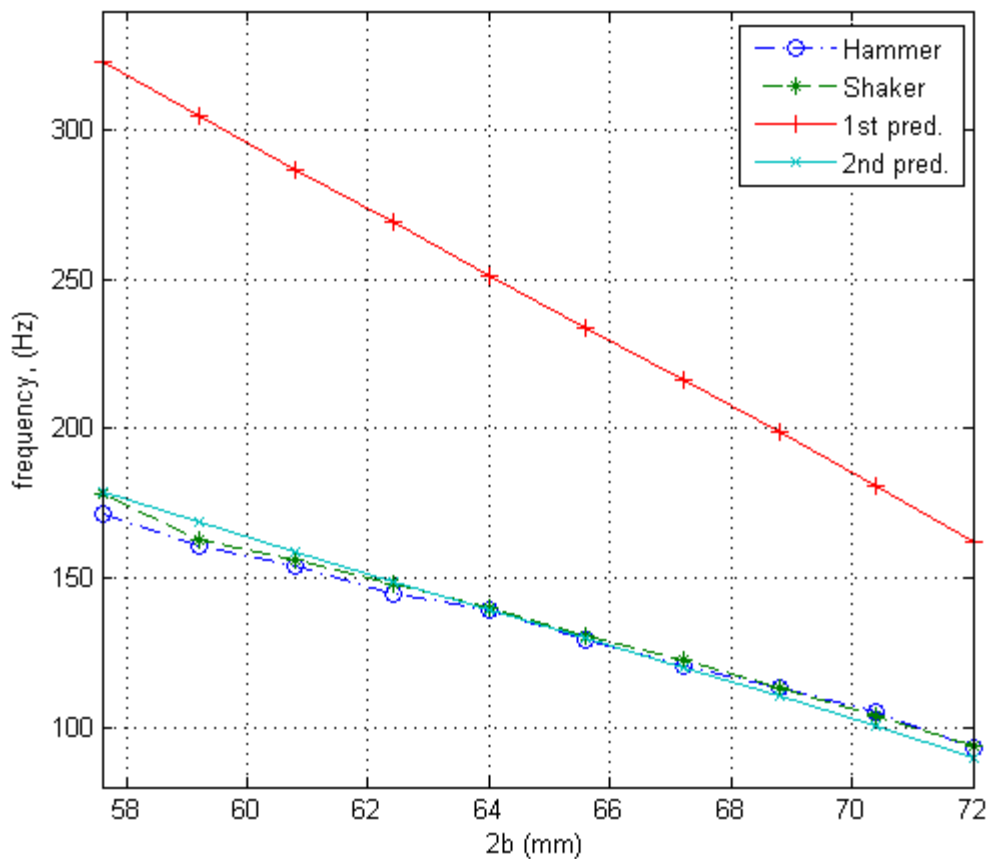


Figure 2-9: Natural frequency variation as a function of separation of cantilevers

As it was expected the frequency decreases from about 180 Hz to 90 Hz while the distance between the cantilevers increases from 57.6 mm to 72 mm. The results from hammer and shaker tests match closely and the difference between experimental results and the second set of predicted numerical results is less than 5%.

The measured data were used to estimate the damping in each position and it is shown in Figure 2-10. The damping is estimated from the peak amplitude in both cases. The damping estimated by the results of the shaker tests is almost twice that obtained from the hammer test for a cantilever separation of 71.2 mm. The mechanism was very damped in some positions which seemed to be a result of the backlash at the adjustment bolt. In some positions it was not firm and caused loss of energy which could be modified by slightly turning the adjustment bolt. To overcome this problem, the damping was measured for slightly different positions which caused two different damping ratios for the mentioned position. There is a good match between the two values for damping for other distances between the cantilevers.

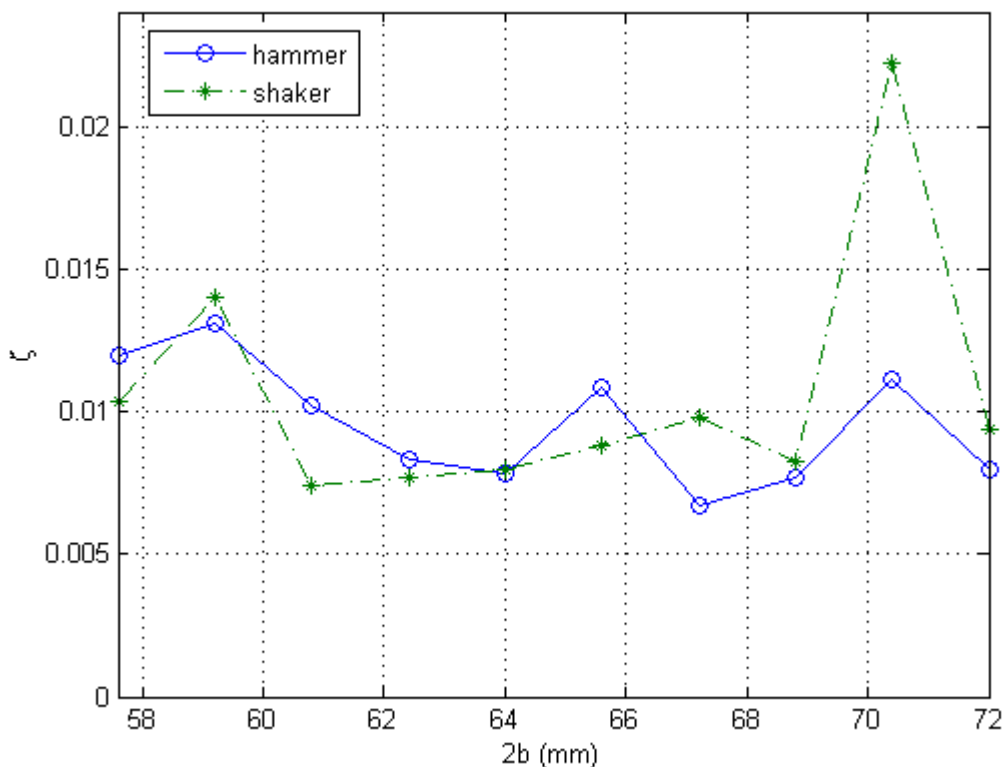


Figure 2-10: Damping ratio ζ for different separation of cantilevers

2.4 A Quasi-Zero-Stiffness mechanism

As noted in the chapter's introduction, vibration isolation can be improved by decreasing the natural frequency of the system and this can be achieved by adding the snap-through mechanism in parallel with an isolator spring. The new arrangement causes a reduction in vibration isolator tangent stiffness. The mechanism studied here is one of the mechanisms that is introduced in reference [9]. The analysis presented in this section is used as a base to obtain the effect of preload on the mechanism in section 2.5 and to compare it with a similar mechanism in section 2.6.

Suppose that the lever mechanism is added to a vertical spring in such a way that both of the springs are un-deformed at the unloaded position. The resulting mechanism is shown in Figure 2-11 (a). The free body diagram of the right lever (Figure 2-11 (b)) is the same as the free body diagram of the mechanism without vertical spring (Figure 2-1 (b)). The force generated by the vertical spring adds to the forces applied to the pivot. The free body diagram of the pivot is shown in Figure 2-11 (c).

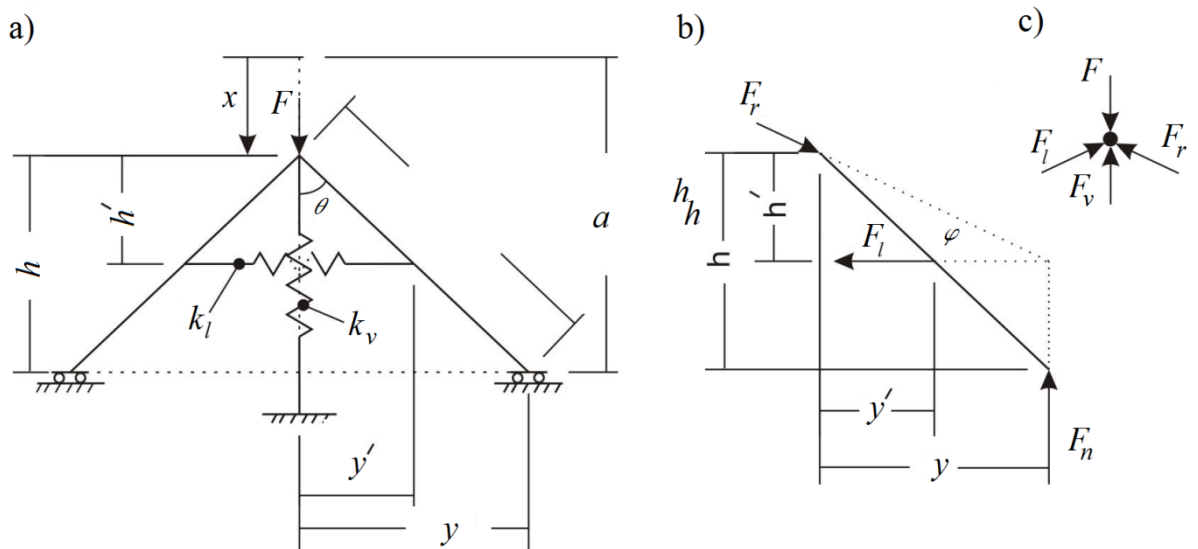


Figure 2-11: a) The QZS mechanism shown at an arbitrary position, b) free body diagram of the right lever, c) free body diagram of hinge

The force of the vertical spring as a function of displacement x is simply,

$$F_v = k_v(x - x_0) \quad (2-18)$$

where x_0 denotes the initial position where the springs are unloaded and can be derived as a function of the initial angle,

$$x_0 = a(1 - \cos \theta_0) \quad (2-19)$$

Equation (2-1) for the force acting on the hinge can be rewritten for this case as,

$$F = F_v + F_r \sin \varphi + F_l \sin \varphi = F_v + 2F_r \sin \varphi \quad (2-20)$$

The force-deflection relation with the vertical spring included becomes,

$$\frac{F}{ak_v} = (\hat{x} - 1 + \cos \theta_0) + 4\gamma\beta^2(1 - \hat{x}) \left(1 - \frac{\sin \theta_0}{\sqrt{2\hat{x} - \hat{x}^2}} \right) \quad (2-21)$$

where k_v is the stiffness of the vertical spring and γ is the ratio between springs stiffness, k_l/k_v . The equation is non-dimensionalised by ak_v . The stiffness can be obtained by differentiating equation (2-21) with respect to \hat{x} .

$$\frac{K}{k_v} = 1 + 4\gamma\beta^2 \left[\frac{\sin \theta_0}{(2\hat{x} - \hat{x}^2)^{\frac{3}{2}}} - 1 \right] \quad (2-22)$$

The minimum stiffness can be found by differentiating equation (2-22) and setting it equal to zero. The minimum is at the horizontal position where the non-dimensional displacement is equal to unity. The minimum stiffness is given by,

$$\frac{K_{min}}{k_v} = 1 + 4\gamma\beta^2(\sin \theta_0 - 1) \quad (2-23)$$

Quasi-Zero-Stiffness behaviour can be achieved by setting the minimum stiffness to zero. From equation (2-23), the stiffness ratio γ for a minimum stiffness of zero can be derived for an arbitrary initial angle,

$$\gamma_{Qzs} = \frac{1}{4\beta^2(1 - \sin \theta_0)} \quad (2-24)$$

The non-dimensional force as a function of non-dimensional displacement of such a QZS mechanism is shown in Figure 2-12 for different initial angles. Equation (2-24) is used here to calculate the stiffness ratio for different initial angles to achieve the QZS mechanism.

The thin straight lines are the non-dimensional force-displacement curves of the vertical spring alone, i.e. as if k_l is set to zero, for the stated initial angles. At the horizontal position the snap-through mechanism produces no vertical force and the QZS mechanism force is due to the vertical spring alone. As a result, the non-dimensional force-displacement curve of the vertical spring alone intersects with that of the QZS mechanism. The first intersection is at the unloaded position where the force is equal to zero for both the vertical and horizontal springs.

As seen in Figure 2-12, the load increases rapidly with displacement initially and then there is a low stiffness region around the horizontal position, i.e. the non-dimensional displacement equal to unity. By increasing the initial angle, the low stiffness region becomes narrower and the load at the minimum stiffness position decreases.

The non-dimensional stiffness as a function of non-dimensional displacement is shown in Figure 2-13. Here again the stiffness ratio is selected in such a way that the minimum stiffness become zero. The mechanism outperforms the vertical spring in the range where the non-dimensional stiffness is less than one. It is apparent that by increasing the initial angle, the displacement range over which the non-dimensional stiffness is less than one becomes narrower. According to equation (2-22), the stiffness of the snap-through mechanism detracts from the stiffness of the vertical spring. The displacement range at which the combined QZS mechanism is less stiff than the vertical spring is the same as the displacement range at which the snap-through mechanism possesses negative stiffness.

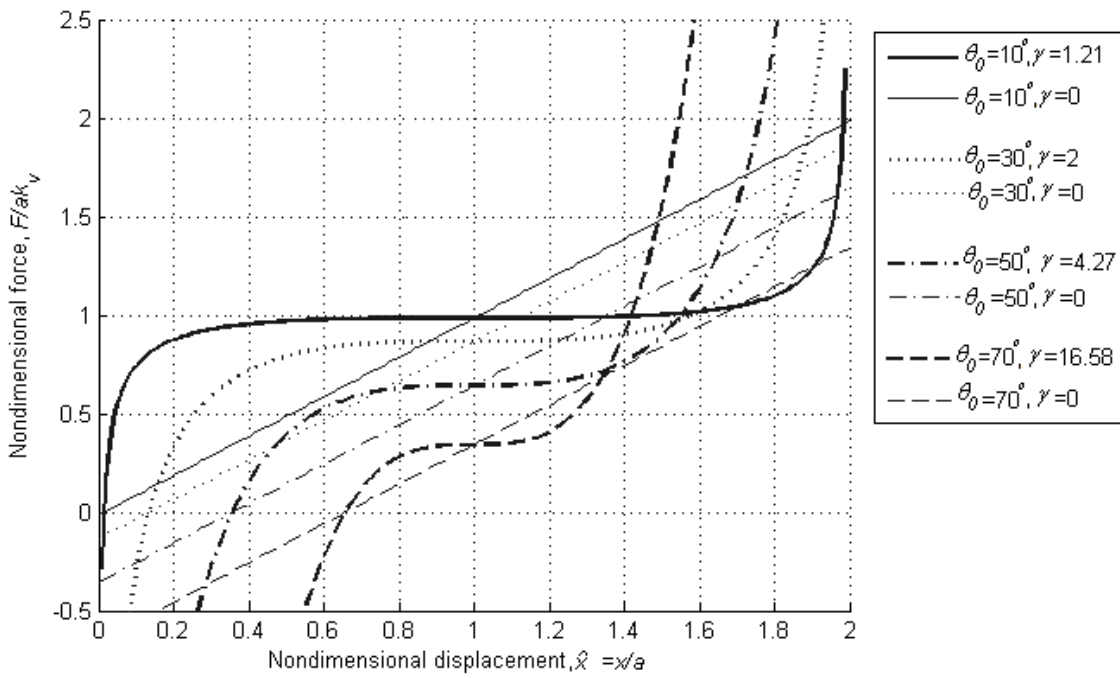


Figure 2-12: The non-dimensional force-displacement of the QZS mechanism for different initial angles and of the vertical spring alone

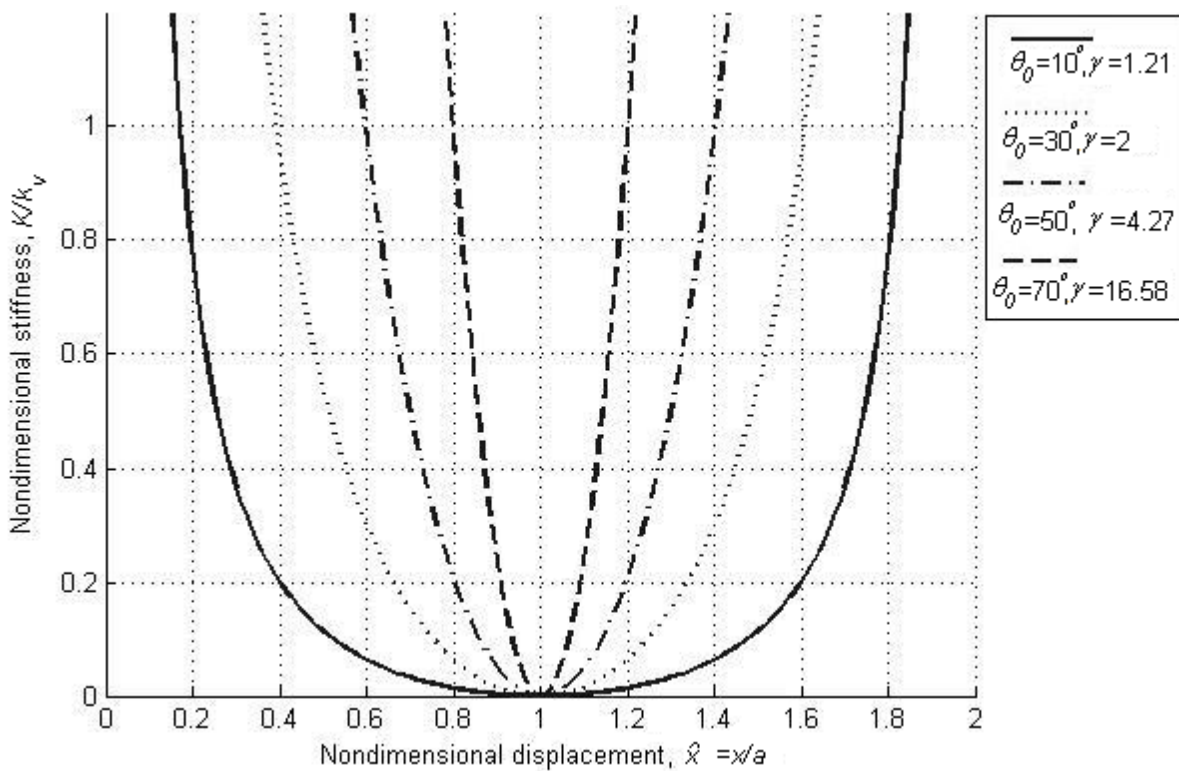


Figure 2-13: Non-dimensional stiffness as a function of non-dimensional displacement for different initial angles

2.5 A QZS system with preload

The QZS mechanism described in the previous section is comprised of the snap-through mechanism and the vertical spring where both springs are unloaded at the same position. The initial angle, θ_0 , is taken as the angle of the position where both springs are unloaded. To consider the effect of preload on the QZS mechanism, a displacement is applied to the vertical spring and then it is attached to the snap-through mechanism. In this section, the initial angle θ_0 only defines the position where the snap-through mechanism is unloaded and not the vertical spring or the preloaded QZS mechanism. The initial positioning of the vertical spring makes it possible to tune the QZS mechanism for different static loads.

The unloaded vertical spring is shown in Figure 2-14 (a). The reference of the displacement is considered a distance equal to the length of the lever, a , above the horizontal position. The position of the vertical spring when unloaded is called x_0 . A displacement equal to δ_p is applied to the vertical spring (Figure 2-14 (b)). In Figure 2-14 (c), the vertical spring is added to the snap-through mechanism which is unloaded at the angle θ_0 . The corresponding position to the angle θ_0 is denoted as x_p . Because the snap-through mechanism is unloaded at this position the force F_p which is needed to keep the mechanism at the position shown in Figure 2-14 (c) is to maintain the preload alone and can be derived from the force-displacement relationship of the vertical spring.

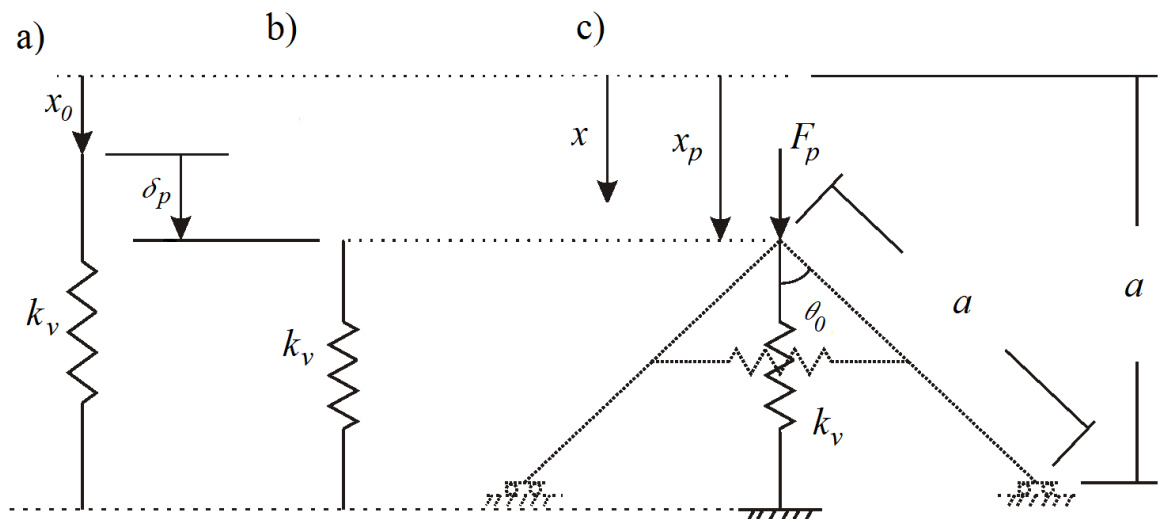


Figure 2-14: The pre-loaded vertical spring, a) unloaded vertical spring, b) preloaded vertical spring, c) the position of preloaded vertical spring regarding snap-through mechanism

$$F_p = \delta_p k_v \quad (2-25)$$

The unloaded position x_0 of the vertical spring can be obtained as a function of δ_p and the unloaded position of the snap-through mechanism, x_p ,

$$x_0 = x_p - \delta_p \quad (2-26)$$

The position x_p can be obtained as a function of θ_0 from Figure 2-14 (c),

$$x_p = a(1 - \cos \theta_0) \quad (2-27)$$

By substituting equations (2-27) and (2-26) into equation (2-18) the force of the vertical spring at any arbitrary position x which is measured from the reference line can be derived for the preloaded vertical spring,

$$F_v = k_v(x - a + a \cos \theta_0 + \delta_p) \quad (2-28)$$

Now, suppose the snap-through mechanism is added to this preloaded spring. The force due to the snap-through mechanism is the same as before and it needs to be added to the above equation which in non-dimensional form is,

$$\frac{F}{ak_v} = (\hat{x} - 1 + \cos \theta_0 + \hat{\delta}_p) + 4\gamma\beta^2(1 - \hat{x}) \left(1 - \frac{\sin \theta_0}{\sqrt{2\hat{x} - \hat{x}^2}}\right) \quad (2-29)$$

where $\hat{\delta}_p$ is the non-dimensional preload displacement, δ_p/a . The above equation is different from equation (2-21) only in first part which is the force generated by the vertical spring. The tangent stiffness of the preloaded QZS mechanism is the same as the tangent stiffness of the QZS mechanism with the same initial angle as θ_0 .

The force-displacement graph of the preloaded mechanism is shown in Figure 2-15. The preload appears to have the effect of moving the force-displacement graph upward or downward. The

positive preload displacement $\hat{\delta}_p$ means the vertical spring is in compression by preload while the negative $\hat{\delta}_p$ refers to the vertical spring in tension while preloaded according to the definition illustrated in Figure 2-14.

The QZS mechanism has low stiffness in the vicinity of the non-dimensional displacement equal to unity where the levers are horizontal. When it is used to isolate a mass, the weight of the mass should load it statically to this position. At this position the force due to the snap-through mechanism has no vertical component and the whole weight of the mass should be carried by the vertical spring. If the weight does not provide the required displacement of the vertical spring to achieve the horizontal lever position, then the inclusion of preload makes it possible to tune the mechanism easily by adjusting the vertical spring position.

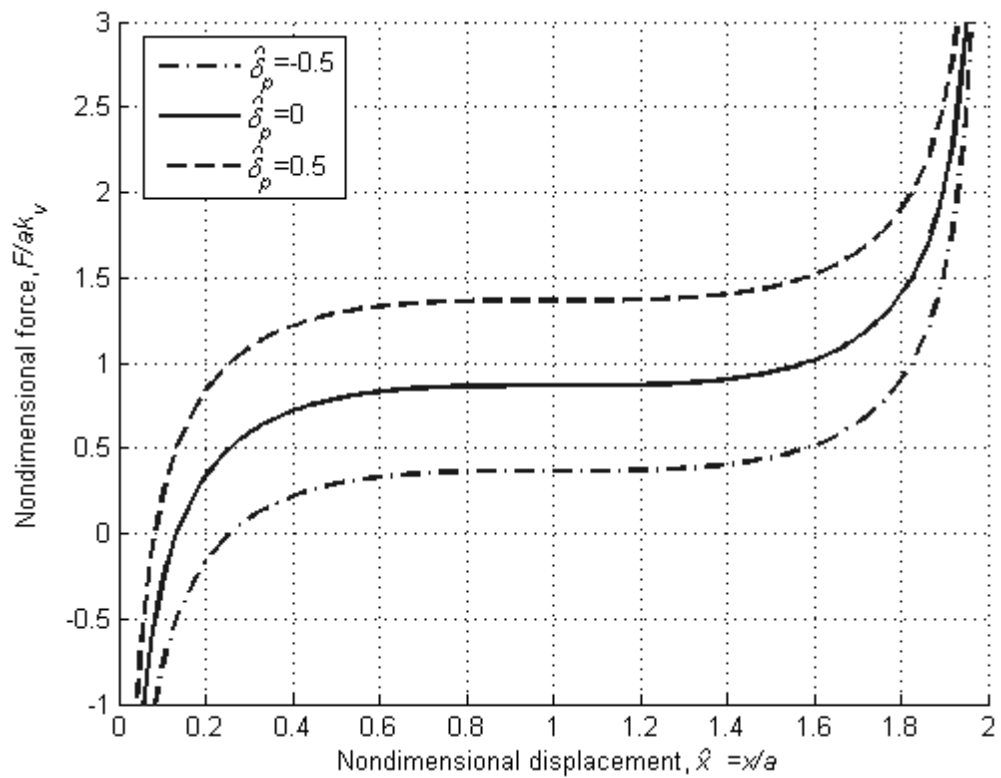


Figure 2-15: The preloaded QZS mechanism ($\beta=0.5$, $\gamma=2$, and $\theta_0=30^\circ$)

2.6 Comparison between two QZS mechanisms

In section 2.2, a snap-through mechanism was introduced to which a vertical spring can be added to achieve a QZS mechanism. There are many other mechanisms with intervals of negative stiffness which cause them to snap through in part of their displacement range. The combination of these mechanisms and a linear spring could similarly form a QZS mechanism. One of these QZS mechanisms is studied by Carrella et al.[3] which is shown in Figure 2-16 (a). It comprises of two oblique springs and one vertical spring, all of them connected together at the top. The two oblique springs are simply supported at the other end. The load is applied at the hinge and the position x of the same point is measured from a reference line. This mechanism will be referred to as the *oblique spring mechanism* henceforth. The QZS mechanism studied in the previous section is shown in Figure 2-16 (b). This mechanism will refer to as the *lever mechanism* in the rest of this chapter. The length of the unloaded oblique spring is taken to be the same as the length of lever to compare the two mechanisms with similar geometry.

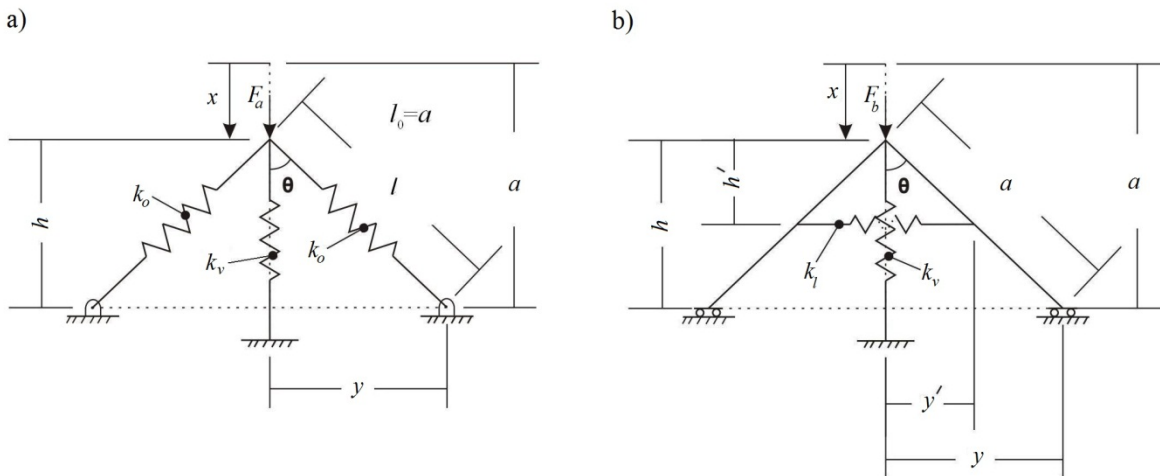


Figure 2-16: QZS mechanisms, a) Oblique spring mechanism, b) lever mechanism

The force-displacement equation given in reference [3] can be rewritten to comply with the oblique spring mechanism definitions used here as follows,

$$\frac{F_a}{ak_v} = (\hat{x} - (1 - \cos \theta_0)) + 2\gamma_a(1 - \hat{x}) \left(\frac{1}{\sqrt{(1 - \hat{x})^2 + (\sin \theta_0)^2}} - 1 \right) \quad (2-30)$$

where force F_a is non-dimensionalised by ak_v , \hat{x} is the non-dimensional displacement equal to x/a , γ_a is the ratio between the oblique spring stiffness and the vertical spring stiffness, and θ_0 is the initial value of the angle θ . The stiffness can be derived by differentiating the force F_a with respect to displacement, thus

$$\hat{K} = 1 + 2\gamma_a \left(1 - \frac{\sin^2 \theta_0}{((1 - \hat{x})^2 + \sin^2 \theta_0)^{\frac{3}{2}}} \right) \quad (2-31)$$

where \hat{K} is the non-dimensional stiffness, k/k_v . The force-displacement and stiffness-displacement relation for the lever mechanism are derived in section 2.4 and are given by equations (2-21) and (2-22) respectively. The non-dimensional force as a function of non-dimensional displacement is plotted in Figure 2-17 for both of the mechanisms. The parameter β for the lever mechanism is chosen as 0.5 in this graph which affects only the stiffness ratio γ . The stiffness ratio is chosen for each initial angle to make the minimum stiffness zero, i.e. QZS. The black lines are the non-dimensional force-displacement curves for the oblique spring mechanism and the cyan lines demonstrate the non-dimensional force-displacement for the lever mechanism.

The slope of the graph is less at the beginning for oblique spring mechanism compared to the lever mechanism and the flat region is narrower for oblique spring mechanism. The curves for both of the mechanisms are anti-symmetric, and both of them demonstrate softening spring behaviour in half of the range until a non-dimensional displacement of unity which is the inflection point of the curves. After this point they behave like a hardening spring. An initial angle of 33° is the optimum initial condition where the oblique spring mechanism has the widest low tangent stiffness range. In the case of the lever mechanism, the range steadily increases with decreasing initial angle. The stiffness ratio of the lever mechanism is higher than the ratio for the oblique spring mechanism.

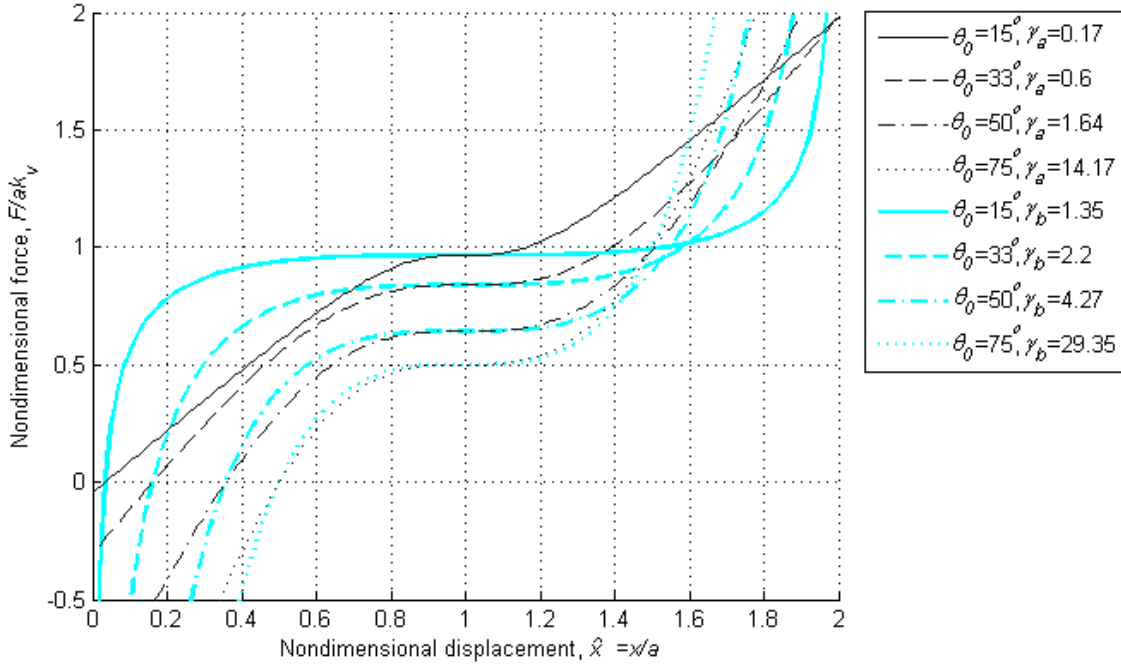


Figure 2-17: Non-dimensional force as a function of non-dimensional displacement, black lines: QZS oblique spring mechanism, cyan line: QZS lever mechanism

The non-dimensional stiffness as a function of non-dimensional displacement is shown in Figure 2-18. A non-dimensional stiffness of less than unity can be interpreted as the positions at which the stiffness of the QZS mechanism is equal to that of the vertical spring alone. The range at which the non-dimensional stiffness of the lever mechanism is less than unity is wider than that of the oblique spring mechanism, but the lever mechanism is stiffer for large excursion from the horizontal position.

In order to explore the reasons for the different behaviours of the systems, the force and stiffness as a function of angle θ can be derived. The stiffness of vertical spring can be set to zero to explore the nonlinearity in the force-deflection of two cases. For $k_v = 0$, the force as a function of θ is given by equation (2-32) for the oblique spring mechanism and by equation (2-33) for the lever mechanism.

$$\frac{F_a}{ak_l} = 2 \cos \theta \left(1 - \frac{\sin \theta}{\sin \theta_0} \right) \quad (2-32)$$

$$\frac{F_b}{ak_l} = 4\beta^2 \cos \theta \left(1 - \frac{\sin \theta}{\sin \theta_0} \right) \quad (2-33)$$

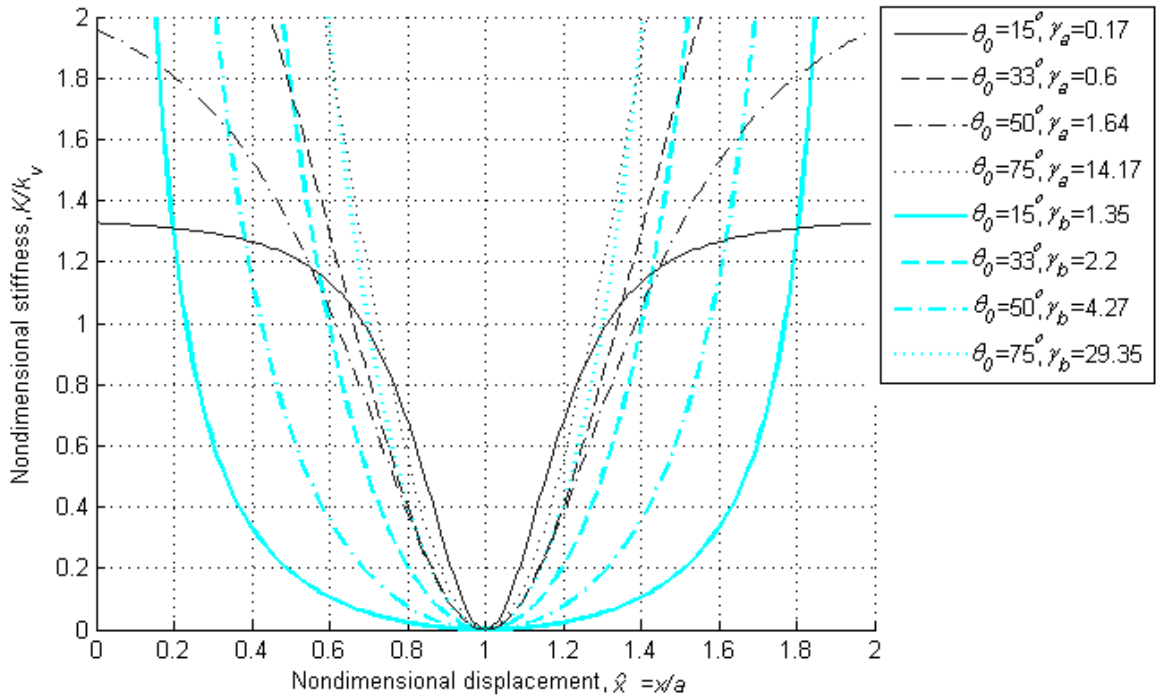


Figure 2-18: Non-dimensional stiffness as a function of non-dimensional displacement, black lines: oblique spring mechanism, cyan lines: lever mechanism

These two equations differ from each other only in the coefficient $2\beta^2$ which affects the level of force. The displacement as a function of angle is given by equations (2-34) and (2-35) for the two mechanisms.

$$x_a = a \left(1 - \frac{\sin \theta_0}{\tan \theta} \right) \quad (2-34)$$

$$x_b = a(1 - \cos \theta) \quad (2-35)$$

It can be noticed that the difference between the two mechanisms is due to the departure in displacement as a function of angle i.e. although the applied force to achieve a specific angle for both mechanisms is the same, the displacement of the hinge point is different. Note also that the displacement of the lever mechanism, x_b , is bounded between 0 and $2a$ whereas the displacement of the oblique mechanism is unbounded.

2.7 Conclusions

A snap-through mechanism that can be incorporated into a vibration isolator is investigated in this chapter. Equations for the restoring force and stiffness as a function of displacement are derived. It is shown that by loading the mechanism it snaps through the horizontal position and there is an interval for which the stiffness is negative. The width of this range depends on the initial angle at which the mechanism is unloaded. The negative stiffness displacement range becomes smaller by increasing the initial angle. The value of minimum stiffness also depends on the initial angle and decreases by increasing the initial angle.

A QZS mechanism is formed by adding a vertical spring to the mechanism and the force and stiffness are derived as a function of displacement. The ratio between vertical spring stiffness and the lateral spring stiffness of the snap-through mechanism can be tuned to form a mechanism with a minimum stiffness of zero and an expression for the required stiffness ratio has been derived.

The vertical spring can also be pre-loaded. The consequence is a shift in force-displacement graphs and the tangent stiffness remains the same which allows one to tune the mechanism for different static loads by simply adjusting the position of the vertical spring.

This QZS mechanism referred to here as a *lever mechanism*, is compared with a so-called *oblique spring QZS mechanism*. It is shown that the lever mechanism has a wider displacement range affording low stiffness. There is also no optimum initial condition for the mechanism and the range increases by decreasing the initial angle. However, the oblique spring mechanism is optimized at an initial angle of about 33° . Although the lever mechanism has a wider range at which its displacement is low it becomes stiffer at large displacements away from the static equilibrium position.

Some measurements were also conducted on an existing test rig, which can be modelled by the snap-through mechanism, to investigate the difficulties in designing a test rig of a nonlinear vibration isolator. The test rig is nonlinear but it is tested for small vibration amplitudes about the unloaded position. The FRF of the rig is measured using an instrumented hammer and a shaker. The backlash at the joint can introduce other modes of vibration in the system. It can also increase the damping of the rig. While the mechanism and the test rig was well suited for

the purpose it is designed for (a tuned vibration absorber), to implement the test rig as a vibration isolator it is necessary to use much softer cantilevers to make it possible to load it to the minimum tangent stiffness position during the experiment. As a result, both the bending moment and axial compression prescribe the deformation of the cantilevers which are known as beam-columns [68]. The lateral stiffness of a cantilever is much lower than its axial stiffness while they can be similar values for a loaded beam-column. This may introduce a flexural mode of vibration with a frequency close to the frequency of the fundamental mode of vibration of the mechanism i.e. the mass on the nonlinear spring. The cantilever cannot also be modelled as a linear spring in this case.

Considering the complexity of designing a test rig based on the QZS mechanism and the effect of higher modes of vibration and joints on its response, it is concluded to try to find alternative methods of forming desirable spring elements for a nonlinear vibration isolator with fewer parts involved. Beams loaded axially and a commercial rubber mount are considered in future chapters for this purpose.

3 Beams as nonlinear springs

3.1 Introduction

In the previous chapter, it was shown that a high static, low tangent stiffness characteristic can be achieved through the introduction of QZS mechanisms. However, their physical complexity makes them difficult to implement in practice for the purpose of this thesis. A suitable alternative to the QZS mechanism must maintain similar nonlinear properties and ideally comprise of a single light component. Reducing the number of components will eliminate the relative displacements of internal parts and also make its construction easier. The aim of this chapter is to investigate the possibility of using beams undergoing large deformations as spring elements of nonlinear vibration isolators and to address the possible shapes of beams that are beneficial for this purpose.

The study requires investigation of large deflection of beams. The common approach to study deflection and vibration of beams is to implement linear theory and to consider small rotations. This approach is valid for many practical cases, since the materials become plastic with increasing deformation before the small rotation assumption becomes invalid. However, there are cases in which beams can violate the assumption of small deflections. For example, thin bars under excessive load or vibration can result in large deflections without going outside the elastic range of their material. Different methods, both numerical and analytical, are suggested in the literature to obtain solution for large deformations of beams. A brief review of the theory is presented at the beginning of this chapter alongside an example of a simple case to clarify the

deformation mechanisms that contribute to characteristics of the beam undergoing large deformation.

A simply supported beam loaded by a harmonic transverse load at its midpoint is addressed as a nonlinear oscillator with softening characteristic in literature [20]. The softening characteristic means a lower tangent stiffness when loaded statically. Thus, it is considered as a candidate for the nonlinear spring in a vibration isolator. However, it is revealed in this study that there is some misinterpretation in the published literature about its nonlinear stiffness characteristic.

Another candidate component with low tangent stiffness is the Euler buckled beam (column). Buckling happens when a structure undergoes large displacement due to compression stresses. The buckling appears as a discontinuity in the force-deflection curve where the beam deflects suddenly under compressive load. Deflection before the buckling point is due to axial deformation which results in a high stiffness. As a result a post-buckled beam can be considered as a component with high static stiffness but low tangent stiffness [29]. The beam must be implemented in its post-buckled range to achieve low tangent stiffness in operation. The sharp change in stiffness at the buckling point results in a system with large nonlinearity which is not generally desirable in isolation. Hence, other configurations such as a curved beam or a straight eccentrically loaded beam are considered here to achieve a smoother transition in stiffness.

The chapter starts with a brief description of the theory of the basic principles of beam bending. Then the special case of a simply-supported beam loaded by a pure bending moment is studied. This case is used to provide a physical explanation for large displacements of beams in general. The solution of the simply-supported beam is the subject of section 3.3. The exact solution is presented first and is followed with an approximate solution using the Galerkin method. A physical explanation concerning the beam's nonlinear static behaviour is provided and this section then concludes with a discussion about the accuracy of method.

Buckling and post-buckling characteristics of an Euler column are investigated in section 3.4. A modified version, a beam loaded eccentrically, is studied next. A curved beam is another alternative which is considered in subsection 3.4.3 followed by an analysis of dynamic and static stiffness of a curved beam. The internal resonances of the beam are also investigated to consider practical limitations. A case study is considered in this section and natural frequencies are obtained. The chapter finishes with conclusions.

3.2 Principal theory of a straight beam's deformation

Shear force and bending moment are the causes of transverse deflection of beams. As mentioned in the introduction, beams that are intended to be used as nonlinear springs must undergo large deformation. This requires implementing thin beams to prevent them from deforming plastically. The effect of shear force can be neglected in deflection of thin beams. Therefore, only the effect of bending moment is considered in this study.

According to Gere and Timoshenko [69], “a beam is a structural member that is subjected to loads acting transversely to the longitudinal axis”. A force applied to a beam causes bending moments to develop inside the beam as well as shear forces and/or axial forces depending on the direction of the applied force. It is assumed that the cross-section of a beam remains plane and is normal to the centre line of the beam. This is true for beams with any homogeneous material properties (elastic or inelastic as well as linear or nonlinear), and is also true for the large deflection of a beams under pure bending [70].

To determine the relationships between strain, deformation and bending moment, the procedure in reference [69] is followed. Consider the section of a beam shown in Figure 3-1(a) in which the bending moment is constant and equal to M . The sign convention is given in Figure 3-1(b). The strain in the beam element is given by,

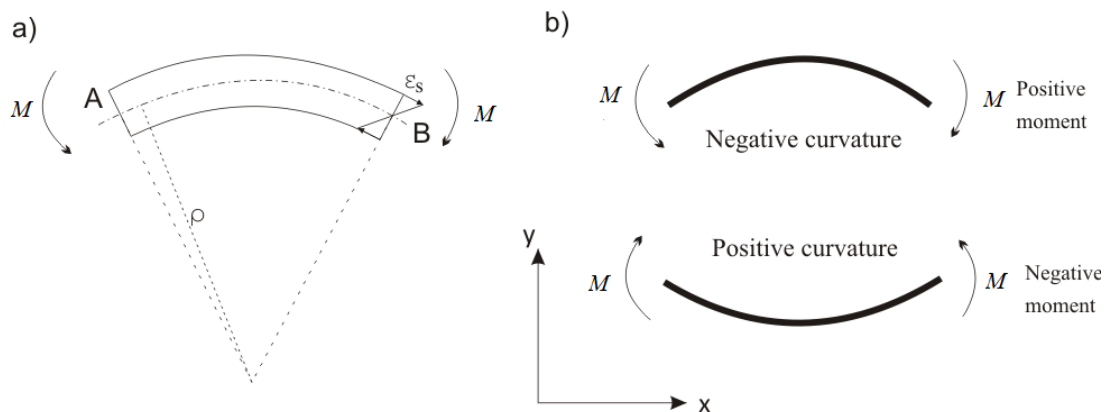


Figure 3-1: a) Deflection of an initial straight beam due to pure bending moment, b) Sign convention for curvature

$$\varepsilon_x = -\frac{h}{\rho} = -\kappa h \quad (3-1)$$

where ρ is radius of curvature and h is the distance from the neutral axis at which the strain is evaluated. The reciprocal of the radius of curvature is called the curvature and is represented by κ . The bending moment is related to the curvature of the beam and can be found by equilibrium of moments to be,

$$M = \int_A \sigma_x h \, dA = \int_A E \varepsilon_x h \, dA \quad (3-2)$$

Substituting for ε_x from equation (3-1) gives,

$$M = -E\kappa \int_A h^2 \, dA \quad (3-3)$$

The integral in equation (3-3) is the second moment of area denoted by I , so the relationship between the curvature and the bending moment can be written as,

$$\kappa = \frac{1}{\rho} = -\frac{M}{EI} \quad (3-4)$$

It should be noted that equation (3-4) is valid for large as well as small deflections. This is the key equation in the derivation of the expressions for beam deflection.

3.2.1 Deflection of a beam due to a pure bending moment

A beam loaded by a pure bending moment is a special case whose deflection can be easily found. This is presented here as an example of large deflection which can be solved analytically and used later to describe the hardening and softening characteristics of beams. Consider the

beam shown in Figure 3-2(a). The beam is of length L and is loaded by a bending moment M at both ends. The distance s is measured along the deflected beam and x is the corresponding lateral distance; y_{max} is the transverse displacement of the beam at the centre and θ_0 denotes angle of the beam at each end.

For the element ds which is shown in Figure 3-2(a), equation (3-4) can be written as a function of $d\theta$ and ds as,

$$\frac{d\theta}{ds} = -\frac{M}{EI} \quad (3-5)$$

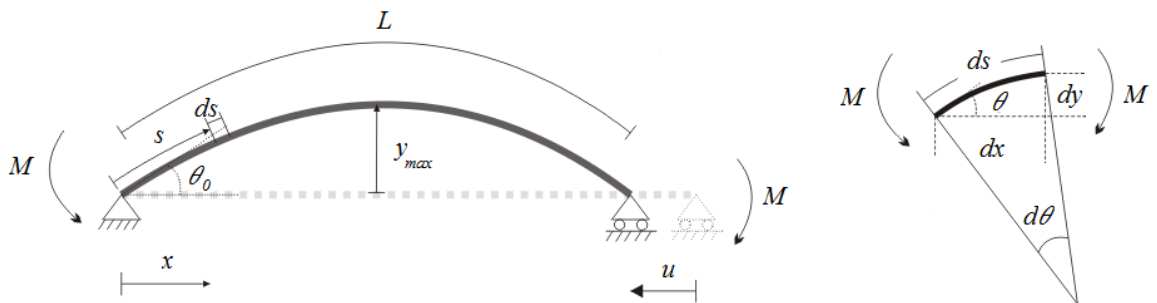


Figure 3-2: Simply supported beam loaded by bending moment, a) deflected beam, b) small section of beam of length ds

The angle at the centre of the beam is zero because of symmetry. Integrating equation (3-5) from $s = 0$ to $s = \frac{L}{2}$ gives,

$$\int_{\theta_0}^0 d\theta = \int_0^{\frac{L}{2}} -\frac{M}{EI} ds \quad (3-6)$$

which can be solved to find the angle at each end of the beam,

$$\theta_0 = \frac{ML}{2EI} \quad (3-7)$$

This shows that there is a linear relationship between the angle and the bending moment and rotational stiffness, $k_r = 2EI/L$. The transverse deflection of the beam can be determined from,

$$y(s) = \int dy = \int_0^s \sin \theta ds \quad (3-8)$$

The maximum transverse deflection occurs at $L/2$. Substituting for $s=L/2$ into equation (3-8), and noting the relationship between θ and s given in equation (3-5) results in,

$$y_{max} = \int_0^{\frac{L}{2}} \sin \theta ds = -\frac{EI}{M} \int_{\theta_0}^0 \sin \theta d\theta \quad (3-9)$$

which evaluates to,

$$y_{max} = \frac{EI}{M} (1 - \cos \theta_0) \quad (3-10)$$

Substituting for θ_0 from Equation (3-7) and dividing through by L , gives the non-dimensional expression for y_{max} , which is,

$$\hat{y}_{max} = \frac{y_{max}}{L} = \frac{1}{2\hat{M}} (1 - \cos \hat{M}) \quad (3-11)$$

where $\hat{M} = \frac{M}{(2EI/L)}$ (which is also equal to θ_0) is the non-dimensional bending moment. The lateral displacement of the tip of the beam can be determined in a similar way. The displacement of the tip is given by,

$$u = L - \int_0^L \cos \theta ds = L - \frac{EI}{M} \int_{\theta_0}^{-\theta_0} \cos \theta d\theta \quad (3-12)$$

The integral can be evaluated in a straightforward manner and the resulting equation divided through by L to give the non-dimensional displacement of the beam tip,

$$\hat{u} = \frac{u}{L} = 1 - \frac{1}{\hat{M}} \sin \hat{M} \quad (3-13)$$

The bending moment as a function of tip displacement is shown in Figure 3-3 with the deformed shape of the beam illustrated for various loads. The radius of curvature is constant over the beam as a result of the constant bending moment along the beam. As a result, the beam forms an arc, then a circle as the bending moment increases. The cross stiffness of the beam \hat{M}/\hat{u} , is softening up to when the angle is about 120° whereupon it becomes hardening.

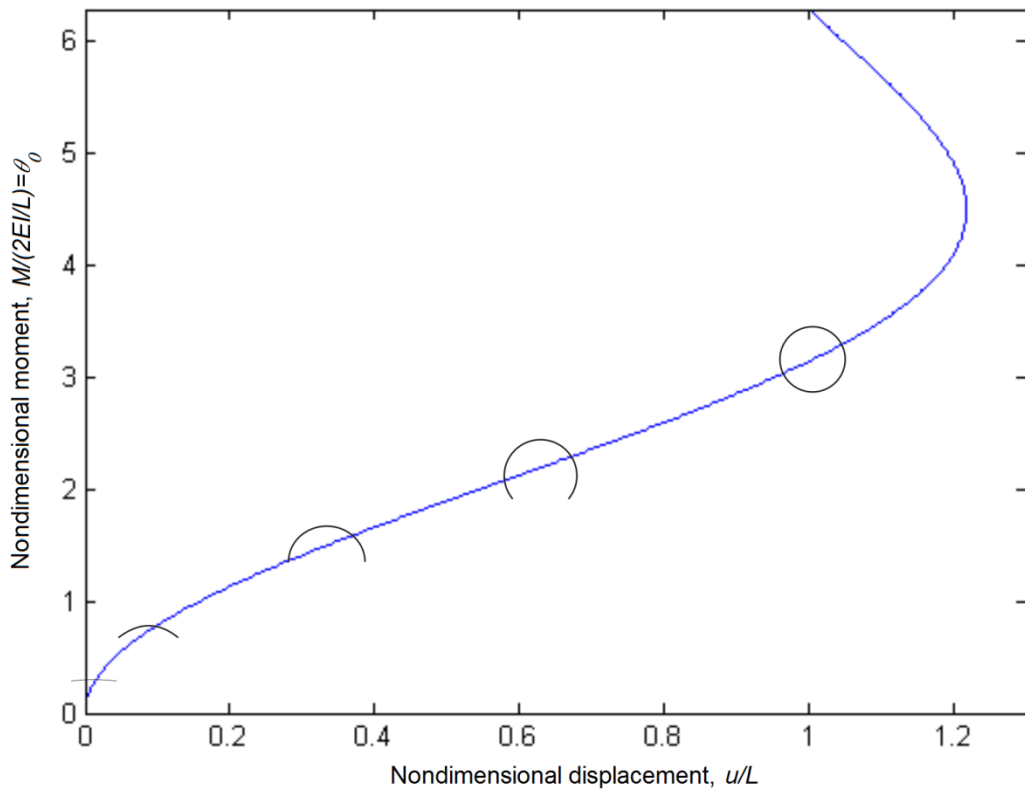


Figure 3-3: Non-dimensional bending moment as a function of non-dimensional lateral displacement of the tip, curves: shape of the deflected beam

The non-dimensional bending moment is plotted as a function of both the transverse displacement and the lateral tip displacement in Figure 3-4. The results obtained from the finite element method using ANSYS are also shown. The BEAM3 element of ANSYS is used in this analysis which is a two dimensional uniaxial element with tension, compression and bending capabilities. It can be used for nonlinear large deflection analysis. Without loss of generality, a

beam was chosen with unit length, unit second moment of area and unit modulus of elasticity, and the results subsequently non-dimensionalised in a consistent way with the analytical results. Since the beam is solved for pure bending moment the dimension of the beam would not affect the non-dimensional results. A hundred elements are used to model the beam. The problem was solved with ANSYS' option of "large displacement static" and 50 sub-steps were used to obtain the nonlinear solution. It can be seen that these match well with the analytical results.

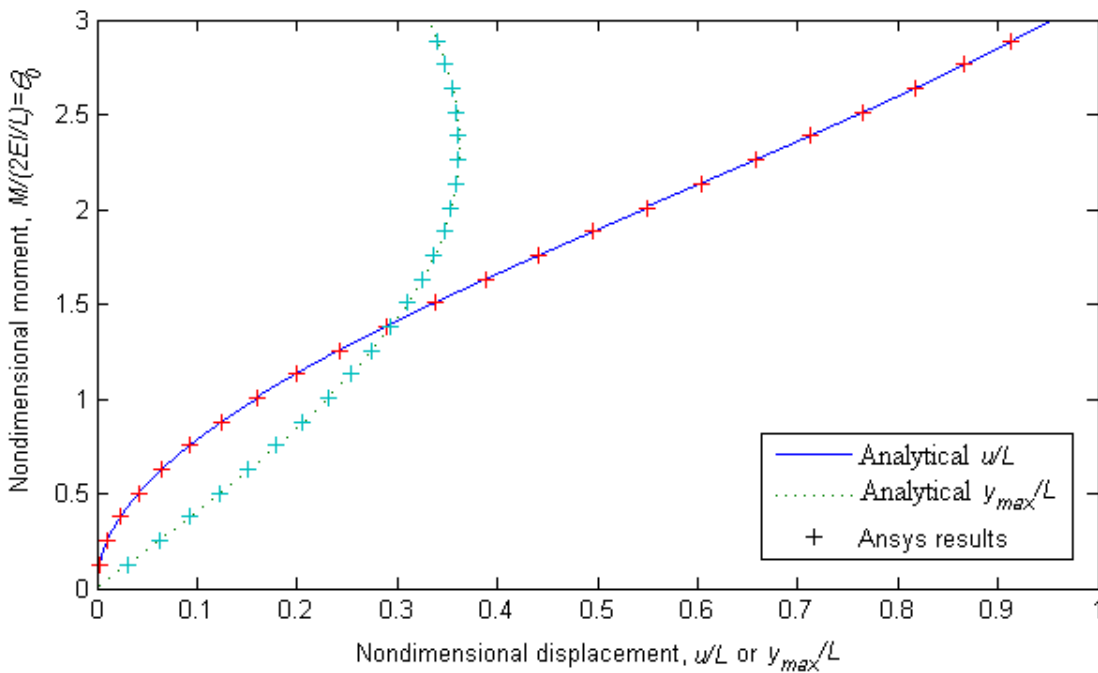


Figure 3-4: Comparison of the analytical results with the results obtained from ANSYS for the axial displacement of the tip of the beam and the transverse displacement at the centre of the beam.

Two cross stiffness \hat{M}/\hat{y} and \hat{M}/\hat{u} are shown in Figure 3-5 as a function of the transverse displacement and the lateral tip displacement respectively. The transverse cross stiffness \hat{M}/\hat{y} , is hardening from the beginning and does not soften for any value of bending moment for the range shown, unlike the axial cross stiffness \hat{M}/\hat{u} , which is softening for relatively small bending moments and then has a hardening characteristic for very large bending moments. The reason of this behaviour is given in the next section by considering the displacement as a result of rotation of beam elements.

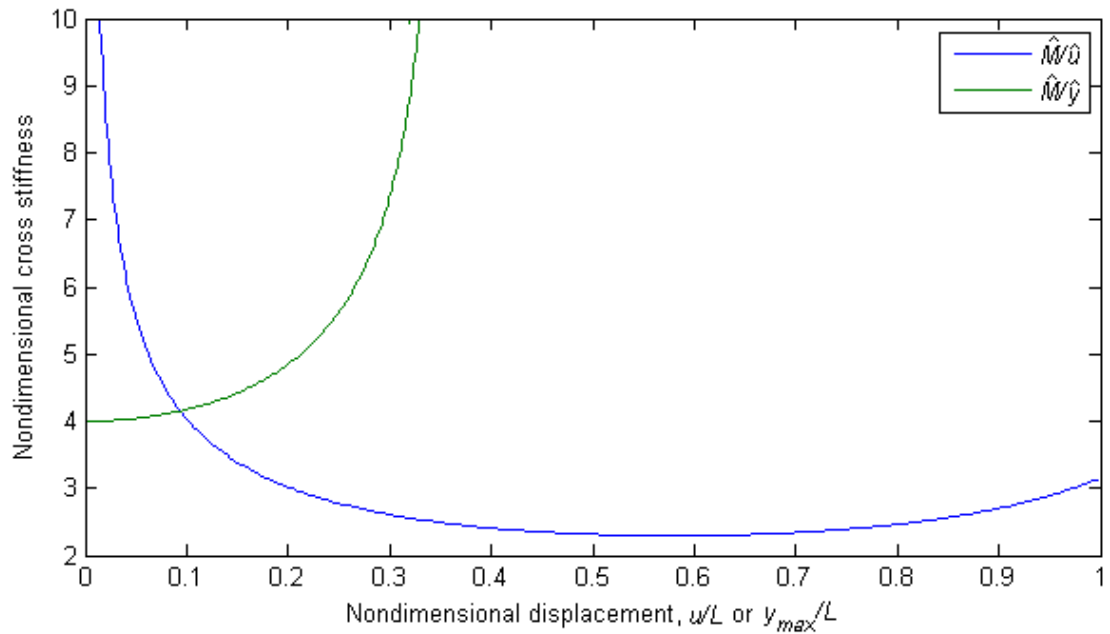


Figure 3-5: Cross stiffness as a function of deflection

3.2.2 Effect of rotation

Applying a bending moment to a beam causes it to deflect and take the shape of an arc. Although the rotational stiffness is constant, the cross stiffness in the axial direction \hat{M}/\hat{u} and transverse direction \hat{M}/\hat{y} are nonlinear, having softening and then hardening, and hardening behaviour respectively. Each segment of the beam rotates as a result of this deformation. Considering a single element, when it rotates its tip moves in both axial and transverse directions. Summing the displacements of all the elements gives the displacement of the beam in both directions. The effect of the angle of rotation on this displacement is the cause of the softening behaviour in the axial direction and the hardening behaviour in the transverse direction.

To illustrate this phenomenon, consider the line shown in Figure 3-6. The dotted line in Figure 3-6(a) is inclined at an angle of 10° to the x axis. By rotating the line by a further 10° , the tip of the line moves to the left by a distance dx . Now, consider the same dotted line making an angle of 70° with the x axis. By rotating it by a further 10° , as before, the projection of

displacement dx is larger than in the previous case. It can thus be seen that for an increasing angle the displacement in the x direction is proportionately larger and the displacement in the y direction is proportionately smaller in the second case.

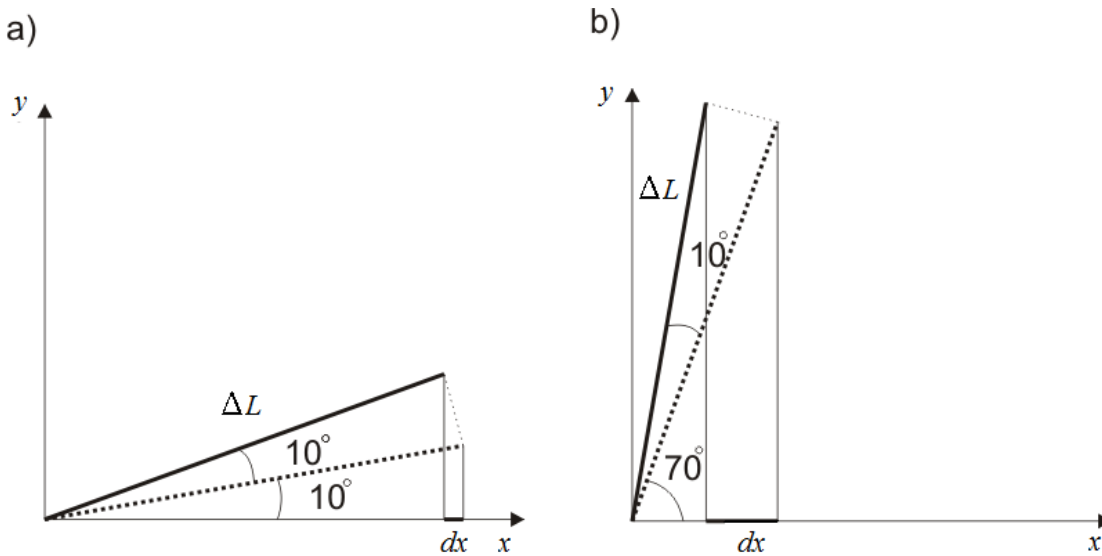


Figure 3-6: Relationship between the angle and the displacement in the x direction.

The tip displacement of the line in the x direction is the difference between its projections onto the x axis for two different positions. This is related to the cosine of the angle and can be derived easily.

Consider now equation (3-12) which describes the axial displacement of the tip of the beam. If the beam is divided into n equal segments, the integral on the right hand side of equation (3-12) can be approximated by a summation over the n segments, so that

$$u = L - \sum_{m=0}^n \cos \theta_m \Delta s \quad (3-14)$$

Because of the constant radius of curvature, the angle, $\Delta\theta$, for each segment Δs is constant, so that

$$\Delta\theta = \frac{\Delta s}{\rho} \quad (3-15)$$

Considering that $\Delta s = L/n$, and $L = 2\rho\theta_0$ then

$$\Delta\theta = \frac{2\theta_0}{n} \quad (3-16)$$

So equation (3-14) can be rewritten as,

$$u = L - \sum_{m=0}^n \cos\left(\frac{2m\theta_0}{n}\right) \Delta s \quad (3-17)$$

Thus, it can be seen that the axial displacement of the tip of the beam is the difference between the length of the beam and the sum of all projections of beam segments onto the x axis. It can also be seen that the relationship between the axial displacement of the beam and the rotation of the beam behaves in a similar way to the line discussed at the beginning of this section. Note that the angle θ_0 is linearly related to the bending moment as shown by equation (3-7) so the axial displacement of the beam subject to a bending moment behaves as a softening spring as discussed previously. This explains the softening behaviour shown in Figure 3-3 up to an angle θ_0 of about 120° . The hardening behaviour of the beam in the transverse displacement can be analysed in a similar way.

3.3 The static stiffness characteristics of a simply supported beam loaded at its centre

A simply supported beam with a movable support loaded by a harmonic transvers force at its midpoint is reported as a nonlinear oscillator with softening stiffness characteristics [20]. The beam is initially straight. The softening characteristics can cause a reduced tangent stiffness at the statically loaded working position. However, it is revealed here that their stiffness characteristic is not softening but hardening type. The same approach is used and developed here to obtain large deflection but considering the change in the distance between the supports which was neglected in the literature. The exact analytical differential equation is extracted here first which is used later to determine results numerically. It is then used as a reference to

validate the approximate solution derived using the Galerkin method in section 3.3.2. The results are also compared with solutions determined using the finite element analysis software ANSYS. The accuracy of the approximate method is also examined by comparing the shape function used with the actual deformed shape of the beam.

3.3.1 Exact solution

A concentrated load p is applied to the middle of the simply supported beam shown in Figure 3-7. As before, the transverse displacement of the beam is denoted by y and y_{max} is the maximum deflection at the middle. Parameter L is used for the length of the beam and is constant while parameter l is used for the distance between two supports and is the projection of the beam on to the horizontal direction which decreases as the transverse load increases. The bending moment at each cross section of the beam at a distance x from the left-hand end is given by,

$$M = \frac{px}{2} \quad \text{for } x < \frac{l}{2} \quad (3-18a)$$

$$M = \frac{p(l-x)}{2} \quad \text{for } x > \frac{l}{2} \quad (18b)$$

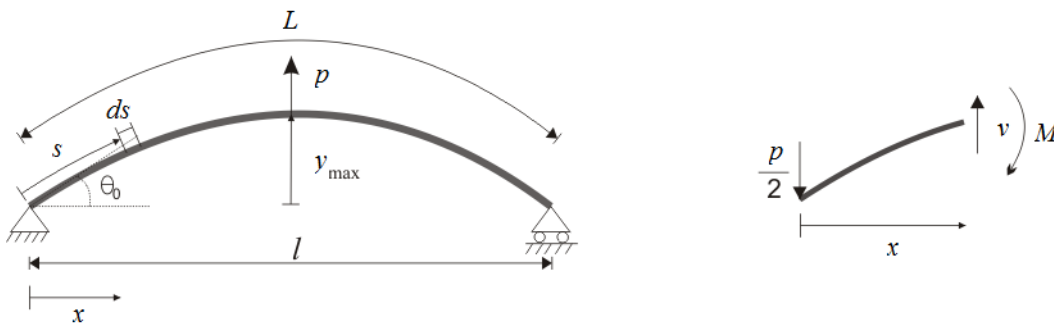


Figure 3-7: Simply supported beam loaded at the centre, a) schematic of the beam, b) a small section of the beam

The solution presented here is similar to that given in references [38, 45]. By substituting the expression for the bending moment from equation (3-18a) into equation (3-5) gives,

$$\frac{d\theta}{ds} = -\frac{px}{2EI} \quad \text{for } x < \frac{l}{2} \quad (3-19)$$

Because of symmetry only half of the beam is considered in the following analysis. The equation for $x > l/2$ would only be slightly different from the equations derived. Differentiating equation (3-19) with respect to s gives,

$$\frac{d^2\theta}{ds^2} = -\frac{p}{2EI} \frac{dx}{ds} \quad (3-20)$$

Now,

$$\frac{dx}{ds} = \cos \theta \quad (3-21)$$

Combining equations (3-20) and (3-21) gives,

$$\frac{d^2\theta}{ds^2} + \frac{p}{2EI} \cos \theta = 0 \quad (3-22)$$

Multiplying equation (3-22) by $d\theta/ds$ gives, after some rearrangement,

$$\frac{d}{ds} \left[\frac{1}{2} \left(\frac{d\theta}{ds} \right)^2 + \frac{p}{2EI} \sin \theta \right] = 0 \quad (3-23)$$

Integrating equation (3-23) gives,

$$\left(\frac{d\theta}{ds} \right)^2 + \frac{p}{EI} \sin \theta = c \quad (3-24)$$

where c is a constant. From equation (3-19), it can be seen that when $x = 0$, then $d\theta/ds = 0$. Also at this position $\theta = \theta_0$. Thus the constant is given by,

$$c = \frac{p}{EI} \sin \theta_0 \quad (3-25)$$

And equation (3-24) can be rewritten as,

$$\frac{d\theta}{ds} = -\sqrt{\frac{p}{EI}} \sqrt{\sin \theta_0 - \sin \theta} \quad (3-26)$$

Note that the minus sign is because of the negative curvature illustrated in Figure 3-1(b). The angle at the left-hand support θ_0 can be found by integrating equation (3-26) from $s=0$ to $L/2$,

$$L = -2 \sqrt{\frac{EI}{p}} \int_{\theta_0}^0 \frac{d\theta}{\sqrt{\sin \theta_0 - \sin \theta}} \quad (3-27)$$

The solution of the integral in equation (3-27) can be found in terms of an elliptical integral whose solution exists as a power series. Noting that $\cos \theta = dx/ds$ and $\sin \theta = dy/ds$, the following equations can be derived by multiplying equation (3-26) by $\cos \theta$ and $\sin \theta$ and integrating to obtain x and y at any point on the beam as a function of θ ,

$$x = 2 \sqrt{\frac{EI}{p}} \sqrt{\sin \theta_0 - \sin \theta} \quad (3-28)$$

$$y = -\sqrt{\frac{EI}{p}} \int_{\theta_0}^{\theta} \frac{\sin \theta d\theta}{\sqrt{\sin \theta_0 - \sin \theta}} \quad (3-29)$$

The angle θ is equal to zero at the middle of the beam where the transverse displacement is maximum. The length between the two supports and the maximum transverse displacement can be determined by setting $\theta = 0$ in equations (3-28) and (3-29) to give,

$$l = 4 \sqrt{\frac{EI}{p}} \sqrt{\sin \theta_0} \quad (3-30)$$

$$y_{max} = \sqrt{\frac{EI}{p}} \int_0^{\theta_0} \frac{\sin \theta d\theta}{\sqrt{\sin \theta_0 - \sin \theta}} \quad (3-31)$$

As described in many publications, the displacement of the beam can be found by way of elliptic integrals using a suitable variable transformation. The other approach is to evaluate the integrals using numerical methods by Matlab. To do this, the applied force p can be found by solving the integral in equation (3-27) for different values of θ_0 . Having a set of forces p and the corresponding set of angles θ_0 , the maximum deflection can be found from equation (3-31) by calculating the integral in this equation numerically for each pair of p and θ_0 . The distance between the supports can be easily calculated using equation (3-30). The shape of the deflected beam can be found from equations (3-28) and (3-29) by considering a set of values of θ varying from θ_0 to zero for each specific value of p .

3.3.2 An approximate solution

For large deflections, the relationship between the radius of curvature and the derivatives of the transverse displacement, y with respect to x (denoted by the superscript ') is [71],

$$\frac{1}{\rho} = \frac{y''}{(1 + (y')^2)^{\frac{3}{2}}} \quad (3-32)$$

By assuming that rotation is finite but not very large, this can be expanded by a Maclaurin series up to the second order of y' to give,

$$\frac{1}{\rho} = y'' \left(1 - \frac{3}{2} (y')^2\right) + O[y']^4 \approx y'' \left(1 - \frac{3}{2} (y')^2\right) \quad (3-33)$$

Combining equation (3-33) with equation (3-4) results in,

$$-\frac{M}{EI} = y'' \left(1 - \frac{3}{2}y'^2\right) \quad (3-34)$$

which is often called second order beam theory in the literature. Here, a sinusoidal shape function is chosen as it represents the shape of a simply supported beam in its first mode of vibration. Thus the transverse displacement of the beam can be approximated by,

$$y(x) = y_{max} \sin(kx) \quad (3-35)$$

The coefficient k can be found by applying the boundary condition $y(l) = 0$. Hence

$$y_{max} \sin(kl) = 0 \quad (3-36)$$

Hence, for the first mode of vibration which is the same as the static deflection of the beam in this case,

$$k = \frac{\pi}{l} \quad (3-37)$$

To find the deflection y_{max} , Galerkin's method is applied to equation (3-34) to give,

$$\int_0^l -\frac{M}{EI} \sin\left(\frac{\pi}{l}x\right) dx = \int_0^l y'' \left(1 - \frac{3}{2}y'^2\right) \sin\left(\frac{\pi}{l}x\right) dx \quad (3-38)$$

By substituting for $y(x)$ from equation (3-35) and M from equation (3-18a) gives,

$$\begin{aligned} \int_0^{\frac{l}{2}} \frac{px}{2EI} \sin\left(\frac{\pi}{l}x\right) dx + \int_{\frac{l}{2}}^l \frac{p(l-x)}{2EI} \sin\left(\frac{\pi}{l}x\right) dx \\ = \int_0^l y_{max} \left(\frac{\pi}{l}\right)^2 \sin^2\left(\frac{\pi}{l}x\right) \left(1 - \frac{3}{2}\left(\frac{y_{max}\pi}{l}\right)^2 \cos^2\left(\frac{\pi}{l}x\right)\right) dx \end{aligned} \quad (3-39)$$

Evaluating the integrals gives,

$$\frac{l^2 p}{2EI\pi^2} + \frac{l^2 p}{2EI\pi^2} = \frac{8y_{max}l^2\pi^2 - 3y_{max}^3\pi^4}{16l^3} \quad (3-40)$$

which can be rearranged to give,

$$p = \frac{EI\pi^4}{2l^3} \left(y_{max} - \frac{3\pi^2}{8l^2} y_{max}^3 \right) \quad (3-41)$$

where the right hand side of equation (3-41) is the same as the stiffness term of equation (3.158) in reference [20]. It may appear at first glance that the beam exhibits softening behaviour because of the negative sign in front of the cubic term. However, the length between the supports is not fixed and reduces in size because the beam is inextensible and the support on the right hand side slides to the left with increasing beam displacement. To determine whether the beam has a hardening or softening characteristic the expression given in equation (3-41) needs to be rewritten in terms of the length of the beam L . To do this the relationship between L and l needs to be determined.

Now,

$$L = \int_0^L ds = \int_0^l \sqrt{1 + (y')^2} dx \quad (3-42)$$

Substituting for y from equation (3-35) gives,

$$L = \int_0^l \sqrt{1 + \left(y_{max} \frac{\pi}{l} \right)^2 \cos^2 \left(\frac{\pi}{l} x \right)} dx \quad (3-43)$$

The integral in equation (3-43) can be evaluated as the sum of two elliptic integrals,

$$L = \frac{l}{\pi} \left(\int_0^{\frac{\pi}{2}} \sqrt{1 + \left(y_{max} \frac{\pi}{l}\right)^2 \sin^2 \theta} d\theta + \sqrt{1 + \left(y_{max} \frac{\pi}{l}\right)^2} \int_0^{\frac{\pi}{2}} \sqrt{1 + \frac{y_{max}^2 \pi^2}{l^2 + y_{max}^2 \pi^2} \sin^2 \theta} d\theta \right) \quad (3-44)$$

Expanding the elliptic integrals as a series up to second order results in,

$$L = l + \frac{y_{max}^2 \pi^2}{4l} \quad (3-45)$$

Rearranging equation (3-45), the distance between the supports can be written in terms of the length of the beam as,

$$l = \frac{1}{2} \left(L \pm \sqrt{L^2 - y_{max}^2 \pi^2} \right) \quad (3-46)$$

Combining equations (3-41) and (3-46) results in,

$$p = \frac{2EI\pi^4 (2y_{max} (L + \sqrt{L^2 - y_{max}^2 \pi^2})^2 - 3y_{max}^3 \pi^2)}{(L + \sqrt{L^2 - y_{max}^2 \pi^2})^5} \quad (3-47)$$

Expanding equation (3-47) as a series up to third order gives,

$$p = \frac{EI\pi^4}{2L^3} \left(y_{max} + \frac{3\pi^2}{8L^2} y_{max}^3 \right) \quad (3-48)$$

Comparing this with equation (3-41) it can be seen that the equations are identical in form with the exception of the sign change in front of the cubic term and the variable L replacing l . The beam has a hardening rather than a softening characteristic. Equations (3-47) and (3-48) can be written in non-dimensional form respectively as,

$$\hat{p} = 2\pi^4 \frac{\left(2\hat{y}_{max} \left(1 + \sqrt{1 - \hat{y}_{max}^2 \pi^2}\right)^2 - 3\hat{y}_{max}^3 \pi^2\right)}{\left(1 + \sqrt{1 - \hat{y}_{max}^2 \pi^2}\right)^5} \quad (3-49)$$

$$\hat{p} = \frac{\pi^4}{2} \left(1 + \frac{3\pi^2}{8} \hat{y}_{max}^2\right) \hat{y}_{max} \quad (3-50)$$

where $\hat{p} = p/(EI/L^2)$ and $\hat{y}_{max} = y_{max}/L$.

Equations (3-49) and (3-50) are plotted in Figure 3-8 together with results calculated from finite element analysis using ANSYS and the numerical solution of equation (3-31). The same ANSYS model as used in section 3.2.1 but loaded at the middle is used here.

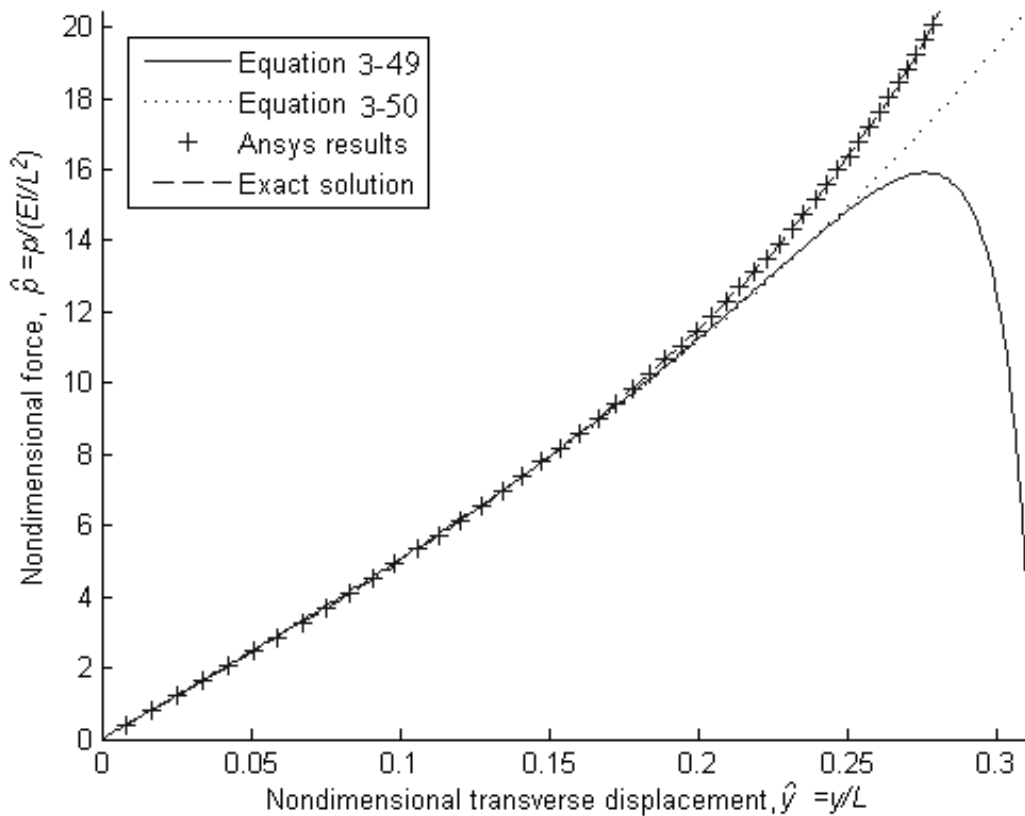


Figure 3-8: Non-dimensional force as a function of non-dimensional transverse displacement

Both equations (3-49) and (3-50) deviate from the exact solution at a non-dimensional transverse displacement of about 0.17. Since equation (3-50) is obtained by expanding equation (3-49) and neglecting higher order terms it is expected that equation (3-49) follows the exact solution more accurately. However, the negative higher order terms in equation (3-49) cause its solution to deviate almost immediately to negative values for a non-dimensional transverse displacement of about 0.27. Whilst, neglecting these higher order terms in obtaining equation (3-50) makes it to have a similar trend as the exact solution.

3.3.3 Discussion

The deflection of a slender beam is mainly due to the internal bending moment, and the effect of shear deformation can be neglected, which is the case in this study. To determine the reason why the beam has a hardening characteristic, the behaviour of the bending moment, which is the main reason for the deflection, is investigated.

Suppose a simply supported beam is loaded by a force equal to p_1 as shown in Figure 3-9(a). The internal bending moment as a function of the distance from the fixed end x is shown in the same figure. The maximum bending moment is at the middle of the beam and is equal to $p_1 l_1 / 4$ where l_1 is the distance between the supports. By increasing the force to $p_2 = \alpha p_1$, the beam deflects more and the distance between the supports l_2 decreases compared to l_1 . Although the force $p_2 = \alpha p_1$, the maximum bending moment $M_{\max 2} < \alpha M_{\max 1}$, because of the decreasing distance between the supports. In other words, the torque arm is smaller in second case compared to the first case.

Thus, as the force increases, the internal bending moment increases at a lower rate. Because of the direct relationship between the bending moment and the curvature, the beam exhibits hardening behaviour. In addition to this, the “rotation effect”, which was described in section 3.2.2, is valid in this case as well, and this also causes the beam to have hardening characteristics.

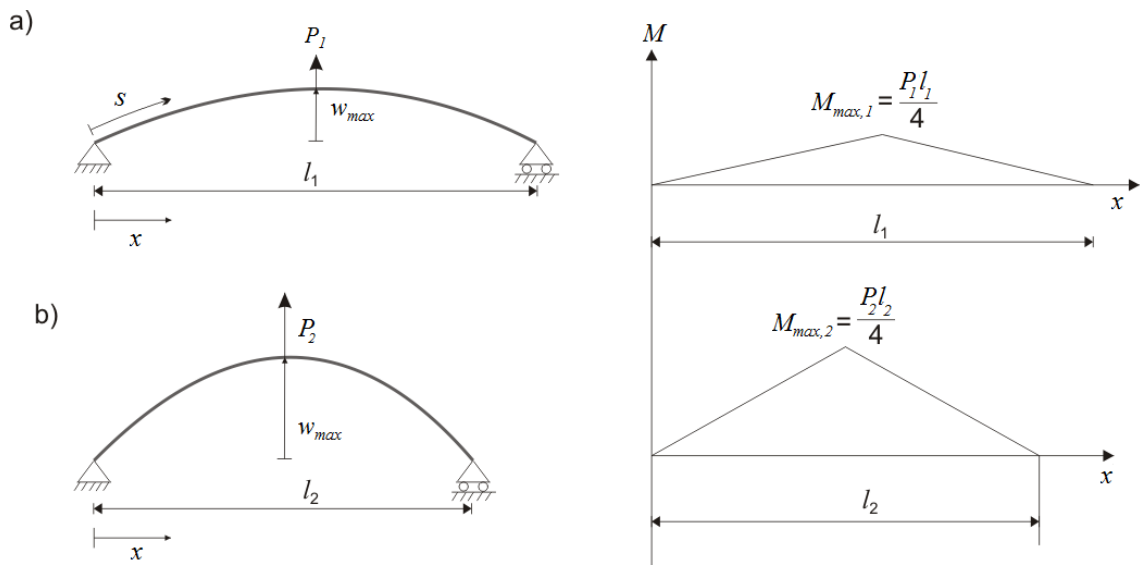


Figure 3-9: The bending moment in a simply supported beam loaded at the centre

3.3.4 Accuracy of the approximate solution

To find a solution for the large deflection of the simply supported beam, two approximations were made. The first one was to consider the deflected shape of the beam to be a Sine function. The second approximation was made in the determination of the length between the beam supports as a function of force and transverse displacement. This was considered to be a second order function of the length of the beam with the higher order terms being ignored. The effect of these approximations is investigated in this section.

The Sine function is considered to be a good candidate for the shape function for a simply supported beam in the Galerkin method. It satisfies the simply supported boundary condition and its first and second derivatives are determinable easily.

To examine its suitability, the shape of the beam modelled by the Sine function is compared with the exact shape of the deflected beam derived from the exact solution of equation (3-29) which is calculated numerically and is shown in Figure 3-10. The dotted line represents the shape of the beam given by $\hat{y}_{max} \sin \pi \hat{x}$. The approximate shape is a reasonable representation of the actual shape of the beam even for large deflections. The Mean Square Error (MSE)

between the actual and the approximate shape normalised by the area bounded by the curves of the deflected shape and the undeflected shape of the beam is shown in Figure 3-11 as a function of the non-dimensional force applied to the beam. The error is small but increases rapidly for non-dimensional forces greater than about 12. As well as errors in the approximate displacement there are errors in the first and second derivatives of transverse displacement as well, and these are investigated next.

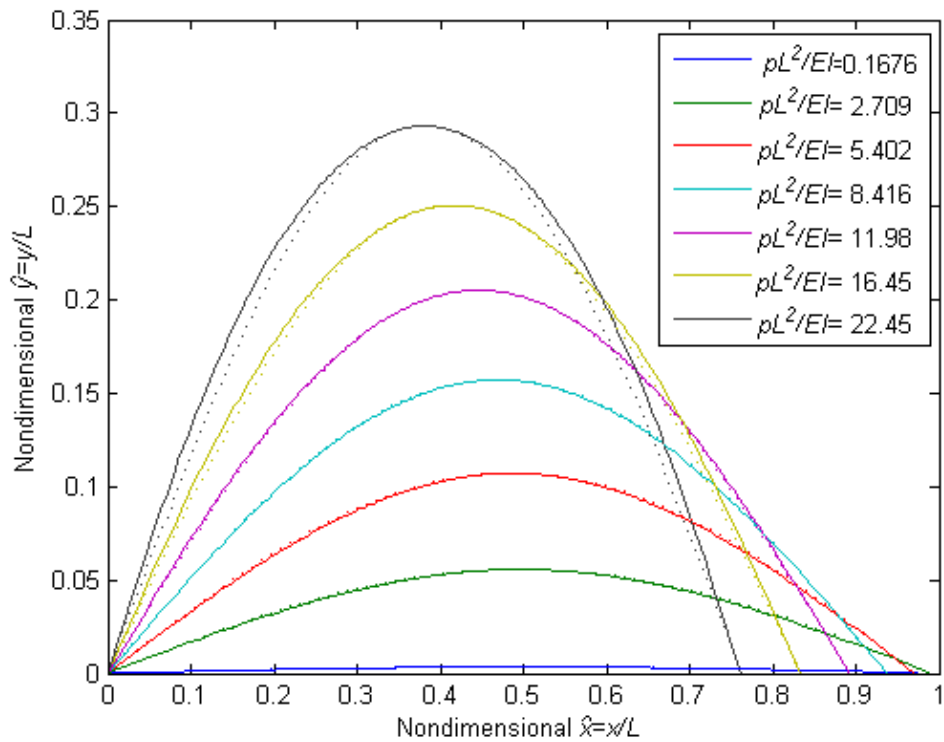


Figure 3-10: Deflected shape of the beam for different values of load, solid lines (-): exact shape, dotted lines (...): shape given by a Sine function

Examining equation (3-38), it can be seen that the first and second derivatives of the transverse displacement have been used to find the deflection of the beam. The first derivative of the transverse displacement with respect to x is shown in Figure 3-12. The Sine function is a good approximation for small displacements, but deviates for higher loads especially close to the ends of the beam. The mean square error of the first derivative (slope) normalised by the area under the curve (as before) is plotted in Figure 3-13. The MSE of the slope increases with the force similar to the MSE of the displacement.

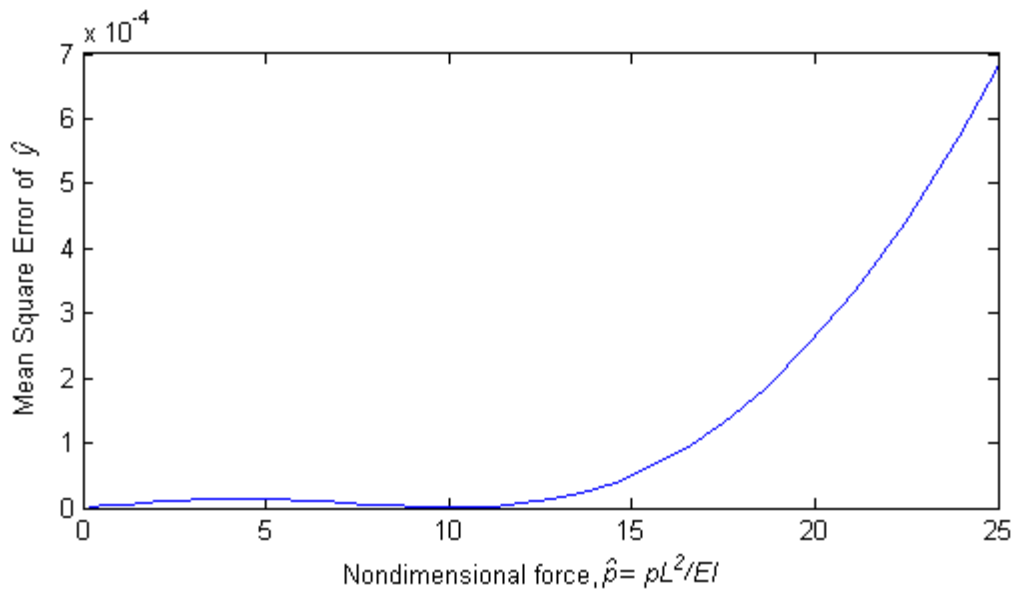


Figure 3-11: Normalised mean square error between the actual and approximate shapes of the beam

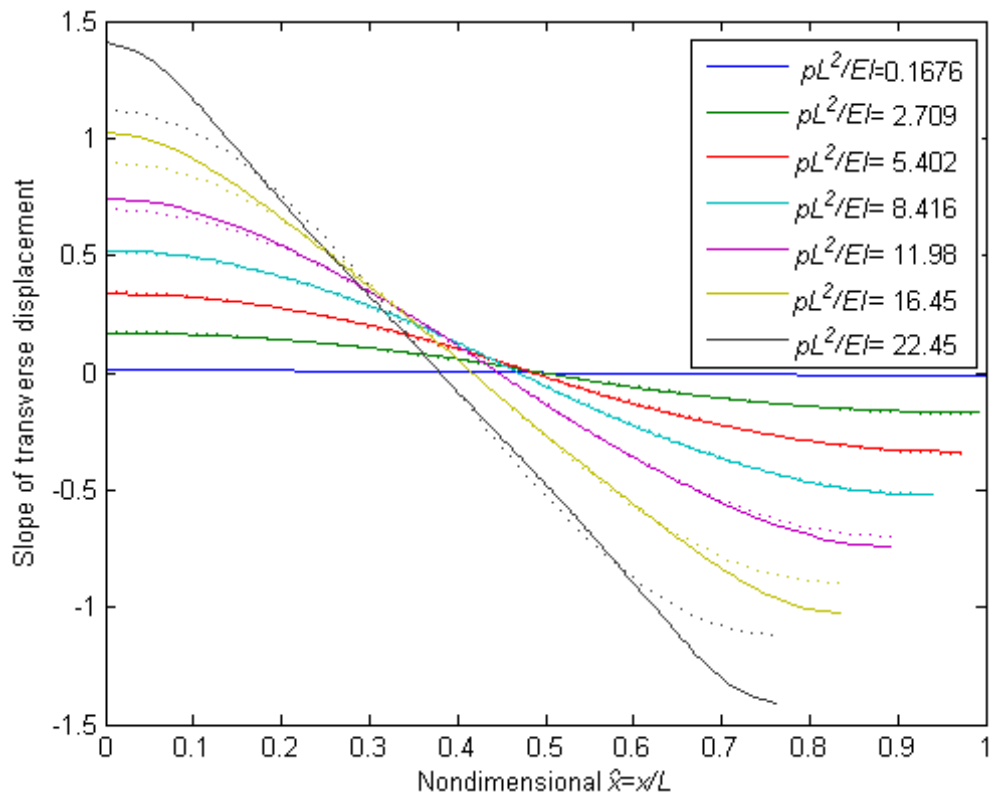


Figure 3-12: Slope of transverse displacement, solid lines (-): exact solution, dotted lines (...): approximate solution

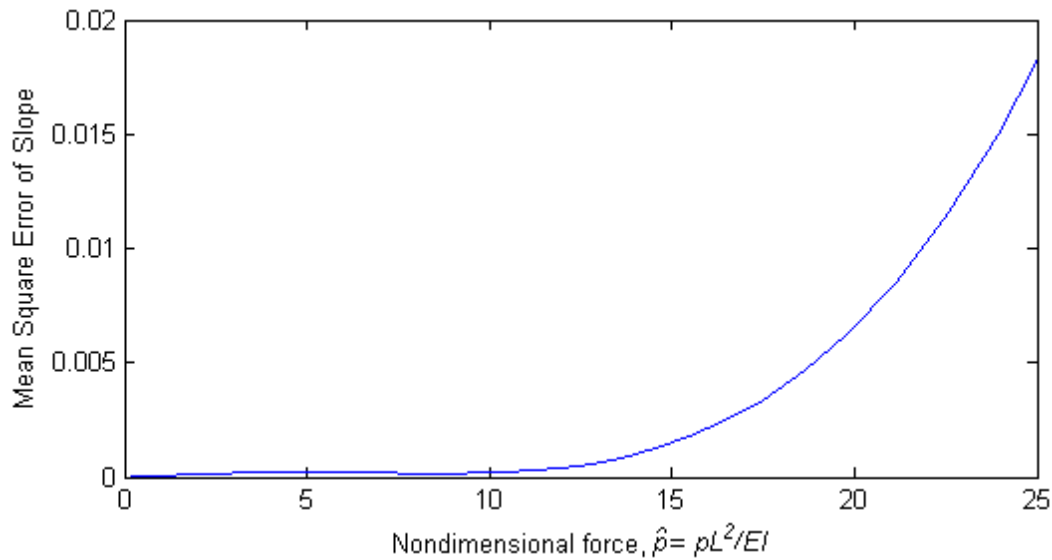


Figure 3-13: Mean Square Error of slope normalised by the area under the curve

The same procedure is followed for the second derivative of the transverse displacement with respect to x . The second derivatives of the exact and approximate solutions are shown in Figure 3-14. It can be seen that the Sine function is no longer a good approximate of the second derivative of the beam. The second derivative is not a smooth function, as there is a discontinuity at the centre of the beam. This can be understood by examining equation (3-34), that the second derivative is a function of the bending moment as well as slope of the beam. The bending moment of a simply supported beam loaded by a force at the centre has a triangular shape with the maximum being in the middle. For small loads, where the slope is small, the second derivative is predominantly a function of the bending moment only. By increasing the force and as a result the deflection, the slope of the beam increases and cannot be ignored in this case. This results in the second derivative having a pronounced discontinuity at the centre of the beam.

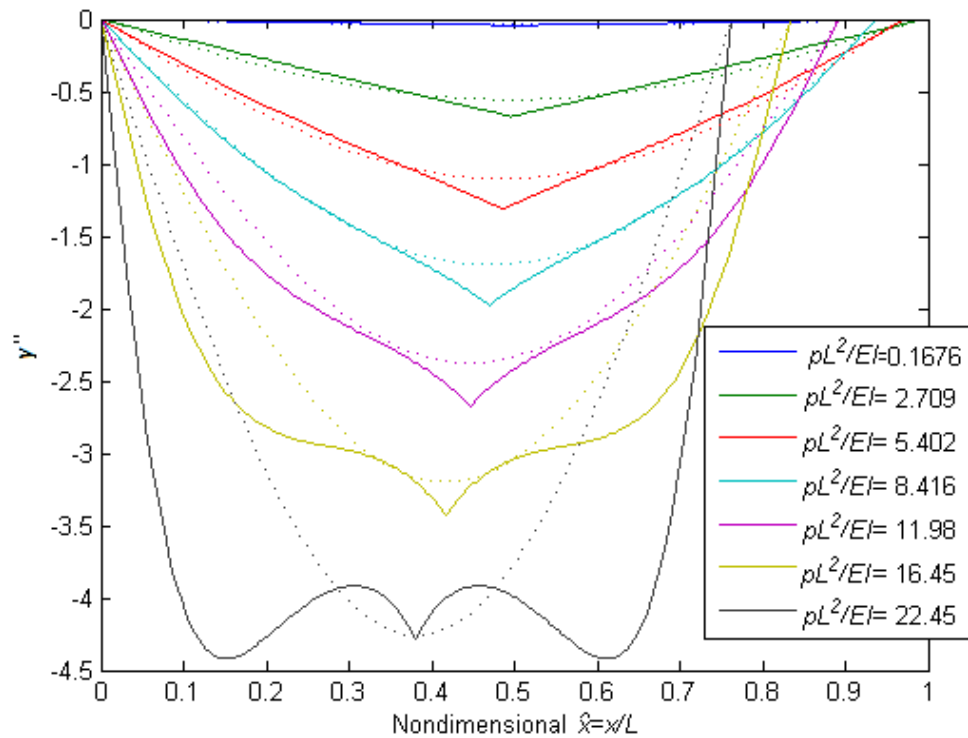


Figure 3-14: Second derivative of the transverse displacement, solid lines (-): exact solution, dotted lines (...): sine function

To obtain the approximate solution, the integral of the product of second derivative and first derivative of deformation is used. Although, the Sine function does not approximate well the second derivative of deformation, the area under the curve is very similar to the actual curve and thus the normalised MSE between the actual and the approximate solutions is small for small loads as shown in Figure 3-15.

The second issue with the accuracy of the approximate solution is the accuracy of the solution for length between the supports. As mentioned in the previous section, the accuracy of equation (3-49) illustrated in Figure 3-8 is linked to the accuracy of the expansion of the integral in equation (3-43) used to derive equation (3-49). The expansion of equation (3-44), which relates the length of the beam to the distance between the beam supports, can be written in a more complete form by including higher order terms to give,

$$L = l + \frac{y_{max}^2 \pi^2}{4l} - \frac{3y_{max}^4 \pi^4}{64l^3} + \frac{5y_{max}^6 \pi^6}{256l^5} - \frac{175y_{max}^8 \pi^8}{16384l^7} + \frac{441y_{max}^{10} \pi^{10}}{65536l^9} - \frac{4851y_{max}^{12} \pi^{12}}{1048576l^{11}} + \dots \quad (3-51)$$

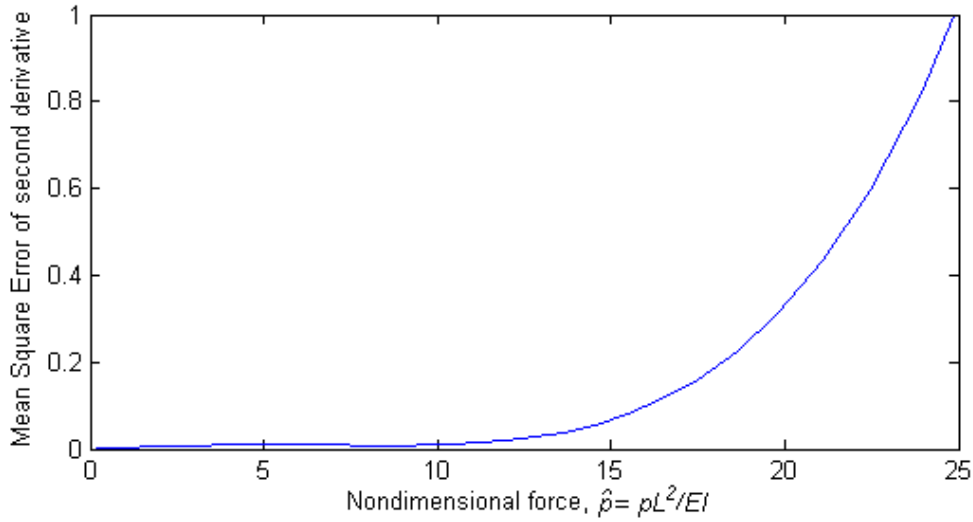


Figure 3-15: Mean Square Error of the second derivative normalised by the area under the curve

Considering this equation, the distance between the beam supports l cannot be derived easily as a function of the beam's length L . The integral in equation (3-43) can be solved numerically to compare the results with the series. A new variable a is introduced to help solve the integral numerically, so that

$$a = \frac{x}{l} \rightarrow dx = l da \quad (3-52)$$

and the integral in equation (3-43) can be rewritten as,

$$\frac{L}{l} = \int_0^1 \sqrt{1 + \left(\pi \frac{y_{max}}{l}\right)^2 \cos^2(\pi a)} da \quad (3-53)$$

Solving this integral for values of y_{max}/l from zero to one gives the results presented in Figure 3-16. Results of the expanded series using the first two, three and seven terms of equation (3-51) are plotted alongside the numerical solution as well. The expansion series results match with the numerical results well for small beam deflections, but deviate rapidly for large deflections. It can be seen that the truncated series given in equation (3-45), which is used to give the analytical results, gives reasonable accuracy up to a value of $y_{max}/l < 0.2$. For approximate solutions with higher orders, the results match with the exact solution up to a slightly larger displacement but then deviates from the exact solution more rapidly. The approximate solution shown in Figure 3-8, deviates from the exact solution at about the same displacement. From these two, it seems that the dominant parameter which affects the accuracy of approximate solution is the accuracy of the approximated distance between the supports, l . The odd number terms in expansion (3-51) have negative sign. As a result, when choosing odd number of terms for approximate solution, e.g. 7 terms, the approximate solution deviates from exact solution towards negative infinity at large displacement. The lower order terms can be neglected at large displacements.

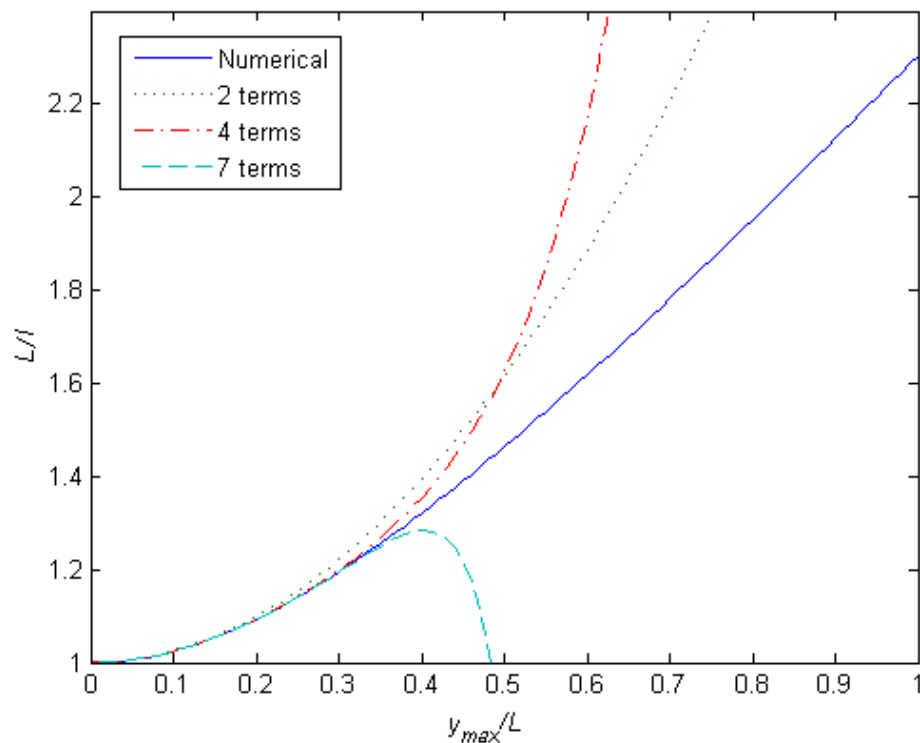


Figure 3-16: Relationship between the distance between the beam supports, its length and the transverse displacement.

3.4 Buckling and post-buckling of beam

In structural stability texts, buckling is defined as a failure of a slender column due to transverse deflection under a compressive force rather than exceeding the compressive strength of its material. “Buckling is the first structural stability problem that was solved historically”[72]. The reduction in the stiffness of the columns at the buckling point makes them a suitable candidate for the stiffness element of nonlinear isolators. They can be loaded beyond the buckling point where the tangent stiffness is less than the static stiffness. Here, the buckling load using Euler theory is obtained first, and then a post buckled beam is investigated to inspect the nonlinear performance of isolators comprising buckled elements. Columns may be referred to as “beams” here for consistency with the rest of this study.

3.4.1 Buckling analysis of beams (Euler Buckling)

Buckling happens when the internal moment due to a transverse perturbation and the axial loading is enough to maintain transverse deflection of the beam. The most well-known formula of buckling of structures is the Euler buckling load which defines the maximum load a column can undergo before large deflection due to buckling happens. The Euler buckling load is derived by employing linear theory of bending and does not provide any information of post-buckling characteristics of beams. A beam loaded axially is shown in Figure 3-17. A buckled beam is shown in Figure 3-17(b) where axial load P is greater than the Euler buckling load, P_E . The internal moment can be obtained by considering the free body diagram of Figure 3-17 (c).

$$M = pw \quad (3-54)$$

By considering small displacement and rotation the following approximation can be derived from equation (3-32) for curvature,

$$\frac{1}{\rho} = w'' \quad (3-55)$$

where ρ is the radius of curvature and prime denotes differentiation with respect to x . By substituting M from equation (3-54) into equation (3-4) and considering the above relation

between radius of curvature and slope, the following linear homogenous differential equation can be derived,

$$w'' + k^2 w = 0 \quad (3-56)$$

where k^2 is equal to P/EI and EI is elastic rigidity. The general solution of the above differential equation is in the form of,

$$w = A \sin kx + B \cos kx \quad (3-57)$$

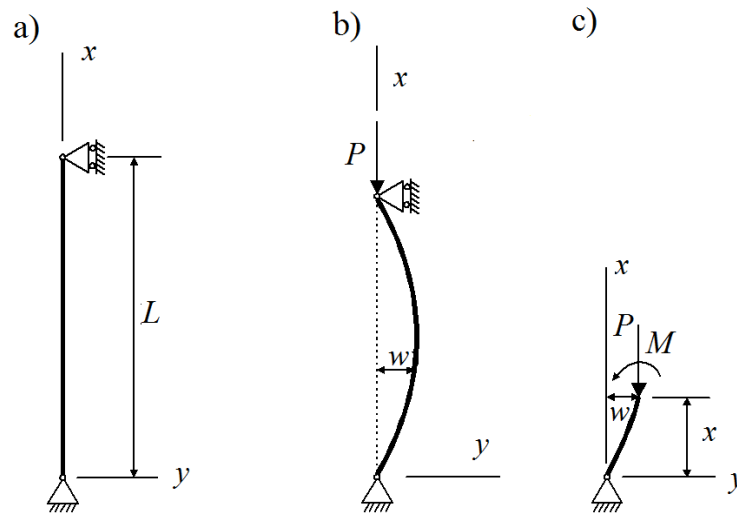


Figure 3-17: Simply supported column, a) unloaded, b) buckled, c) free body diagram

By applying boundary conditions for a simply supported beam,

$$w(0) = 0 \quad \Rightarrow \quad B = 0 \quad (3-58)$$

$$w(L) = 0 \quad \Rightarrow \quad A \sin kL = 0 \quad (3-59)$$

The nontrivial solution is,

$$\sin kL = 0 \quad \Rightarrow \quad kL = n\pi \quad (3-60)$$

This solution defines the load required to obtain a transversely deflected shape. It does not provide information about the magnitude of deflection since A can be any arbitrary value. The solution defines the minimum load that makes transverse deflection possible. By substituting k and setting n equal to 1, the lowest buckling load will be,

$$P_E = \frac{\pi^2 EI}{L^2} \quad (3-61)$$

Buckling is a neutral stability. The column can buckle to left or right, or axial deformation can continue if there is no perturbation and the beam and loading are ideal. When the beam buckles it undergoes large deformation. Hence, the small deflection assumption is no longer valid and large deflection theory must be employed to investigate post-buckling of the beam.

3.4.2 A post-buckled straight beam

Nonlinear finite deflection theory is employed to obtain the deflection of a post-buckled axially loaded straight beam. The analysis presented in this section is similar to that presented in reference [71]. The buckled beam is shown again in Figure 3-18 where a new coordinate s is defined which is measured from the beam's end along the deflected curve. By neglecting the axial strain (inextensible beam), the slope angle θ and coordinate s will be used instead of x and w in the following analysis. Equation (3-5) can be rewritten by substituting the moment M which is equal to Pw as,

$$\frac{d\theta}{ds} = -\frac{Pw}{EI} \quad (3-62)$$

By differentiating both sides with respect to s and noting that dw/ds is equal to $\sin\theta$ the following nonlinear differential equation can be derived,

$$EI\theta'' = -P \sin\theta \quad (3-63)$$

where prime denotes differentiation with respect to s . Kirchhoff was the first to solve this problem. He noticed that it is identical to the differential equation for large oscillations of a

pendulum [71]. The equation is rewritten by substituting $\sin\theta$ by its half angle equivalent and multiplying both sides by θ' ,

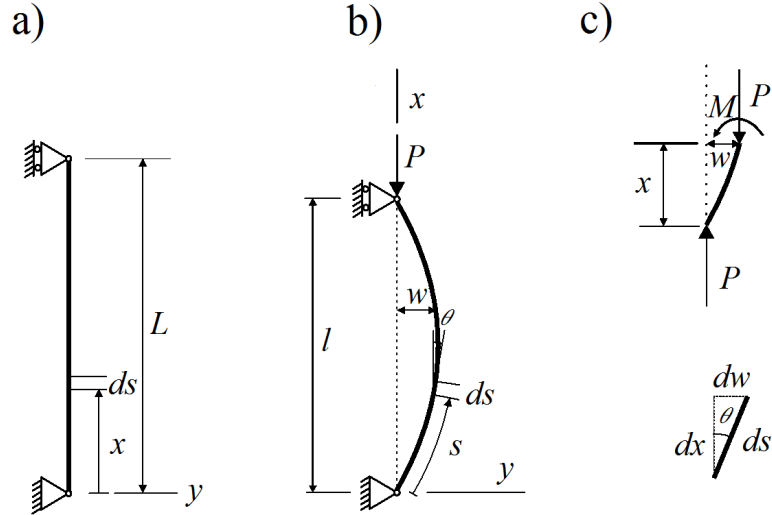


Figure 3-18: Simply supported beam under axial load, a) unloaded, b) buckled, c) free body diagram

$$EI\theta''\theta' = -2P \sin\left(\frac{\theta}{2}\right) \cos\left(\frac{\theta}{2}\right) \theta' \quad (3-64)$$

which is equal to,

$$\frac{EI}{2} \frac{d}{ds} (\theta'^2) = -2P \frac{d}{ds} \left(\sin^2 \frac{\theta}{2} \right) \quad (3-65)$$

By integrating the above equation,

$$\frac{1}{4k^2} \theta'^2 = -\sin^2 \frac{\theta}{2} + c^2 \quad (3-66)$$

where $k^2 = P/EI$ and c is a constant of integration. The bending moment is zero at the tips of the beam ($s = 0$ and $s = L$) which, from equation (3-62), results in $d\theta/ds$ equal to zero at the same positions. Denoting the angle at $s=0$ by θ_0 , the constant of integration can be obtained as,

$$c = \sin \frac{\theta_0}{2} \quad (3-67)$$

To solve the nonlinear differential equation (3-66) the variables can be separated, and by taking square root,

$$\frac{\pm d\theta}{\sqrt{c^2 - \sin^2 \frac{\theta}{2}}} = 2kds = \frac{2\pi}{L} \sqrt{\frac{P}{P_E}} ds \quad (3-68)$$

The \pm defines buckling to the left and to the right. The minus sign is considered hereafter. The integral of the above equation defines the curve of the deflected beam completely which is known as an elastica. It can be converted to an elliptic integral by proper variable substitution,

$$\sin \frac{\theta}{2} = c \sin \varphi \quad d\theta = \frac{2c \cos \varphi d\varphi}{\cos(\theta/2)} = \frac{2c \cos \varphi d\varphi}{\sqrt{1 - c^2 \sin^2 \varphi}} \quad (3-69)$$

The slope angle at the tip is θ_0 which results in $\sin \varphi_0 = 1$ or $\varphi_0 = \pi/2$, and the angle of the slope at the middle is equal to zero which yields $\sin \varphi = 0$ or $\varphi = 0$. The slope angle at the tips of the beam θ_0 can be obtained by taking the integral of equation (3-68) from $s=0$ to $s=L/2$,

$$\frac{\pi}{2} \sqrt{\frac{P}{P_E}} = \int_0^{\pi/2} \frac{d\varphi}{\sqrt{1 - c^2 \sin^2 \varphi}} \quad (3-70)$$

This is an elliptical integral of the first kind to which a solution exists as a power series and θ_0 can be solved as a function of P . If a small end rotation of θ_0 is considered, the constant c would be a very small number which results in $c^2 \sin^2 \varphi$ being much smaller than unity. A Taylor series can be used to expand the left side of the integral and higher order terms can be neglected,

$$\frac{1}{\sqrt{1 - c^2 \sin^2 \varphi}} = 1 + c^2 \sin^2 \varphi \quad (3-71)$$

The integral of equation (3-70) can be solved by this modification easily for small rotation to result in,

$$P = P_E \left(1 + \frac{\theta_0^2}{8} \right) \quad (3-72)$$

For a very small angle of deflection θ_0 , the applied force would be equal to the Euler buckling load which is in agreement with linear theory. The other conclusion that can be made from the above equation is that the load increases by increasing deflection (stiffness is positive and thus the buckled beam is statically stable).

To obtain the displacement of the tip of the beam, equation (3-68) can be multiplied by $(1+\cos\theta)$, noting that $ds \cos\theta$ is equal to dx ,

$$-\frac{2(1 - \sin^2(\theta/2))}{\sqrt{c^2 - \sin^2(\theta/2)}} = 2k(ds + dx) \quad (3-73)$$

By applying the same substitution of variables as introduced in equation (3-69) and by integrating the right hand side from $s=0$ to $s=L/2$,

$$l = L \left(\frac{4}{\pi} \sqrt{\frac{P_E}{P}} \int_0^{\pi/2} \sqrt{1 - c^2 \sin^2 \varphi} d\varphi - 1 \right) \quad (3-74)$$

where l is the distance between the supports. The axial displacement is,

$$u = L - l = 2L \left(1 - \frac{2}{\pi} \sqrt{\frac{P_E}{P}} \int_0^{\pi/2} \sqrt{1 - c^2 \sin^2 \varphi} d\varphi \right) \quad (3-75)$$

An approximate solution can be obtained by considering small rotation, $(1 - c^2 \sin^2 \varphi)^{1/2} \approx 1 - \frac{1}{2} c^2 \sin^2 \varphi$ and $\sin \theta_0 \approx \theta_0$. Then the axial displacement is,

$$u = 2L \left(1 - \left(1 - \frac{\theta_0^2}{16} \right) \sqrt{\frac{P_E}{P}} \right) \quad (3-76)$$

The tip slope angle can be substituted from equation (3-72) into the above equation to find a direct relation between force and deflection,

$$u = L \left(2 - 3 \sqrt{\frac{P_E}{P}} + \sqrt{\frac{P}{P_E}} \right) \quad (3-77)$$

Numerical analysis can be employed to obtain the exact solution for the buckled beam. The force-deflection for a buckled beam can be solved numerically from equations (3-70) and (3-76). The applied force can be calculated by solving the integral of equation (3-70) numerically for different values of tip angle θ_0 . Having applied force P and its corresponding tip slope angle θ_0 , the axial displacement can be found from equation (3-75). The exact solution obtained by this method alongside the approximate solution of equation (3-77) is shown in Figure 3-19. The approximate solution deviates from the exact solution at the non-dimensional displacement of about 0.2 which makes it suitable for most practical analysis. It can be seen that the post-buckled beam perform as a hardening spring. The minimum tangent stiffness can achieve at the buckling point.

To obtain the minimum stiffness at the buckling point, equation (3-77) can be differentiated in non-dimensional form,

$$d\hat{u} = \left(\frac{3}{2(\sqrt{\hat{P}})^3} + \frac{1}{2\sqrt{\hat{P}}} \right) d\hat{P} \quad (3-78)$$

where \hat{P} is the non-dimensional force and is equal to P/P_E and \hat{u} is the non-dimensional displacement and is equal to u/L . If a value of unity is taken for the non-dimensional force, the non-dimensional stiffness can be obtained as,

$$\hat{k}|_{P=P_E} = \frac{d\hat{P}}{d\hat{u}}|_{P=P_E} = \frac{1}{2} \quad (3-79)$$

Thus the asymptotic relation can be obtained as,

$$\hat{P} = 1 + \frac{1}{2}\hat{u} \quad (3-80)$$

The asymptotic relation is shown in the Figure 3-19 with a dashed-dot line. This defines the minimum tangent stiffness achievable with a buckled beam. It should be mentioned that compression of the beam is neglected in this analysis.

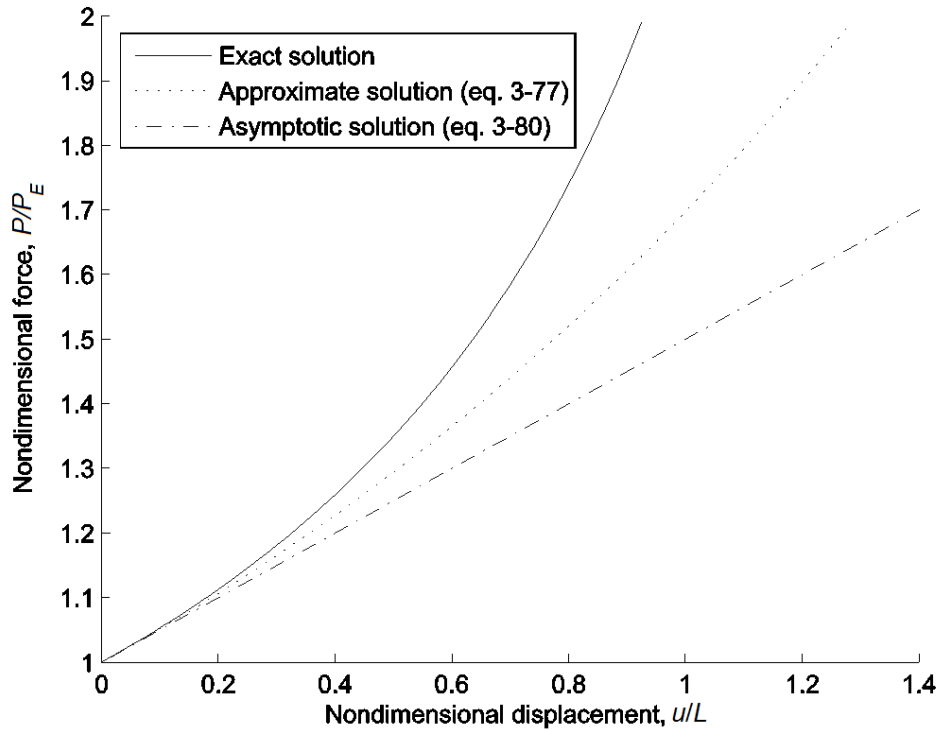


Figure 3-19: Non-dimensional force-displacement of inextensible buckled beam

To investigate the advantages of implementing a post-buckled beam as a stiffness element of a nonlinear isolator the static stiffness must be compared with the minimum tangent stiffness. The

displacement of the beam tip before buckling is due to axial stiffness. The displacement can be obtained from the following equation,

$$u_a = \frac{PL}{EA} \quad (P \leq P_E) \quad (3-81)$$

where A is the cross section area of the beam. The axial displacement at the buckling point can be found by replacing the axial load with the buckling load from equation (3-61) in the above formula,

$$u_0 = \frac{\frac{\pi^2 EI}{L^2} L}{EA} = \frac{\pi^2 I}{LA} \quad (P = P_E) \quad (3-82)$$

where u_0 is the beam tip displacement just before buckling. The displacement only depends on the geometry of beam and the material does not affect it. To consider the overall displacement of the post-buckled beam, the force-displacement curves shown in Figure 3-19 must be shifted to the right by u_0/L . A schematic graph of force-displacement of a buckled beam is shown in Figure 3-20 which also demonstrates the force-displacement prior to buckling.

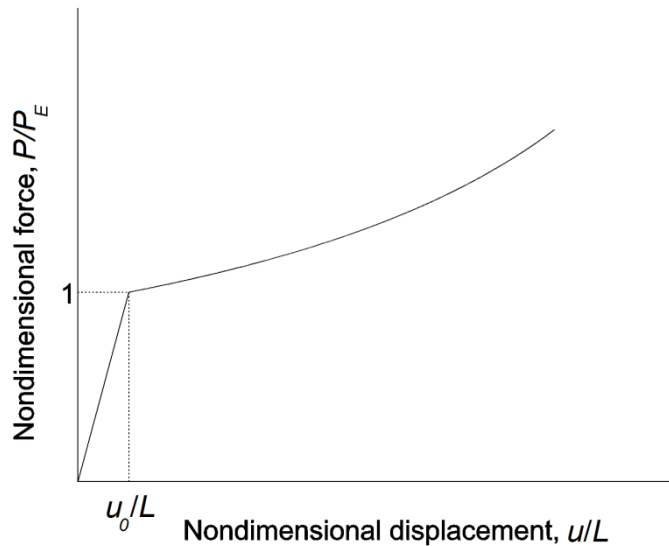


Figure 3-20: Schematic diagram of force-deflection before and after buckling

The buckling of an axially loaded straight beam happens when the bending moment developed in the beam due to its lateral deflection is large enough to establish such a deflection. In ideal conditions where there are not any disturbances, the beam will deflect only axially whatever the force. This is an unstable equilibrium state and by introducing a small transverse disturbance, for a load bigger than the buckling load, the beam will deflect laterally to its stable equilibrium deformed shape. This is why in structural stability texts it is called a bifurcation point, where the beam can choose its deformed shape, deflecting to the right, left, or unstable axial deflection. The imperfections can be modelled as a load applied off- axis or initial curvature of the beam, or both.

The buckling point, where the tangent stiffness is a minimum, may be considered as a possible working point of a nonlinear isolator. The non-dimensional displacement would be $\pi^2 I/L^2 A$ for this point. However, there is a singularity in force-deflection curve of a beam due to buckling. This singularity is undesirable and will cause strong nonlinearity effects to appear in the dynamic response of the system. Thus the beam must be statically loaded beyond buckling to avoid the buckling point from occurring in the displacement range of the isolator. The approximate asymptotic solution can be used to model the isolator in this range, but the actual tangent stiffness will be higher than the asymptotic solution suggests. The other way to overcome the problem of singularity in force-displacement relation is to modify the beam to have a smoother force-displacement curve. This can be achieved by applying the load eccentrically or by implementing a curved beam instead of a straight beam.

3.5 Beam loaded eccentrically

A straight beam loaded eccentrically is shown in Figure 3-21 where the eccentricity is denoted by e . The application of the off- axis load causes a bending moment to be applied to the beam as well as the axial load. Compared to the straight beam studied previously, the newly introduced bending moment causes the beam to deflect laterally from the outset of load application in contrast to the former one which deflects laterally only after buckling. The lateral deflection of the beam from the beginning removes the singularity in force-deflection curve. The bending moment of the beam in this case is,

$$M = P(w + e) \quad (3-83)$$

Hence equation (3-62) can be rewritten as,

$$\frac{d\theta}{ds} = -\frac{P(w + e)}{EI} \quad (3-84)$$

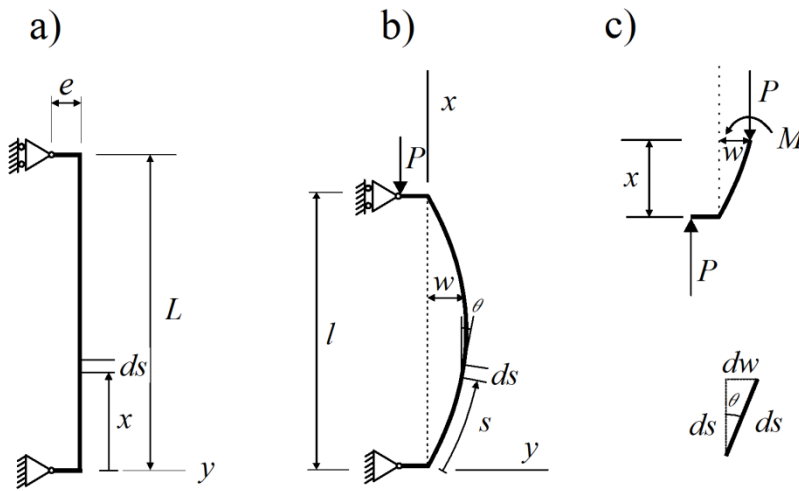


Figure 3-21: Simply supported beam under axial eccentric load, a) unloaded, b) loaded, c) free body diagram

Differentiating both sides with respect to s , the same equation as equation (3-63) is derived. Thus, the differential equation describing the beam loaded eccentrically is exactly the same as the straight beam. The eccentricity appears in the constant of integration in equation (3-66). The bending moment is not zero at its tips and the constant of integration c will be given by,

$$c^2 = \frac{1}{4k^2} \left(\frac{Pe}{EI} \right)^2 + \sin^2 \frac{\theta_0}{2} = \frac{\pi^2}{4} \left(\frac{e}{L} \right)^2 \left(\frac{P}{P_E} \right) + \sin^2 \frac{\theta_0}{2} \quad (3-85)$$

Considering this new constant of integration equation (3-75) can be solved to find the force-displacement relation for beam with non-dimensional eccentricity e/L . This is shown in Figure 3-22. The singularity at the buckling point has disappeared and the beam tangent stiffness decreases gradually. As expected, the deflection of the beam for the same load increases by increasing the eccentricity. It seems that the curves are almost parallel in part of

displacement range which implies similar tangent stiffness but for bigger deflection where eccentricity is larger. The stiffness of a beam with eccentricity and a curve beam are both examined later in this chapter to investigate their suitability as vibration isolators.

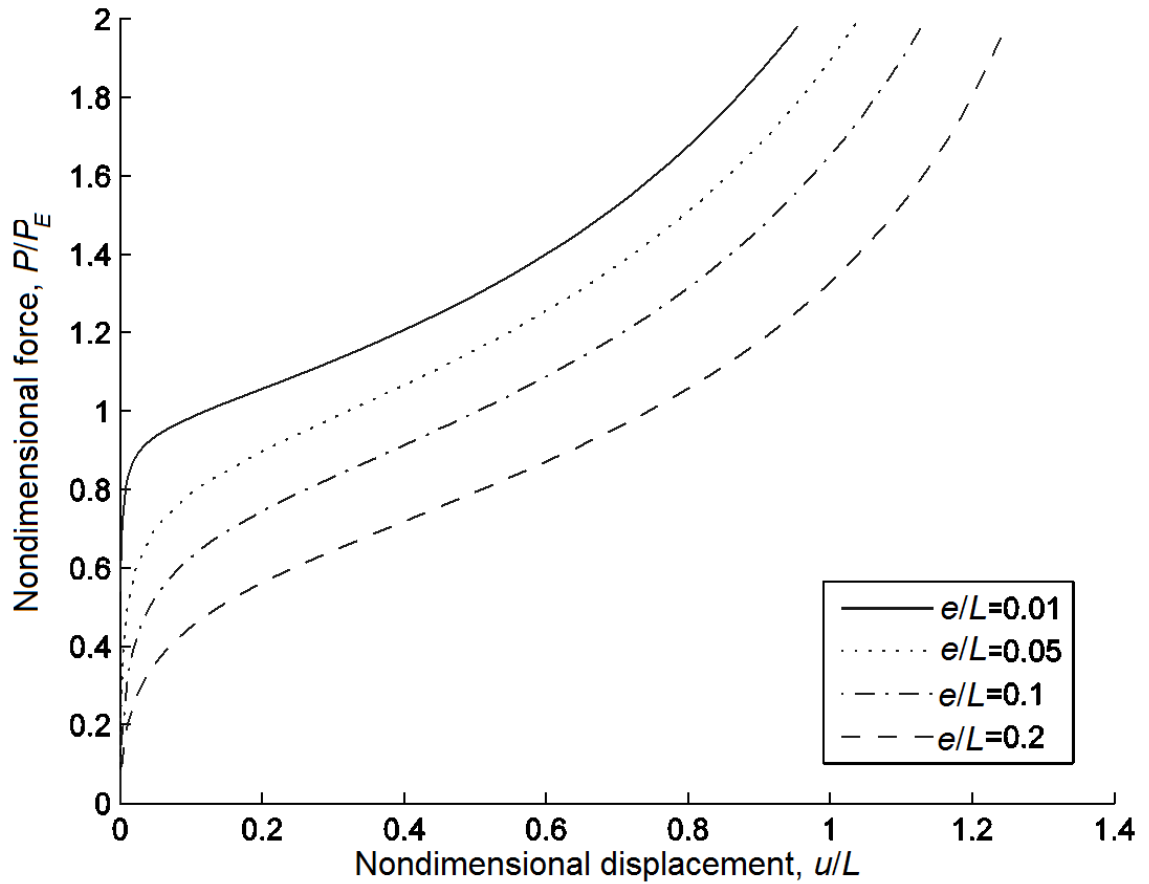


Figure 3-22: Non-dimensional force-displacement of inextensible beam loaded eccentrically

3.6 Curved beams

A beam with constant initial curvature is shown in Figure 3-23. A bending moment develops in the curved beam by loading it axially in a similar way as for the beam loaded out of axis. The distribution of internal bending moment is different in the two cases which results in different force-displacements graphs. The internal bending moment causes the beam to deflect laterally

even when the load is small. This prevents forming a buckling point where the deflection increases suddenly with a small increase in load and a corresponding singular point in the graph. The following relation between the magnitude of the bending moment and curvature for a thin curved beam is given in reference [73],

$$EI \left(\frac{1}{\rho} - \frac{1}{R} \right) = -M \quad (3-86)$$

where ρ is the radius of curvature of the loaded beam and R is the initial radius of the curved beam. The equation for bending moment is the same as for the straight beam and is equal to pw . The same differential equation as equation (3-63) for a straight beam can be obtained for a curved beam by substituting for the bending moment from the above equation and differentiating with respect to s .

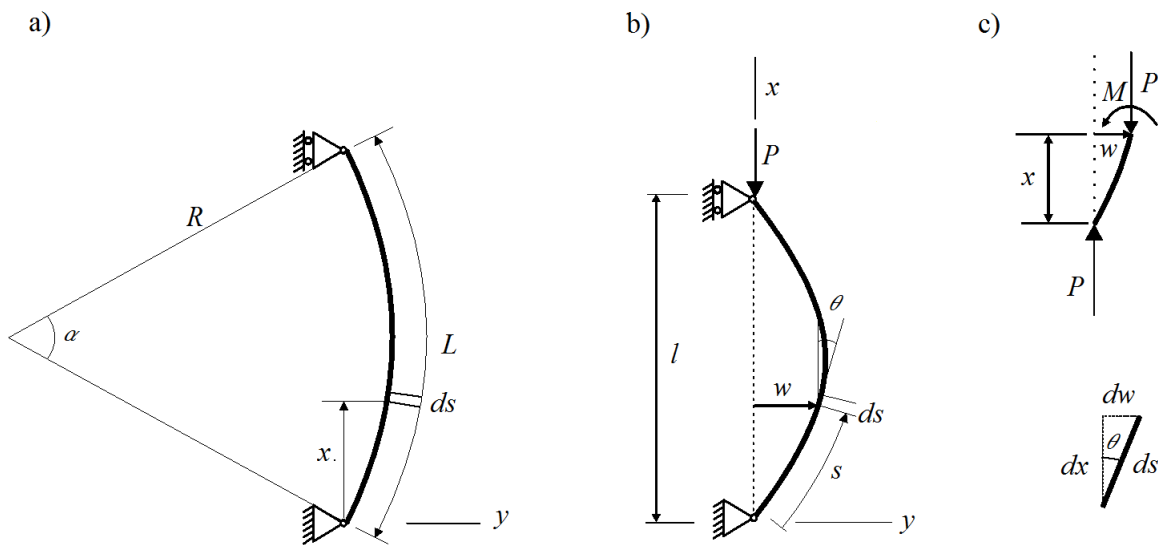


Figure 3-23: Curve beam, a) unloaded, b) loaded, c) free body diagram

The same procedure as the case of a straight beam can be followed to obtain the same equation as equation (3-66) for a curved beam. However, the constant of integration c is different in this case. The curvature at the tips of the beam is no longer zero. Since the beam is simply supported the bending moment is zero at the tips of the beam, so from equation (3-86),

$$\frac{1}{\rho} \Big|_{s=0} = \frac{1}{R} = \frac{\alpha}{L} \quad (3-87)$$

Hence the integration constant c is given by,

$$c^2 = \frac{\alpha^2}{4\pi^2} \left(\frac{P_E}{P} \right) + \sin^2 \frac{\theta_0}{2} \quad (3-88)$$

An equation similar to equation (3-75) can be obtained for the axial displacement of the curved beam,

$$u = 2R \sin \frac{\alpha}{2} - l = 2L \left(\frac{1}{\alpha} \sin \frac{\alpha}{2} - \frac{2}{\pi} \sqrt{\frac{P_E}{P}} \int_0^{\pi/2} \sqrt{1 - c^2 \sin^2 \varphi} d\varphi \right) \quad (3-89)$$

This equation can be solved numerically again here by considering the new integration constant c for different values of α . The force displacement relations of beams with varying curvatures are shown in Figure 3-24. There is no singularity in these curves. The shape of the curves for smaller curvatures implies a higher degree of nonlinearity which could be disadvantageous in dynamic analysis.

To validate the results, the nonlinear force-deflection of the curved beams are obtained by FEM for different curvature angles. The BEAM4 element in ANSYS, which is a three dimensional uniaxial element, is used for the model. Curved beams are modelled with a hundred elements in each case. All displacement and in-plane rotation were set to zero at one end of the beam, whilst at the other end where the load is applied the displacement in the axial direction is allowed and other displacement and in-plane rotation are set to zero. The nonlinear static solver with 100 sub-steps is used to obtain the results. The force-displacement of curved beams alongside the results obtained from ANSYS are shown in Figure 3-25 for some curvature angles. As it can be seen, there is a perfect match between the results obtained by ANSYS and the results of solving the constitutive equations.

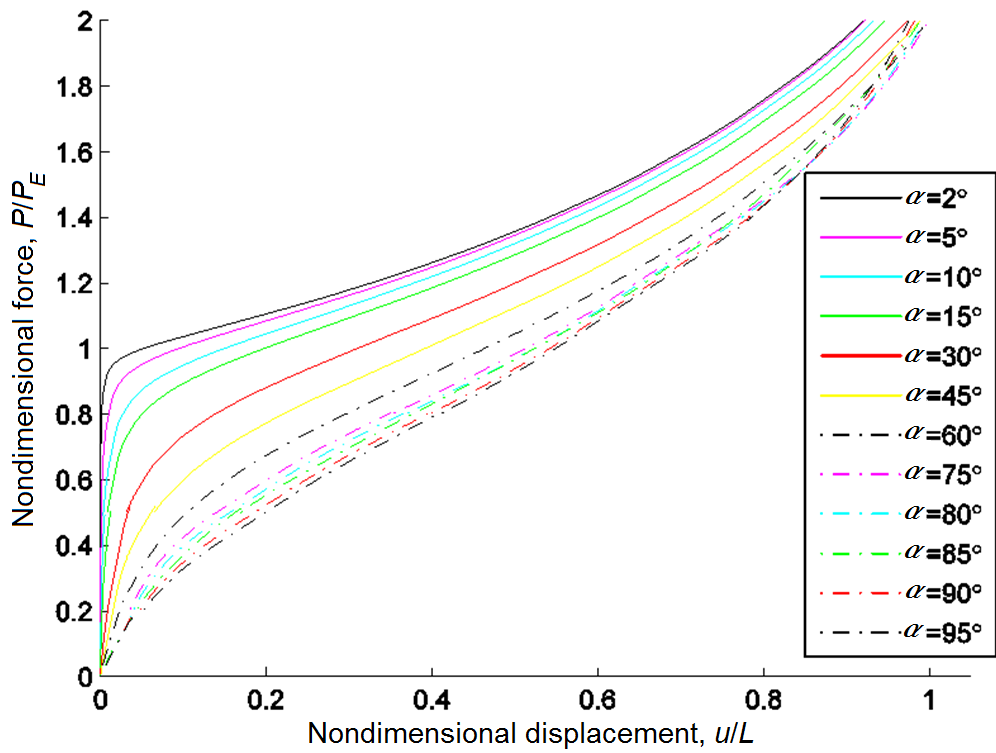


Figure 3-24: Non-dimensional force-displacement of an inextensible curved beam

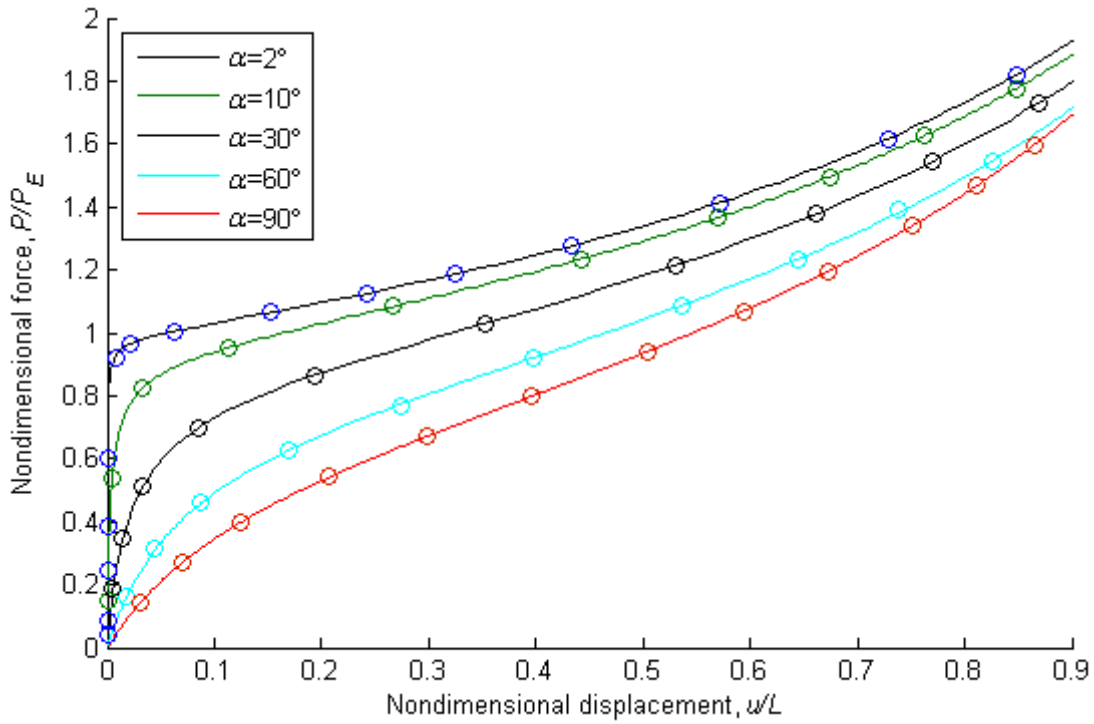


Figure 3-25: Non-dimensional force-displacement of inextensible curved beam, circles: ANSYS results

The stiffness of curved beams with different initial angles as a function of non-dimensional displacement is shown in Figure 3-26. The stiffness of the curved beam is asymmetric. The minimum tangent stiffness shifts to the right by increasing the initial curvature angle and its value increases. The tangent stiffness and static stiffness of the curved beam is examined in the next section to investigate its potential benefit in vibration isolators.

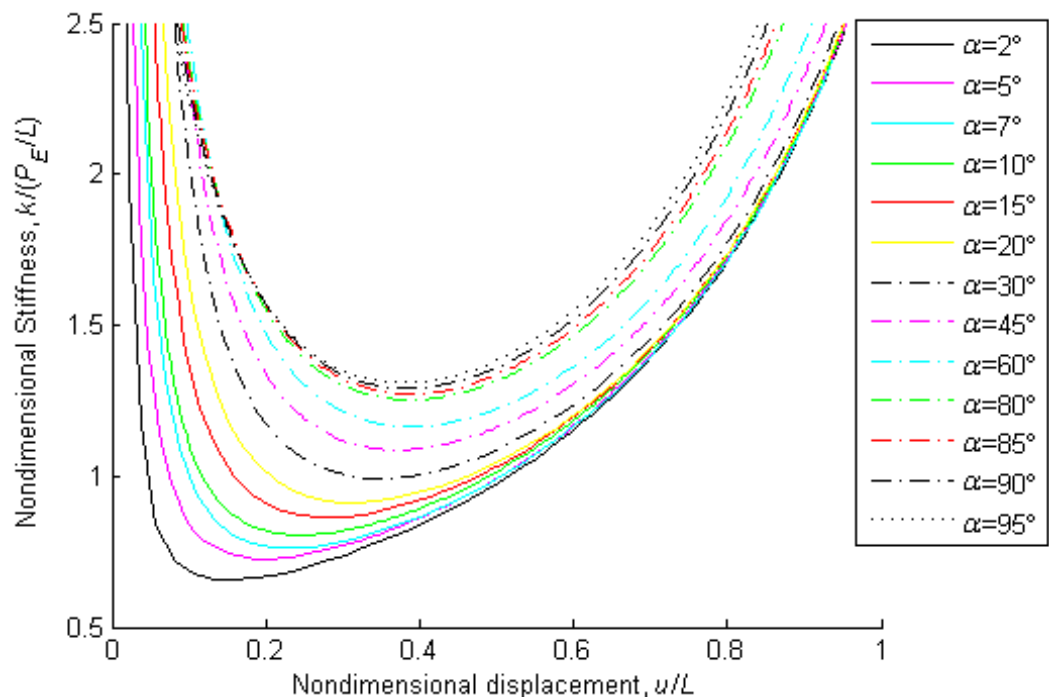


Figure 3-26: Non-dimensional tangent stiffness of inextensible curved beams

3.7 Dynamic and static stiffness of beams

The tangent stiffness of a nonlinear vibration isolator should be low to achieve good isolation while the static stiffness at the statically loaded position should be high to prevent large static deflection. Therefore, the dynamic and static stiffness of the proposed beams are investigated here. The tangent stiffness of a curved beam and a beam loaded eccentrically are obtained numerically as a function of non-dimensional displacement. The minimum tangent stiffness is then extracted and the static stiffness at the same displacement is calculated in each case.

The minimum tangent stiffness and its corresponding static stiffness is shown in Figure 3-27 for a beam with eccentric loading. The minimum tangent stiffness is almost constant for the beam loaded eccentrically. Higher static stiffness makes smaller eccentricity more desirable but strong nonlinearity of a beam with small eccentricity may affect the choice of eccentricity for optimum isolation.

The non-dimensional minimum tangent stiffness and corresponding static stiffness of the curved beam is shown in Figure 3-28. The minimum tangent stiffness increases by increasing the curvature angle while the static stiffness at the corresponding position decreases. This makes the beam with small curvature more desirable but, again, there is a trade-off between the level of nonlinearity in force-displacement (Figure 3-24) and its stiffness characteristics.

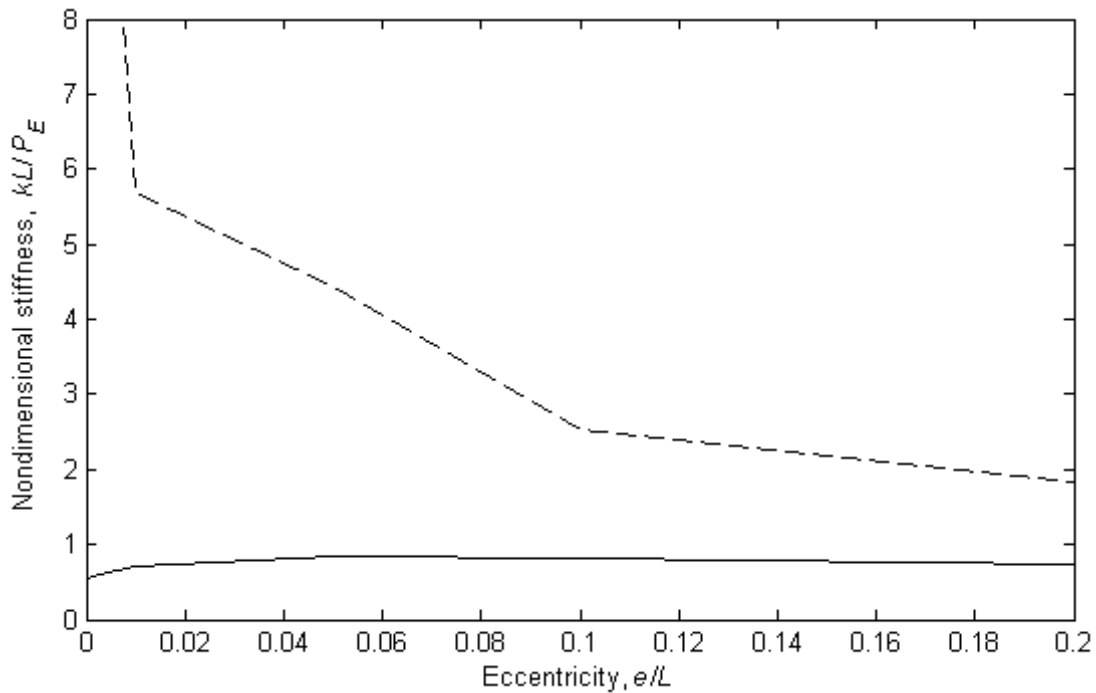


Figure 3-27: Minimum tangent stiffness and its corresponding static stiffness of the straight beam loaded eccentrically (solid line: minimum tangent stiffness, dashed line: corresponding static stiffness)

It should be mentioned that the stiffness calculated here, assuming that the beam is inextensible which is reasonable assumption for metallic beams with a high modulus of elasticity. The non-dimensional minimum tangent stiffness approaches 0.5 when either eccentricity or curvature tends to zero, which corresponds to a straight axially loaded beam. It can be concluded that an

order of magnitude reduction in stiffness when compared to a linear spring is achievable but only for small eccentricity or curvature in which case the stiffness can be highly nonlinear.

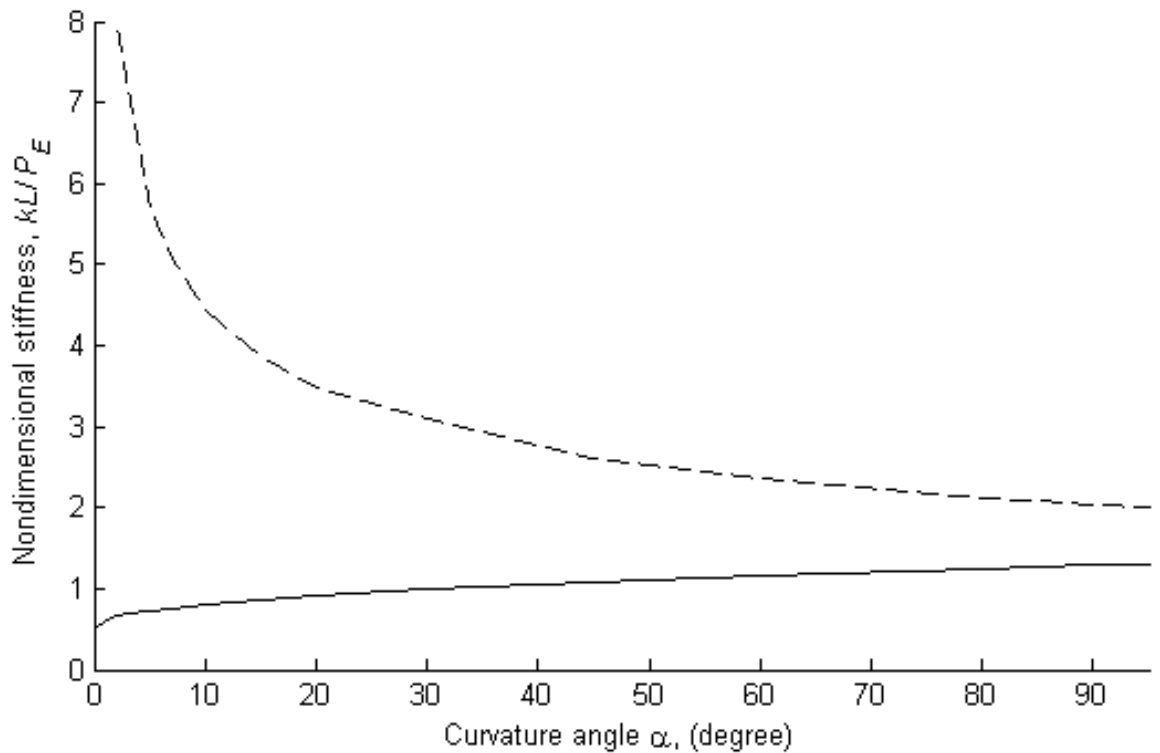


Figure 3-28: Minimum tangent stiffness and corresponding static stiffness for a curved beam as a function of angle of curvature (solid line: minimum tangent stiffness, dashed line: corresponding static stiffness)

3.8 Internal resonances

The spring of a vibration isolator model is usually considered as an ideal element. It does not possess any mass and it has no resonances in itself. In contrast, beams are not ideal elements and comprise of distributed mass and stiffness which means that standing waves can arise in them. To investigate the performance of a beam as an isolator, the transmissibility of the continuous coupled system must be considered. The mobility approach provides a strong tool to inspect the coupled system. However, the equations for mobility and impedance of the curved

beam are complex and beyond the scope of this thesis. An easier approach is to consider the resonance frequencies of the beam with suitable boundary condition as an approximation of the resonances of the coupled system. An example is used to explain the approach. The transmissibility of a rod carrying longitudinal waves is cited and its relation to resonances of the rod is presented. It is desirable for these higher resonances to be as high as possible to achieve a wide frequency range of isolation.

3.8.1 Resonances of rod isolator

Yan et al. [74] studied distributed parameter isolators and categorized them as non-dispersive and dispersive isolators. They investigated longitudinal, torsional and bending waves in a straight beam. Here, the basics of the mobility approach are presented and the impedance of a linear uniform undamped rod due to longitudinal waves is obtained. The peak in transmissibility of the coupled system of the mass and the isolator is then obtained using this method and it is compared with the natural frequencies of the rod. The schematic diagram of a distributed parameter isolator is shown in Figure 3-29 where m is the isolated mass, Z_m is its impedance, Z_i is the impedance of isolator, f_1 and f_2 are internal forces acting on the isolator, f_m is the load acting on isolated mass, u_m is the displacement of mass and u_b is the displacement of base.

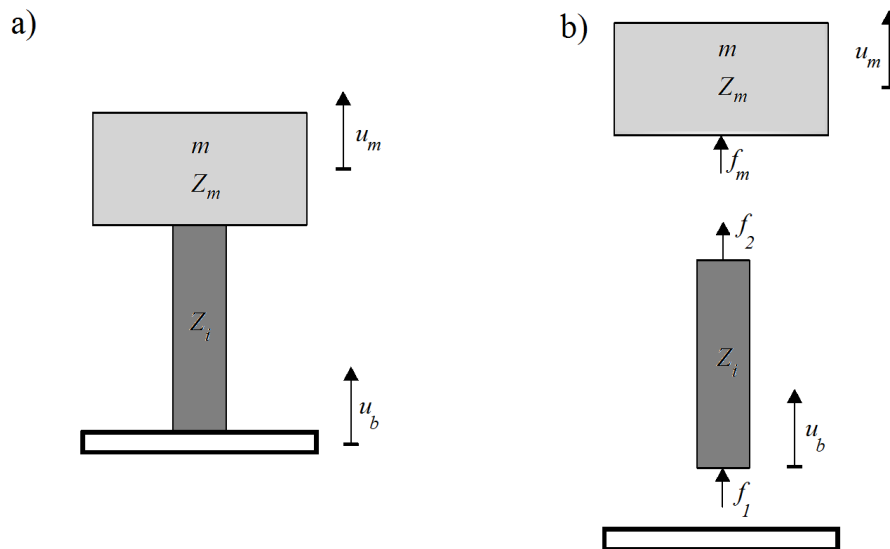


Figure 3-29: a) Schematic diagram of a distributed parameter isolator, b) free body diagram

The relationship between force and velocity can be rewritten as,

$$f_m = Z_m \dot{u}_m \quad (3-90)$$

and,

$$\begin{bmatrix} f_1 \\ f_2 \end{bmatrix} = \mathbf{Z}_i \begin{bmatrix} \dot{u}_b \\ \dot{u}_m \end{bmatrix} \quad (3-91)$$

where dot denotes differentiating with respect to time and \mathbf{Z}_i is the impedance matrix of the isolator,

$$\mathbf{Z}_i = \begin{bmatrix} Z_{11} & Z_{12} \\ Z_{21} & Z_{22} \end{bmatrix} \quad (3-92)$$

The velocity transmissibility can be obtained from the above equations noting that $f_m = -f_2$,

$$T = \frac{\dot{u}_m}{\dot{u}_b} = \frac{-Z_{21}}{Z_{22} + Z_m} \quad (3-93)$$

Z_{22} is the point impedance of the isolator at the connection point to the supported mass. The resonances of the coupled system occur at the frequencies where the denominator of the right hand side of the above equation becomes zero. The impedance of the mass Z_m is $j\omega m$ where m is the mass, and ω is circular frequency. The driving point impedance of a rod can be found from the following equation [75],

$$Z_{11} = Z_{22} = -jA\sqrt{\rho E} \cot\left(\sqrt{\frac{\rho}{E}}L\omega\right) \quad (3-94)$$

where A is the cross-section area of the rod, E is the modulus of elasticity, ρ is density, L is the length of the rod. The impedance can be non-dimensionalised by introducing a frequency ratio as $\Omega = \omega/\omega_e$ where ω_e is the fundamental natural frequency due to the interaction of the isolated mass and the static stiffness of the isolator. It is equal to $\sqrt{k_L/m}$ for the longitudinal isolator where $k_L = EA/L$ is the longitudinal stiffness of the rod. The non-dimensional impedance then will be,

$$\frac{Z_{11}}{\sqrt{k_L m}} = \frac{Z_{22}}{\sqrt{k_L m}} = -j\sqrt{\mu}\cot(\sqrt{\mu}\Omega) \quad (3-95)$$

$$\frac{Z_m}{\sqrt{k_L m}} = -j\Omega \quad (3-96)$$

where μ is the mass ratio and is equal to $\rho AL/m$. The moduli of the non-dimensional impedances of the rod and the mass are plotted in Figure 3-30. The resonances occur at the intersection of the two curves where the impedances are the same in modulus and opposite in phase according to equation (3-93). The first intersection at non-dimensional frequency Ω equal to 1 is the fundamental natural frequency of the mass on the static stiffness of the rod. Since the impedance of the mass is proportional to the frequency, it becomes larger at higher frequencies. Thus, later intersections of the two impedances, and as a result the resonances of the coupled system, are close to the peaks in the impedance curve of the rod.

The resonance frequencies of a rod can be obtained from the following equation [76]

$$f_i = \frac{\lambda_i}{2\pi L} \left(\frac{E}{\rho}\right)^{1/2} \quad (3-97)$$

where $\lambda_i = n\pi, n = 1,2,3, \dots$ for fixed-fixed boundary conditions and $\lambda_i = \frac{(2n-1)}{2}\pi, n = 1,2,3, \dots$ for fixed-free boundary condition. The resonance frequencies of the fixed-fixed and fixed-free rod are shown in Figure 3-30 by dash-dotted line and dotted line respectively. The resonance frequencies of fixed-fixed rod are the same as the peak frequencies of the point impedance Z_{22} and resonance frequencies of fixed-free rod are those frequencies at which Z_{22} is minimum. This analogy between natural frequencies and extrema of point impedances can be explained by referring to the definition of point impedance. The following equation can be obtained by expanding the second row of the matrix equation (3-91),

$$f_2 = Z_{21}\dot{u}_b + Z_{22}\dot{u}_m \quad (3-98)$$

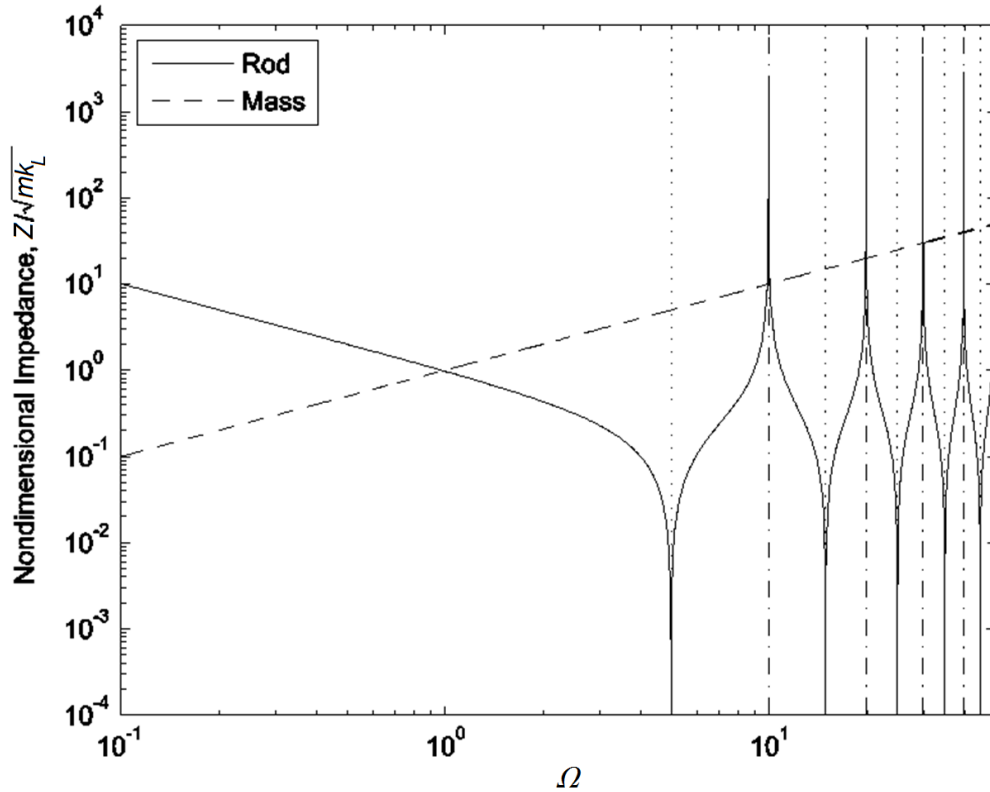


Figure 3-30: Non-dimensional impedances of a rod ($Z_{22}/\sqrt{k_L m}$) and mass ($Z_m/\sqrt{k_L m}$) alongside non-dimensional natural frequencies of the rod for $\mu=0.1$ (dash-dotted line: fixed-fixed boundary condition, dotted line: fixed-free boundary condition)

The impedance Z_{22} can be obtained by fixing point 1 (setting \dot{u}_b to zero) and measuring force and velocity at point two which is equivalent to fixed boundary condition,

$$Z_{22} = \frac{f_2}{\dot{u}_m} \Big|_{\dot{u}_b=0} \quad (3-99)$$

The peaks of the impedance occur where the velocity at point 2, \dot{u}_m , tends to zero while the force has limited value according to the above equation. This resembles a rod with fixed-fixed boundary conditions. The amplitude of vibration of a fixed-fixed rod tends to infinity for a limited force at the resonance frequency.

Although the above description is given for a rod, the impedance relations (3-91) and (3-93) are independent of the isolator type and are valid for any type of isolator. It can be concluded that the peak in the point impedance Z_{22} occurs at the resonance frequencies of a bounded-bounded

isolator. The direct relation between impedance of the mass and the frequency of excitation implies that the resonances of the coupled system will be close to the peaks in impedance Z_{22} or the resonances of the isolator with bounded-bounded boundary condition. A case study has been considered here to investigate the resonance frequencies of a coupled system implementing curved beam as the spring element of the isolator. The impedance equation for a curved beam can be obtained from dynamic stiffness matrix which can be found in references [66, 77], however they are complex and beyond the scope of this thesis. The finite element method is used here instead to obtain the natural frequencies.

3.8.2 Case study, isolating a one kg mass with curved beams

Complexity in the governing differential equation of curved beams results in complicated approximate solution for the natural frequencies and mode shapes of the unloaded curved beam. A dimensional special case is considered hereafter to illustrate the effect of internal resonances. The curved beams are sized to isolated a one kilogram mass and achieve 1Hz fundamental natural frequency by loading them to their minimum tangent stiffness position and considering infinitesimally small dynamic displacements. A schematic diagram of an vibration isolator implementing curved beams is shown in Figure 3-31.

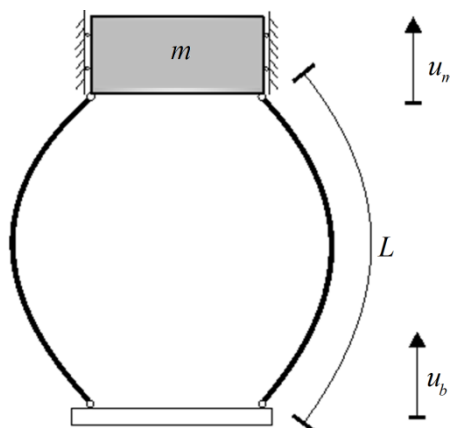


Figure 3-31: Schematic diagram of a vibration isolator with curved beams as springs

The required minimum tangent stiffness can be calculated from the natural frequency equation of a SDOF; a minimum tangent stiffness of 19.7 N/m for each curved beam is required to

achieve 1Hz natural frequency in this case. The ratio between minimum tangent stiffness and its corresponding static stiffness is unique for different curvature angles and this is obtained numerically. The static stiffness can be obtained from this ratio and the required minimum tangent stiffness. Having the static stiffness and considering 1kg as the static load, the static deflection can be calculated. The non-dimensional displacement for the optimally loaded beam is obtained by numerical solution and it is non-dimensionalised by the length of the beam. The static deflection and its non-dimensional equivalent are used to calculate the length of the beam for each curvature.

The Euler buckling load is used to non-dimensionalise the loads in obtaining the equation for curved beams. From the calculated data the Euler buckling load can be calculated as well. Knowing the value of the Euler buckling load the dimension of the cross section can be obtained. The calculated dimensions are shown in Table 3-1 for different values of initial curvature where α is the initial curvature angle, δ is deflection due to the weight of the isolated mass, k_s is static stiffness as the ratio between the static load and δ , L is the length of the isolator, P_E is the buckling load, I is the second moment of area, w is the width of the curve beam, t is the thickness of the curve beam, and μ is the mass ratio between the mass of both curved beams and the isolated mass, 1kg.

Table 3-1: Dimensions of curved beam for different curvature angle

α (degree)	k_s (kN/mm)	δ (mm)	L (mm)	P_E (N)	I (mm ⁴)	w (mm)	t (mm)	μ
2	240	24	154	4.6	.053	24	.3	.017
10	108	45	188	4.6	.079	35	.3	.031
30	60	81	244	4.8	0.139	62	.3	.071
60	40	122	321	5.4	0.271	120	.3	.18
75	34	141	363	5.8	0.37	164	.3	.28
90	31	157	411	6.2	0.511	227	.3	.44

If two curved beams in the schematic diagram of the nonlinear isolator were replaced with two linear springs the static deflection to achieve 1 Hz fundamental frequency would be 248 mm. As expected, the static deflection is smaller than a linear spring for all the cases. A smaller curved beam can be achieved with smaller initial angle.

The natural frequencies obtained from analytical formulas for an unloaded curved beam are presented in Figure 3-32. The formulas for natural frequencies of a curved beam are presented in Table 9-2, page 209 of reference [76]. Among the formulas presented there, the lowest natural frequency belongs to the in-plane flexure. This formula is for a simply supported beam while one of the supports is not fixed in the axial direction. Therefore, the results from Belevins' book are different from the ANSYS results where both ends were bounded in the axial direction.

The natural frequency of the in-plane flexure mode can be obtained from the following equation for mode shapes that are antisymmetric in the radial direction and symmetric in the tangential direction about the mid-span,

$$f_i = \frac{i^2 \pi^2}{2\pi(R\alpha)^2} \left(\frac{\left(1 - \left(\frac{\alpha}{i\pi}\right)^2\right)^2}{1 + 3\left(\frac{\alpha}{i\pi}\right)^2} \right)^{\frac{1}{2}} \sqrt{\frac{EI}{\rho A}} \quad (3-100)$$

where $i=2,4,6,\dots$. The natural frequencies for i equal to 2 for in-plane flexure mode that is antisymmetric in radial direction and symmetric in tangential direction about mid-span is shown in Figure 3-32 (marked by plus).

Additionally, ANSYS is used to find the lowest natural frequency of the unloaded and loaded curved beam. The optimized values obtained by the procedure described above are used to model the curve beam for each curvature angle. The natural frequencies of the first mode for the unloaded curved beam (marked with stars) are shown in Figure 3-32. The BEAM4 element which is a three dimensional uniaxial element with compression, tension, bending and torsion capabilities is used to make the model. It is also capable of stress stiffening and large deflection. Stress stiffening is the stiffening or weakening of a structure due to its stress state [78]. Curved beams are modelled with a hundred elements in each case. All displacement and in-plane

rotation were set to zero at both ends of the beam. The modal solver of ANSYS is used to obtain the natural frequencies.

To obtain the natural frequency of the statically loaded beams using ANSYS, the static large deformation of the beam is first solved while the option is chosen in the software to obtain the stress stiffening matrix. This matrix is the linearised stiffness matrix about the statically loaded position. Then, two methods are used to obtain the natural frequencies for the statically loaded curved beam using the ANSYS modal solver. As discussed in section 3.8.1, the natural frequencies of a curved beam with bounded boundary conditions should be the same as the natural frequency of internal modes of the curved beam isolator when the isolated mass is considered in the finite element model. First, the natural frequencies of the statically loaded beam are obtained while all displacement and in-plane rotations are set to zero at both ends and are shown with dots in Figure 3-32. Secondly, the natural frequencies of the statically loaded curved beams when a mass element is added to one of its end and the axial displacement at that end was relaxed are obtained. The first mode of vibration was very close to 1 Hz, the frequency to which it is sized to produce. The second mode should be close to the bounded curved beam natural frequency when loaded statically which was marked by circles in Figure 3-32. It can be seen that the two results match very well, which confirms the conclusions of section 3.8.1.

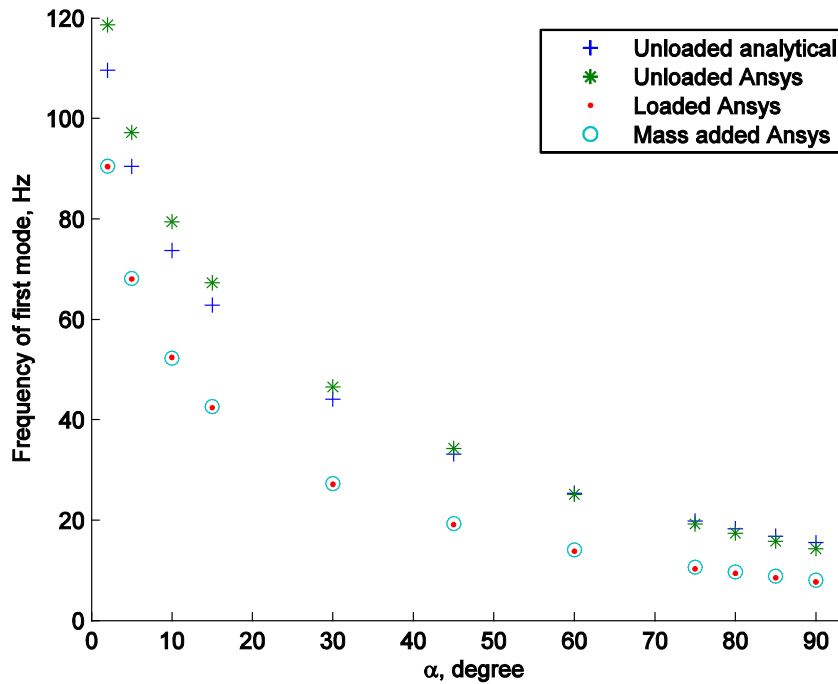


Figure 3-32: Lowest natural frequency of curve beam sized to achieve 1 Hz fundamental frequency, +: in-plane flexure mode of analytical solution [76], *: finite element model of unloaded curve beam bounded both ends, dots: finite element model of statically loaded curve beam bounded both ends, o: finite element model of curve beam supporting mass at one end simply supported

The first four mode shapes of a beam with an initial curvature angle equal to 5 degrees are shown in Figure 3-33. As it can be seen in this figure, the tip where the mass is added (shown by a star at the top) is displaced only in the first mode of vibration and in three other mode shapes the mass is fixed. This is to be expected because of the high impedance of the mass at high frequencies.

The smaller angles are better both considering the size of the curve beams and the internal resonances. However, the effect of nonlinearity must be considered in implementing the curved beam as elements of nonlinear isolators. There is strong nonlinearity for small angles of curvature.

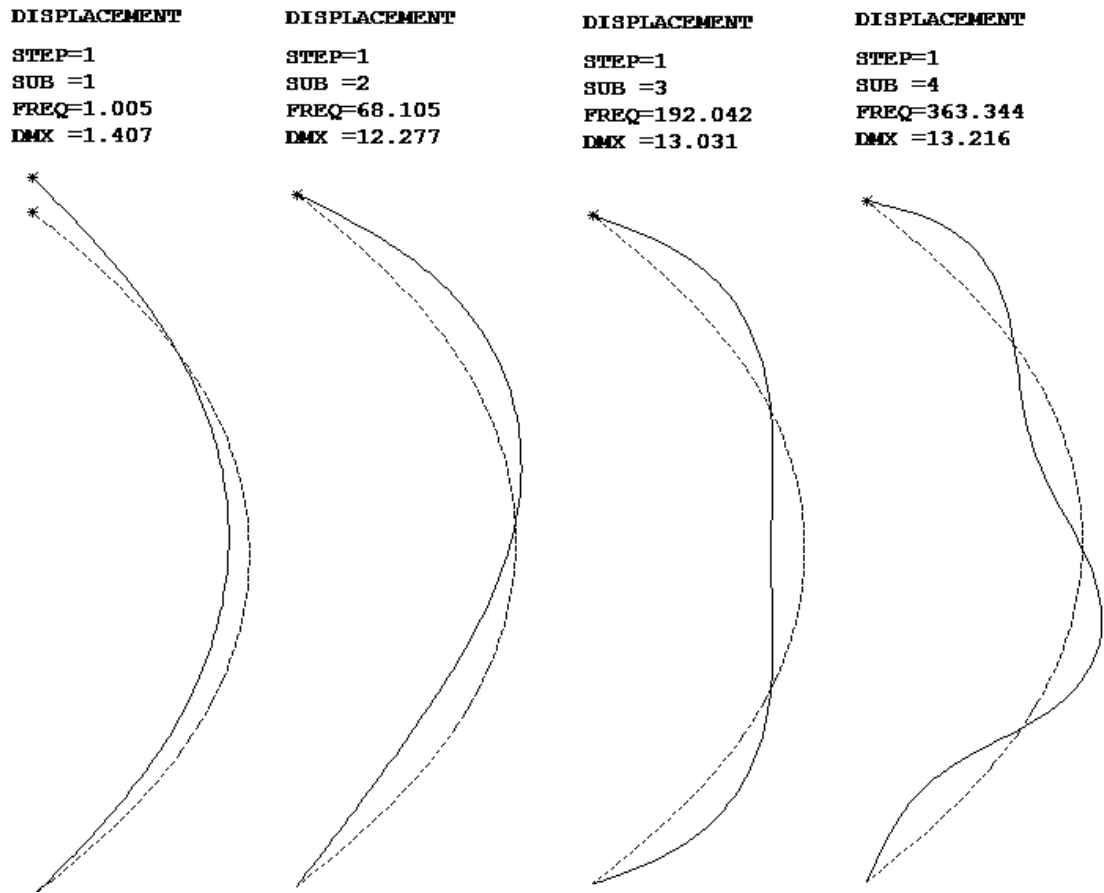


Figure 3-33: Mode shape of curved beam with initial angle equal to 5 degree

These results of the modal analysis that was solved by ANSYS to find the natural frequencies of the coupled system can be used to calculate the harmonic response of the curved beam isolator to forced vibration with infinitesimally small amplitude. The mode superposition method is used by ANSYS to find the force transmissibility of a curved beam with initial curvature angle equal to 5 degrees as shown in Figure 3-34. The damping ratio is considered equal to 0.5%. The first peak is the fundamental mode of vibration which is 1 Hz by design. There is wide frequency range where isolation occurs before the first internal resonance. The amplitude of the internal resonance can be controlled by the damping which is limited to -18dB here. The decay rate is 40 dB per decade after the first peak and before the second one which complies with the theory. It should be mentioned here that this graph is produced with the assumption of small vibration and linearization about the statically loaded position.

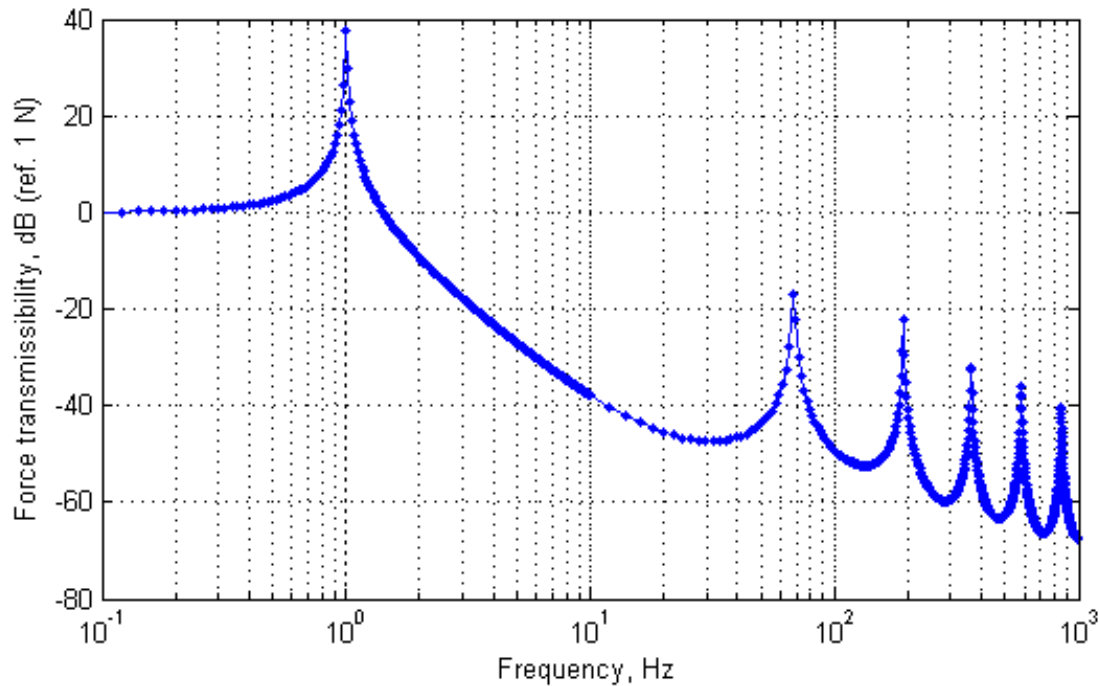


Figure 3-34: Force transmissibility of curved beam isolator of initial curvature angle α equal to 5 degree and damping ratio equal to 0.5% obtained by finite element method

3.9 Conclusions

The nonlinear stiffness properties of beams are investigated in this chapter. It is shown that a simply supported beam loaded in the middle can be modelled by approximate model with hardening nonlinearity. Galerkin's method is used to obtain the approximate model and the analytical exact solution and the FEM have been used to validate the results. It is shown that the sine function is a suitable shape function in Galerkin's method for this purpose.

Buckled beams are then considered in the context of nonlinear vibration isolators with low tangent stiffness. It is shown that the post-buckled straight beam possesses hardening stiffness characteristics. The drop in tangent stiffness at the buckling point makes axially loaded beams a suitable choice for forming a nonlinear vibration isolator with low tangent stiffness and high static stiffness characteristics. However, buckling causes a singularity in force-deflection curve. The static load should be increased to avoid the buckling from occurring in the range of

dynamic displacements which results in a higher tangent stiffness. The other approaches to avoiding singularity are to introduce eccentricity to the loading or initial curvature to the beam.

It is shown that both loading eccentrically and introducing initial curvature have a smoothing effect on force-displacement curve. This is because of developing a bending moment with low axial forces which results in transverse displacement of the beam. So there is not a specific load for which the beam suddenly deflects to the sides and causes a discontinuity in tangent stiffness. The minimum tangent stiffness and corresponding static stiffness are obtained for each case and it is shown that an order of magnitude reduction in stiffness is possible for small initial curvature of the beam. This static analysis implies a reduced natural frequency and hence improved isolation. However, a buckled beam spring has distributed mass and therefore internal resonances which must be investigated.

A case study is considered to obtain a practical estimate of the performance of curved beams as nonlinear springs for isolators. A 1 kg mass is isolated with two curved beams and the beams are sized to achieve their lowest tangent stiffness when loaded statically. The second mode of a mass-curved beam coupled system was at about 70 Hz for an initial curvature angle of 5 degrees. The ANSYS software is used to obtain the natural frequencies. It is also used to obtain force transmissibility of the curved beam isolator. It can be concluded that a lower initial curvature is better in both achieving a lower dynamic to static stiffness ratio as well as moving the second peak in transmissibility to higher frequencies. The transmissibility and natural frequencies are obtained with the assumption of linearization of the system about the statically loaded position. The nonlinearity effect must also be considered especially for small initial curvatures which introduce more nonlinearity in the force-deflection relation that can affect the transmissibility of large amplitudes of vibration. This issue is addressed in chapter 6.

4 Bubble mounts

4.1 Introduction

Vibration isolation mounts are available commercially in different shapes, sizes and from different materials. Rubber is the most common material used to construct vibration isolator mounts. Its stiffness and damping characteristics alongside its ability to be formed and manufactured easily have made it a popular choice. Rubber is a viscoelastic material and its stiffness and damping depend on the loading frequency, amplitude, static preload and temperature [79].

Some of the commercially available mounts are intended to have nonlinear stiffness and/or damping properties. A desirable characteristic for a nonlinear vibration isolator is low tangent stiffness at the statically loaded position. The “Bubble mount” is a commercially available mount, which appears to have a low tangent stiffness at the working position from the sales brochure. It is a bell shape rubber vibration isolation mount, see photograph shown in Figure 4-1. It is expected that the nonlinearity in its stiffness characteristics is due to its geometry primarily, with material nonlinearity making a contribution of secondary order.



Figure 4-1: Bubble mount

The bubble mount has an axisymmetric curved shape that, geometrically speaking, may be considered as a curved beam that is rotated about its vertical axis. In this chapter, the force-deflection of the bubble mount is measured and it is attempted to model its force-deflection with that of a curved beam which is obtained in the previous chapter. This is intended to establish whether the mechanism responsible for low tangent stiffness is similar to that of a curved beam.

One might expect that, ideally, a nonlinear isolator should be loaded to its minimum tangent stiffness position statically to exploit it fully as a nonlinear vibration isolation mount. Any deviation from the optimum loaded position results in a higher level of tangent stiffness, which undermines the advantage of using a nonlinear mount. The sample-to-sample variability in the stiffness of bubble mounts can cause the static equilibrium position to deviate from its optimally loaded position. The force-deflection characteristics for a set of ten bubble mounts is measured here to evaluate this variability.

The aim of this chapter is to evaluate if the bubble mount can be modelled with a curved beam and to investigate the variability in their characteristics. Measurements of the force-deflection characteristics of the bubble mount are presented in section 4.2. It is attempted to model the bubble mount with curved beams in section 4.3. The dimensions of curved beams are optimised to obtain the best possible fit to the measured force-deflection of the bubble mounts. The force-deflection and stiffness of the set of ten bubble mounts are considered in section 4.4. The tangent stiffness and static deflection of the set loaded statically by a nominal mass are also compared. A set of conclusions is presented in section 4.5.

4.2 Force-deflection characteristics

The natural frequency of a mass supported by a nonlinear isolation mount can be estimated from the tangent stiffness of the isolation mount for a small amplitude of vibration. The dynamic and static stiffness of an isolation mount can be obtained from its force-displacement curve. The force-displacement curves of different sizes of bubble mounts are shown in Figure 4-2, which is reproduced from the manufacturer's catalogue. The graph suggests that a smaller bubble mount, with a lower load bearing capability, possesses the widest low tangent stiffness range. Thus,

type 50640 is the most suitable candidate for this study and all measurements presented hereafter belong to this type of isolator.

It is easier to apply a displacement to the bubble mount and measure the generated blocked force in order to obtain its force-displacement curves, rather than to apply a force and measure its displacement. The former can be done to high precision using an Instron testing machine. The measurements were done in quasi-static mode with a displacement rate of 0.2 mm/s and at a room temperature that was almost constant for all tests. The set-up for the test rig is shown in Figure 4-3. In the first instance, the rod was connected directly to the bubble mount (Figure 4-3(a)) and the bubble mount could become concave on top when loaded to large displacements (Figure 4-3 (b)). In practice, it may be connected to an item of equipment such that the top would not become concave. To model such a situation, a disk was added to the set-up to resemble the practical condition as shown in Figure 4-3 (c and d).

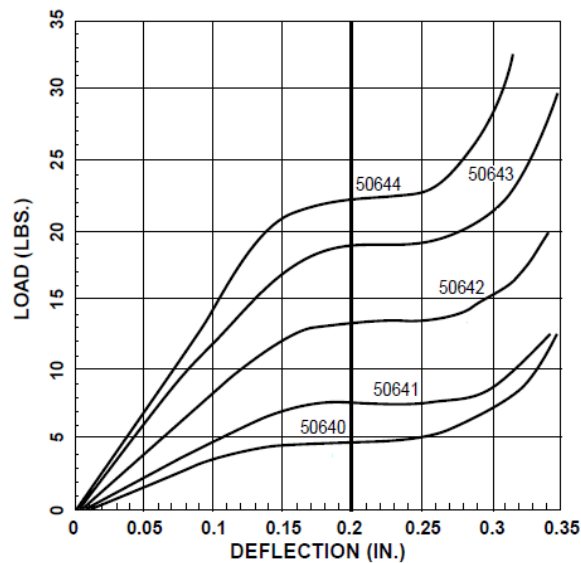


Figure 4-2: Force-deflection of different sizes of bubble mount (Tech Products Corporation)

The measured load-deflection curves for a bubble mount without and with the disk are shown in Figure 4-4. The results are shown for a single loading cycle. The upper lines belong to loading and the lower ones demonstrate unloading in both graphs. The effect of contact between the rubber and the ring can be seen in Figure 4-4 (b), where the load increases more rapidly with the increase in deflection compared to the same curve without the ring. The difference between the two cases is significant for deflection greater than about 9 mm.

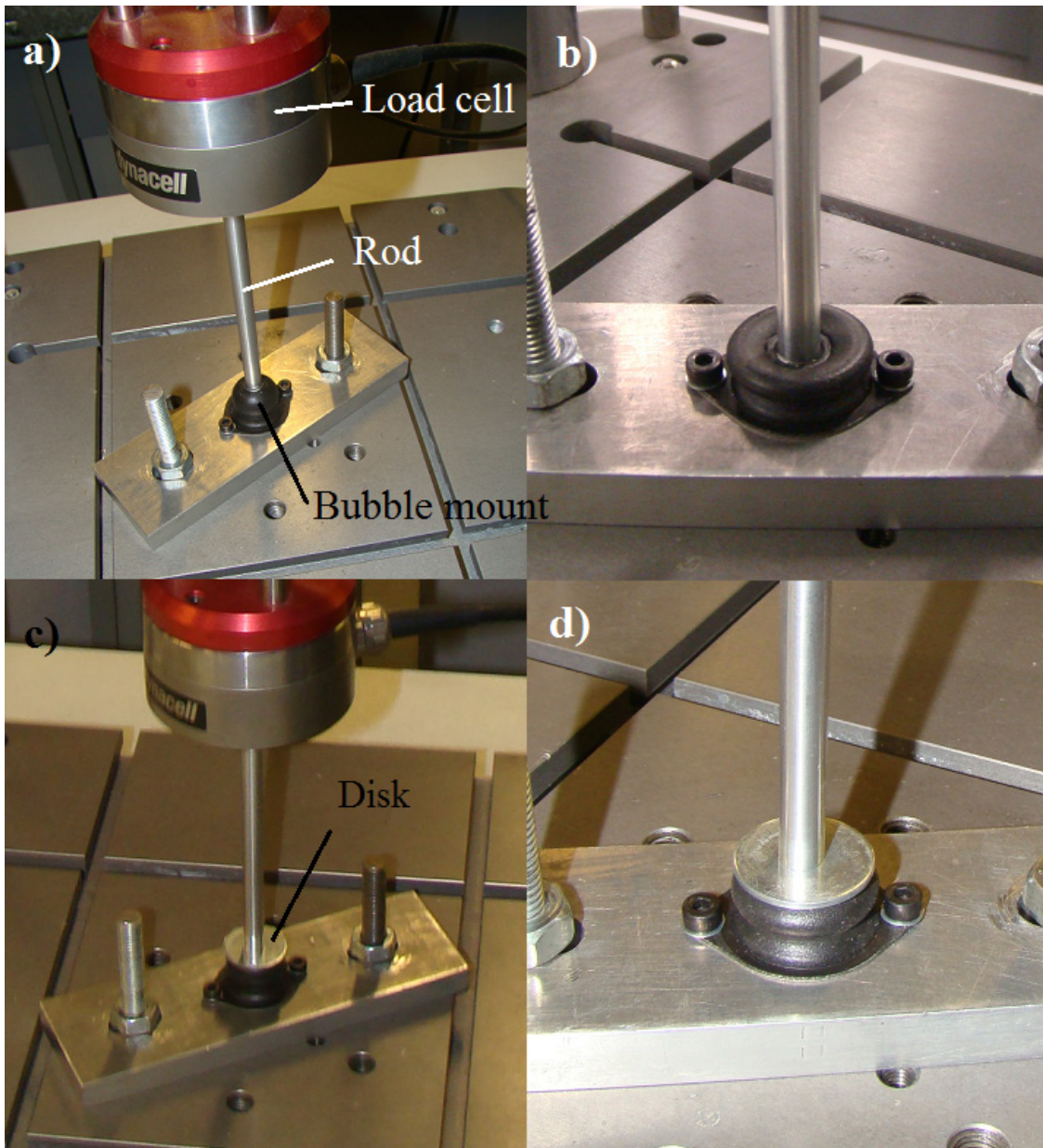


Figure 4-3: Bubble mount test rig, a) connecting the load cell directly to the bubble mount by a rod, b) loaded bubble mount, c) a disk installed to resemble contact with the isolated mass, d) loaded bubble mount with a disk on the top

The focus of this study is on the stiffness rather than damping properties of the nonlinear isolators, so the average of the loading and unloading curves is considered hereafter. The average force-displacement curves are shown in Figure 4-5 for the bubble mount tested with and without the disk. The average force-deflection curve is not as flat as suggested in the catalogue and thus a higher tangent stiffness is expected.

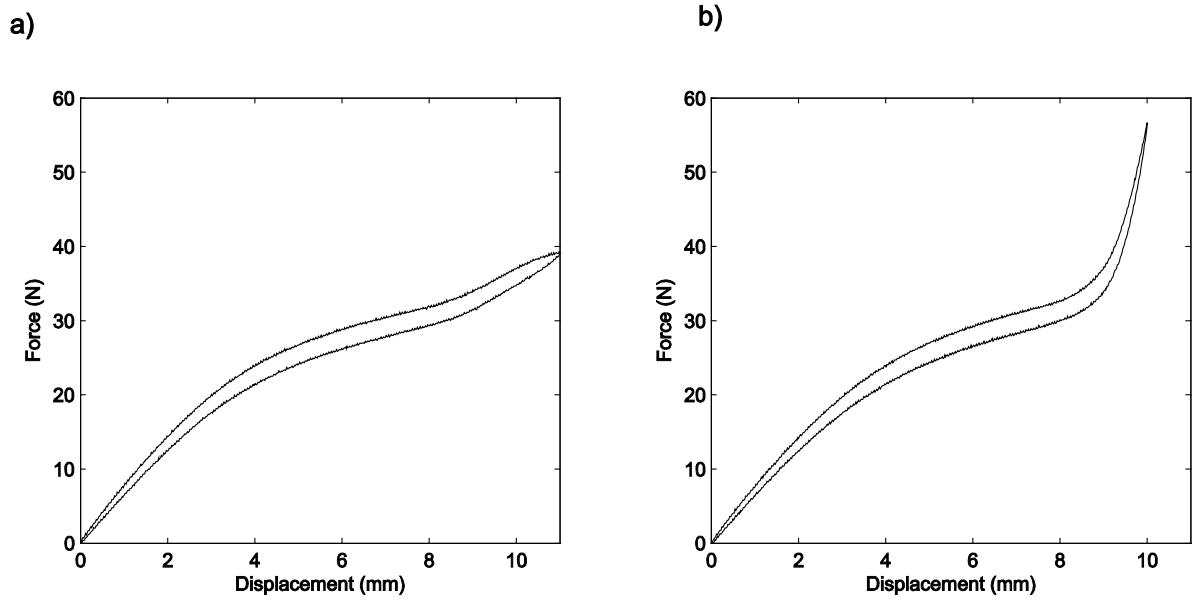


Figure 4-4: Force-deflection of bubble mount loaded quasi-statically , a) displacement applied directly through rod, b) disk added between rod and bubble mount

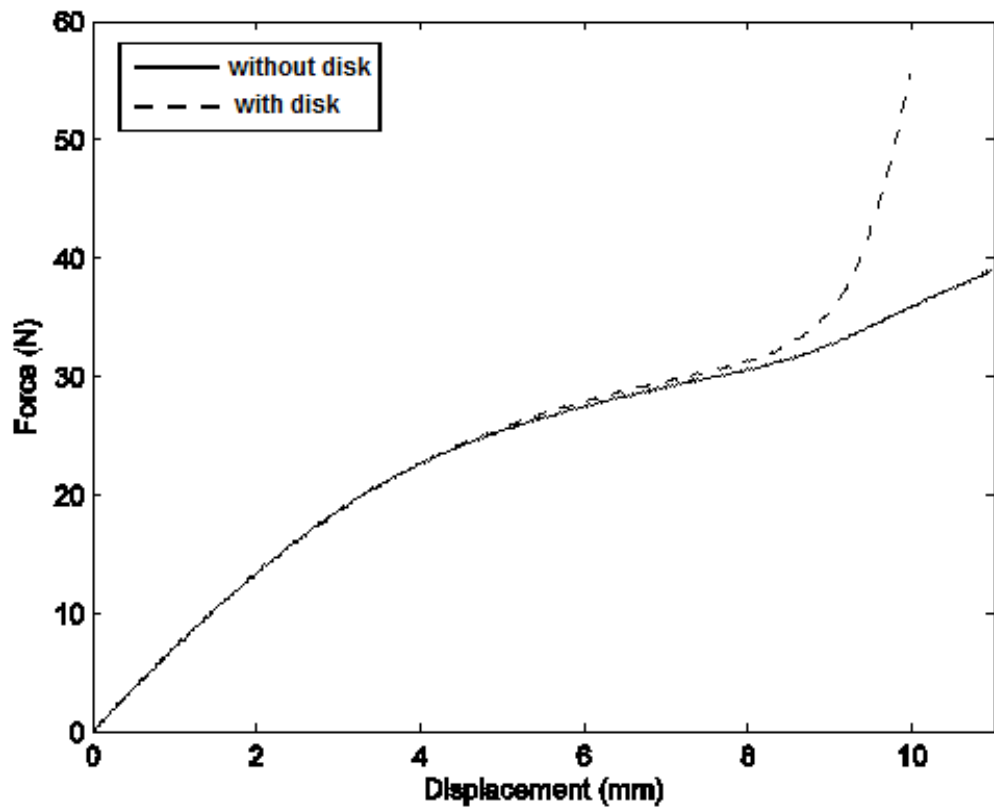


Figure 4-5: Average force-displacement graph obtained by averaging the loading and unloading curves

4.3 Modelling the bubble mount with curved beams

The cross section of a bubble mount is shown in Figure 4-6. The bubble mount takes the appearance of a curved beam which is rotated around a vertical axis. Hence, it seems appropriate to model the bubble mount as a curved beam. A constant thickness and initial radius of curvature are assumed here. Different angles of curvature and dimensions for the curved beams are considered to obtain the dimensions that provide a similar force-deflection curve to that of the bubble mount. These parameters are adjusted by minimizing the square of the difference between the two sets of data i.e. the measured force-deflection of the bubble mount and the force-deflection of the curved beam model.

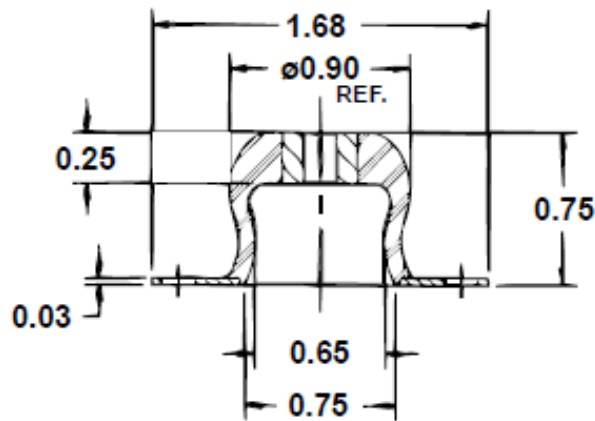


Figure 4-6: Cross section of bubble mount (Tech Products Corporation)

The force-deflection characteristics of a curved beam are presented in non-dimensional form in chapter 3. There, the buckling load of a straight beam with the same length and cross section as the curved beam was used to normalize the force and the length of the curved beam was used to non-dimensionalise deflection. Initial estimates for the dimensions of the equivalent curved beam are obtained by setting the inflection point in the curved beam model to that in the measured force-deflection. Notional values for the buckling load of the equivalent straight beam and length of the curved beam are obtained by this method. These calculated values are shown in Table 4-1 for the buckling load of the equivalent straight beam and the length of the curved beam for different curvature angles.

Table 4-1: Initial values of length of curved beam and buckling load for different curvature angles

α (Degree)	10	20	30	45	60	75	80	90	95
Euler Buckling Load of the equivalent straight beam (N)	26.2	26.3	27.3	28.9	30.6	32.4	33.8	35.6	36.6
Length (mm)	29.2	22.3	20.8	19.2	18.4	17.8	18.4	18.7	18.8

The Mean Square Error (MSE) between the measured data and the force-deflection of the dimensional curved beam model is shown in Figure 4-7 as a function of length and curvature angle. The MSE is shown on the logarithmic axis. The notional buckling load is chosen from Table 4-1 for different initial angles. The MSE is obtained by varying the length from 50 per cent to 150 per cent of notional length listed in Table 4-1. It is smaller for larger initial curvature angle and there is a minimum over length at about the notional length.

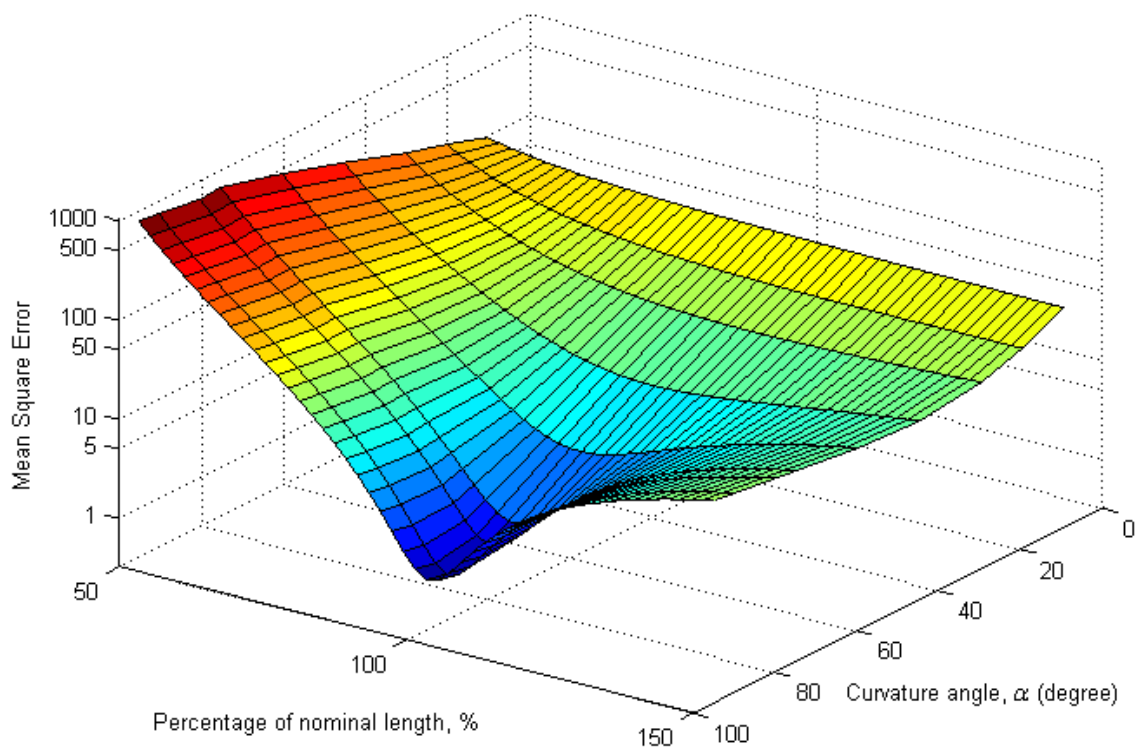


Figure 4-7: Mean square error as a function of length and initial curvature angle for fixed buckling load

Alternatively, the minimum mean square error can be found by varying the buckling load, which is shown in Figure 4-8, for the notional lengths chosen from Table 4-1 according to initial curvature angle. The MSE is shown on the logarithmic axis. The higher initial curvature angles agree more closely with the bubble mount and there is also a minimum over buckling load at about the notional buckling load.

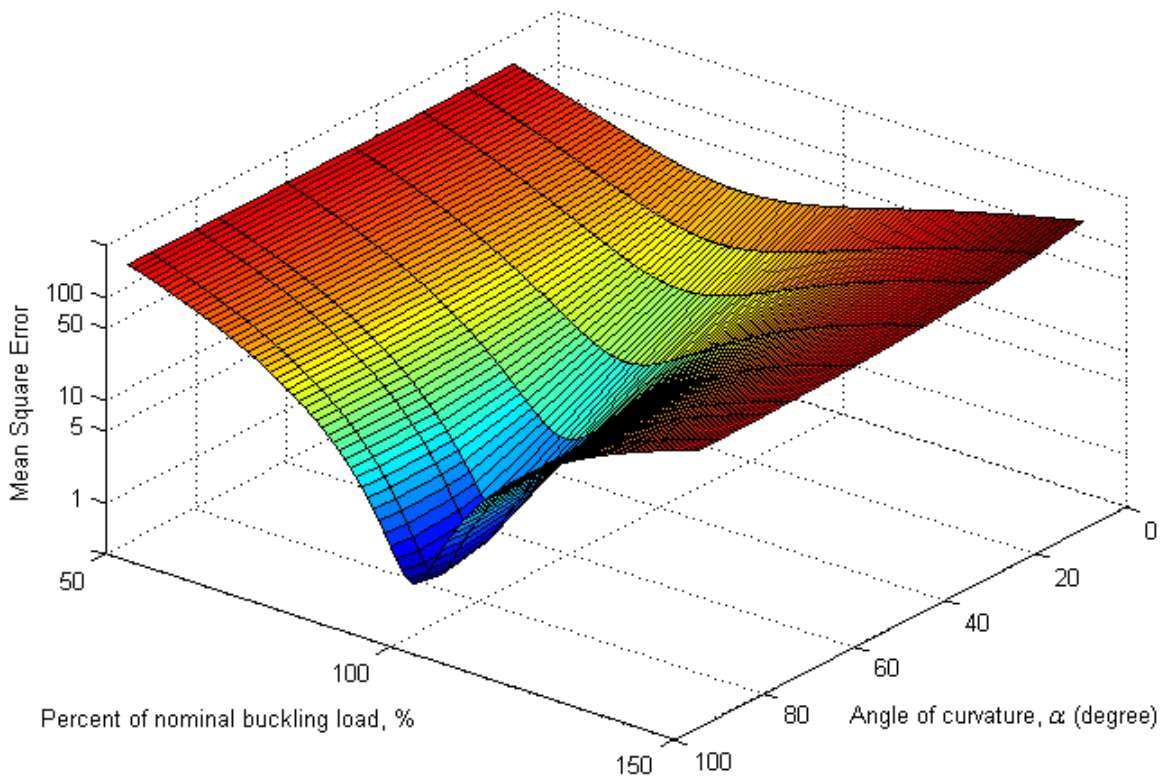


Figure 4-8: Mean square error as a function of curvature angle and buckling load for fixed length

Whilst Figure 4-7 and Figure 4-8 are useful for visualisation purposes, the mean square error can of course be optimized for both of the length of the curved beam and the buckling load simultaneously; the length of the beam is varied and in each step the optimization is run for different values of buckling load. The force-deflection curve for the curved beam with optimized buckling load and length is shown in Figure 4-9 alongside the measured force-deflection curve of the bubble mount. It can be seen that the result of the curved beam model is not a good match for the bubble mount, especially at large displacements.

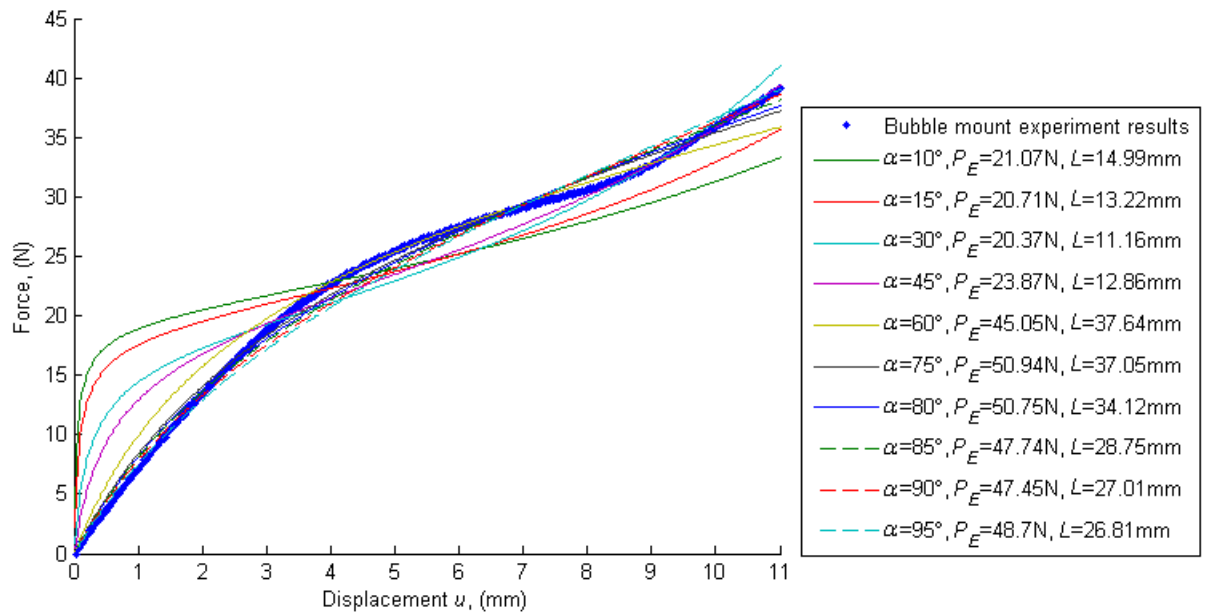


Figure 4-9: Force-displacement of the bubble mount and optimized curved beams

Only the measured data up to the inflection point is considered in a second attempt to fit the curved beam model to the measured data for modest displacement. The physical dimensions of the bubble mount are also considered in obtaining an equivalent length for the curved beam. A range of lengths that seems to be realistic for the bubble mount is chosen and the MSE is minimized on these lengths and the buckling load. The force deflection obtained using this approach is shown in Figure 4-10. The second approach has not resulted in an appropriate match between the two sets of data either.

The mismatch between the bubble mount and the curved beam model can be due to various reasons. The force-deflection of the curved beam is obtained by assuming that it behaves as a slender beam, which is not necessarily valid for the bubble mount. In addition to this, the curvature of the bubble mount is not constant along its length. The bubble mount is also axisymmetric and the circumferential stress could affect its characteristics. Material properties are another potential source of disagreement between the bubble mount and the curved beam. There is also a thick part on the top which can affect the large deflection characteristics of the bubble mount. The bubble mount internal walls also become in contact at large deformations.

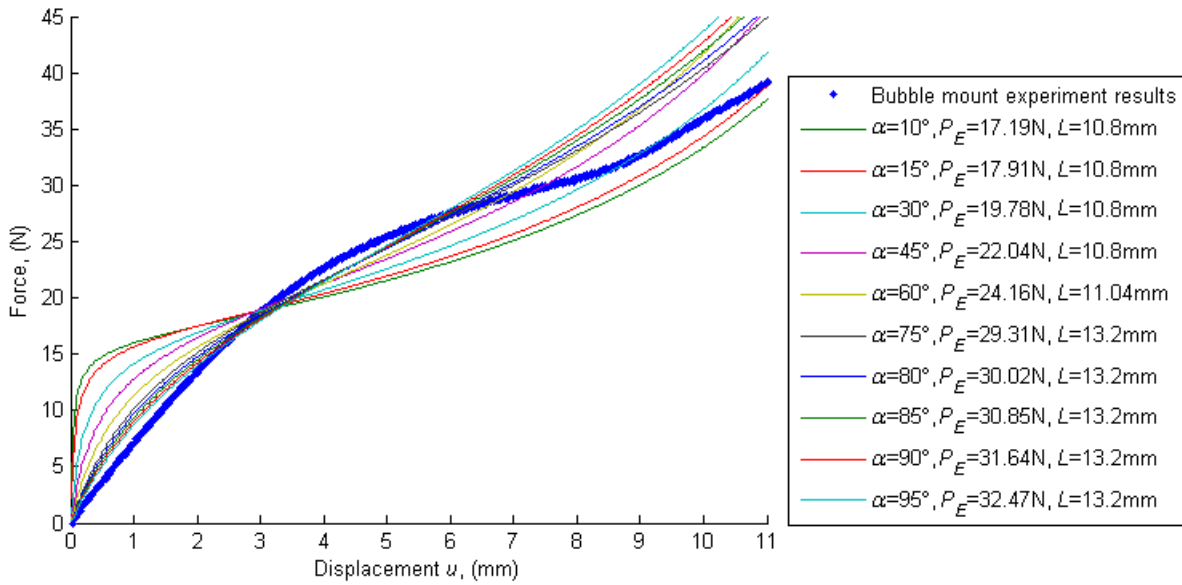


Figure 4-10: Force-displacement of bubble mount and optimized curved beams. (Data up to the minimum tangent stiffness point is considered and length is chosen to match physical dimension of bubble mount)

4.4 Variability in the properties of bubble mounts

The performance of a nonlinear mount as a vibration isolator depends on the tangent stiffness of the statically loaded mount. Any deviation from the minimum tangent stiffness position, due to manufacturing variability for example, results in a higher natural frequency of a mass supported by the nonlinear mount. In addition to this, different tangent stiffness values can result in coupled rigid body modes in practice where a piece of equipment is supported by a number of mounts.

The force-deflection curves of ten different bubble mounts were measured and their characteristics are compared. The bubble mounts used here were bought from the same manufacturer and received in the same package. The measurements were conducted by the same method as described in section 4.2.

The force-deflection curves were obtained for five cycles of loading and unloading up to a displacement of 11 mm with a speed of 0.2 mm/s. Only the last cycle is used for analysis and

this is shown in Figure 4-11. The unloaded position is considered as the origin of the measurements. The first notable difference in the characteristics of bubble mounts is the maximum force at a displacement of 11 mm. It seems that the static stiffness at the maximum deflection differs between bubble mounts and the maximum load varies from 39 N to 47 N. However, there are similarities in the shapes of force-deflection curves for the ten mounts.

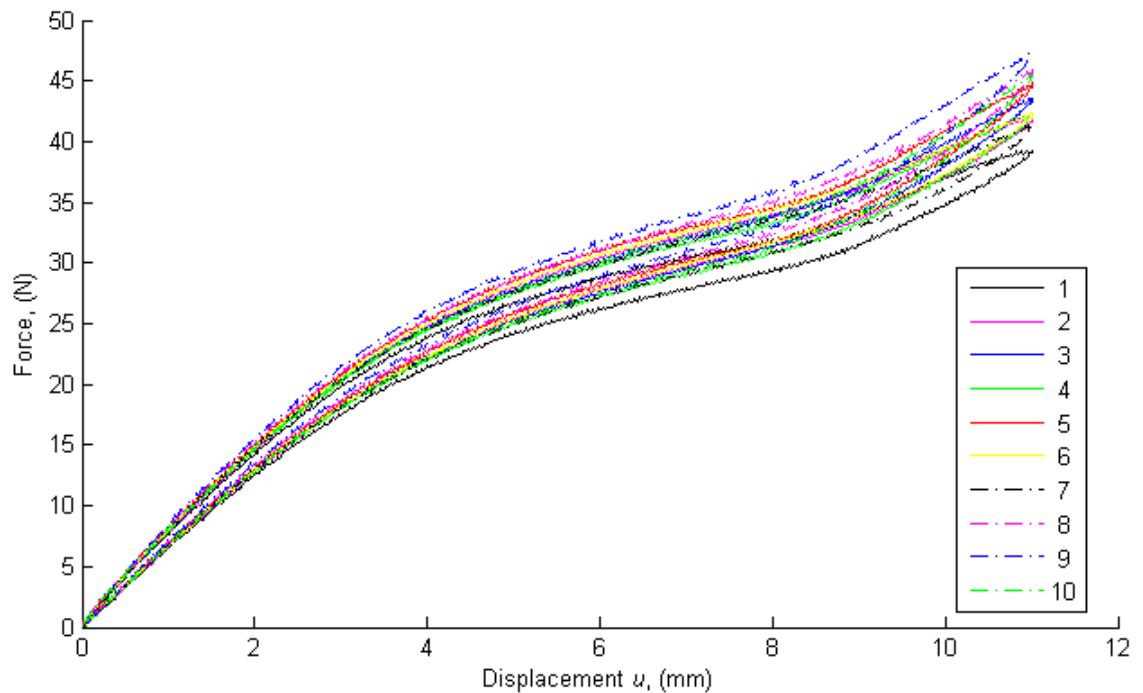


Figure 4-11: Force-displacement of ten nominally identical bubble mounts, last cycle of loading is considered

To quantify the similarity between the shapes of the force-deflection curves, the correlation matrix between different bubble mounts has been obtained and this is shown in Table 4-2. The element in the i^{th} row and j^{th} column corresponds to the correlation between the i^{th} and j^{th} mounts, where the order is the same as in the legend in the Figure 4-11. Column 11 and row 11 correspond to a linear spring which is introduced here as a benchmark. The correlation coefficient between different bubble mounts is very close to one, which shows strong agreement in the shape of the force-deflection curves. From the difference between the values it can be said that some of them are more similar than others. The highest correlation coefficient is 0.9999 for example between mounts two and six. The smallest coefficient between bubble mounts arises from the comparison of mounts number one and ten, where the correlation coefficient is 0.9976.

The correlation coefficient between any pair of mounts is considerably higher than between any mount and the linear spring.

Table 4-2: Correlation matrix for force-deflection of bubble mounts

No.	1	2	3	4	5	6	7	8	9	10	11
1	1	0.9997	0.9990	0.9995	0.9991	0.9997	0.9998	0.9987	0.9980	0.9976	0.9623
2		1	0.9994	0.9997	0.9994	0.9999	0.9999	0.9991	0.9985	0.9981	0.9672
3			1	0.9999	0.9999	0.9993	0.9992	0.9999	0.9996	0.9995	0.9718
4				1	0.9998	0.9996	0.9995	0.9997	0.9994	0.9992	0.9691
5					1	0.9993	0.9991	0.9999	0.9996	0.9995	0.9702
6						1	0.9999	0.9990	0.9983	0.9979	0.9671
7							1	0.9988	0.9981	0.9977	0.9647
8								1	0.9998	0.9997	0.9728
9									1	0.9999	0.9737
10										1	0.9741
11											1

Symmetric

The minimum tangent stiffness and the corresponding static stiffness of the same bubble mount loaded to its optimum position are key characteristic parameters of a nonlinear vibration isolator. The minimum tangent stiffness defines the resonance frequency and isolation frequency of a nonlinear isolator, providing that the oscillation amplitude is small enough for a linearised model to be valid. The corresponding static stiffness defines the deflection of the mount due to the weight of the isolated mass.

The force-deflections in loading and unloading were averaged to eliminate the effect of damping and then an order nine polynomial was fitted to the data in order to smooth the effect of noise and find the minimum tangent stiffness. This high order polynomial is used to obtain an accurate fit and does not carry any physical interpretation. The fitted polynomial is used to obtain the minimum tangent stiffness for each bubble mount. The minimum tangent stiffness is normalised by its mean and presented as a percentage in Figure 4-12. The minimum tangent stiffness varies from less than 85 per cent of its average value for bubble mount number 1 to

about 112 per cent for bubble mount number 8. The corresponding static stiffness is fluctuating in a narrower range, about ± 5 per cent of its average value.

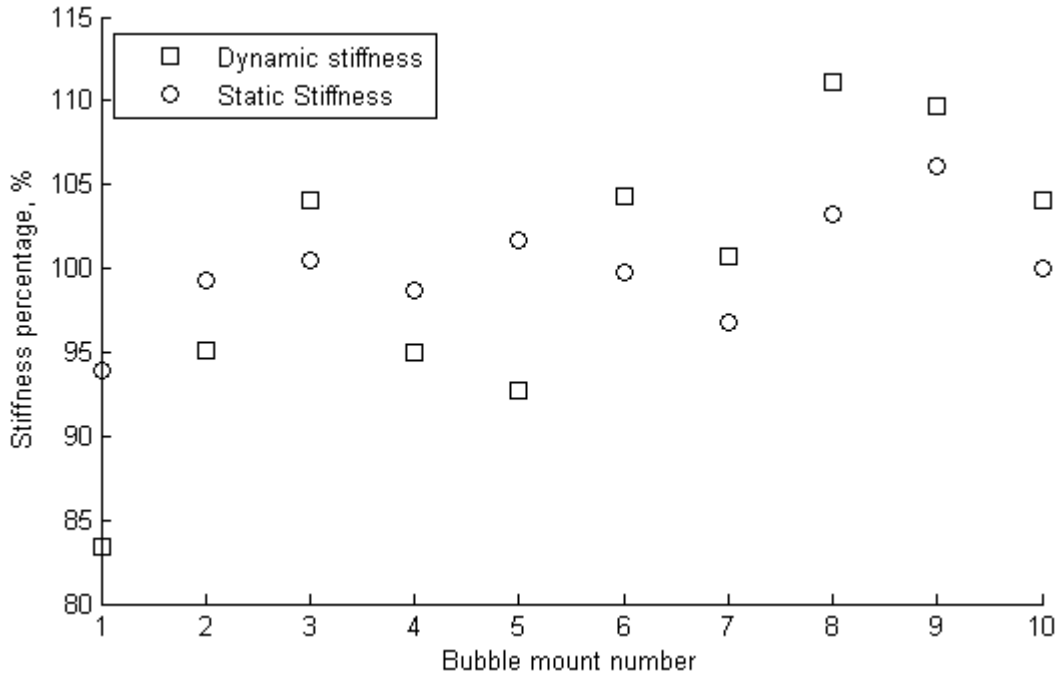


Figure 4-12: Variation of tangent stiffness and corresponding static stiffness in percentage from their mean values for different bubble mounts

The minimum tangent stiffness as a function of its corresponding static stiffness is shown in Figure 4-13. The line of best fit that passes through the origin is also shown. The positive slope of the linear fit shows that the minimum tangent stiffness increases with the static stiffness. However, it seems that the variance is large. The slope of the line is almost 0.39, which corresponds to a 61 per cent reduction in tangent stiffness as compared with static stiffness.

The variation in stiffness of the bubble mounts from some nominal or average value removes any guarantee that it will be loaded to its minimum tangent stiffness position by a specific mass. A nominal mass is considered here and the static deflection and tangent stiffness of the bubble mounts are obtained for this load. The nominal mass is obtained by averaging the required mass to load each bubble mount to its minimum tangent stiffness position. The changes in stiffness of nominally loaded bubble mounts are a measure of their variability.

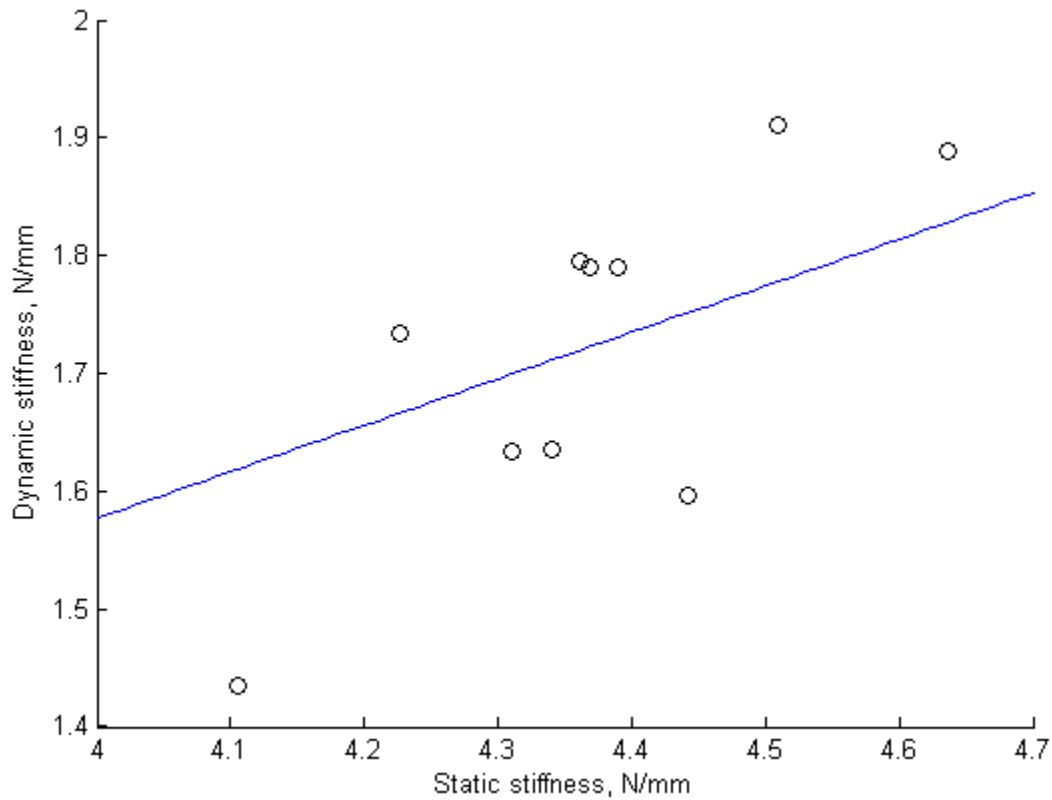


Figure 4-13: Minimum Tangent stiffness as a function of static stiffness for each bubble mount (circles) alongside best linear fit (solid line)

Pieces of equipment are usually supported with three or more mounts. The mounts are required to displace equally under static load in some cases, such as where there is a requirement for alignment between connected equipment. The static deflection due to the nominal mass is shown in Figure 4-14 (a) for the different bubble mounts examined here. The displacements are normalised by the average displacement. It can be seen that the range of variation in displacement is 20%, which is considerable.

The tangent stiffness values at the position obtained when loaded by the nominal mass are shown in Figure 4-14 (b) for different bubble mounts. The tangent stiffness values are normalised by the average minimum tangent stiffness. The tangent stiffness varies between 95 per cent and more than 115 per cent of the average tangent stiffness. On this basis, the corresponding natural frequency of a nominal mass supported by a bubble mount would vary between 98 per cent and 108 per cent of the average natural frequency of the optimally loaded bubble mount.

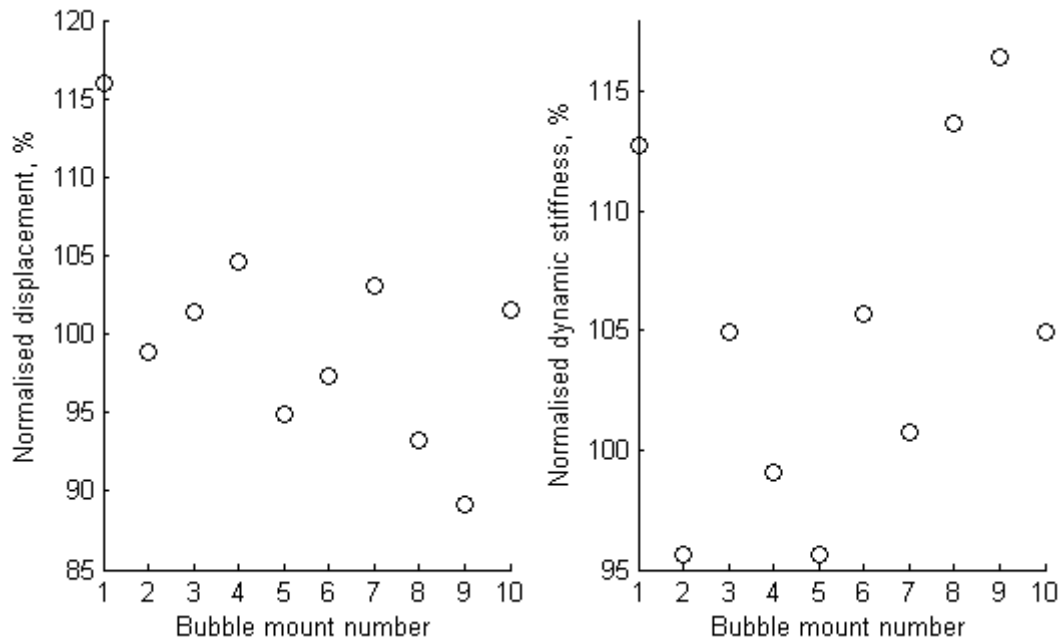


Figure 4-14: a) Displacement due to optimal load normalised by average displacement, b) Tangent stiffness of optimally loaded bubble mount, normalised by averaged minimum tangent stiffness

4.5 Conclusions

The stiffness characteristic of a commercially available isolation mount, known as a “bubble mount”, is studied in this chapter. The force-deflection of the bubble mount was measured using an Instron machine in a quasi-static manner. The forces in loading and unloading are averaged to consider only the effect of stiffness and not hysteresis. The measured force-deflection curve is different from that given in the manufacturer’s catalogue.

Due to the bell shape of the bubble mount, it was hypothesised that it would behave like a curved beam and attempts have been made to model the bubble mount as such. The length and Euler buckling load of a straight beam with the same length as the curved beam have been obtained by minimizing the mean square error between the measured force-deflection of the bubble mount and curved beams. It is revealed that a curved beam is not a good model for the bubble mount. This may be due to the thickness of the bubble mount which is not slender, and also its cross section shape, which is not uniformly curved.

The variability in the properties of bubble mounts is evaluated in section 4.4. A set of ten bubble mounts which were purchased at the same time from the same manufacturer were considered. Their force-deflection relations were measured and compared. The correlation coefficient of their force-deflection curves is considered here as a measure of the similarity in the shape of their force-deflection curves. A linear spring is used as a reference to compare the correlation coefficients. The correlation coefficients are very close to unity.

The minimum tangent stiffness and corresponding static stiffness are obtained for different bubble mounts. The static stiffness is generally greater for the mounts that possess higher minimum tangent stiffness. A nominal mass is also considered by averaging the required mass to load the bubble mounts to their minimum tangent stiffness position. The variation in bubble mounts is negligible in practice, however the change in tangent stiffness may cause some degree of mode coupling in practice for a piece of equipment that is supported by several mounts. The static deflection of the nominally loaded bubble mounts varies between 90 and 115 per cent of its average value which may cause difficulties in devices that are required to be aligned with other equipment.

The differences in bubble mounts can be due to tolerances in the manufacturing process and the variability in the properties of rubber which depends very much on its composition. The variability in the force-deflection curve of bubble mounts is illustrative of the inherent variability in all mounts. This has particular consequences for nonlinear mounts which are tuned devices. The effect of mistuning on the performance of a different nonlinear isolator is dealt with in chapter 5.

5 Force transmissibility of an asymmetric Duffing oscillator

5.1 Introduction

Some mechanisms and elements that have a low tangent stiffness and a high static stiffness were investigated in the preceding chapters. It was presupposed that this is an attractive property for a vibration isolator, at least for small amplitudes of vibration, where it may be assumed that such a system can be described satisfactorily by an equivalent linear model. For larger amplitudes, however, it is necessary to study the nonlinear forced response in order to evaluate the performance of a nonlinear vibration isolator.

A nonlinear vibration isolator that is loaded statically to its minimum tangent stiffness position may be modelled by the classic Duffing oscillator which is a single degree of freedom system with a cubic stiffness term to represent a nonlinear restoring force. The force-deflection curve of the Duffing oscillator is symmetric about the intervening point of inflection, which is also the minimum tangent stiffness position. However, a symmetric force-deflection characteristic is not the case for all nonlinear springs. An asymmetric characteristic is observed in the force-deflection characteristics of both the bubble mount and the curved beam presented in the previous chapters. A simple example of a nonlinear oscillator with asymmetric force-deflection curve about the working position is a Duffing oscillator preloaded by a static force. The forced response of such an oscillator is investigated by Koviach et al. [80, 81]. The force transmissibility of such an oscillator is studied in this chapter to assess the performance of a nonlinear vibration

isolator with asymmetric force-deflection characteristics. As an alternative scenario to the static preload, the effect of a mistuned mass on the nonlinear dynamics of a Duffing oscillator is also investigated in this chapter. The Harmonic Balance Method (HBM) is used to obtain approximate analytical solutions for the forced response of the nonlinear systems in this chapter. The results are compared with the numerical simulation in the time domain.

This chapter aims to assess the performance of a nonlinear isolator with asymmetric stiffness in isolating harmonic forces and to establish the effects of a static preload and a mistuned mass as sources of asymmetry on a nonlinear isolator. Different forms of the equation of motion for the forced response of a Duffing oscillator are presented in the first section of this chapter. The mechanism with oblique springs presented in chapter 2 is reintroduced in section 5.3 as an example of a nonlinear isolator. It is used to attribute physical meaning to the parameters that have been used in this chapter. The effect of static preload on a Duffing oscillator with a cubic stiffness term only is investigated in section 5.4. The Duffing oscillator with a cubic stiffness term only loaded by a mistuned mass is considered in section 5.5. The addition of a linear stiffness to the equation of motion and forming the common form of Duffing oscillator is considered in section 5.6. Conclusions are presented in section 5.7 and the accuracy of the approximate solutions given in this chapter is assessed in Appendix A.

5.2 Equations of motion for forced response of a Duffing oscillator

The Duffing equation is a common form of nonlinear differential equation that has been widely used to study nonlinear systems including nonlinear vibration isolators [82]. The equation of motion for time-harmonic forced excitation of a Duffing oscillator can be expressed in the following non-dimensional form,

$$x'' + 2\zeta x' + \kappa x + \gamma x^3 = f_1 \cos(\Omega\tau) \quad (5-1)$$

where $(\bullet)'$ denotes differentiating with respect to non-dimensional time τ . The stiffness element of the isolator described by the κx and γx^3 terms of the above equation possesses symmetric force-deflection characteristics. However, practical nonlinear springs can exhibit asymmetric

force-deflection such as the curved beam and bubble mount presented in the previous chapters. The addition of a quadratic term to the above equation is a simplistic way to introduce asymmetry about the origin. The corresponding differential equation with the additional quadratic term is called the Helmholtz-Duffing equation,

$$x'' + 2\zeta x' + kx + \mu x^2 + \gamma x^3 = f_1 \cos(\Omega\tau) \quad (5-2)$$

The above equation can be transformed to the Duffing equation by appropriate variable transformation [59] ,

$$z'' + 2\zeta z' + \kappa z + \gamma z^3 = f_0 + f_1 \cos(\Omega\tau) \quad (5-3)$$

where,

$$z = x + \delta, \quad \delta = \frac{\mu}{3\gamma}, \quad \kappa = k - \frac{\mu^2}{3\gamma}, \quad f_0 = \frac{k\mu}{3\gamma} - \frac{2\mu^3}{27\gamma^2} \quad (5-4)$$

The linear stiffness can be zero in the special case that k is equal to $\mu^2/3\gamma$. The term f_0 can be thought as a static preload which depends on the stiffness terms of the original equation. Therefore, the Helmholtz-Duffing equation can be recast as a Duffing oscillator with a static preload.

The Duffing oscillator with cubic stiffness only ($\kappa=\mu=0$) has been investigated widely in the literature (e.g. in references [16, 59, 80, 81, 83]). The same type of oscillator is considered here first. Such a system is an example of a quasi-zero-stiffness mechanism, since its minimum tangent stiffness is zero.

5.3 Example of a QZS nonlinear isolator modelled by a cubic nonlinearity

The oblique spring mechanism presented in chapter two is reintroduced here as an illustration of a nonlinear vibration isolator described by the Duffing equation, such that physical meaning can be attributed to the parameters that are used later in this chapter. The nonlinear isolator

comprised of two oblique springs and a vertical spring is shown in Figure 5-1. All the springs are connected together when in their undeformed state. The two oblique springs are simply supported at their other ends. The displacement of the mass is shown by x and is measured from the mass loaded position. The weight of the mass is cancelled out by the restoring force of the springs. The origin of the displacement x is different from that was chosen in section 2.6 for the same mechanism. The spring force applied on the mass in the vertical direction due to deflection x can be found from the following equation ,

$$F_s = k_v x + 2k_o \left(1 - \frac{l_0}{\sqrt{x^2 + l^2}} \right) x \quad (5-5)$$

where l_0 is the unloaded length of the oblique springs, l is their length at the equilibrium position, k_o is the stiffness of oblique springs and k_v is the stiffness of the vertical spring. Equation (5-5) can be approximated using the Maclaurin series,

$$F_s = \left(k_v + 2k_o \left(1 - \frac{l_0}{l} \right) \right) x + \frac{k_o l_0}{l^3} x^3 + O(x^5) \quad (5-6)$$

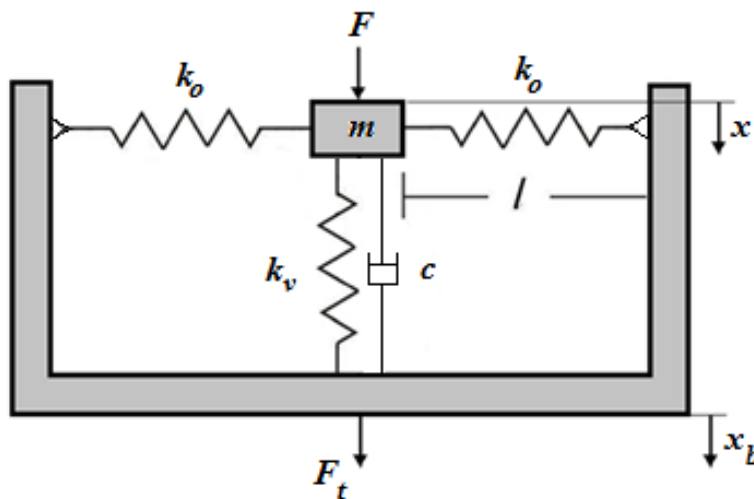


Figure 5-1: QZS mechanism with oblique springs as nonlinear vibration isolator, loaded statically at the zero stiffness position

The above equation is symmetric about the selected origin and so does not comprise any even power terms. However, if the origin were selected at a different position, such as that of the unloaded spring, the equation would be asymmetric and even terms would appear in the

equation. The approximate equation of forced response for a nonlinear isolator can be obtained by considering equation (5-6) for force-deflection of springs and considering harmonic and static forces applied at the same time on the mass,

$$m \ddot{x} + cx' + \left(k_v + 2k_o \left(1 - \frac{l_0}{l} \right) \right) x + \frac{k_o l_0}{l^3} x^3 = F_0 + F_1 \cos(\omega t) \quad (5-7)$$

It was also shown in reference [4] that the geometry of the nonlinear isolator can be optimised to obtain the widest displacement range for low stiffness (where the stiffness would be less than the vertical spring stiffness). The ratio of spring lengths (l/l_0) equal to $2\sqrt{6}/9$ maximises the low stiffness range. The linear stiffness term can be made zero by choosing an appropriate ratio of oblique spring to vertical spring stiffness (k_o/k_v) depending on the spring length ratio (l/l_0). For the optimum arrangement (i.e. the widest low stiffness range) the stiffness ratio should be equal to $9/(4\sqrt{6} - 18)$.

The nonlinear vibration isolator can be compared with a linear vibration isolator easily by choosing proper normalizing parameters. One important characteristic of a nonlinear vibration isolator is its static deflection. Thus, static deflection is chosen as the normalizing parameter for displacement. The static deflection is equivalent to the displacement of the vertical spring due to the weight of the isolated mass. Note that at the equilibrium position, the vertical component of the reaction force from the oblique springs is zero. Since, the above equation has a dimension of force, stiffness k_v is chosen as the second parameter for normalizing. By choosing these specific normalizing parameters, the nonlinear vibration isolator can be compared with a linear vibration isolator that has the same static deflection due to the weight of the mass, and has a non-dimensional natural frequency of unity,

$$y'' + 2\zeta y' + \kappa y + \gamma y^3 = f_0 + f_1 \cos(\Omega \tau) \quad (5-8)$$

where $(\bullet)'$ denotes differentiating with respect to non-dimensional time τ ,

$$\begin{aligned} \tau = \omega_n t, \quad \Omega = \omega/\omega_n, \quad y = x/x_s, \quad x_s = mg/k_v, \quad \zeta = c\omega_n/2m, \quad \omega_n = \sqrt{k_v/m}, \\ f_1 = F_1/k_v x_s, \quad f_0 = F_0/k_v x_s, \quad \kappa = 1 + 2\frac{k_o}{k_v} \left(1 - \frac{l_0}{l} \right), \quad \gamma = \frac{k_o l_0}{k_v l} \left(1 - \left(\frac{l_0}{l} \right)^2 \right) \end{aligned} \quad (5-9)$$

This method of normalising results in a constant damping coefficient for the nonlinear oscillator. Equation (5-8) for an optimum QZS nonlinear isolator that has zero linear stiffness reduces to the following form by considering optimum values for the stiffness and length ratios,

$$y'' + 2\zeta y' + \gamma y^3 = f_0 + f_1 \cos(\Omega\tau) \quad (5-10)$$

where $\gamma = \frac{3}{8}\sqrt{6} + \frac{27}{16} \approx 2.606$. The other value for cubic nonlinearity that is used in subsequent sections of this chapter is γ equal to 0.0783. This coefficient has been used in reference [81]. It is for the same mechanism where the oblique springs are softening nonlinear springs and the mechanism is optimized to obtain a QZS mechanism that has the widest low stiffness displacement range. Equation (5-10) will be used to investigate the performance of a nonlinear vibration isolator first, and then the effect of adding linear stiffness to it is also investigated.

The schematic force-deflection curve for a nonlinear spring that has been defined by equation (5-10) is shown in Figure 5-2. The curve is symmetric about the origin where the tangent stiffness is minimum and equal to zero. By applying static load f_0 , the equilibrium position for the mechanism would move to x_0 . The force-deflection curve is not symmetric about the new equilibrium position and is hardening in one direction whereas it is softening in the other direction up to the zero displacement point. The tangent stiffness is the slope of the tangent line, which is shown by the dashed line on the graph and marked by k_{dyn} for the statically loaded position x_0 .

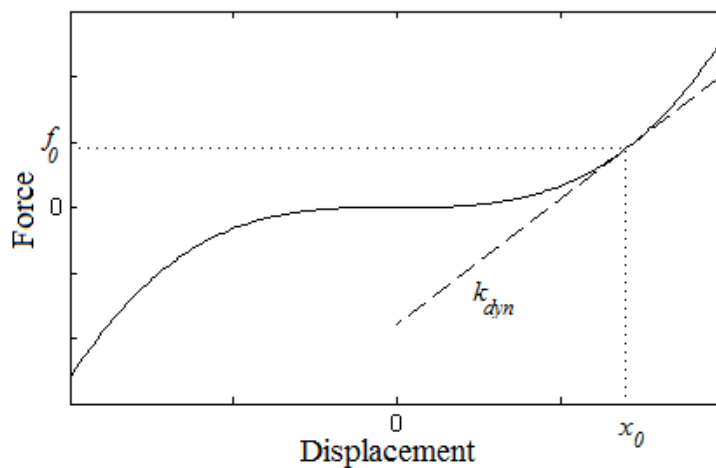


Figure 5-2: Schematic of force-deflection curve for a nonlinear spring with cubic nonlinearity, dashed line: tangent to the curve at the statically loaded position

5.4 Effect of static preload on the dynamic response of nonlinear vibration isolator with cubic stiffness

The existence of asymmetry in the force-deflection curve of nonlinear springs in practice makes it important to consider its effect on the performance of nonlinear vibration isolators. A simple means to form a nonlinear vibration isolator with asymmetry in force-deflection curve is to apply an additional static preload to a nonlinear isolator with cubic stiffness term only. The effect of static preload on the forced response of such an oscillator is studied by Kovacic et al [80, 81]. The purpose of this section is to examine the performance of such an oscillator in transmitting force.

The Harmonic Balance Method (HBM) is used here to obtain the dynamic response of the system in the steady state. The forced response is evaluated in subsection 5.4.1, as previously published by Kovacic et al [80, 81]. It is followed by obtaining force transmissibility in subsection 5.4.2 which, to the author's knowledge, has not been studied before for asymmetric systems. This provides a tool to examine the effectiveness of a statically preloaded Duffing oscillator in isolating harmonic forces.

5.4.1 Forced response

The HBM is used here to approximate the system response at the excitation frequency. The response of a nonlinear oscillator to harmonic excitation is usually comprised of different frequencies. The HBM assumes that the response can be represented by a limited number of harmonics of the excitation frequency. In order to assess the validity of this assumption, the solutions from the HBM can be compared with the results of numerical simulation.

To obtain the transmissibility, the forced response of the system must be obtained first. The response is assumed to consist of a static term and a harmonic term at the excitation frequency [80, 81],

$$y = A_0 + A_1 \cos(\Omega\tau + \phi) \quad (5-11)$$

By substituting the above solution for y in equation (5-10) and equating the corresponding terms on both sides of the equation, the following set of equations can be obtained for the amplitude of the response and its phase with respect to the input,

$$\begin{aligned} \gamma A_0^3 + \frac{3}{2} \gamma A_0 A_1^2 &= f_0, & -A_1 \Omega^2 + 3\gamma A_0^2 A_1 + \frac{3}{4} \gamma A_1^3 &= f_1 \cos \phi, \\ & & -2\zeta A_1 \Omega &= f_1 \sin \phi \end{aligned} \quad (5-12) \text{ (a-c)}$$

The following is obtained for the amplitude of response by summing the squares of equations (5-12) (b) and (c),

$$A_1^2 \Omega^4 - 6\gamma A_1^2 A_0^2 \Omega^2 - \frac{3}{2} \gamma A_1^4 \Omega^2 + 9\gamma^2 A_0^4 A_1^2 + \frac{9}{2} \gamma^2 A_0^2 A_1^4 + \frac{9}{16} \gamma^2 A_1^6 + 4\zeta^2 A_1^2 \Omega^2 = f_1^2 \quad (5-13)$$

The above equation can be recognised as a quadratic function of frequency squared. A_0 can be obtained as a function of A_1 from equation (5-12) (a). The equation can be solved numerically by assuming different positive real values for A_1 and obtaining real solutions for the non-dimensional frequency.

The phase angle at the peak amplitude of a lightly damped linear isolator would be approximately -90 degrees. The same assumption is considered here for the nonlinear isolator. The phase angle for peak harmonic amplitude A_1 can be found by differentiating the equation (5-12) (c) with respect to ϕ ,

$$\frac{dA_1}{d\phi} = \frac{\partial A_1}{\partial \phi} + \frac{\partial A_1}{\partial \Omega} \frac{d\Omega}{d\phi} = 0 \quad (5-14)$$

$$\frac{dA_1}{d\phi} = -\frac{f_1 \cos \phi}{2\zeta \Omega} + \frac{f_1 \sin \phi}{2\zeta \Omega^2} \frac{d\Omega}{d\phi} \quad (5-15)$$

By neglecting the second term in the right hand side of the above equation, the derivative of A_1 with respect to ϕ can be approximated by,

$$\frac{dA_1}{d\phi} \approx \frac{\partial A_1}{\partial \phi} = -\frac{f_1 \cos \phi}{2\zeta\Omega} \quad (5-16)$$

Thus, the phase angle at the resonance is -90° ($dA_1/d\phi = 0$). The locus of amplitudes with a phase angle equal to -90 degrees is found from equation (5-12) (c) which would be an approximate locus for peak of harmonic amplitude A_1 ,

$$A_1|_{\phi=-90^\circ} = \frac{f_1}{2\zeta\Omega} \quad (5-17)$$

The locus of A_1 is independent of the nonlinear stiffness term γ and static preload f_0 . However, the value of $A_1|_{\phi=-90^\circ}$ for a specific case implicitly depends on the nonlinear stiffness γ and static preload f_0 through the non-dimensional frequency. Substituting $A_1|_{\phi=-90^\circ}$ from the above equation in equation (5-12)(b) and solving for A_0 the following equation can be obtained for the value of the bias term,

$$A_0|_{\phi=-90^\circ} = \frac{\sqrt{-3\gamma(3\gamma f_1^2 - 16\zeta^2\Omega^4)}}{12\gamma\zeta\Omega} \quad (5-18)$$

A thorough analysis for the force response of this system is presented in reference [80, 81]. The solutions are presented here for the same set of values for static and harmonic forces as used in reference [81] to demonstrate the important characteristics of the response. In the following set of Frequency Response Curve (FRC) plots, solid and dotted lines are obtained by the HBM. There are regions that multiple solutions exist simultaneously, where the stability of these solutions, which are merely periodic states of equilibrium, must be evaluated [57]. A periodic solution is stable if, when slightly disturbed, the effect of the disturbance decays by time. Stability of periodic oscillations can be calculated using Floquet theory. It is shown in reference [81] that the vertical tangents to the FRCs are at the stability limits. These results are used here, and the solid line is used for the stable solution and the dotted line for the unstable solution. The discrete dots in the figure are obtained by evaluating the forced response in the time domain numerically and obtaining the amplitude at the excitation frequency by the Fast Fourier Transform (FFT). The ode45 solver of Matlab has been used to obtain the time domain solution. The solution has been obtained for over 4000 non-dimensional units of time to ensure that

steady state has been reached. There are regions in which the HBM solutions do not match with the results obtained from the time domain simulation. This can be due to existence of other harmonics in the response which is not considered in the solution given by equation (5-11). The accuracy of the solutions is discussed in Appendix A.

The harmonic amplitude of response A_1 is shown in Figure 5-3 (a). The dashed line is the locus of $A_1|_{\phi=-90^\circ}$ that is obtained from equation (5-17). The FRCs bend to the left and then to the right as non-dimensional frequency is increased. This behaviour is discussed in detail in reference [80, 81] where it is related to the instantaneous stiffness.

For small amplitudes, the vibration should be about the statically loaded position, which is shown in Figure 5-2. The force-deflection characteristic is hardening when the displacement is increasing and softening when it is decreasing. Since displacement of the mass in the softening range requires a lower level of force; it is expected to have a dominant softening behaviour by increasing the amplitude up to a certain level. This explains the bend to the left at first in the FRCs. For negative displacements, after passing through the unloaded position, the force-deflection curves become hardening again. By increasing vibration amplitude even more, the hardening characteristic becomes dominant and FRCs bend to the right.

The phase of the FRCs for different values of static load is shown in Figure 5-3 (b). The phase angle seems to be equal to -90 degree at the same frequency as the peak amplitude as previously assumed in equations (5-17) and (5-18).

The bias term of the response as a function of frequency is shown in Figure 5-4. It is expected that the isolator will oscillate around the statically loaded position, which is shown in Figure 5-2 by x_0 . This position is introduced in equation (5-11) by the bias term A_0 . Thus the bias term should increase with increasing static load. The same trend can be seen in Figure 5-4, except for around the resonance frequency where A_0 drops to its minimum. The curves bend to the left then to the right with increasing frequency for a static load greater than 0.2.

The dependency of force on the cubic displacement results in very large forces at large displacements. As a consequence, the mass oscillates close to the minimum tangent stiffness position at large amplitudes because of higher stiffness at large displacements. Thus the bias

term has a minimum value at the resonance frequency while the harmonic term is at its peak. The dashed line is the locus of $A_0|_{\phi=-90^\circ}$ which is obtained by equation (15). The locus also corresponds to the minimum value of the bias term.

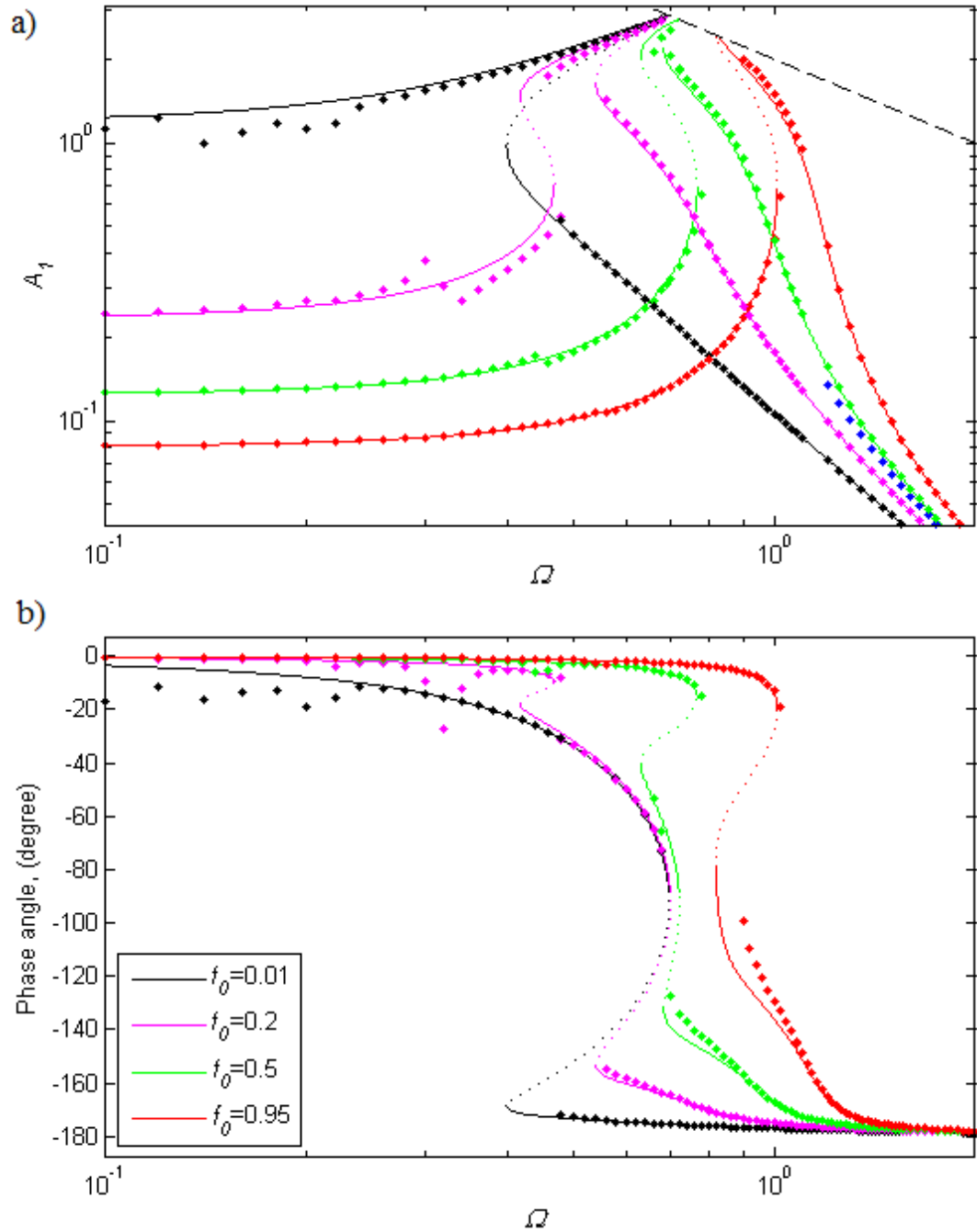


Figure 5-3: a) Magnitude of FRC of the harmonic term, b) phase angle of FRC for different values of static preload, $\gamma=0.0783$, $\zeta=0.025$, and $f_1=0.1$, solid lines: stable branch, dotted lines: unstable branch, dots: time domain solutions, dashed line: locus of $A_1|_{\phi=-90^\circ}$

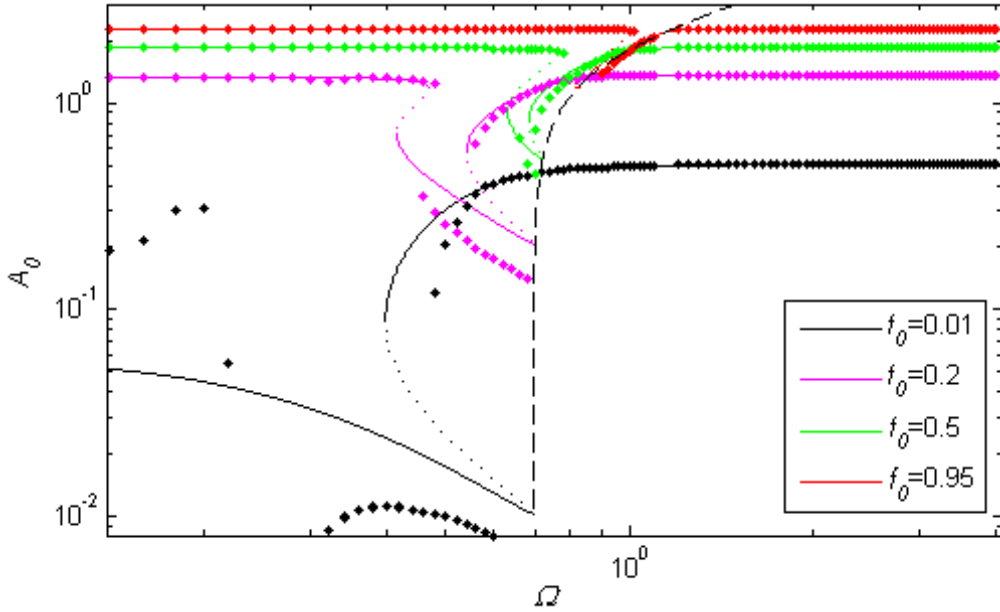


Figure 5-4: FRC of bias amplitude for $\gamma=0.0783$, $\zeta=0.025$, and $f_1=0.1$, solid lines: stable branch, dotted lines: unstable branch, dots: time domain solutions, dashed line: locus of $A_0|_{\phi=-90^\circ}$

5.4.2 Force transmissibility

The transmitted force to the base is obtained here to evaluate the performance of the nonlinear isolator. The transmitted force can be obtained from the following equation,

$$f_t = 2\zeta y' + \gamma y^3 \quad (5-19)$$

It can be written as a function of the applied force and acceleration by substituting $2\zeta y' + \gamma y^3$ from equation (5-10) in the above equation,

$$f_t = f_0 + f_1 \cos(\Omega\tau) - y'' \quad (5-20)$$

The transmitted force can be considered as the combination of a static transmitted force and a harmonic term at the same frequency as the excitation frequency,

$$f_t = f_{t0} + f_{t1} \cos(\Omega\tau + \phi_t) \quad (5-21)$$

An equation for the harmonic and bias terms of the transmitted force can be obtained from equations (5-20) and (5-21). Substituting for acceleration that was obtained by differentiating equation (5-11),

$$f_{t0} + f_{t1} \cos(\Omega\tau + \phi_t) = f_0 + f_1 \cos(\Omega\tau) + A_1\Omega^2 \cos(\Omega\tau + \phi) \quad (5-22)$$

The bias and harmonic terms of the transmitted force can be obtained by expanding and equating the corresponding terms of the above equation,

$$f_{t0} = f_0$$

$$f_{t1} \cos(\phi_t) = f_1 + A_1\Omega^2 \cos(\phi) \quad (5-23) \quad (\text{a-c})$$

$$f_{t1} \sin(\phi_t) = A_1\Omega^2 \sin(\phi)$$

The static force transmits to the base without any attenuation and is independent of frequency. The harmonic part of the transmitted force can be obtained from equation (5-23) (b and c) and is given by,

$$f_{t1} = \sqrt{f_1^2 + A_1^2\Omega^4 + 2f_1A_1\Omega^2 \cos(\phi)} \quad (5-24)$$

The transmissibility can be obtained by substituting the $\cos(\phi)$ term from equation (5-12) (b) into the above equation and dividing it by f_1 ,

$$T_1 = \sqrt{1 + \frac{A_1^2}{f_1^2}\Omega^2 \left(6\gamma A_0^2 + \frac{3}{2}A_1^2\gamma - \Omega^2\right)} \quad (5-25)$$

The locus of transmissibility that has a phase angle equal to -90 degree can be found by setting ϕ equal to -90 degrees in equations (5-23) (b and c) and substituting A_{1max} from equation (5-18) into equation (5-23) (b),

$$T_1|_{\phi=-90^\circ} = \sqrt{1 + \frac{\Omega^2}{4\zeta^2}} \approx \frac{\Omega}{2\zeta} \quad (5-26)$$

Although the locus of peaks is not explicitly dependent on the nonlinearity coefficient γ and the amount of dynamic loading, a specific peak depends on these parameters due to the dependency of the non-dimensional frequency Ω on them. The transmissibility for the nonlinear vibration isolator of equation (5-10) is plotted in Figure 5-5 as a function of non-dimensional frequency for the same set of values as in previous figures. The same trend of bending to the left and to the right can be seen here as previously for the forced response amplitude. It can be seen that the locus of the transmissibility at which phase angle is -90 degrees is the locus of the peaks.

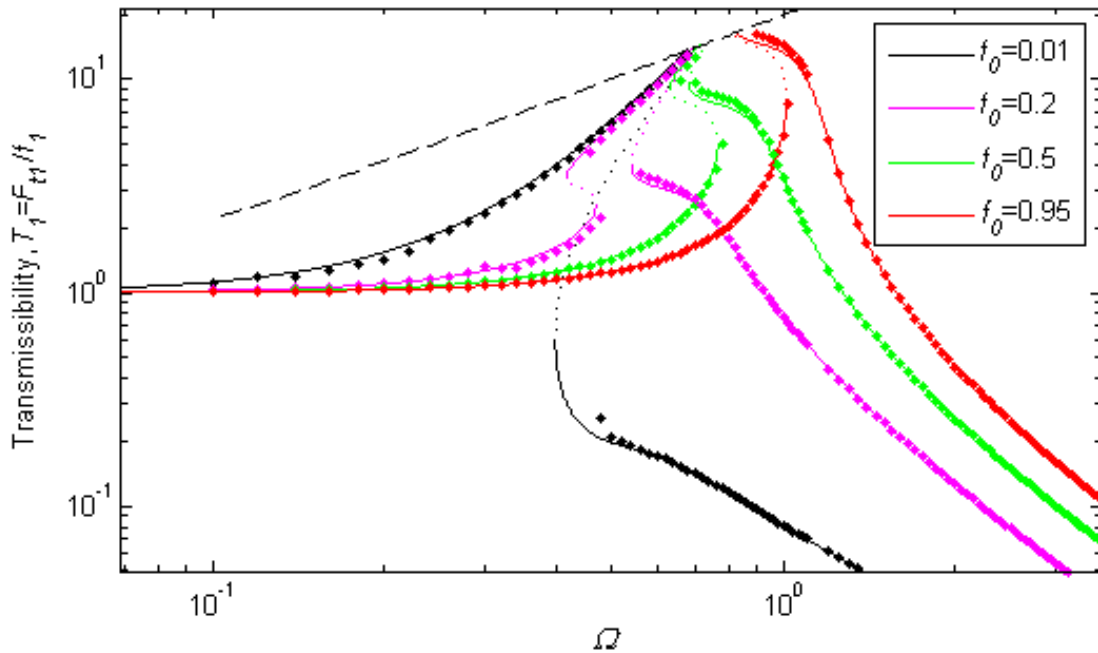


Figure 5-5: Transmissibility as a function of non-dimensional frequency Ω for $\gamma=0.0783$, $\zeta=0.025$, and $f_1=0.1$, solid lines: stable solution, dotted lines: unstable solutions, dots: time domain solutions, dashed line: locus of transmissibility at which phase angle is -90°

The FRCs shift to the right on increasing the static force is due to the increase in tangent stiffness at the statically loaded position. The static displacement due to preload f_0 is $(f_0/\gamma)^{1/3}$. The tangent stiffness of a nonlinear spring with cubic stiffness is $3\gamma x^2$. By substituting for the static deflection, the tangent stiffness at the statically loaded position is obtained,

$$k_d = 3\gamma^{2/3} f_0^{1/3} \quad (5-27)$$

The transmissibility curves of a *linear* isolator whose stiffness is equal to the tangent stiffness at the statically loaded position are plotted in Figure 5-6 alongside the transmissibility of the nonlinear isolators. An increase in static load causes an increase in tangent stiffness and the transmissibility curves shift to the right. The nonlinear isolator deviates from the linear model for relatively large amplitudes. Hence around resonance only, bending to the right or left can be seen that is due to the nonlinearity. It can also be seen that the effect of nonlinearity is more severe for small values of the preload, f_0 . The tangent stiffness is low around zero displacement which results in relatively large amplitudes of oscillation. Thus for small preloads, the large oscillation amplitude causes deviations from the linear model over a wider frequency range, more clearly seen in Figure 5-6 for f_0 equal to 0.01.

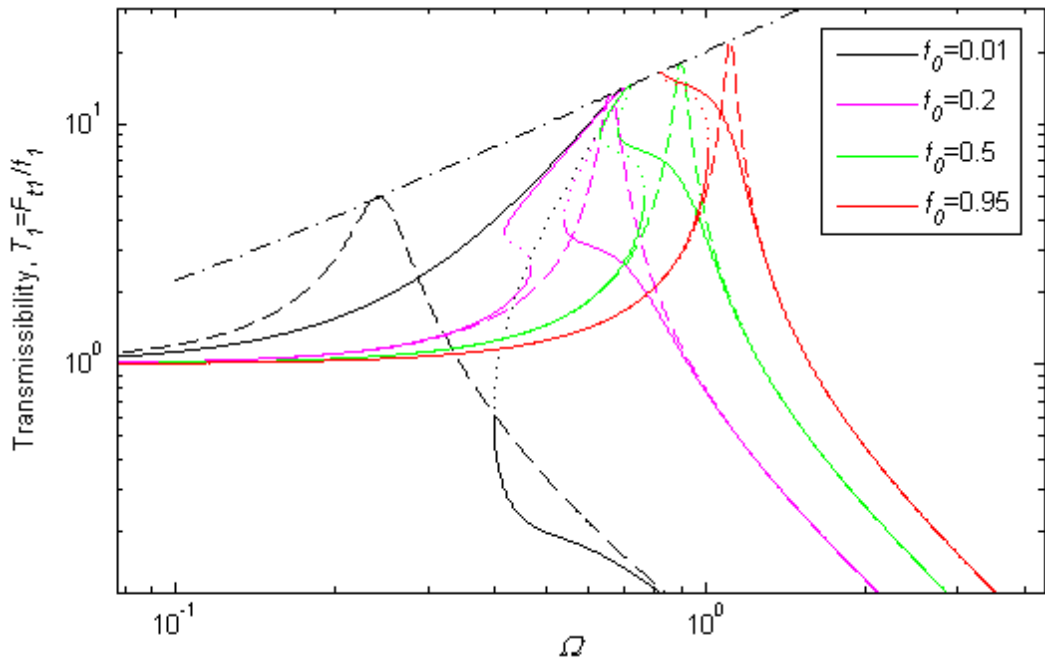


Figure 5-6: Transmissibility as a function of non-dimensional frequency Ω for $\gamma=0.0783$, $\zeta=0.025$, and $f_1=0.1$, solid lines: stable solution, dotted lines: unstable solutions, dashed line: transmissibility of equivalent linear isolators, dashed-dot line: locus of peaks

The transmissibility for the cubic stiffness coefficient γ of 2.606, which is the cubic coefficient for the optimum oblique spring mechanism with linear oblique springs is shown in Figure 5-7. The transmissibility curves for $\gamma=0.0783$ are also shown in the figure by grey lines. The higher nonlinear term γ causes the FRCs to bend more to the right and left. The FRCs are also shifted to the right which can be explained by the increased tangent stiffness at the statically loaded position due to the larger nonlinear stiffness coefficient. The curve for a static load equal to 0.95 still demonstrates a hardening effect by bending to the right for large amplitudes about the resonance frequency compared to the curve of Figure 5-5 which only bends to the left.

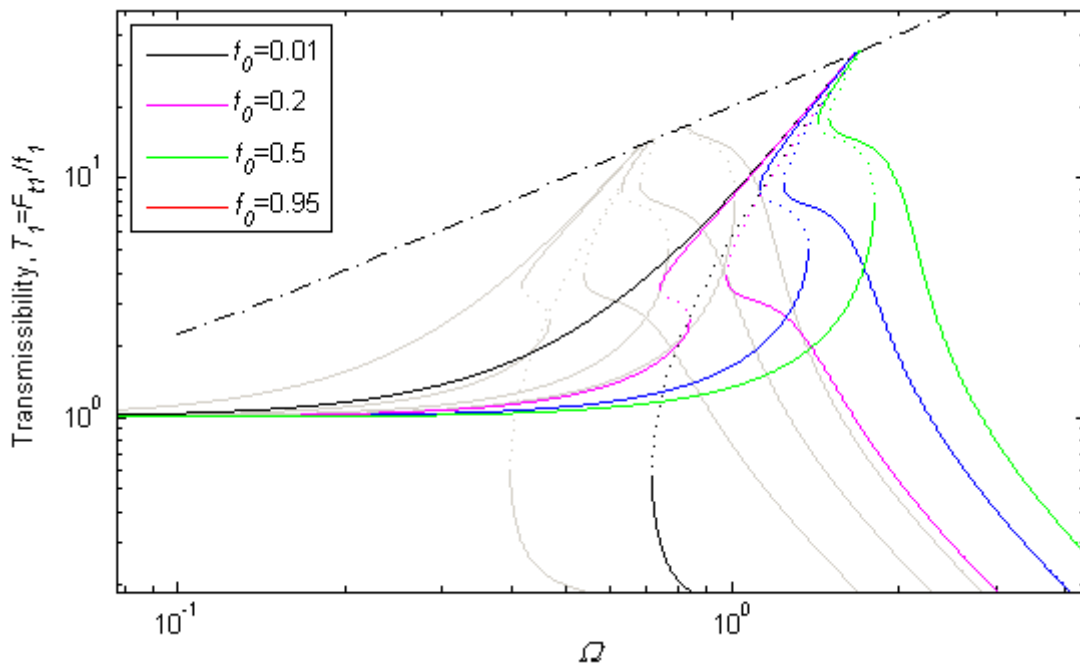


Figure 5-7: Transmissibility as a function of non-dimensional frequency Ω for $\gamma=2.606$, $\zeta=0.025$, and $f_1=0.1$, solid lines: stable solution, dotted lines: unstable solutions, dashed-dot line: locus of peaks, Grey lines: transmissibility curves for $\gamma=0.0783$

The frequency at which the amplitude of transmissibility is less than unity is called *the isolation frequency* here. This is the key parameter that defines the performance of an isolator. As shown in Figure 5-6, at small amplitudes of response, the nonlinear isolator can be approximated by a linear isolator whose stiffness is equal to the tangent stiffness of the nonlinear isolator at the statically loaded position. Thus, the isolation frequency is $\sqrt{2}$ times the natural frequency of the equivalent linear isolator. However, bending to the right in the FRC of a nonlinear isolator can cause the peak to occur at a higher frequency than the frequency at which the transmissibility

drops below unity on the high frequency branch. The frequency of the peak must be compared with $\sqrt{2}$ times the natural frequency and the higher of these defines the isolation frequency of the nonlinear vibration isolator.

The isolation frequency of a nonlinear vibration isolator is shown in Figure 5-8. If the jump down frequency defines the isolation frequency, it is shown with a circle on the graph; otherwise it is shown by a dot. The curves are produced for two different values of nonlinear coefficient γ and three different levels of dynamic load. The dotted line defines a frequency of $\sqrt{2}$ times the natural frequency of a comparable linear isolator that has the same static deflection due to the weight of the mass. At low static load, the tangent stiffness is very low and the bending to the right due to the hardening effect causes the peak frequency to become the definitive frequency for isolation. The tangent stiffness becomes larger on increasing the static load and the FRC bends to the left and then to the right. For large values of the static load, they only bend to the left. As a consequence, the frequency at which the transmissibility drops below unity becomes the definitive isolation frequency at large values of the static load.

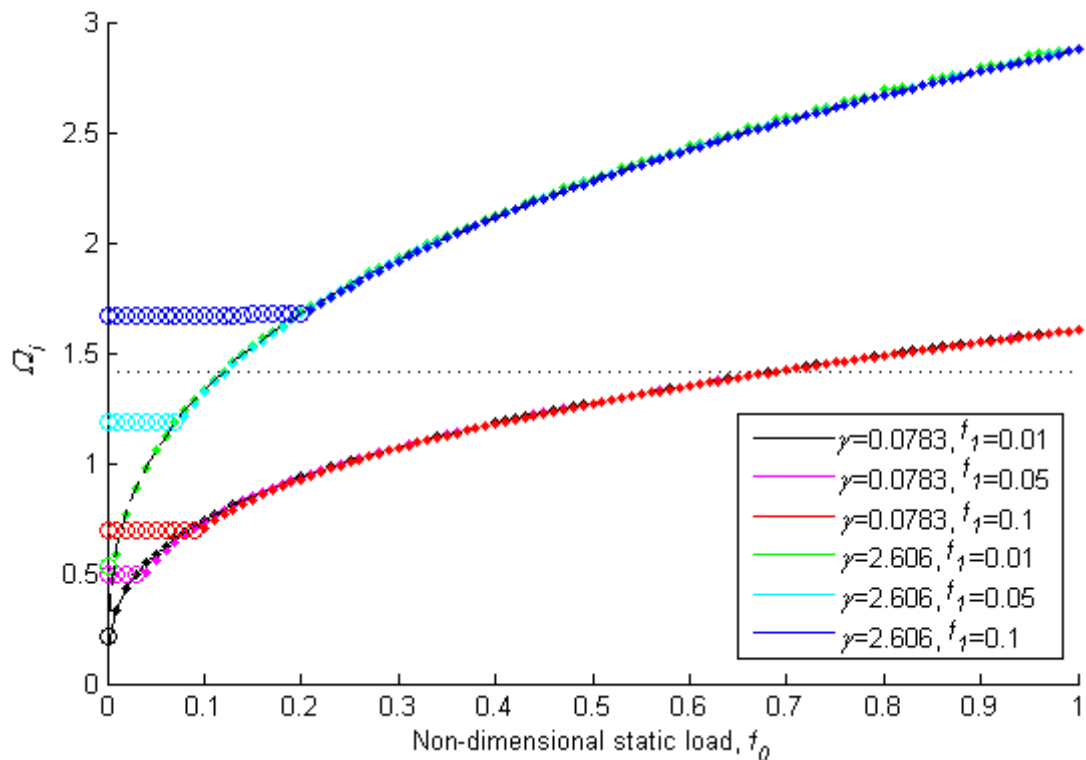


Figure 5-8: Isolation frequency as a function of static load, circles: peak frequency dominant, dots: transmissibility less than one, lines: isolation frequency of equivalent linear isolator with stiffness equal to tangent stiffness, (solid line: $\gamma=0.0783$, dashed line: $\gamma=2.606$), dotted line: isolation frequency of linear isolator with the same static deflection due to the mass

A nonlinear vibration isolator with a low level of nonlinearity ($\gamma=0.0783$) performs better than a linear isolator with the same static deflection due to mass up to a non-dimensional static load of about 0.7. For the isolator with a higher nonlinearity ($\gamma=2.606$), it performs worse than the linear isolator for higher dynamic loads ($f_1=0.1$). For lower levels of dynamic load it is advantageous over linear isolator up to a non-dimensional static load of about 0.12.

5.5 Effect of a mistuned mass on a nonlinear isolator with cubic stiffness

If an incorrect nonlinear isolator is used for a specific mass, the mass will not load the isolator statically to its minimum tangent stiffness position which is the optimum working position. The force-deflection characteristics about this new equilibrium position would be asymmetric. This is formulated by introducing a ratio between two masses, the isolated mass (mistuned or non-optimum mass) and the optimum mass for the implemented nonlinear isolator, in the equation of motion. Hence, it is called mistuned mass in this thesis. The difference between this case and that of the statically loaded isolator would be the effect of the mass on the inertia term of the differential equation. Equation (5-10) can be rewritten for a different mass m_2 without static preload,

$$\mu y'' + 2\zeta y' + \gamma y^3 = \mu - 1 + f_1 \cos(\Omega\tau) \quad (5-28)$$

where μ is the mass ratio m_2/m and m is the original mass. The added mass ratio, which is equal to $\mu-1$, is a substitute for the static preload and should have a similar effect. The natural frequency of a linear oscillator would decrease for increased mass and the FRCs would shift to the left. If the mass decreases then the natural frequency would increase and the FRCs would shift to the right. The FRCs of a nonlinear isolator are also expected to shift in this manner as a result of changes to the mass.

5.5.1 Forced response

The HBM is used to find an approximate solution for equation (5-28). Equation (5-11) is used to describe the response here also. By substituting it in equation (5-28), a set of equations for the harmonic amplitude, the bias term and the phase angle can be found which are slightly different from those in equation (5-12),

$$\begin{aligned} \gamma A_0^3 + \frac{3}{2} \gamma A_0 A_1^2 &= \mu - 1, & -\mu A_1 \Omega^2 + 3\gamma A_0^2 A_1 + \frac{3}{4} \gamma A_1^3 &= f_1 \cos(\phi), \\ -2\zeta A_1 \Omega &= f_1 \sin(\phi) \end{aligned} \quad (5-29) \text{ (a-c)}$$

A quadratic equation in Ω^2 can be found from equation (5-29) (b and c),

$$\begin{aligned} \mu^2 A_1^2 \Omega^4 + \left(-6\mu A_1^2 \gamma A_0^2 - \frac{3}{2} \gamma A_1^4 \mu + 4\zeta^2 A_1^2 \right) \Omega^2 + \frac{9}{16} \gamma^2 A_1^6 + 9\gamma^2 A_0^4 A_1^2 + \frac{9}{2} \gamma^2 A_1^4 A_0^2 &= f_1^2 \\ &= f_1^2 \end{aligned} \quad (5-30)$$

A_0 can be obtained as a function of A_1 from equation (5-29) (a). This equation can be solved numerically by assuming different positive real values for A_1 and obtaining real solutions for the non-dimensional frequency.

The locus for harmonic amplitude A_1 when the phase angle is -90 degrees is the same as the oscillator considered previously that is subjected to a static preload and can be found from equation (5-17). The locus for the bias term is different in only one term,

$$A_0|_{\phi=-90^\circ} = \frac{\sqrt{-3\gamma(3\gamma f_1^2 - 16\mu\zeta^2\Omega^4)}}{12\gamma\zeta\Omega} \quad (5-31)$$

The above equation depends on the mass ratio μ , in addition to other parameters. The FRCs of the bias term for a nonlinear isolator with mistuned mass and nonlinearity coefficient γ equal to 0.0783 are shown in Figure 5-9. The mass ratios are selected in a way to have the same constant

on the right side of equation (5-28) as the static preloads that were used to plot the previous graphs. The locus obtained from the above equation is not shown since there is a different line for each mass. A similar trend to the static preload case can be seen here. By increasing the mass, the static deflection becomes larger and as a result, the bias term increases at both high and low frequencies.

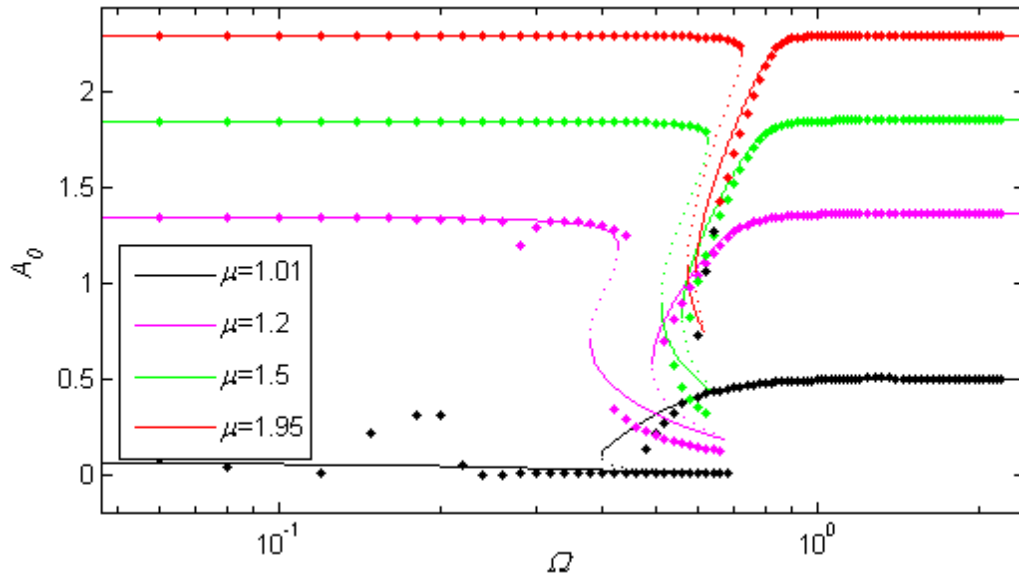


Figure 5-9: FRC of bias amplitude for $\gamma=0.0783$, $\zeta=0.025$, and $f_1=0.1$, solid lines: stable branch, dotted lines: unstable branch, dots: time domain solutions

The forced response FRCs of harmonic amplitude A_1 are shown in Figure 5-10. Again the same trend in bending to the left and then to the right can be seen here. It can also be seen that when there is a maximum in harmonic amplitude, the bias amplitude is at a minimum. The increased mass causes the curve to shift to the left compared to Figure 5-3. The locus of $A_1|_{\phi=90^\circ}$, which is the locus of peaks in the harmonic term is the same as in the previous case with the static preload. The peak amplitude is inversely related to the frequency and the shift of the curves to a lower frequency causes the peaks to increase.

There are also frequency ranges where the results from the approximate solution obtained by the HBM do not match with exact time domain simulations for μ equal to 1.01 and 1.2. This is due to the existence of other harmonics in the response that are not considered in the approximate solution. This is similar to case of an isolator with a static preload as discussed in Appendix A.

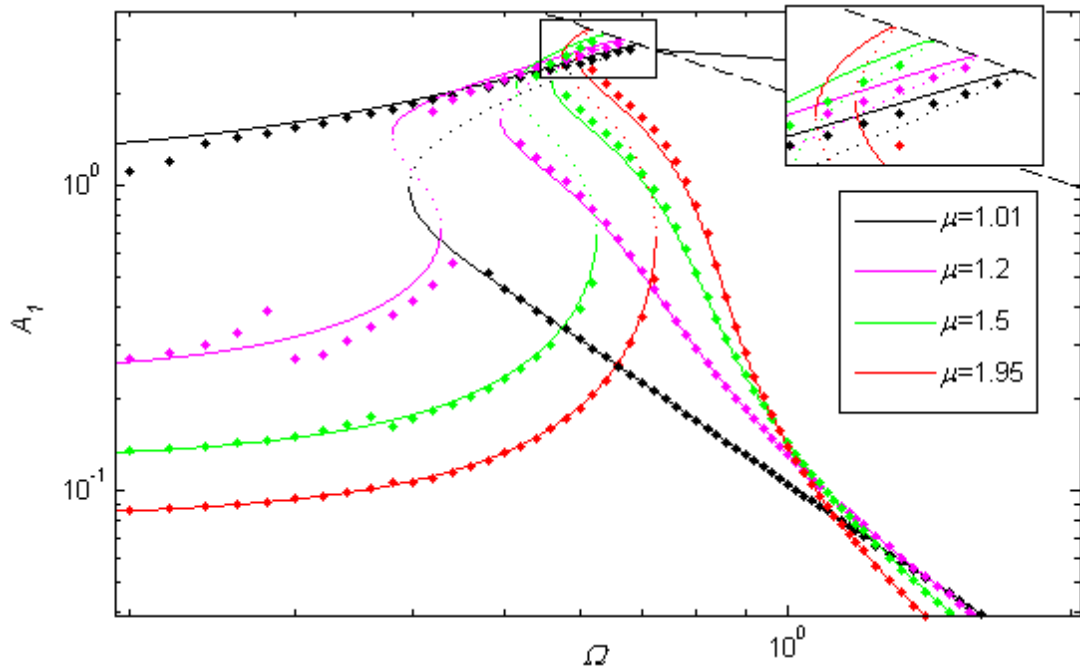


Figure 5-10: FRCs of harmonic amplitude for $\gamma=0.0783$, $\zeta=0.025$, and $f_1=0.1$, solid lines: stable branch, dotted lines: unstable branch, dots: time domain solutions, dashed line: locus of $A_1|_{\phi=-90^\circ}$

The amplitude of the FRCs of the harmonic response term of the corresponding static preload and mistuned mass ($f_0 = \mu - 1$) demonstrate different characteristics. To clarify this, the FRC of the harmonic amplitude for static preload f_0 equal to 0.95 and μ equal to 1.95 are plotted on the same axes in Figure 5-11. The FRC of the harmonic term of the statically preloaded nonlinear oscillator is bending to the left only while for the mistuned mass it is bending to the left and then to the right. While both of these two cases have the same static deflection, the mistuned mass has a larger amplitude. The instantaneous stiffness becomes hardening for large amplitudes around the peak. The hardening effect appears as a small bend to the right about the peak for the mistuned mass case.

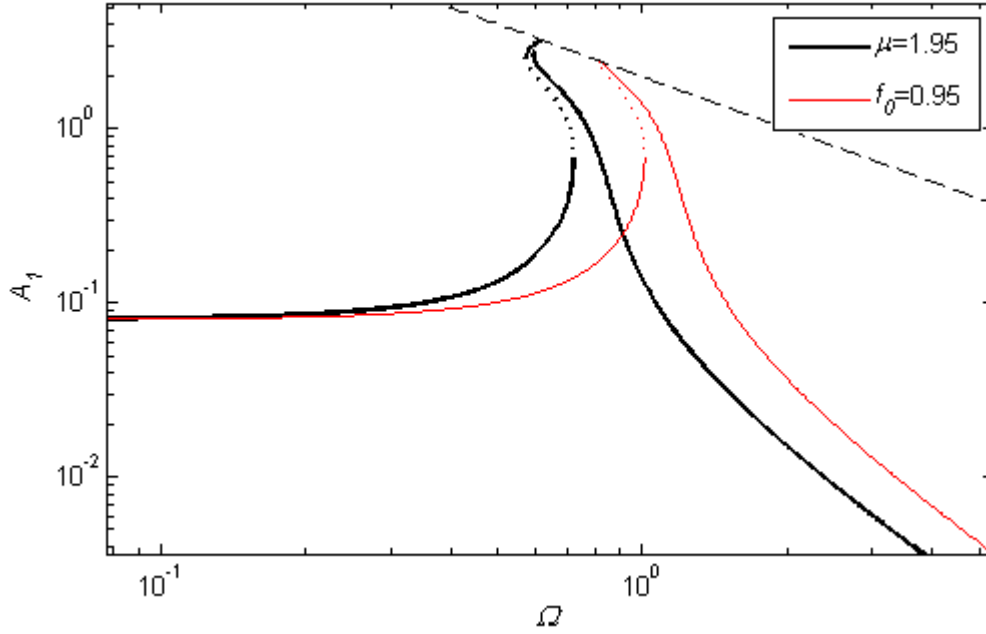


Figure 5-11: FRC of harmonic amplitude for $\gamma=0.0783$, $\zeta=0.025$, and $f_1=0.1$, solid lines: stable branch, dotted lines: unstable branch, dashed line: locus of $A_1|_{\phi=-90^\circ}$

5.5.2 Force transmissibility

By following the same procedure as in section 5.4.2, the force transmissibility for an oscillator with a mistuned mass can be obtained,

$$T_1 = \frac{1}{f_1} \sqrt{f_1^2 + 6\mu A_1^2 \Omega^2 \gamma A_0^2 - \mu^2 A_1^2 \Omega^4 + \frac{3}{2} \gamma A_1^4 \mu \Omega^2} \quad (5-32)$$

The locus of transmissibility that has a phase angle equal to -90 degrees can be obtained by following the same method,

$$T_1|_{\phi=90^\circ} = \frac{1}{2} \sqrt{4 + \frac{\mu^2 \Omega^2}{\zeta^2}} \approx \frac{1}{2} \frac{\mu \Omega}{\zeta} \quad \text{for } \zeta \ll 1 \quad (5-33)$$

As for the bias term of the response, it depends on the mass ratio μ . The transmissibility curves for the same set of parameters as were used for the forced response are shown in Figure 5-12. The curves are shifted to the left because of the added mass. From equation (5-33), it can be noticed that the peak of transmissibility is proportional to the mass ratio and the ones with higher mass ratio have larger peak values. This is the opposite of the case of static preload where peaks at lower non-dimensional frequency are smaller.

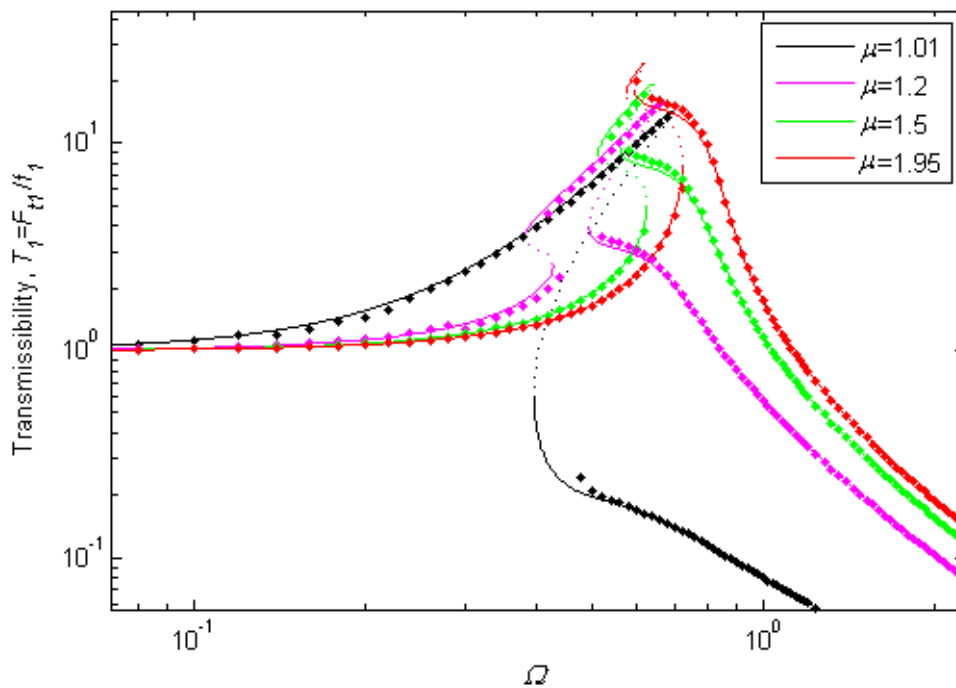


Figure 5-12: Transmissibility as a function of non-dimensional frequency Ω for $\gamma=0.0783$, $\zeta=0.025$, and $f_1=0.1$, solid lines: stable solution, dotted lines: unstable solutions, dots: time domain solutions

The shift of the curves to the left gives rise to a reduced isolation frequency. In the case of a reduced mass which is not plotted here, the curves shift to the right and isolation frequency increases. The isolation frequency as a function of mistuned mass is shown in Figure 5-13. Circles are used to indicate points at which the peak frequency (the jump down frequency) defines the isolation frequency. Dots are used to mark frequencies at which the reduction of transmissibility below unity on the high frequency branch defines isolation. A mass ratio equal to one defines the position where the tuned mass is employed and it can be compared to zero static preload. The graph is not symmetric about this point. Similarly to the case of static preload, the range at which a nonlinear isolator has a better isolation frequency than a linear one depends on the dynamic load level and the nonlinearity coefficient γ .

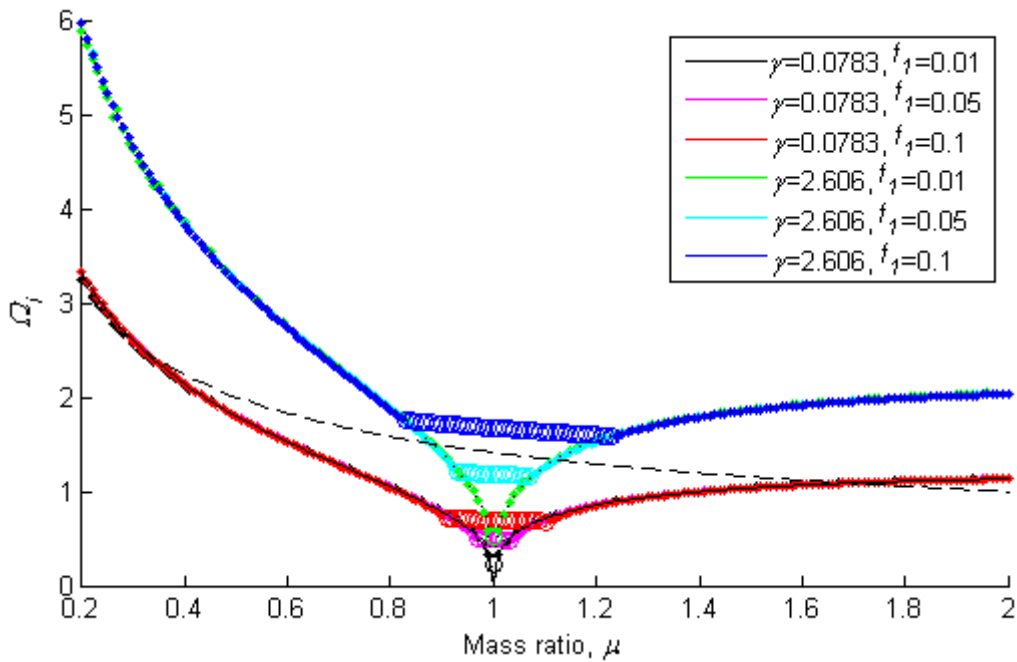


Figure 5-13: Isolation frequency as a function of mass ratio, circles: peak frequency dominant, dots: transmissibility less than one, lines: isolation frequency of equivalent linear isolator with stiffness equal to tangent stiffness, (solid line: $\gamma=0.0783$, dotted line: $\gamma=2.606$), dashed line: isolation frequency of linear isolator

The isolation frequency for a linear isolator also decreases by increasing the mass and increases by reducing the mass. It is shown by the dashed line in the figure. For a nonlinearity coefficient γ equal to 0.0783, the isolation performance of the nonlinear isolator is better than the linear isolator up to a mass ratio of about 1.69, while from Figure 5-8 for the static preload case, it is 0.69. The mass ratio and static preload for a nonlinearity coefficient of 2.606 are 1.12 and 0.12 respectively. Although the isolation frequency of the mistuned mass case is different from those of the static preload case, the range at which the nonlinear isolator performs better than a linear isolator is the same for the mistuned mass and static preload cases. The isolation curve is not symmetric about the optimum mass ratio of unity. However, from the graph, the range at which the nonlinear isolator performs better than its linear counterpart seems to be symmetric about the mass ratio of unity.

5.6 The effect of the linear term on the performance of a nonlinear vibration isolator

The Duffing oscillator with pure cubic stiffness is a special case of a nonlinear oscillator that has a minimum tangent stiffness of zero. To investigate the Duffing oscillator in its complete form, an additional linear stiffness term must be added to the differential equation (5-10). The differential equation of the nonlinear oscillator with the additional linear term loaded statically and harmonically is,

$$y'' + 2\zeta y' + \kappa y + \gamma y^3 = f_0 + f_1 \cos(\Omega\tau) \quad (5-34)$$

where κ is the non-dimensional linear stiffness. Due to the similarity between the effect of mistuned mass and the effect of static preload on a nonlinear oscillator, only the effect of static preload is considered here. HBM is employed to find an approximate solution to the above equation. By considering the same response as equation (5-11) and setting equal the corresponding terms on both sides of the equation the following set of equations can be found,

$$\kappa A_0 + \gamma A_0^3 + \frac{3}{2}\gamma A_0 A_1^2 = f_0, \quad \kappa A_1 - A_1 \Omega^2 + 3\gamma A_0^2 A_1 + \frac{3}{4}\gamma A_1^3 = f_1 \cos(\phi), \quad (5-35) \text{ (a-c)}$$

$$-2\zeta A_1 \Omega = f_1 \sin(\phi)$$

Equations (5-35) (a and b) differ from (5-12) (a and b) only in an additional term κA_0 and κA_1 term respectively. Equations (5-35) (c) and (5-12) (c) are the same. The quadratic equation in the square of non-dimensional frequency can be obtained from the above set of equations,

$$A_1^2 \Omega^4 + \left(-2\kappa A_1^2 - \frac{3}{2}A_1^4 \gamma - 6A_1^2 \gamma A_0^2 + 4\zeta^2 A_1^2 \right) \Omega^2 + \kappa^2 A_1^2 + \frac{9}{16}\gamma^2 A_1^6 + 6\kappa A_1^2 \gamma A_0^2 \quad (5-36)$$

$$+ \frac{3}{2}\kappa A_1^4 \gamma + \frac{9}{2}\gamma^2 A_0^2 A_1^4 + 9\gamma^2 A_0^4 A_1^2 - f_1^2 = 0$$

The numerical method can be used as before to find the solution for the forced response with different parameters. The locus of harmonic response for a phase angle of -90° can be obtained

from equation (5-35) (c). It is the same as the previous case which is obtained from equation (5-18). The bias term A_0 is plotted for different values of linear stiffness as a function of non-dimensional frequency in Figure 5-14, for static preload f_0 equal to 0.5. The addition of linear stiffness has appeared as an increase in the stiffness of the oscillator. The bias term drops for higher values of linear stiffness.

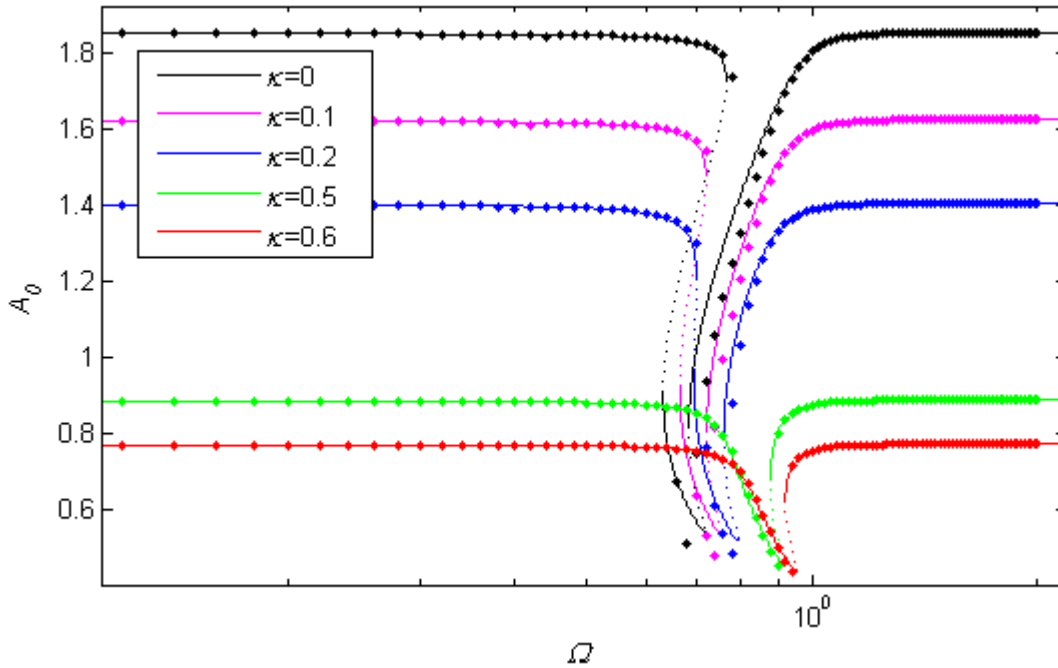


Figure 5-14: FRC of bias amplitude for $\gamma=0.0783$, $\zeta=0.025$, $f_0=0.5$ and $f_1=0.1$, solid lines: stable branch, dotted lines: unstable branch, dots: time domain solutions

The amplitude of the harmonic term of response A_1 is shown in Figure 5-15 for a static preload equal to 0.5, harmonic load $f_1=0.1$ and different levels of linear stiffness. It can be seen that by increasing the linear stiffness the curves are shifted to the right, due to increased tangent stiffness. The lower level of harmonic term A_1 at low frequencies is also due to the increased tangent stiffness. The bending to the left disappears by increasing the linear stiffness and only curves for κ equal to 0.5 and 0.6 demonstrate the hardening effect, bending to the right. An oscillator with larger linear stiffness has smaller static deflection compared to those without linear stiffness or a small linear stiffness. The stiffness reduces from the statically loaded position toward the unloaded position and in this range the stiffness is of the softening type. The decrease in static deflection is the equivalent of a reduced range where instantaneous stiffness is

softening. Thus, higher static preload must be applied to the oscillators with higher linear stiffness to achieve softening characteristics and bending of the FRCs to the left.

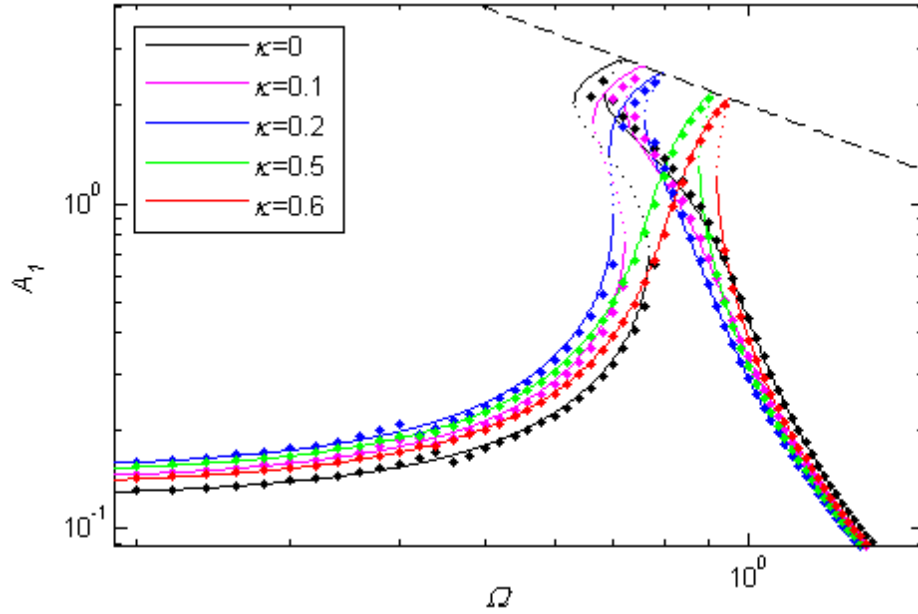


Figure 5-15: FRC of harmonic term of response for $\gamma=0.0783$, $\zeta=0.025$, $f_0=0.5$ and $f_1=0.1$, solid lines: stable branch, dotted lines: unstable branch, dots: time domain solutions, dashed line: locus of $A_1|_{\phi=90^\circ}$

The performance of a nonlinear isolator in transmitting force can be evaluated by obtaining the force transmissibility. The force transmissibility can be found by following the same procedure as in section 5.4.2,

$$T_1 = \frac{1}{f_1} \sqrt{f_1^2 - A_1^2 \Omega^4 + 6A_1^2 \Omega^2 \gamma A_0^2 + \frac{3}{2} A_1^4 \Omega^2 \gamma + 2A_1^2 \Omega^2 \kappa} \quad (5-37)$$

The locus of peaks of transmissibility can be found as before, by assuming a phase angle equal to -90 degrees,

$$T_1|_{\phi=90^\circ} = \frac{1}{2} \sqrt{4 + \frac{\Omega^2}{\zeta^2}} \approx \frac{\Omega}{2\zeta} \quad (5-38)$$

The transmissibility as a function of non-dimensional frequency is shown in Figure 5-16. The curves are shifted to the right by increasing the linear stiffness. The higher tangent stiffness also causes the peaks to have larger values at high frequencies. The locus of peaks which is obtained by equation (5-38), does not explicitly depend on linear stiffness. However, for a specific set of parameters the frequency at which transmissibility is at a maximum depends on the oscillator parameters including linear stiffness as discussed earlier in this chapter.

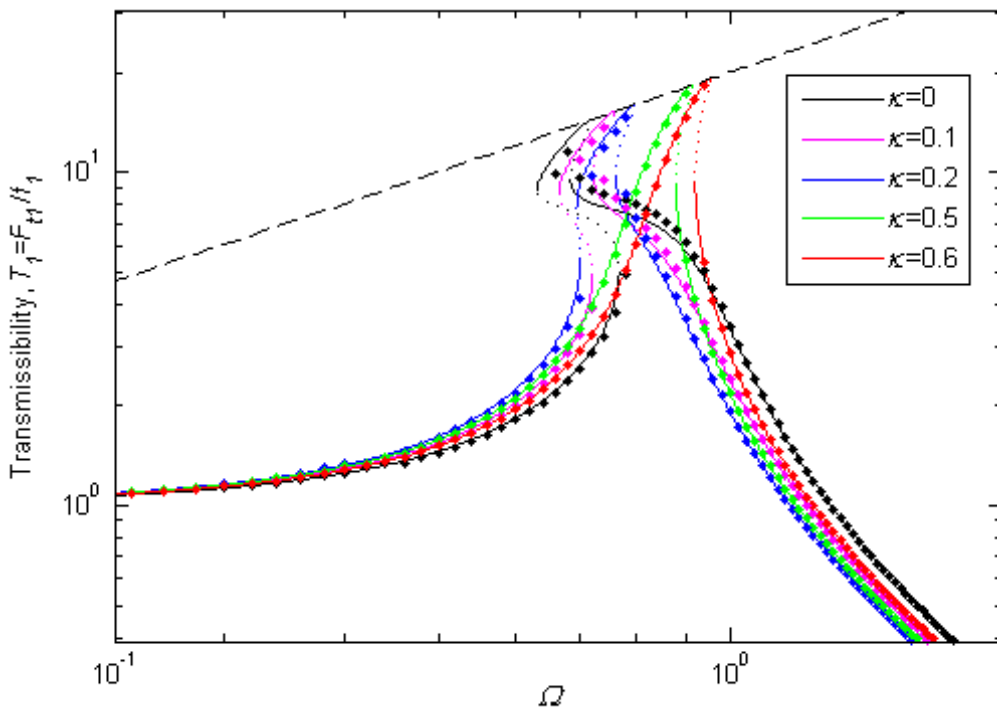


Figure 5-16: Transmissibility as a function of non-dimensional frequency Ω for different linear stiffness and $\gamma=0.0783$, $\zeta=0.025$, $f_0=0.5$, and $f_1=0.1$, solid lines: stable solution, dotted lines: unstable solutions, dots: time domain solutions, dashed line: locus of transmissibility at which phase angle is -90°

The isolation frequency as a function of static preload is shown in Figure 5-17 for $\gamma=0.0783$, $\zeta=0.025$, and $f_1=0.1$. The frequency of isolation due to jump down increases by increasing the linear stiffness. The linear model with stiffness equal to the tangent stiffness at the statically loaded position can model the nonlinear isolator at small amplitudes of vibration. It can be seen that the dots which are obtained by solving the nonlinear model match the linear equivalent isolation frequency with acceptable accuracy because of the small amplitude.

The isolation frequency is reduced by increasing the linear stiffness at large static preloads while it becomes larger when the linear stiffness is increased at low static preloads. The static deflection is smaller for greater values of linear stiffness. The tangent stiffness comprises of linear and nonlinear terms. The nonlinear term depends on the static deflection. The reduced static deflection results in smaller tangent stiffness. Thus, the range at which the isolation frequency of nonlinear isolator is smaller than that of a linear isolator is wider for larger values of linear stiffness.

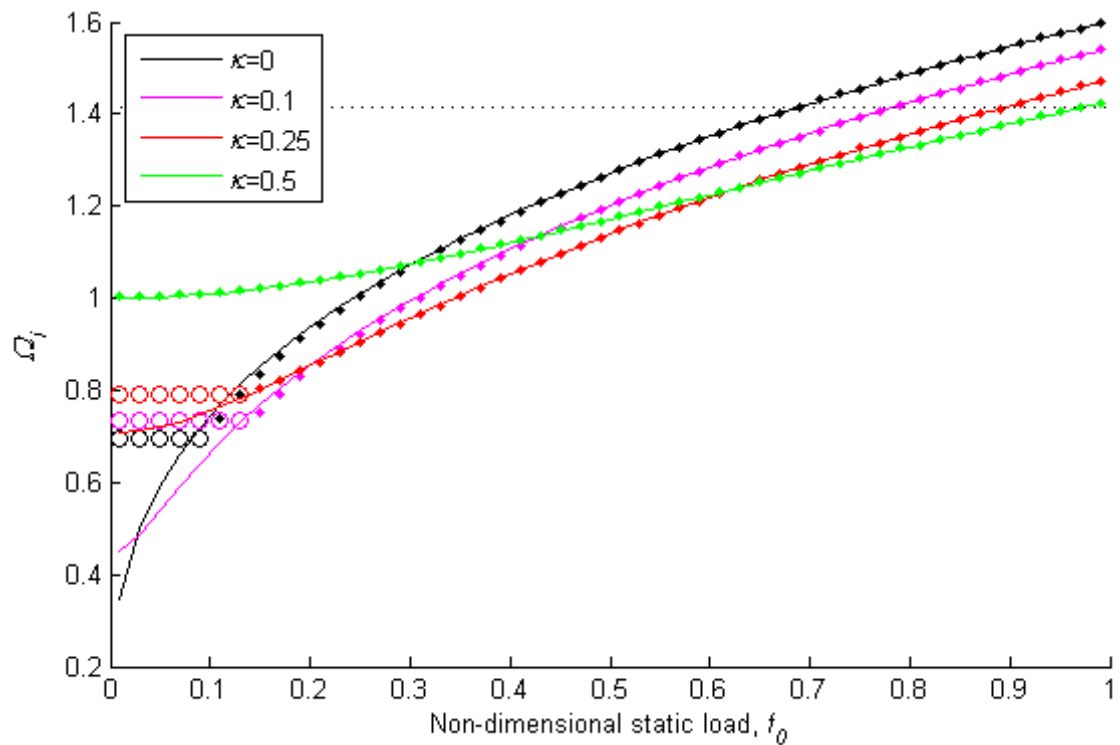


Figure 5-17: Isolation frequency as a function of static preload for $\gamma=0.0783$, $\zeta=0.025$, and $f_1=0.1$, circles: peak frequency dominant, dots: transmissibility less than one, lines: isolation frequency of equivalent linear isolator with stiffness equal to tangent stiffness, dotted line: isolation frequency of linear isolator

5.7 Conclusions

The nonlinear dynamics of a Duffing oscillator loaded statically was investigated in this chapter to evaluate the performance of a nonlinear oscillator with asymmetric force-deflection characteristics in isolating harmonic forces. The HBM was used to obtain the approximate

solution for response. These solutions were compared with the results of the time domain simulation in order to assess their accuracy. Different variations of Duffing equations were introduced. The equation of motion for an oscillator with linear, quadratic, and cubic stiffness terms can be converted to a Duffing equation with linear and cubic stiffness by axis transformation and by introducing an additional constant term which can be treated as a static preload.

The first case considered was a Duffing oscillator with pure cubic stiffness subjected to a static preload. The forced response has been studied before thoroughly but is presented here for consistency [80, 81]. The response is of a hardening type for small levels of static preload and bends to the right depending also on the parameters of the system. There is a combination of hardening and softening for larger static preloads and purely softening type for very large static preloads. The response can comprise of multiple jump frequencies depending on the level of the static preload.

The same trend in bending to the right and left is visible in the force transmissibility graphs. An approximate equation for the locus of the peak of transmissibility was obtained. The frequency at which the transmissibility drops below unity is considered as a measure for evaluating performance of the isolator and it is called the isolation frequency. The graph for isolation frequency as a function of static preload is produced and is compared with the isolation frequency of a linear isolator. For the hardening type nonlinearity the jump down frequency defines the isolation frequency while for linear or softening type nonlinearity the drop of transmissibility below unity on the high frequency branch identifies it. It depends on the dynamic load level in addition to the nonlinear stiffness and damping. A weakly nonlinear isolator can perform better than a linear one up to a large static preload.

The effect of a mistuned mass on the dynamic response of a Duffing oscillator with only cubic nonlinearity was investigated. The mistuned mass moves the statically loaded position away from the optimum position in a similar way to the static preload but differs in that the inertia term of forced equation of motion is affected by the mistuned mass. The FRCs shift to the left for an increased mass and to the right for decreased mass. Oscillators which are loaded to the same position statically due to mistuned mass or static preload show different types of FRC. The shift in FRCs causes a change in the response amplitude which affects the instantaneous stiffness and the shape of the FRCs.

The same trend is visible in the transmissibility graph for a nonlinear isolator that is loaded with a mistuned mass. The isolation frequency as a function of mass ratio is also produced. The isolation frequency is different from that of a statically preloaded case, but the range at which it performs better than a linear isolator loaded by the same mass is the same for the statically loaded case and the mistuned mass case.

The effect of a linear term in the dynamic response of a Duffing oscillator is also investigated. The nonlinear effects such as bending to the right and left become weaker when the linear stiffness is increased. The additional linear stiffness term also brings an increase in the effective tangent stiffness. The static deflection reduces due to the additional linear stiffness. The tangent stiffness at the statically loaded position is increasing for small static preloads due to the additional linear stiffness while it is decreasing at large static preloads due to reduced static deflection. As a result, the isolation frequency increases for small static preloads due to the additional linear stiffness term and it decreases for large static preload.

6 Dynamic response of a curved beam isolator

6.1 Introduction

Axially loaded curved beams are investigated in chapter 3 as nonlinear elements that can provide low tangent stiffness while maintaining high static stiffness, this being a desirable characteristic for springs elements of a nonlinear vibration isolator. A case study of an isolator that is comprised of curved beams as its springs, hereafter referred to as a “curved beam isolator”, is introduced in chapter 3 to illustrate the achievability of a low natural frequency with modest static deflection. The FEM was used to evaluate the potentially detrimental effect of modes of the isolator itself on the isolator performance. The FEM solution was obtained by considering a linearized model about the statically loaded position. In addition to the linear analysis of chapter 3, the nonlinear dynamics must also be examined to assess the performance of such an isolator when excitation is not small. A similar configuration was studied by Bonello et al. [66, 77]. They used a mass supported by curved beams for an adaptive tuned vibration absorber.

The nonlinear dynamics of the Duffing oscillator with a static preload or a mistuned mass was examined in the previous chapter using the Harmonic Balance Method. The possibility of modelling a curved beam isolator about its statically loaded position with such a Duffing oscillator is investigated here. A third order polynomial is fitted to the force-deflection curve of a curved beam to obtain an approximate model in the form of the Duffing oscillator. The HBM

is used to obtain the forced response of the Duffing oscillator. It is compared with the forced response of the curved beam isolator obtained in the time domain using the exact force-deflection curve. While the time domain simulation fulfils the purpose of this chapter, the approximate Duffing oscillator model is examined to assess the applicability of the method presented in chapter 5 to the curved beam isolator and to provide an insight into the nonlinear characteristics of the system.

The purpose of this chapter is to assess the performance of a nonlinear isolator comprised of curved beam in isolating transmitted force considering its nonlinear dynamics. The method that is used to model the curved beam isolator is described in section 6.2. The schematic graph of the isolator is introduced and its force-deflection relation and polynomial fit are presented. The forced response of a mass on the curved beam isolator is obtained for different amplitudes of harmonic force. The approximate forced response obtained by applying the HBM to the Duffing oscillator model of the curved beam isolator is compared with the exact solution obtained by time domain simulation. The effect of additional static preload is explored in section 6.4 for the curved beam isolator with an initial curvature angle of 2 degrees. The performance of the isolator in transmitting force is evaluated in the following section. The force transmissibility is obtained for different amplitudes of harmonic load. The transmissibility graphs are also produced for different static preload and the transmitted force is analysed. The wave form of the transmitted force is investigated in section 6.6 which highlights an issue arising from strong asymmetry in the force-deflection curve. This issue is addressed and a method to overcome it is introduced. The chapter finishes with conclusions.

6.2 Modelling of a curved beam isolator

A schematic view of a curved beam isolator is shown in Figure 6-1(a). It is the same as the isolator that has been used in chapter 3. The model of the curved beam isolator is shown in Figure 6-1(b) where the nonlinear spring's force-deflection curve is that of two curved beams in parallel. The beams are assumed to be massless in the model. The fundamental mode of vibration of a mass supported by the curved beam isolator can be obtained from the model presented here. The linear spring k_c is added in series with the isolator to overcome a

convergence problem that arises in the time domain simulation due to the high stiffness at about the unloaded position and beyond that in tension. By choosing a large stiffness for the linear spring the force-deflection curve of the curved beam isolator is hardly affected in its intended operation range, i.e. in compression. The linear spring is also used in section 6.6 to improve the performance of the isolator. A dashpot is considered in parallel to model damping. The equation of motion for the dynamic system subject to a time-harmonic force is,

$$m\ddot{x} + c\dot{x} + F_k(x) = F \cos(\omega t) \quad (6-1)$$

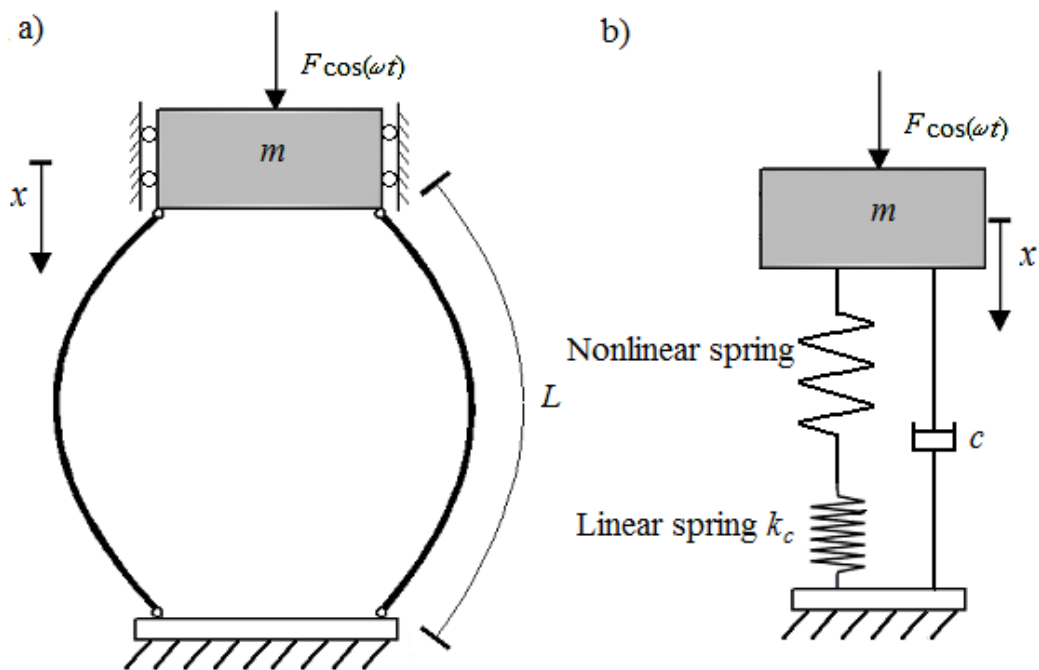


Figure 6-1: a) Schematic view of the curved beam isolator, b) Model of the curved beam isolator with additional linear spring to overcome convergence problems in the numerical simulation (it is also used in section 6.6 to improve the performance of the isolator.)

where F_k is the restoring force due to the spring. Equation (6-1) can be written in terms of non-dimensional parameters and variables as,

$$y'' + 2\zeta y' + f_k(y) = f_1 \cos(\Omega\tau) \quad (6-2)$$

here $(\bullet)'$ denotes differentiating with respect to non-dimensional time τ ,

$$\tau = \omega_n t, \quad \Omega = \omega/\omega_n, \quad y = x/x_s, \quad k_s = mg/x_s, \quad \omega_n = \sqrt{k_s/m},$$

$$\zeta = c/2m\omega_n, \quad f_1 = F/mg, \quad f_k = F_k/mg$$

and x_s is the static displacement of the isolator due to the weight of the isolated mass. This method of normalizing makes it possible to compare the nonlinear isolator with a linear isolator with the same static deflection due to the mass since its non-dimensional natural frequency is unity. Note that, as the previous chapter, ω_n is the natural frequency of a comparable linear isolator which has the same static displacement x_s . The damping parameter $\zeta = c/2m\omega_n$ is therefore *not* the equivalent damping ratio of the system, which can be defined as dependent on the natural frequency of the nonlinear system when linearized about its equilibrium position.

It is shown in chapter 3 that for small amplitudes of oscillation, a smaller initial angle of curvature achieves a smaller minimum tangent stiffness and hence better isolation. However, the nonlinear dynamics such as bending to the right of the frequency response curve can undermine the benefits of using small initial curvatures since they result in higher stiffness nonlinearity. Three initial curvature angles of 2°, 5°, and 15° are chosen to examine the dynamic response of the curved beam isolators.

It is assumed that the curved beam isolators are loaded to their minimum tangent stiffness position by the isolated mass which is considered to be the optimum static loading condition. For analysis purposes, the force-deflection curves are also transformed to have their origin at the minimum tangent stiffness position i. e. x in Figure 6-1 is measured from equilibrium position. The stiffness of the linear spring is normalized with the static stiffness of the optimally loaded curved beams. The non-dimensional force-deflection curves for the combination of curved beam and high stiffness spring (k_c) are shown in Figure 6-2 with dashed lines. The force-deflection curves are normalized by the force and displacement at the minimum tangent stiffness position of the combination of linear springs and curved beams, for consistency with the previous chapter. Stiffness k_c is chosen equal to 100 for these force-deflection curves. Such a high stiffness for the linear spring lessens the steepness of the curve around $x/x_s=-1$ to an imperceptible degree but sufficiently to ensure numerical convergence of the time domain solution.

Fitting a third order polynomial to the curved beam force-deflection curve is not possible in its whole range and so the system can be adequately modelled as a Duffing oscillator for sufficiently small oscillation. Thus a range, centred at statically loaded position, is chosen to fit the third order polynomial to it. The inclusion of a quadratic term in the fitted polynomial is to model asymmetry in the force-deflection about the statically loaded position. It is shown in the previous chapter that the quadratic term of a third order polynomial can be omitted by proper transformation of the axes. The new fit is in the form of the Duffing equation with an additional constant term which can be considered as a static preload.

The polynomial fits and the ranges over which they are fitted are shown in Figure 6-2 with dotted and solid lines respectively. The third order polynomial fits the force-deflection curve on the specified range but at displacements of about -1, where the stiffness is very high, the fits do not represent the true curves at all well. At large positive displacements, they also start to deviate from the exact solutions.

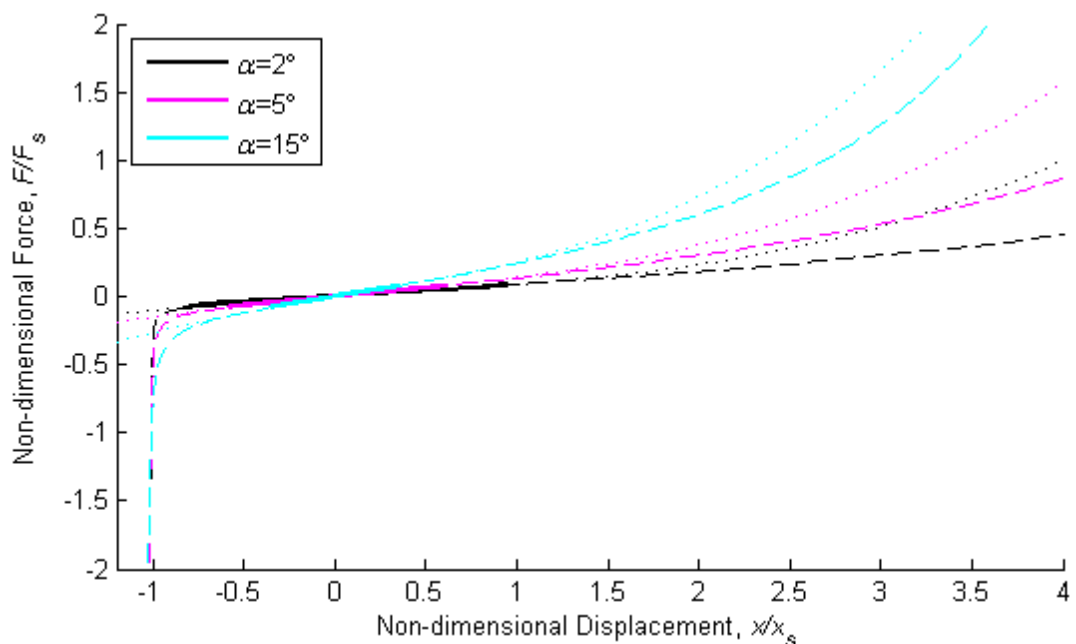


Figure 6-2: Non-dimensional force-deflection curve for curved beam isolator and polynomial third order fit for different initial angles and $k_c=100$, (Dashed line: exact solution of chapter 3, solid line: Range that data is fitted to, dotted line: Fitted third order polynomial)

The coefficients for the fits are shown in Table 6-1 alongside the corresponding coefficients when the equations are transformed to eliminate the quadratic terms where γ and κ are the cubic and linear stiffness respectively, f_0' is the constant arising from the transformation as given by equation (4) of chapter 5, and δ is the transformation of the axes. The cubic stiffness is small compared to the values used in the previous chapter while the linear stiffness is comparably large. Consequently, a lower level of nonlinearity is predicted for the fitted Duffing oscillator compared to the previous chapter. The coefficients of the transformed polynomial are used in the next section to find the dynamic response of this equivalent Duffing oscillator by the Harmonic Balance method.

Table 6-1: Coefficients of the fit of the form $ax^3 + bx^2 + cx = 0$ to the force-deflection of the curved beam isolator about its minimum tangent stiffness position and transformed polynomial of the form $z^3 + \kappa z = f_0'$, ($z=x+\delta$)

Initial curvature angle (degree)	Fitted polynomial			Transformed polynomial			
	a	b	c	γ	κ	f_0'	δ
2	0.0121	-0.0064	0.0814	0.0121	0.0803	-0.0142	-0.176
5	0.0178	-0.0048	0.1273	0.0178	0.1269	-0.0114	-0.089
15	0.0380	-0.0042	0.2223	0.0380	0.2221	-0.0082	-0.037

6.3 Forced response of a curved beam isolator

The polynomial fits obtained allow modelling the isolator as a Duffing oscillator with static preload for a small range in the vicinity of the statically loaded position. The harmonic balance method is applied to obtain the approximate forced response in a similar way to the previous chapter. A harmonic force with non-dimensional amplitude f_1 and non-dimensional frequency Ω is applied to the isolated mass. The response of the curved beam isolator is considered to be of the same form as before comprising a harmonic term at the excitation frequency with amplitude A_1 and a bias term, A_0 .

The approximate results are not expected to match the true response of the isolator for large amplitudes. To investigate this, the response of the isolator obtained by direct numerical integration is compared with the approximate solution. The time domain numerical integration is performed by using the ode45 function in Matlab in which the exact force-deflection of the curved beam isolator is used, as obtained in section 3.6. The amplitude of the response at the excitation frequency and the bias term of the response can be obtained from the steady state response by applying the Fast Fourier Transform.

The harmonic term of the response A_1 is shown at the top of Figure 6-3 for $f_1=0.01$, $\zeta=0.025$, and $k_c=100$. The coefficients of the approximate Duffing oscillators are given in Table 6-1 and the obtained results are shown by solid lines. The corresponding results from the time domain simulations are shown by the dots on the same graph. For this small amplitude of dynamic force (1 per cent of the weight of the isolated mass here), the isolator behaves similarly to a linear isolator. There is no unstable range nor any bending of the peak to the right or left. The Duffing oscillator can be seen to model the harmonic response of the system. The curved beams with smaller initial curvature angles provide better isolation compared to the isolator with higher initial angles due to lower tangent stiffness. The linear isolator with the same static deflection due to the isolated mass would have a non-dimensional natural frequency of unity. The peak frequency of the nonlinear isolator is well below unity in all three cases which is indicative of better isolation performance compared to the linear equivalent.

The bias term of the forced response for the same set of parameters is shown in bottom part of Figure 6-3. Solid lines represent results from the HBM for the approximate Duffing model where the coefficients are given in Table 6-1. The curves are corrected for transformation by δ which was introduced previously to eliminate the quadratic terms of the polynomial fits. As a result, bias term is measured from the minimum tangent stiffness position. The bias term of the response is very small comparing to harmonic amplitude of the response. The approximate model cannot predict the bias term which can be due to strong asymmetry in the force-deflection of the curved beam. The statically loaded position of the approximate Duffing model is different from that of the curved beam isolator due to the error in the polynomial fit. For a very small bias term, the difference becomes significant and the approximate model predicts a larger bias term.

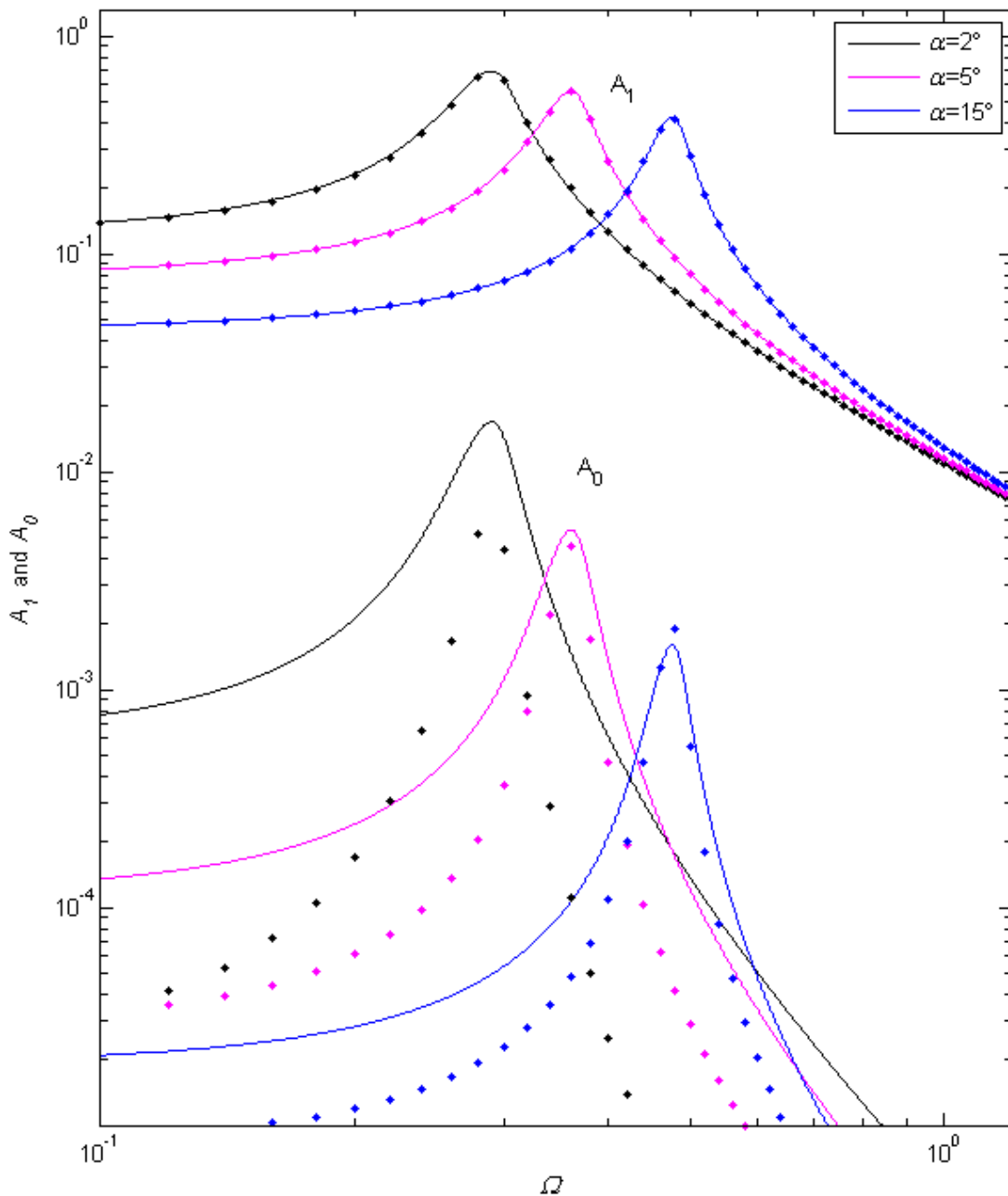


Figure 6-3: Harmonic term of forced response A_1 and bias term of forced response A_0 for curved beam isolator loaded to its minimum tangent stiffness position, $f_1=0.01$, $k_c=100$, and $\zeta=0.025$, approximate solutions from the HBM are obtained by using coefficients given in Table 6-1. (Solid line: approximate results, dots: accurate solution from the time domain simulation)

The effect of nonlinearity can be expected to become more apparent when increasing the harmonic load amplitude. The harmonic response term A_1 is shown in Figure 6-4 for $f_1=0.1$. The solid and dashed lines are obtained by the HBM for the approximate Duffing models (Table 6-1) and are the stable and unstable branches respectively. Dots represent the exact

response obtained from direct numerical integration with the correct force-deflection relation. The third order polynomial does not represent the curved beam isolator force-deflection for large amplitudes. As a result, the forced-response cannot be predicted from the approximate model at about resonance where the amplitude becomes large. The amplitude follows the resonance branch when increasing frequency and jumps down at the peak which is shown by the letter d on the graph. For decreasing frequencies, the amplitude follows the high frequency branch and then jumps up to the peak resonance branch which is indicated by the letter u on the graph.

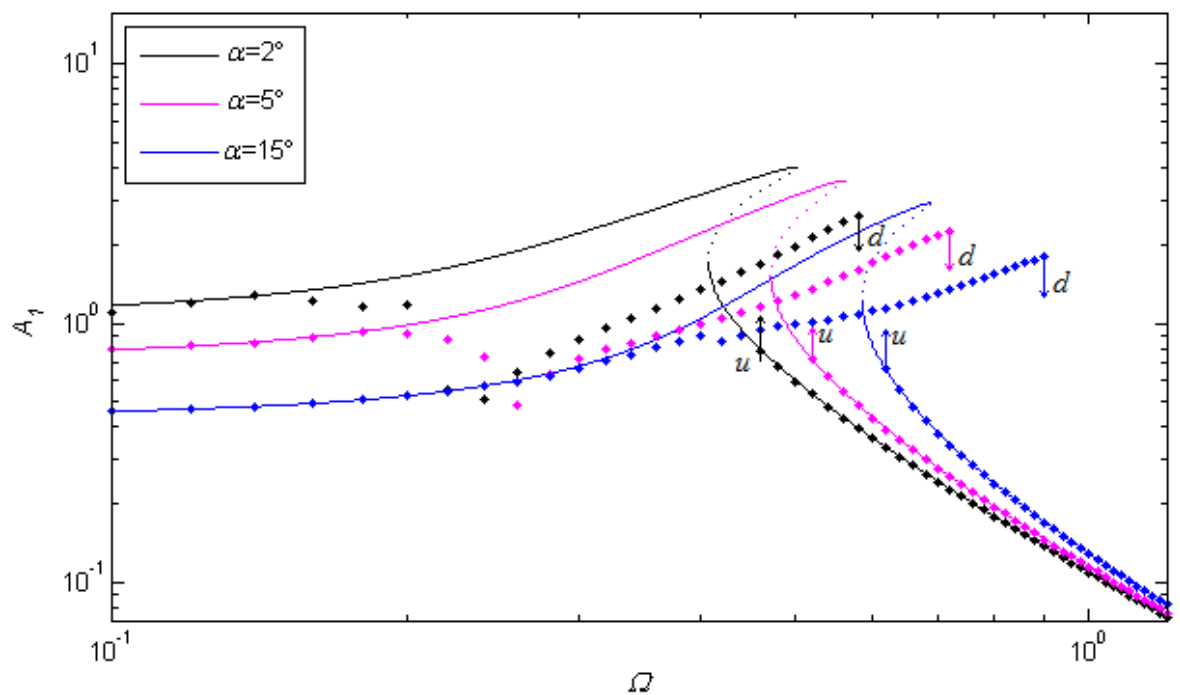


Figure 6-4: Harmonic term of forced response A_1 for curved beam isolator for $f_1=0.1$, $k_c=100$, and $\zeta=0.25$, (solid line: HBM results stable branch, dotted line: HBM results unstable branch, dots: time domain simulation)

It seems that the resonance branches of the exact solutions are different from those obtained from approximate Duffing models. The shift is due to the increased instantaneous stiffness at about the unloaded position which becomes effective at larger harmonic amplitudes. There is a transition range between the frequency at which the harmonic amplitude starts to deviate from the approximate solution until the frequency it begins to follow a different resonant branch.

The harmonic amplitude curve is shown again in Figure 6-5 for only an initial angle of 2° . The range at which transition happens is shown on the graph. The steady state time response of the same isolator is shown in Figure 6-6 for four different excitation frequencies Ω . At low excitation frequency, Figure 6-6 (a), the oscillation is almost sinusoidal where at its minima it flattens slightly due to the high stiffness range at a non-dimensional displacement of about -1, i.e. the unloaded position. The waterfall spectrum of the forced response is shown in Figure 6-7. It can be seen that the excitation harmonic is dominant, with the higher harmonics of the excitation frequency having very small amplitudes. At the higher excitation frequency of $\Omega=0.2$, see Figure 6-6 (b), the time history is not sinusoidal at a single frequency. The amplitude of the second harmonic is increased as can be seen in Figure 6-7.

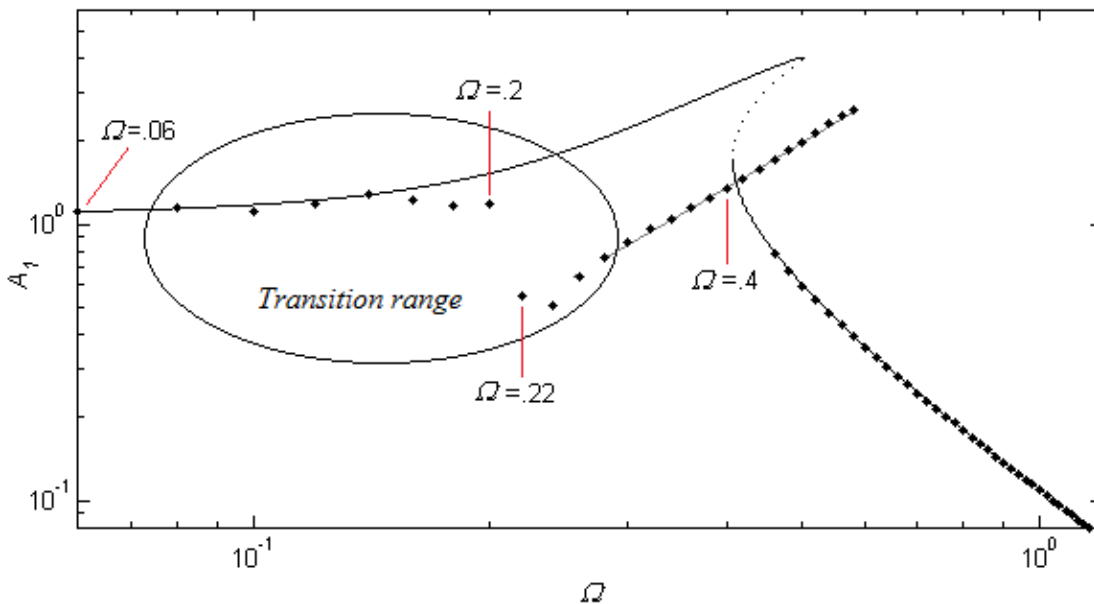


Figure 6-5: Harmonic term of forced response A_1 for curved beam isolator for $f_1=0.1$, $k_c=100$, $\zeta=0.25$, and $\alpha=2^\circ$, (black solid line: HBM results stable branch, black dotted line: HBM results unstable branch, ($\kappa=0.08$, $\gamma=0.0143$, $f_0=-0.019$), grey line: fitted line to the time domain data, dots: time domain simulation)

At a non-dimensional frequency Ω of 0.22, there is a sudden drop in harmonic amplitude. The time history of the oscillation for this excitation frequency is shown in Figure 6-6 (c). The second harmonic is at its peak at this frequency. By increasing the excitation frequency further, the shape of the response time history changes again, Figure 6-6 (d). This is the region which is shown by a grey line in Figure 6-5. The amplitude of the main harmonic keeps increasing by

increasing the frequency, while the amplitude of the second harmonic is almost constant in this range (Figure 6-7). The shape of the time history remains the same up to the jump down frequency. At a non-dimensional frequency of 0.6 the amplitude of the main harmonics jumps down and the higher harmonics disappear, where for small amplitudes it becomes a linear like oscillation.

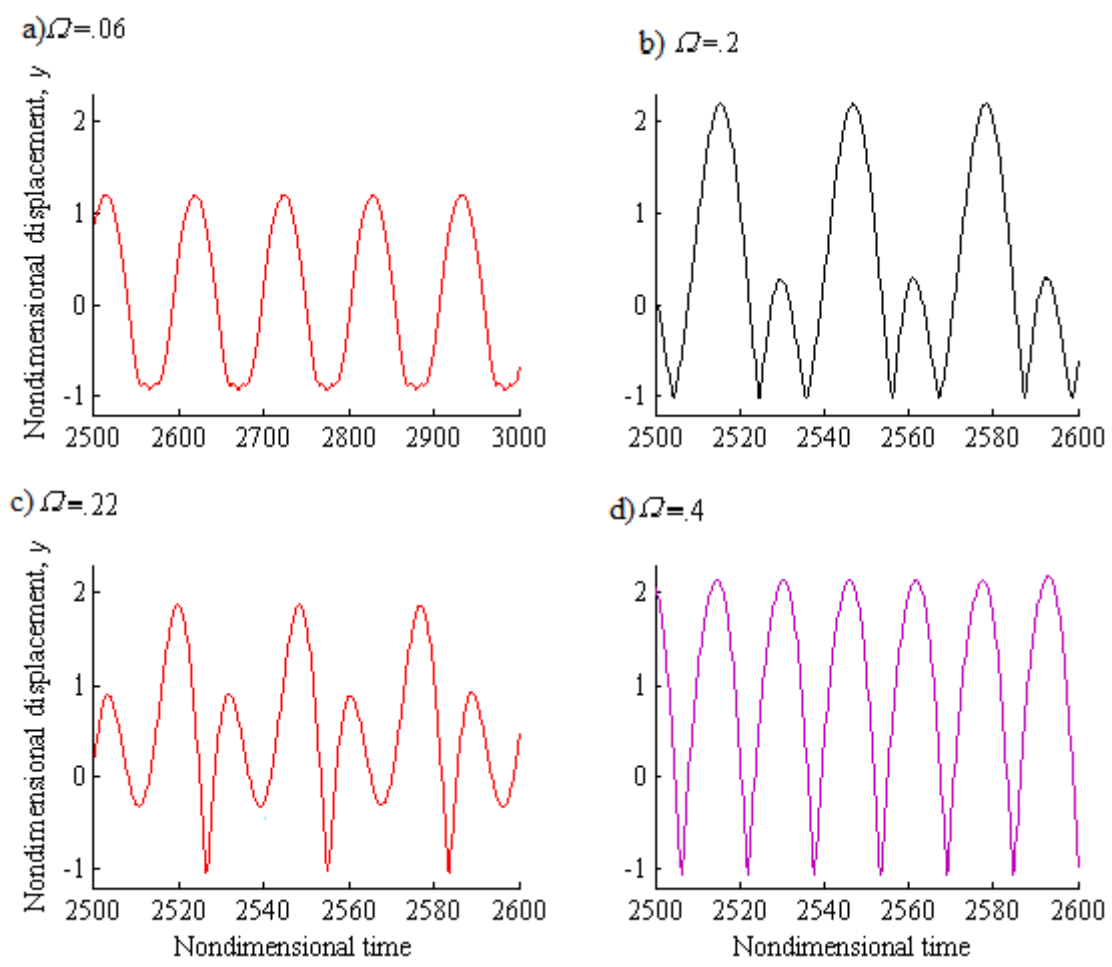


Figure 6-6: Curved beam isolator oscillation time history (exact time domain solution) for $\alpha=2^\circ$, $f_1=0.1$, $\zeta=0.025$, and $k_c=100$, dashed line: applied harmonic force

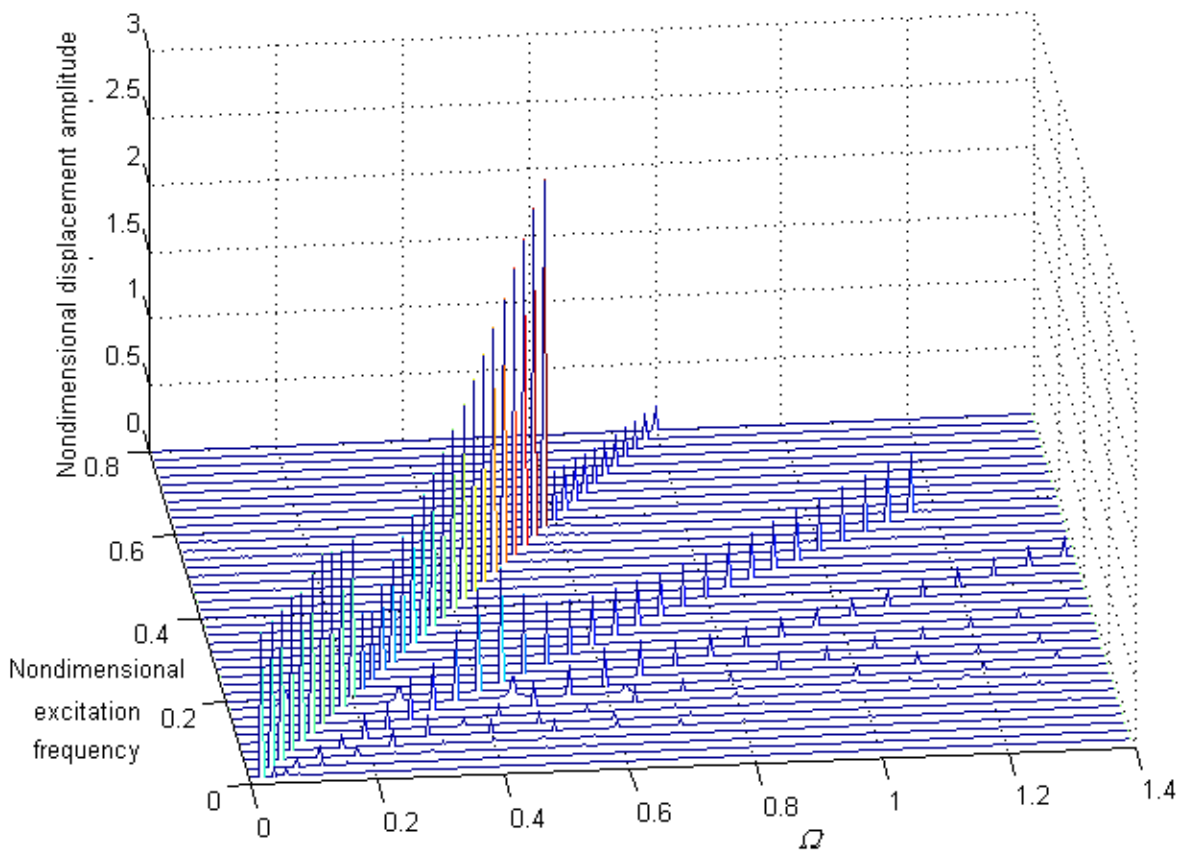


Figure 6-7: waterfall spectrum of forced response for curved beam isolator for $f_1=0.1$, $k_c=100$, $\zeta=0.25$, and $\alpha=2^\circ$

The bias term of the forced response is shown in Figure 6-8 for $f_1=0.1$. The coefficients for the approximate Duffing oscillator are given in Table 6-1 for the results shown on this graph. The Duffing oscillator model does not match with the frequency response from the exact solution here either. The strong asymmetry in the force-deflection at negative displacement shifts the centre of oscillation further into the deformed region while there is not such a high stiffness as the fitted third order polynomial. At high frequencies, the obtained bias term by the approximate solution is larger than the exact solution in the time domain due to the poor polynomial fit.

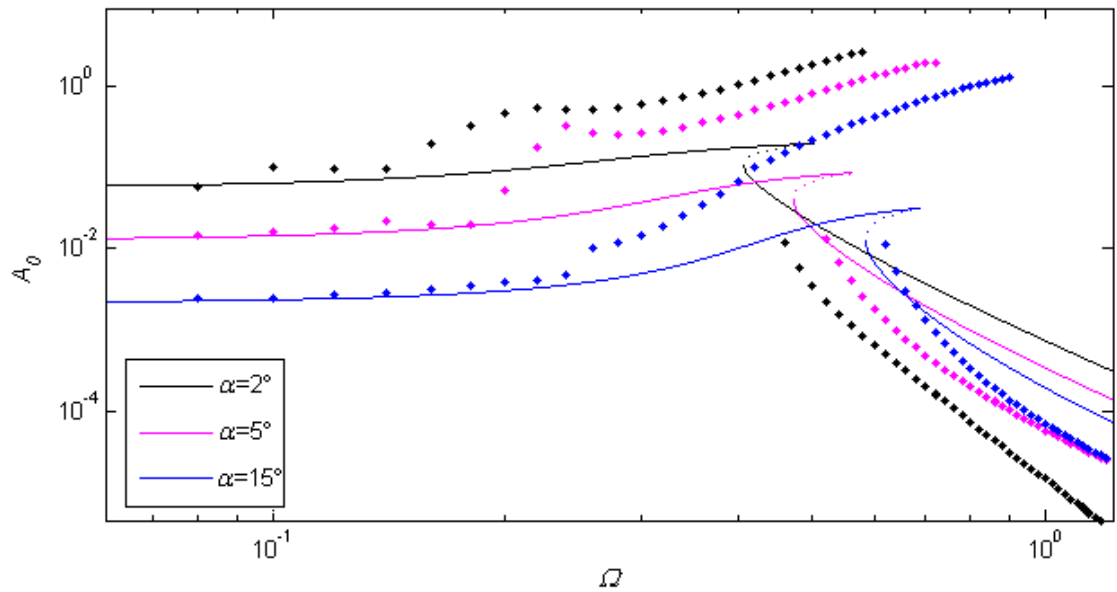


Figure 6-8: Bias term of forced response A_0 for the curved beam isolator for $f_1=0.1$, $k_c=100$, and $\zeta=0.25$, (The coefficient for approximate Duffing oscillator is given in Table 6-1, solid line: Approximate model, stable branch, dotted line: approximate model, unstable branch, dots: exact model)

6.4 Curved beam isolator loaded statically

The curved beam isolator is assumed to be loaded to its minimum tangent stiffness position in the previous section. A vibration isolator might not be loaded to its optimum position in practice due to a static preload or a mistuned mass. The effect of applying a static preload is investigated in this section to obtain the forced response of a nonlinear vibration isolator with suboptimal static loading.

The curved beam isolator is modelled by a Duffing oscillator with a static preload in the previous section where the static preload appeared due a coordinate transformation to eliminate the quadratic term of the fitted polynomial. An actual static preload, f_s , is applied to the mass in this section. A third order polynomial is fitted about this statically loaded position. The quadratic term of the fitted polynomial is again eliminated by appropriate axis transformation. As a result of this transformation, a constant is introduced in the equation which is also treated as a static load. The static preload that appears in the Duffing oscillator forced response model

is the sum of the applied static preload f_s and the constant appearing due to the axis transformation, and are shown by f_0 in this section.

The effect of static preload on the curved beam isolator with initial curvature angle of 2° is investigated here. It is shown in the previous section that a smaller initial curvature angle provides a lower jump down frequency which is desirable in a vibration isolator. The harmonic terms of forced response of the curved beam isolator are shown in Figure 6-9 for different positive static preloads. The coefficients that have been used to obtain the approximate response for the Duffing oscillator model are shown in Table 6-2.

Table 6-2: Coefficients of the Duffing oscillator model ($\ddot{x} + 2\zeta\dot{x} + \kappa x + \gamma x^3 = f_1 \cos(\Omega t) + f_0$) of the curved beam isolator with initial curvature angle α of 2° , $k_c=100$

f_s	κ	γ	f_0	δ (axis transformation)
0	.08	0.0143	-0.019	-0.238
0.1	0.09	0.004	0.039	-0.768
0.2	0.08	0.0013	0.249	-0.612
0.4	0.1	0.0022	0.336	-0.835

The mass moves further into the deformed region by increasing the static preload which results in an increased separation between the statically loaded position and the high stiffness region near the unloaded position. Thus higher amplitudes of response are achievable before straying into the high stiffness region where the Duffing oscillator model cannot predict the response of the isolator. It can be seen in Figure 6-9 that for larger statically preloaded isolators the deviation from the Duffing oscillator model occurs for comparably larger amplitudes of oscillation. Also, a larger amplitude of response is possible before the high stiffness region controls the motion in the extensional direction.

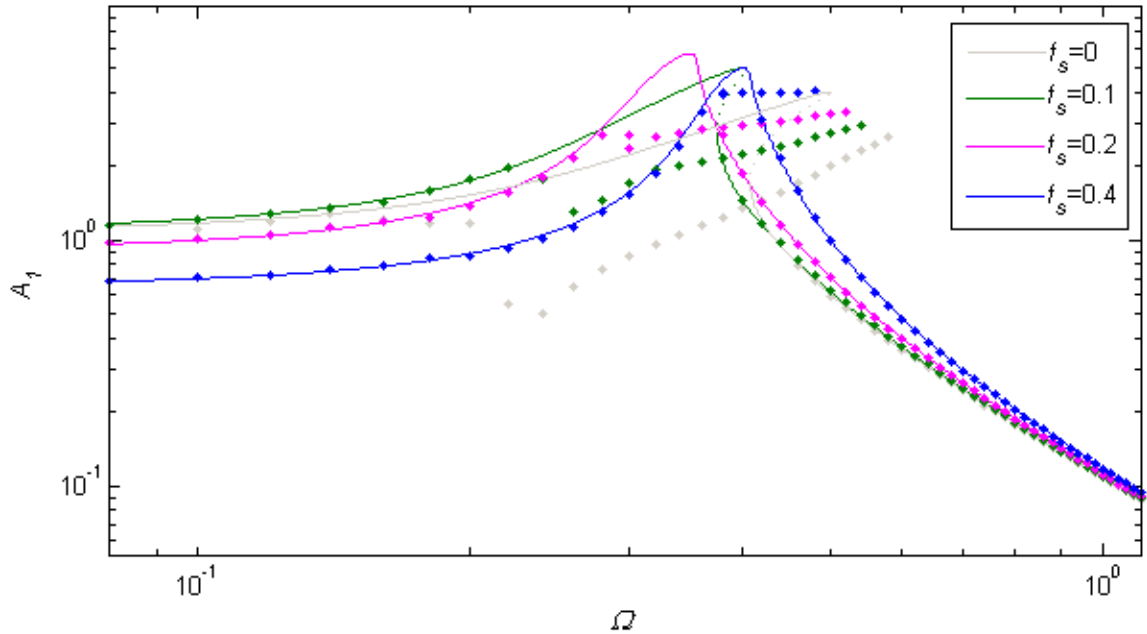


Figure 6-9: Harmonic term of forced response for curved beam isolator with initial curvature angle $\alpha=2^\circ$ for different static loads f_s , $f_1=0.1$, $k_c=100$, and $\zeta=0.025$, (solid line: approximate model, stable branch, dotted line: approximate model, unstable branch, dots: exact model)

The bias term of the forced response is shown in Figure 6-10. The coefficients for the approximate Duffing model are given in Table 6-2. The bias increases with static preload as expected. The approximate Duffing oscillator model predicts a trough at the resonance for the bias term which is explained in the previous chapter in section 5.4.1. However, the bias term obtained from the exact solution in the time domain increases at about resonance due to strong asymmetry in the force-deflection curve. The high stiffness of the beam in tension acts as a rigid-end stop and shifts the centre of oscillation further into the deformed region. As a result the bias term increases for large amplitudes.

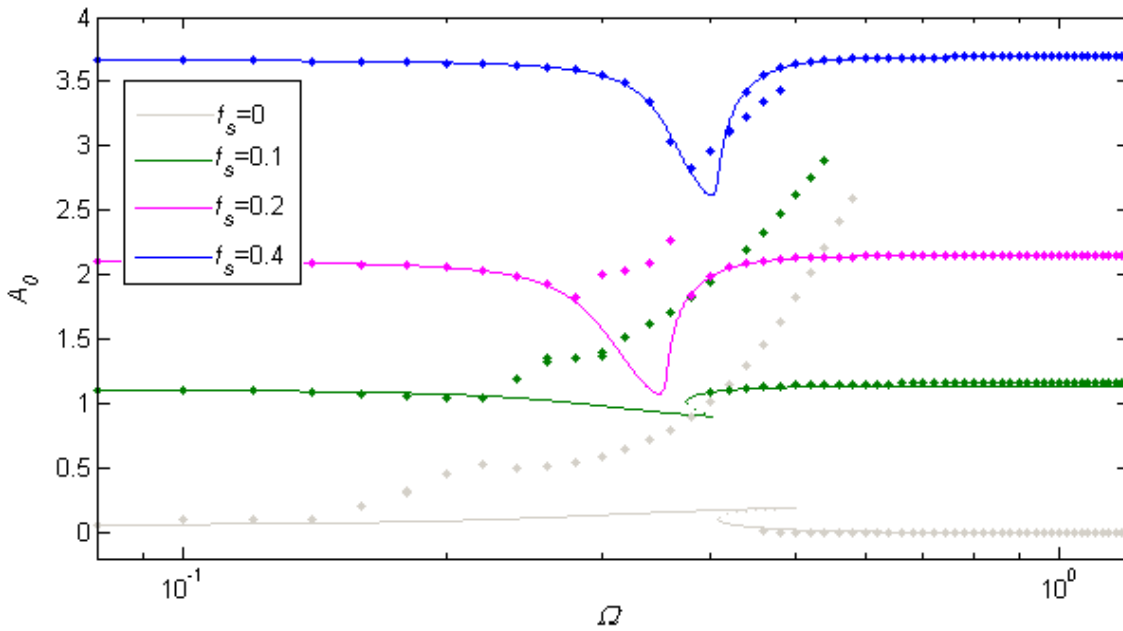


Figure 6-10: Bias of forced response for the curved beam isolator with initial curvature angle of 2° for different static preloads f_s , $f_1=0.1$, $k_c=100$, and $\zeta=0.025$, (solid line: approximate model, stable branch, dotted line: approximate model, unstable branch, dots: exact model)

6.5 Force transmissibility of a curved beam isolator

The force transmissibility is used to assess the performance of the curved beam isolator in reducing the transmitted force. The transmitted force can be considered as a combination of a harmonic force at the excitation frequency and a static component. In the previous chapter, it is shown how the transmissibility of a Duffing oscillator with a static preload can be obtained and the effect of different parameters on it investigated. The same method can be applied here by using the polynomial fit to approximate the curved beam to a Duffing oscillator. The results are compared with exact results obtained by the time domain simulations of the curved beam isolator using the exact force-deflection relation.

The force transmissibility obtained by both the approximate and exact models are shown in Figure 6-11 for three different initial curvature angles and a non-dimensional forcing amplitude of 0.01. The coefficients for the approximate Duffing oscillator model are given in Table 6-1. For small oscillations, the isolator can be modelled by a linear oscillator with the same stiffness as the tangent stiffness as at the statically loaded position. The force transmissibility of the curved beam is, as one might expect, very similar to that of a linear system and there is no

unstable region and no jump down and jump up frequencies. The smaller the initial angle, the lower is the minimum tangent stiffness and thus the isolation occurs at lower frequencies. The isolation frequency (where transmissibility drops below unity) for the curved beam isolator with initial curvature angle of 2° occurs at a non-dimensional frequency of about 0.4, which is just over one quarter of the isolation frequency for a linear isolator which possesses the same static deflection due the isolated mass.

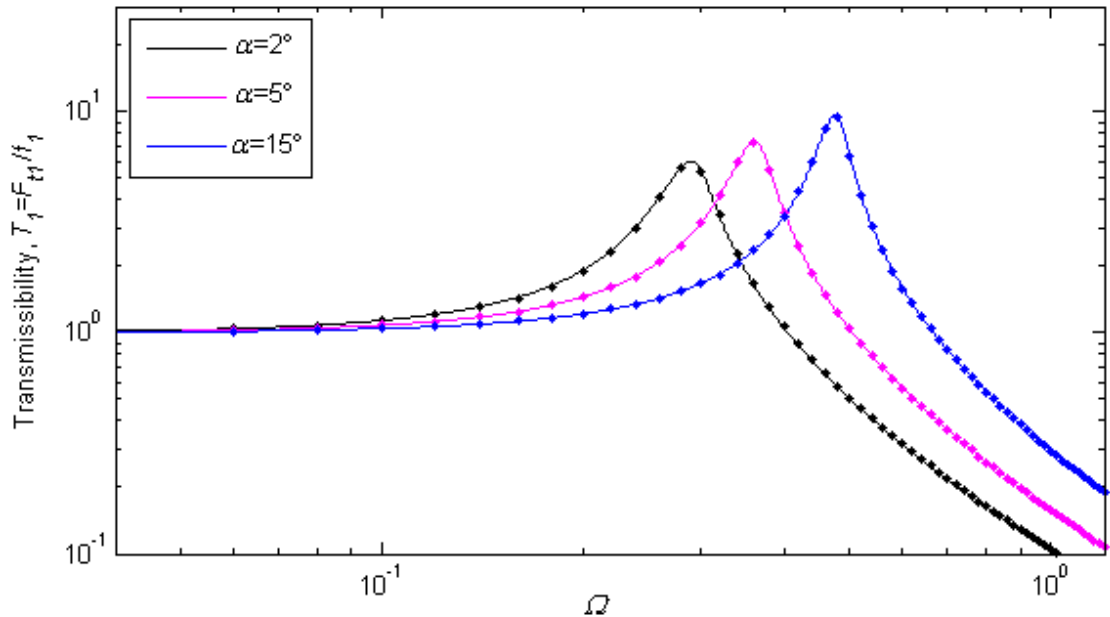


Figure 6-11: Transmissibility as a function of non-dimensional frequency Ω for the curved beam isolator with three different initial angles α , for $\zeta=0.025$ and $f_1=0.01$, $k_c=100$, solid lines: approximate solution (coefficients for Duffing oscillator model is given in Table 6-1), dots: results of exact model

The force transmissibility of the same set of curved beam isolators for a harmonic load of 0.1 is shown in Figure 6-12. The Duffing oscillator model cannot predict the transmissibility at frequencies for which the amplitude of vibration is large. The jump-down frequency is shifted to the right for larger initial curvature angles. The transmissibility at jump-down is also larger for higher initial curvature angle which is the reverse of what was observed for the forced response in section 6.3 (the transmissibility is also proportional to frequency due to force being transmitted through the damper). Because of the strong nonlinearity and bend to the right, the jump down frequency defines the isolation frequency. For initial curvature of 2° and non-dimensional force of 0.1, the jump down frequency is about 0.6 is still less than half of $\sqrt{2}$ which is the isolation frequency of the comparable linear isolator with the same static deflection due to the isolated mass.

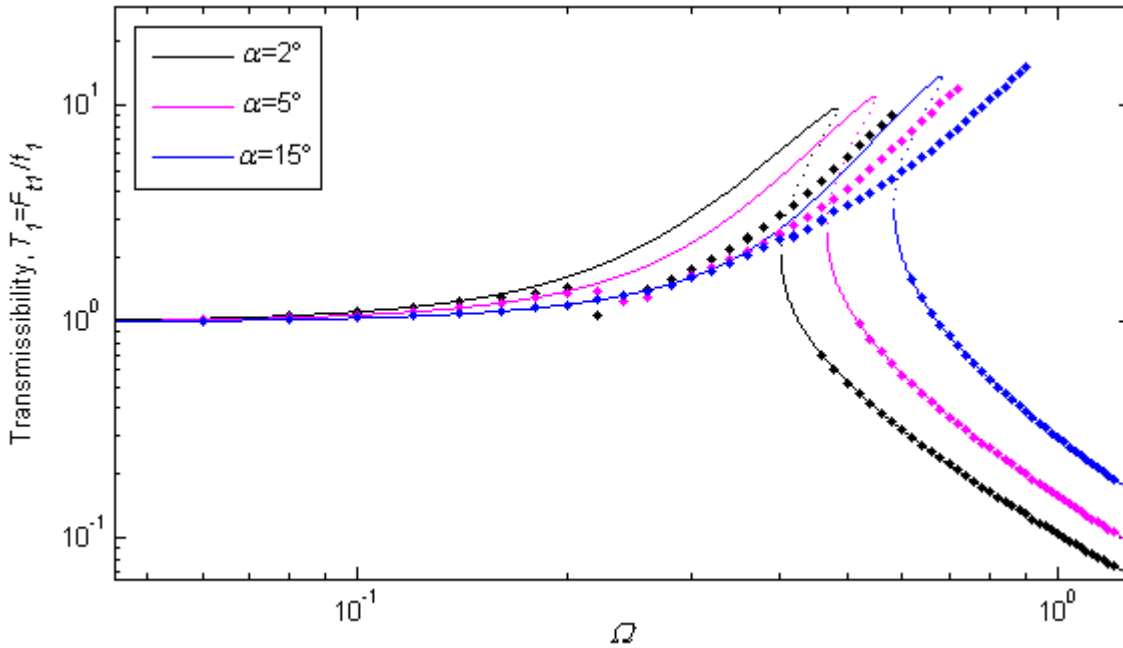


Figure 6-12: Transmissibility as a function of non-dimensional frequency Ω for the curve beam isolator with three different initial angles α , for $\zeta=0.025$, $f_1=0.1$, $f_s=0$, and $k_c=100$, (Parameters for approximate solution from Table 6-1) solid lines: approximate solution stable branch, dotted lines: approximate solution unstable branch, dots: results of exact model of the time domain simulation

The effect of static preload on the forced response of the curved beam isolator with initial curvature angle of 2° is shown in the previous section. The transmissibility for the isolator with the same set of parameters is shown in Figure 6-13. The jump down occurs at lower frequencies for larger values of static preload f_s and as a result achieves a lower frequency of isolation. In this respect, one might conclude that the minimum stiffness position is not the optimal working position when large dynamic loads are considered. However, the extra deflection due to static load is not considered in normalising the parameters that are used to obtain this graph and only the deflection due to the weight of the isolated mass is used for normalising. By considering the static deflection due to both of weight of the mass and the static force, a new set of transmissibility curves are obtained and are shown in Figure 6-14. The isolators are now compared in such a way that all of them have the same static deflection. The dynamic load level is also adjusted to have the equivalent amplitude of $f_1 = 0.1$ for the unloaded isolator. It can be seen that the jump down frequency occurs at a higher frequency for larger static load f_s . The performance of the isolator is poorer with static preload when the extra static deflection due to the preload is considered in normalising the parameters.

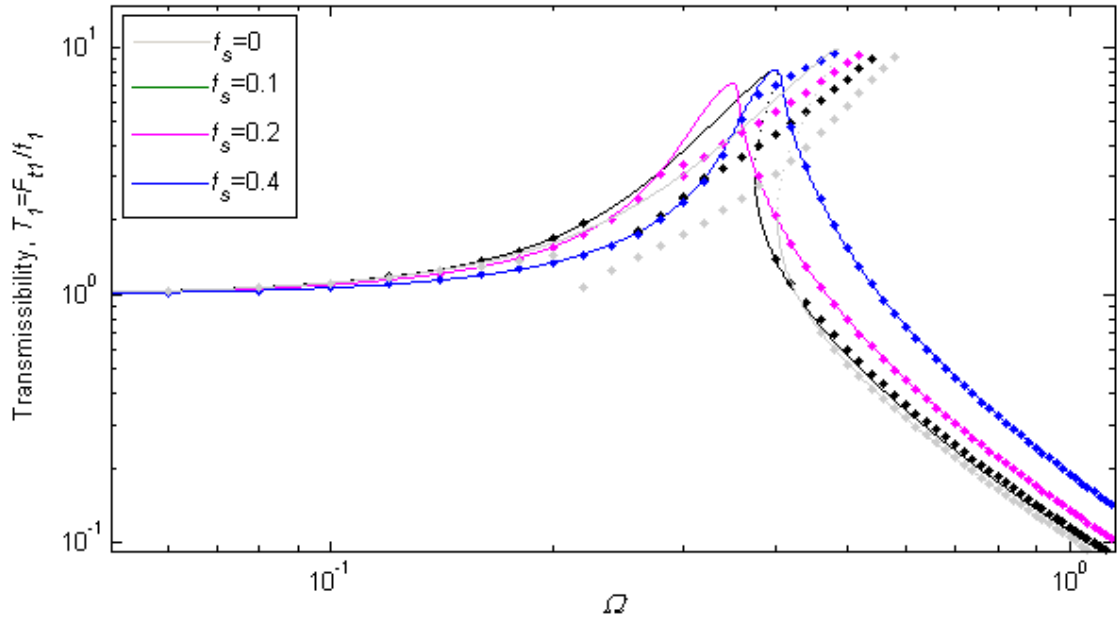


Figure 6-13: Force transmissibility for curved beam isolator with initial curvature angle $\alpha=2^\circ$ for different static preloads f_s , $f_1=0.1$, $k_c=100$, and $\zeta=0.025$, parameters for approximate Duffing oscillator are given in Table 6-2 (solid line: approximate results stable branch, dotted line: approximate results unstable branch, dots: exact results of the time domain simulation)

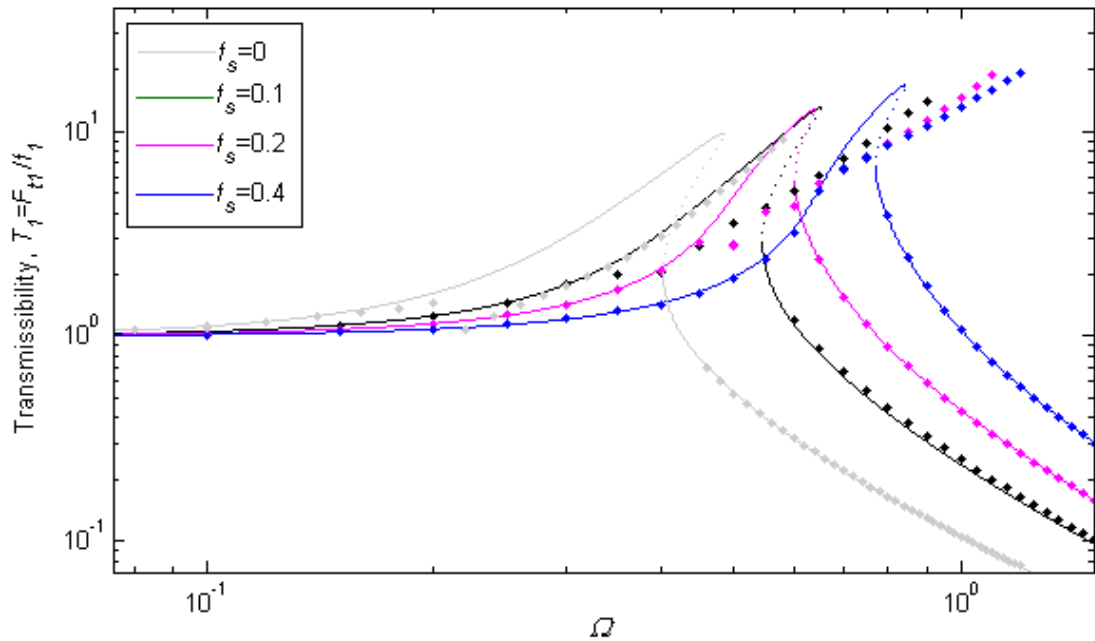


Figure 6-14: Force transmissibility for curved beam isolator with initial curvature angle $\alpha=2^\circ$, (isolators are normalised with the total static deflection and dynamic load, f_1 , is adjusted to have the equivalent dynamic force of $f_1=0.1$), for different static preloads f_s , $k_c=100$, and $\zeta=0.025$, (solid line: approximate results stable branch, dotted line: approximate results unstable branch, dots: exact results of the time domain simulation)

6.6 Transmitted force in the time domain

The force transmissibility of the isolator presented in the previous section considers only the component of the response at the excitation frequency. However, it is important to investigate the existence of any other harmonic in the response of the system. The time history of the transmitted force of the curved beam isolator with an initial angle of 2° for an excitation frequency of 0.58, which is the jump-down frequency, is shown in Figure 6-15. There is a narrow trough in each cycle of very large absolute value. This is caused by the high beam's stiffness for negative displacement about a non-dimensional displacement of -1. The existence of this trough makes it extremely undesirable to implement the isolator with the same set of parameters in practice even though the transmitted force component at the excitation frequency is limited.

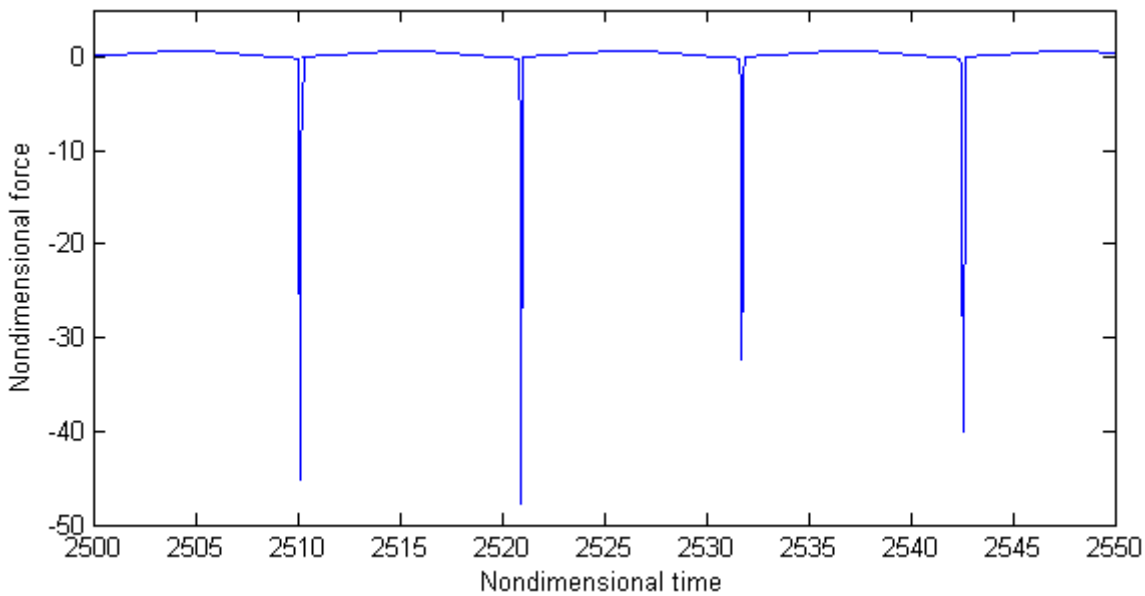


Figure 6-15: Time history of transmitted force through curved beam isolator for excitation frequency of 0.58 for $\alpha=2^\circ$, $f_1=0.1$, $\zeta=0.025$, $f_s=0$, and $k_c=100$

The total harmonic distortion (THD) is a measure of the contribution of harmonics to the overall response [84, 85] and is defined as,

$$\text{THD} = \frac{\sum_{i=2}^N A_i^2}{A_1^2} \quad (6-3)$$

where A_1 is the amplitude of the fundamental, A_i are the amplitudes of the harmonics, and N is the number of harmonic components included. The amplitude is obtained by applying FFT on a cycle at excitation frequency and N is chosen equal to 200. The THDs are shown in Figure 6-16 for three different initial curvature angles. The solid line is produced by increasing the frequency and the dashed line by reducing the frequency. The two lines match except the frequency range between jump-up and jump-down. There are also some disagreements between curves for increasing and decreasing frequency for example at a non-dimensional frequency of about 0.4 for $\alpha = 15^\circ$. This is due to the existence of subharmonics which are not considered in obtaining the THD. The excitation frequency is the dominant frequency in most of the range for all three different initial curvature angles. The only exception is at a non-dimensional frequency of 0.2 where the second peak in the time history exists, as shown previously in Figure 6-6. At high frequencies, the oscillation becomes sinusoidal and the THD is almost zero.

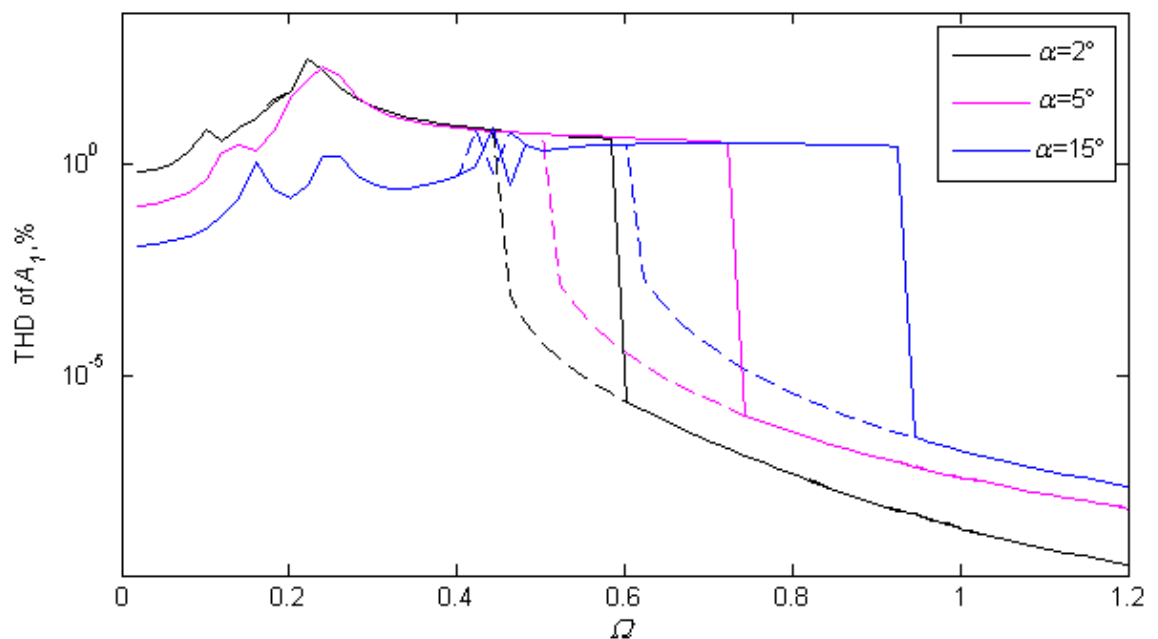


Figure 6-16: Total Harmonic Distortion (THD) of harmonic term of forced response A_1 in per cent as a function of non-dimensional frequency for $f_1=0.1$, $\zeta=0.025$, $f_s=0$, $k_c=100$, (solid line: increasing frequency, dashed line decreasing frequency)

The total harmonic distortion for the transmissibility of the curved beam isolator with static preload is shown in Figure 6-17. The existence of other harmonics due to the narrow deep trough in the time history of the transmitted force makes its THD significantly larger than the THD of the harmonic term A_1 . In the case of forced response, the high stiffness for negative

displacements limits the amplitude of oscillation. However, in the case of force transmissibility, the force is transmitted to the base at other frequencies in addition to the excitation frequency.

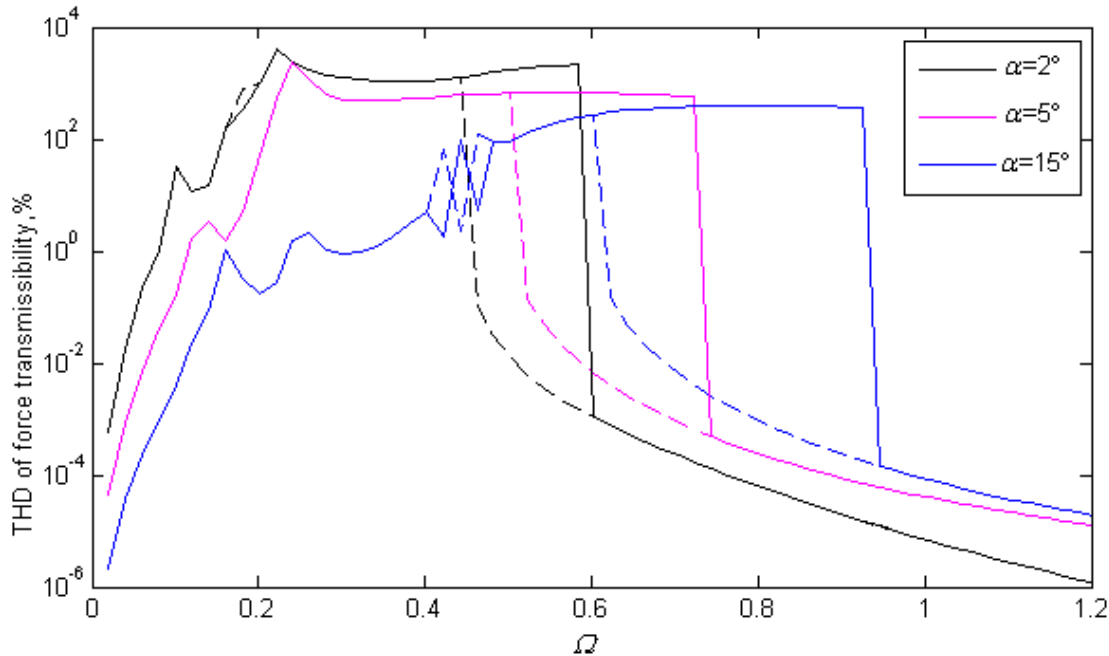


Figure 6-17: Total Harmonic Distortion (THD) of force transmissibility in per cent as a function of non-dimensional frequency for $f_1=0.1$, $\zeta=0.025$, $f_s=0$, $k_c=100$, (solid line: increasing frequency, dashed line: decreasing frequency)

The high stiffness about the statically unloaded position can be controlled by the stiffness of the linear springs. The non-dimensional stiffness k_c of the linear springs is chosen to be unity in the following analysis, i.e. the stiffness of the linear spring is equal to the static stiffness of the curved beam at its optimal position. The force deflection curve of the curved beam isolator is shown in Figure 6-18 for $\alpha=2^\circ$, $k_c=1$ and $k_c=100$. The force-deflection is normalized by force and displacement at the minimum tangent stiffness position of the combined system of the curved beam and the linear spring. The stiffness at negative displacements towards the unloaded position is linear and is controlled by the linear spring while at the optimally loaded position it is controlled by the curved beam with low tangent stiffness. The stiffness at negative displacements is reduced considerably at a cost of increasing the minimum tangent stiffness of the isolator for $k_c=1$.

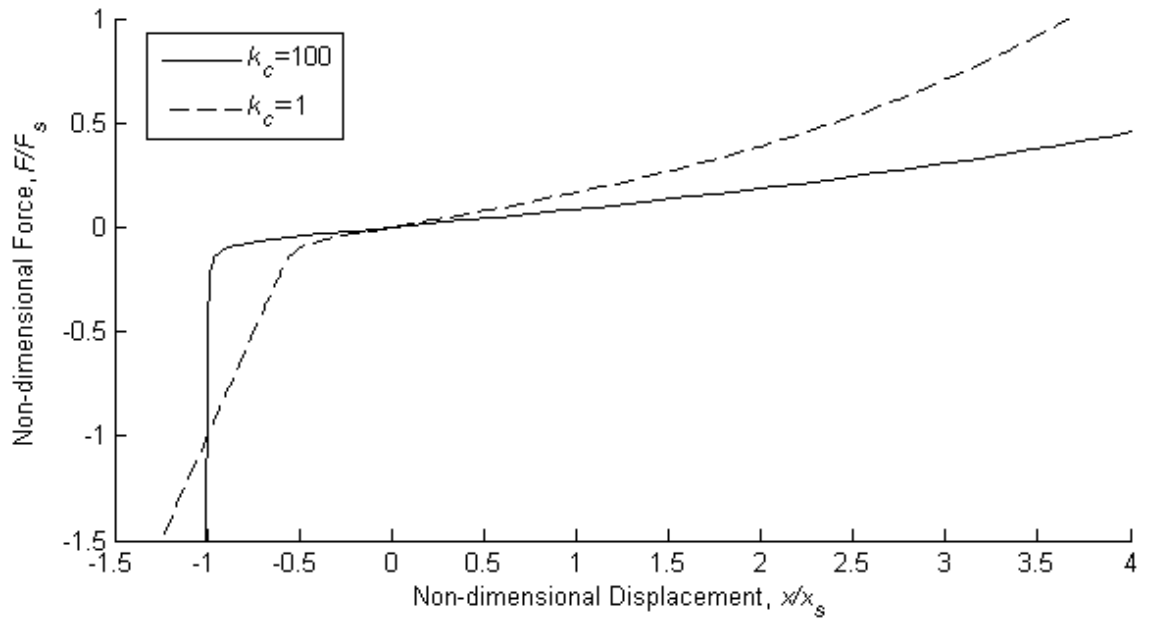


Figure 6-18: Non-dimensional force-deflection curve of the curved beam isolator for initial curvature angle $\alpha=2^\circ$

The harmonic amplitude of the forced response of the curved beam isolator is shown in Figure 6-19 for two different values of linear spring stiffness, $k_c=1$ and $k_c=100$. The coefficients for the approximate Duffing oscillator model for this graph are given in Table 6-3. The amplitude A_1 is smaller for k_c equal to unity at low frequency due to the increased tangent stiffness. The jump down frequency has increased to a non-dimensional frequency of 0.68 whereas it was 0.58 for the isolator with k_c equal to 100. At high frequencies, the two curves approach each other asymptotically where the oscillation is mass controlled.

Table 6-3: Coefficient of the Duffing oscillator model ($\ddot{x} + 2\zeta\dot{x} + \kappa x + \gamma x^3 = f_1 \cos(\Omega t) + f_0$) of the curved beam isolator with initial curvature angle α of 2°

k_c	κ	γ	f_0	δ (axis transformation)
1	0.15	0.0694	-0.014	-0.095
100	0.08	0.0143	-0.019	-0.238

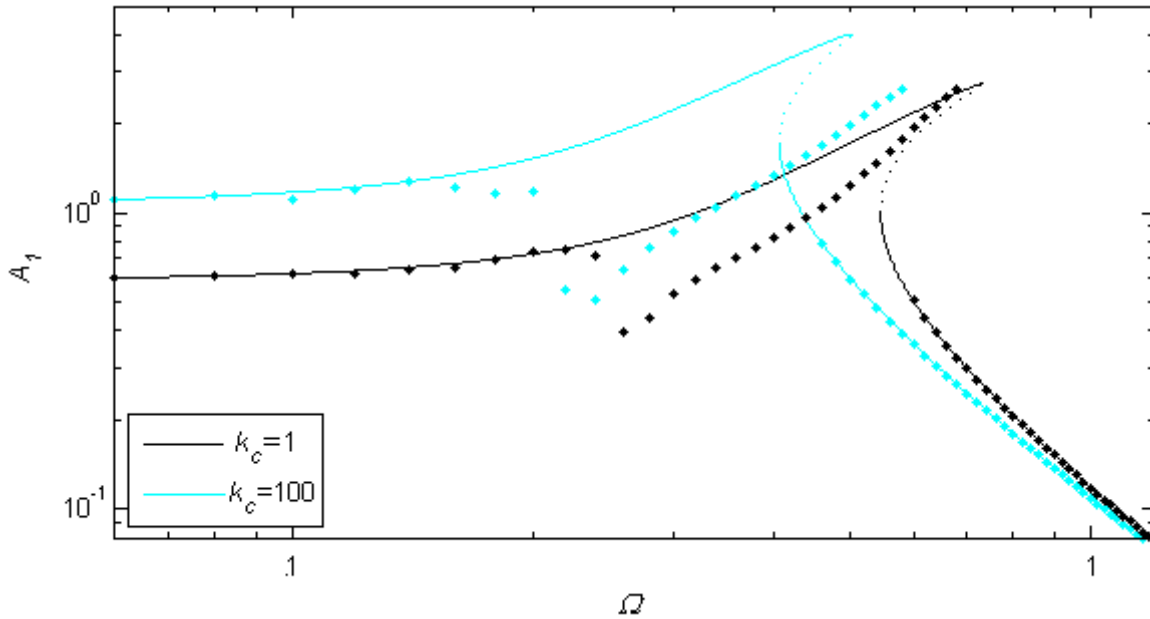


Figure 6-19: Harmonic term of forced response A_1 for curved beam isolator for $\alpha=2^\circ$, $f_1=0.05$, $f_s=0$ and $\zeta=0.25$, (Approximate Duffing model of Table 6-3; solid line: approximate solution stable branch, dotted line: approximate solution unstable branch, dots: time domain simulation)

The transmissibility curve of the curved beam isolators for two different linear spring stiffness values, $k_c=1$ and $k_c=100$, are shown in Figure 6-20. The coefficients for the approximate Duffing oscillator model are given in Table 6-3. The transmissibility of the linear isolator with the same static deflection due to the mass is also shown in the same figure by the dotted-dashed line. The jump-down frequency increased to 0.68 for the curved beam isolator with k_c equal to unity. It is also the isolation frequency of the curved beam isolator. Compared to the linear isolator with the same static deflection, the isolation frequency of the curved beam isolator is still less than half of the linear one. After jump down, the transmissibility of the curved beam isolators is lower than the linear isolator while the one with a smaller linear spring stiffness k_c has higher transmissibility. At a non-dimensional frequency of $\sqrt{2}$ which is the isolation frequency of the linear isolator and is shown by dotted line on the graph, the transmissibility of the curved beam isolator with k_c equal to unity is smaller than one tenth of the linear one.

Were the transmissibility curves plotted to high frequencies, e.g. $\Omega \sim 100$, one would see that they converge to the same asymptote of the transmissibility of the equivalent linear isolator ($T = 2\zeta/\omega$). This is because of the fixed damping ratio for the equivalent linear system. However, the effective damping ratio of the nonlinear system depends on resonance frequency.

In practice, one might instead employ lighter damping for the nonlinear isolator in order to maintain an acceptable resonant response while reducing the transmission at high frequencies.

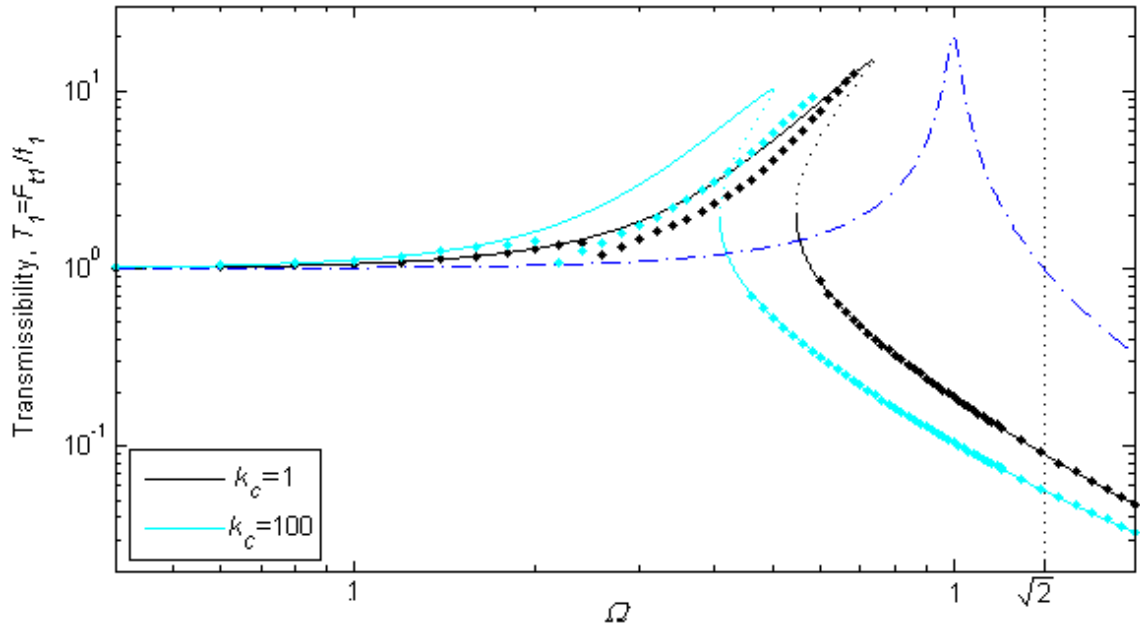


Figure 6-20: Transmissibility as a function of non-dimensional frequency Ω for the curved beam isolator with two different linear springs stiffness k_c , for $\zeta=0.025$, $f_1=0.1$, $f_s=0$, (Approximate Duffing model of Table 6-3; solid line: approximate solution stable branch, dotted line: approximate solution unstable branch, dotted-dashed line: linear isolator with the same static deflection due to the isolated mass)

The time history of a few cycles of the transmitted force for the curved beam isolator and the linear isolator with the same static deflection are shown in Figure 6-21. The stiffness of the linear springs of the curved beam isolator is equal to unity. The non-dimensional excitation frequency for which the time history of the curved beam isolator is produced is chosen equal to 0.68 which is the jump down frequency of the curved beam isolator. There is still a dip in the time history of the transmitted force of the curved beam isolator but its absolute value has decreased to a more acceptable level.

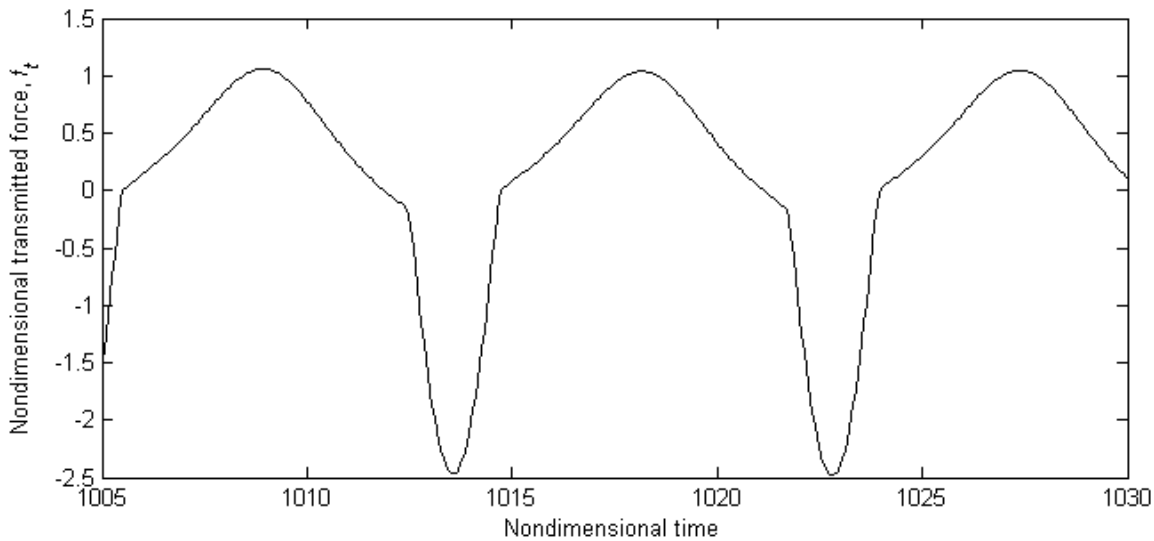


Figure 6-21: Steady state time history of the transmitted force of the curved beam isolator at non-dimensional frequency $\Omega = 0.68$ for $k_c = 1$, $\zeta = 0.025$, $f_1 = 0.1$, and $f_s = 0$

6.7 Conclusions

The nonlinear dynamics of a curved beam vibration isolator are investigated in this chapter to assess its performance in isolating harmonic forces. A mass on the curved beam isolator is modelled as a single degree of freedom system whose spring is nonlinear and has the force-deflection of the curved beam as obtained in chapter 3. The model of the curved beam isolator is slightly modified by adding a linear spring in series to overcome a convergence problem in the time domain simulations due to the high stiffness range about the unloaded position and beyond that in extension. A third order polynomial was fitted to the force-deflection curve to model it as a Duffing oscillator for small displacements about the statically loaded position. The HBM is used to obtain the approximate response of the Duffing oscillator model. The exact solutions are obtained by time domain simulations using the true force-deflection relation of the curved beam.

Three initial curvature angles of 2, 5 and 15 degrees are chosen and the isolators comprised of them are compared. The isolators are assumed to be loaded to their minimum tangent stiffness position and the response at the excitation frequency is considered. The approximate model fails to predict the response for large amplitudes near resonance. The frequency response curves are of a hardening type which bends to the right and there is a jump frequency in the FRCs. It is

revealed that the curved beam isolators with smaller initial curvature angles have lower jump down frequencies.

The bias term is almost zero up to the frequency range around resonance. The sudden change in tangent stiffness at about the statically unloaded position performs as a rigid-end stop and prevents the movement of the mass in the negative direction for large amplitudes. It forces the centre of oscillation further into the deformed range which results in a large bias at about resonance.

The effect of additional static preload on the forced response and force transmissibility of the curved beam isolator is explored as a breach of the optimum working condition. The positive static preload moves the mass further into the deformed region away from the high stiffness end. The jump down frequency decreases with increasing static preload. Because of the bend to the right in the transmissibility curve, the jump down frequency is a measure of the performance of the isolator, and one may argue that the preloaded isolator is better. However, the extra deflection due to static load is not accounted for in the normalisation. By considering this extra deflection, i.e. comparing the isolator with the same static deflection at the loaded position, it is observed that the isolator loaded to the minimum tangent stiffness position outperforms the others.

In time history of the transmitted force a dip with very large absolute value appears due to the high tangent stiffness in effect at about the unloaded position. The existence of such a dip introduces other harmonics in the frequency response and its large absolute value is undesirable. The difficulty is overcome by reducing the stiffness of the linear springs to a value comparable to the static stiffness of the curved beam at their optimum position. A curved beam in series with a linear spring outperforms a linear isolator with the same static deflection.

Overall, it may be concluded that a nonlinear isolator with strong asymmetry in its force-deflection curve can have a better isolation performance than a linear one providing that the tangent stiffness is limited. The smaller minimum tangent stiffness provides better isolation. The mass should be chosen to load the isolator to its minimum tangent stiffness position. The nonlinear isolator can accommodate static preloads but the resulting static deflection is undesirable and larger than the corresponding linear isolator.

7 Concluding remarks and future works

The performance of vibration isolators with nonlinear stiffness characteristics has been investigated in this thesis. A static analysis of mechanisms that can be used to achieve desirable stiffness characteristics has been presented. The Duffing oscillator with static preload or mistuned mass was considered as a nonlinear vibration isolator with asymmetric stiffness and its nonlinear dynamic response has been investigated in order to evaluate its performance. In the last part of the thesis, the nonlinear dynamics of a vibration isolator comprising of curved beams was studied to assess its performance. The main conclusions from this work are as follows:

A mechanism called a *snap through mechanism* that has a negative stiffness in part of its displacement range was investigated statically in chapter 2. It was shown that the displacement range over which negative stiffness is shown depends on the angle at which the mechanism becomes unloaded, becoming larger as this angle is reduced. A QZS mechanism can be formed by adding a vertical spring to the mechanism and adjusting the ratio between the vertical spring stiffness and the stiffness of the snap-through mechanism. The mechanism can be tuned for different static loads by simply adjusting the position of the vertical spring. Finally, it is shown that this QZS mechanism has a wider displacement range affording low stiffness than a similar mechanism that was proposed in a previous work.

Some measurements on an existing test rig that can be modelled as a snap-through mechanism was done. Although, the test rig well suited its design purpose, an adaptive tuned vibration absorber, it is necessary to use elements that can accommodate large deflections in order to make it possible to use the rig as a QZS mechanism for vibration isolation. This implies using much thinner cantilevers, which have higher modes of vibration within the frequency range of interest. It was decided that an alternative arrangement for a nonlinear vibration isolator, which

has fewer parts, would be required to avoid the problems encountered with the existing rig when it deforms with large deflections.

The nonlinear stiffness properties of beams were investigated in the third chapter of the thesis. A simply supported beam loaded transversally at its midpoint is addressed as a nonlinear oscillator with softening characteristics in the literature [20] and was considered as a potential stiffness element for a nonlinear vibration isolator. However, it has been revealed here that it has a hardening stiffness nonlinearity.

The reduction in tangent stiffness with deflection of an axially loaded buckled beam makes it suitable for use as a nonlinear vibration isolator. Buckling of the beam causes a singularity in the force-deflection curve and this can be avoided by increasing the static load of the system to move the buckling point out of the dynamic range. Alternative methods to avoid the singularity due to buckling are the introduction of eccentricity to the loading or initial curvature in the beam. It was shown that both of these have a smoothing effect on the force-displacement curve. The minimum tangent stiffness and corresponding static stiffness were obtained for them and it was shown that an order of magnitude reduction in stiffness can be achieved for a beam either with small initial curvature or small eccentricity to the loading.

To investigate the effect of higher modes of vibration on the performance of an isolator comprising a curved beam, a case study was considered to isolate a mass of 1 kg and achieve 1Hz fundamental frequency. The FEM was used to study the higher modes of vibration and forced transmissibility of an axially-loaded beam. It was found that lower initial curvature is helpful with regard to achieving a higher static to tangent stiffness ratio and also in moving the second peak in the transmissibility curve to higher frequencies. The transmissibility and natural frequencies were obtained by assuming the system behaves linearly about the statically loaded position using FEM and nonlinear dynamic effects were not considered at this stage.

Due to the bell shape of a commercially available isolation mount, the 'bubble mount', it was thought that it could be modelled as a curved beam. The dimensions of the curved beam model were obtained by minimising the mean square error between the measured force-deflection curve of the bubble mount and the result of the curved beam model. It was found that a curved beam is not a suitable model for the bubble mount. This may be due to the thickness of the

bubble mount, which is not slender, or to its shape in cross section, which is not uniformly curved.

The variability in the properties of bubble mounts was also evaluated. The force-deflection characteristics of ten nominally identical bubble mounts were measured and compared. It was found that the variability in the natural frequency when mass-loaded was negligible; however the variability in tangent stiffness may cause some degree of mode coupling in practice for a piece of equipment that is supported by several of these mounts. This would also cause mounts to be loaded to positions other than their minimum tangent stiffness positions that must be considered in any further study of nonlinear isolators. The differences in bubble mounts can be due to manufacturing tolerances and to the variability in the properties of rubber, which depends very much on its composition.

The nonlinear dynamics of a Duffing oscillator with asymmetric stiffness resulting from a static load or a mistuned mass was investigated in chapter 5. The force transmissibility for a Duffing oscillator with cubic stiffness only, subject to a static preload was obtained first. It is revealed that the FRC of transmissibility is similar to that of forced response. It is of the hardening type for small levels of static preload and bends to the right depending on the parameters of the system. There is a combination of hardening and softening for larger static preloads and its stiffness is of the purely softening type for very large static preloads. The FRCs can consist of multiple jump frequencies, depending on the level of static preload. An approximate equation for the locus of the peak amplitudes of the response and the transmissibility was presented. The frequency at which the transmissibility drops below unity was used as a measure for evaluating the performance of the isolator and it is called the isolation frequency here. The plot for the isolation frequency as a function of the static preload was produced and compared with the isolation frequency of a linear isolator. For the hardening type of nonlinearity, the jump-down frequency defines the isolation frequency. It is shown that a weakly nonlinear isolator can perform better than a linear one up to a large static preload.

The same analysis was performed for a Duffing oscillator with purely cubic stiffness and a mistuned or non-optimum mass. The variability in isolator characteristics as observed for the bubble mount or changing load (isolated mass) in a real system can result in an isolator that is not loaded with the mass that it had been designed to support. The mistuned mass moves the statically loaded position away from the optimum position in a similar way to static preload, but

differs in that the inertia term of the equation of motion is affected by the addition of the mistuned mass. The change in inertia term causes a change in the response amplitude compared to the equivalent statically loaded isolator, which affects the instantaneous stiffness and the shape of the FRCs. The isolation frequency as a function of mass ratio was determined. The isolation frequency was different from that of a statically preloaded case, but the range at which it performs better than a linear isolator was the same for the mistuned mass oscillator and the equivalent statically loaded oscillator.

Finally in chapter 5, the Duffing oscillator in its complete form, i.e. with linear and cubic stiffness terms, was investigated. Nonlinear effects such as bending to the right and left become weaker when the linear stiffness is increased. The additional linear stiffness term also brings an increase in the effective tangent stiffness. The isolation frequency increases for small static preloads and it decreases for large static preload compared to an isolator with cubic stiffness only.

The nonlinear dynamics of a nonlinear isolator comprising of curved beams in series with linear springs was investigated in chapter 6 to assess its performance in isolating harmonic forces. A mass on this isolator was modelled as a single degree of freedom system with a nonlinear spring that has the force-deflection characteristic of the nonlinear isolator.

The FRCs of forced response are of the hardening type that bend to the right with a jump down frequency. The high tangent stiffness at about the statically unloaded position behaves as a rigid-end stop and prevents movement of the mass in the negative direction for large amplitudes and pushes the centre of oscillation further into the buckled range. This results in a large bias term of response near resonance. It also causes distortion in the steady state time history of the oscillation and shifts the frequency response curve of the harmonic term in the response to the right and jump-down therefore occurs at higher frequencies than those predicted by the approximate Duffing model. The approximate model fails to predict the response for large amplitudes about resonance.

The force transmissibility curves of the curved beam isolator are of the hardening type and bend to the right. The jump-down frequency defines the isolation frequency which is lower for a small curvature angle. Compared to a linear isolator with the same static deflection, there is a reduction in the isolation frequency of about 60% for the curved beam isolator with an initial

curvature angle of 2° . It was shown that in the case of applying a static preload, the jump-down frequency is reduced by an increase in the static preload. Although the jump-down frequency was reduced, the effect of the additional static deflection due to preload was not considered. By considering this static deflection, it was observed that the curved beam isolator loaded to its minimum tangent stiffness position outperforms the other ones.

In the time history of the transmitted force a dip with very large absolute value appears due to the high tangent stiffness occurring at about the unloaded position. The existence of such a dip introduces other harmonics in the frequency response and its large absolute value is undesirable. The difficulty is overcome by reducing the stiffness of the linear springs to be comparable to the static stiffness of the curved beam at their optimum position at the cost of a slight increase in the jump down frequency.

It may be concluded that a nonlinear isolator with an asymmetric force-deflection curve outperforms a linear isolator with the same static deflection. The lower level of tangent stiffness at the statically loaded position provides better isolation performance and the mass should be chosen to load the isolator to this position. In the case of a strong asymmetry in the force-deflection curve, tangent stiffness should not be excessive to have an acceptable level of transmitted force at frequencies close to the resonance. A nonlinear isolator can accommodate static preloads but the static deflection due to a preload is larger than a linear isolator as expected.

7.1 Recommendations for future work

The performance of a nonlinear vibration isolator has been considered in some detail in this thesis, but there are aspects of this issue that require further study. Firstly, only the force transmissibility has been studied here. Unlike a linear system, the displacement transmissibility of a nonlinear isolator is not the same as the force transmissibility. Therefore, a study of the displacement transmissibility of a nonlinear mount could provide useful information about its ability to isolate vibration at its base. Further, the isolation achieved at the excitation frequency is considered here, while the effects of the other harmonics are not investigated thoroughly.

This is also worthy of further study. Nonlinear phenomena such as chaos could also be considered in order to determine the conditions required for their occurrence.

It is recommended here that a test rig is built for the curved beam isolator, so that measurements can be made for the nonlinear dynamic response of the system. These measurements could then be used to evaluate the ability of a mathematical model to predict the response, including the displacement transmissibility.

It was shown in chapter 3 that beams loaded eccentrically are an alternative to the post buckled straight beam. The dynamic response of a nonlinear isolator comprised of beams loaded eccentrically could be obtained in future work and compared with that for a curved beam isolator in order to identify the best solution for isolation performance. This may also provide an improved understanding of nonlinear mechanisms.

Single-degree-of-freedom systems only are considered in this study. In practice, a piece of equipment has six rigid body dofs and is isolated with several mounts. It is necessary to consider the nonlinear effects on a multi-degree-of-freedom system with such isolators.

Finally, it is recommended here that sets of plots are produced for use in engineering design of nonlinear vibration isolation systems, based on analytical and experimental data. For example, plots for the isolation frequency with different sets of non-dimensional parameters could be very useful in the design of nonlinear isolation mounts.

Appendix A. Accuracy of solutions

There is no exact analytical solution for the Duffing equation although approximate analytical solutions can be obtained by methods such as the HBM. It is assumed that the response of the system is harmonic and the excitation frequency is dominant in the response, so the other harmonics can be neglected. However, the response contains other harmonics and can also be chaotic at some excitation frequencies for specific parameters [86]. For a Duffing oscillator, Szemplinska-Stupnicka and Bajkowski [83] studied the existence of different harmonics in the response, their stability and appearance of chaos in the response. They concluded that the oscillator can exhibit chaotic motion in a narrow zone where loss of stability of $\frac{1}{2}$ sub-harmonics is predicted theoretically.

The solution of the HBM does not match with the amplitude obtained from simulation in the time domain for a non-dimensional static load of 0.01 for frequencies smaller than 0.25 as it is shown in Figure 5-3 and Figure 5-4. The phase portrait for some frequencies up to 0.34 is shown in Figure A-1. The loops in the phase portrait are due to the existence of other frequencies in response. By increasing the non-dimensional frequency the number of loops reduces where at $\Omega=0.26$ they disappear. This is consistent with the frequencies at which the time domain solution and HBM solution demonstrate good consistency. Although the phase portraits for frequencies higher than this do not match exactly with the expected phase portrait of sinusoidal single frequency oscillation (oval or circular shape depending on axis aspect ratio), the assumption of HBM leads to sufficient accuracy.

To obtain an estimate of how much other harmonics contribute to the response at each excitation frequency, the Total Harmonic Distortion or THD is used. It is defined as the relative signal energy at non-fundamental harmonics to that at the fundamental frequency [84, 85]. The THD is calculated here from the spectrum of the time domain simulation obtained by the Fast Fourier Transform (FFT). The result is shown in Figure A-2 for a static preload equal to 0.01, dynamic load equal to 0.1, γ equal to 0.0783 and ζ equal to 0.025. The THD for increasing frequency is shown with dots and a solid line whereas for decreasing frequency it is shown with dashed line and squares. There are peaks in the low frequency region where the results of the time domain analysis do not match with the HBM solution and also where loops in phase portrait were evident.

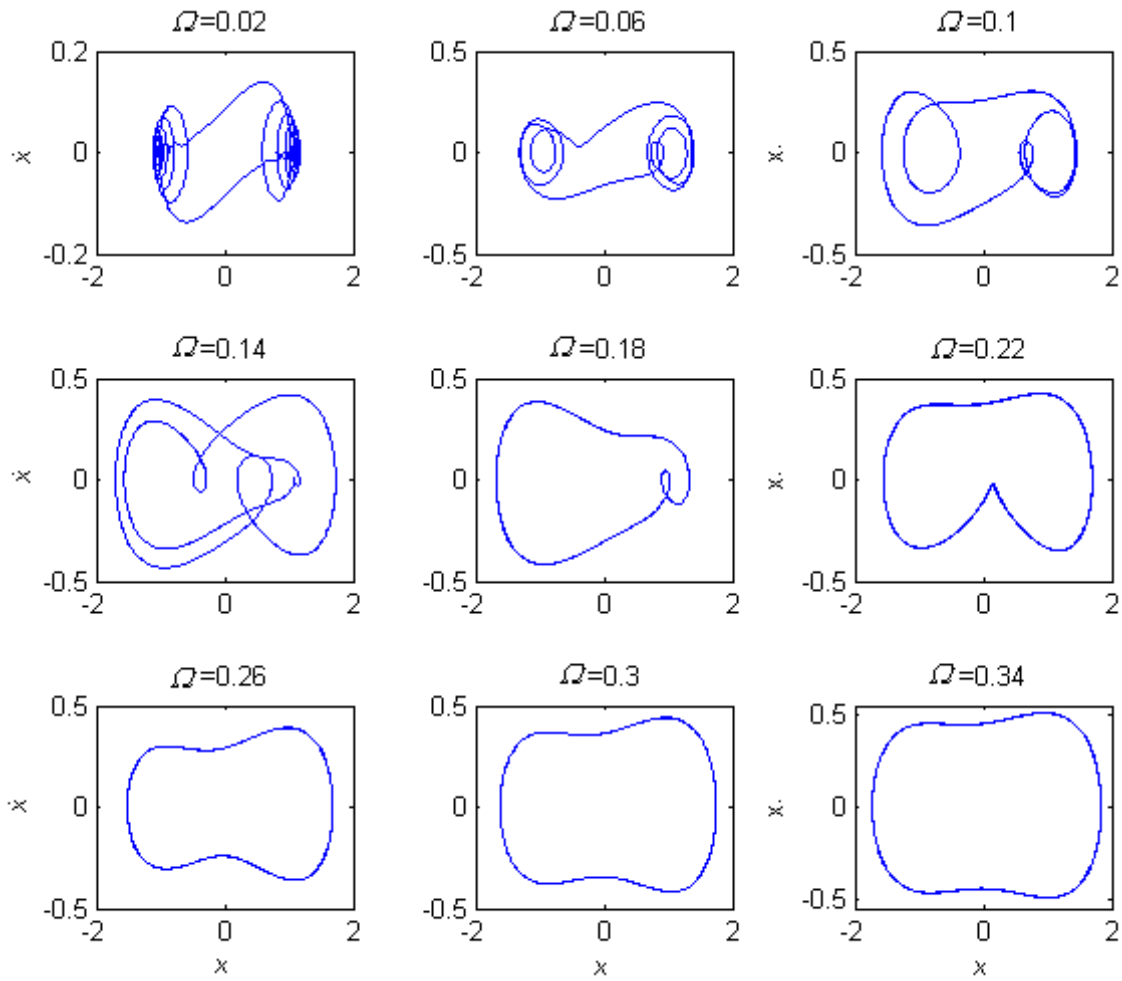


Figure A-1: Phase portrait of nonlinear vibration isolator for $\zeta = 0.025$, $\gamma = 0.0783$, $f_1 = 0.1$, and $f_0 = 0.01$

The THD obtained by increasing frequency and by decreasing frequency match except at a frequency range between 0.45 and 0.75 and also at a small frequency range between 0.1 and 0.2.. The former range is between jump up and jump down frequencies where solution follows different branches for increasing and decreasing frequencies. By referring to Figure 5-3, it can be seen that for the time domain simulation, the jump up occurs at a higher frequency than that predicted by the HBM. The peak in the THD shows that the existence of other harmonics prevents sinusoidal oscillations at the excitation frequency only as it is the assumption of HBM here and jump up happens sooner while decreasing frequency. The phase portraits for these frequencies are presented in Figure A-3. It can be seen how other harmonics appear as an additional loop and disappear after jump-up. The mismatch between two curves at a frequency

range between 0.1 and 0.2 in Figure A-2 is due to the existence of subharmonics in response which are not considered in THD according to its definition.

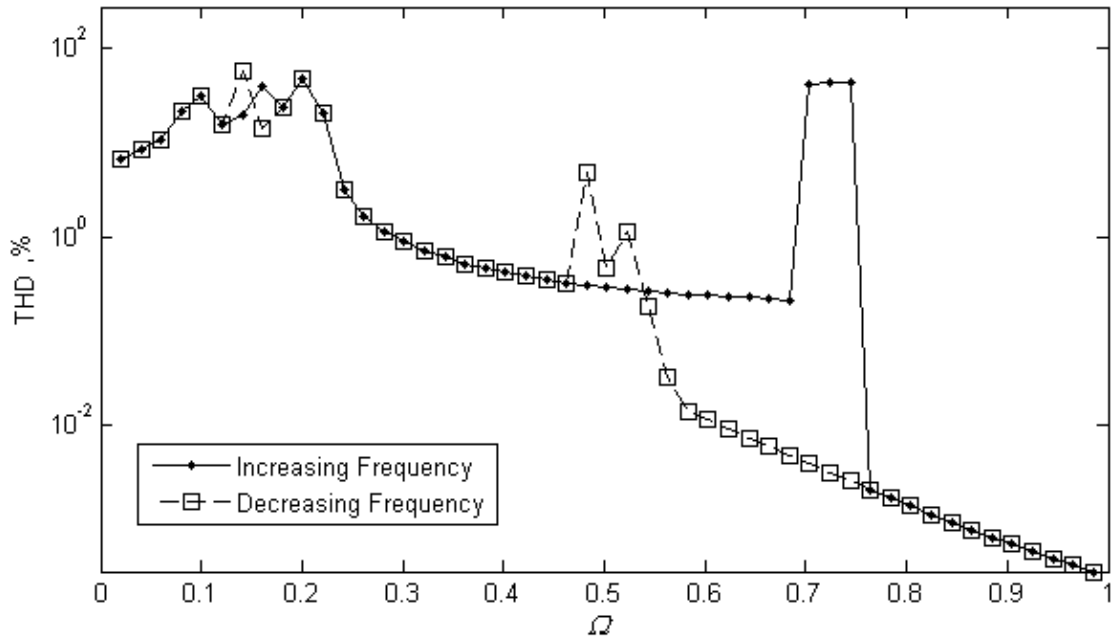


Figure A-2: Total harmonic distortion as a function of non-dimensional frequency for $\zeta = 0.025$, $\gamma = 0.0783$, $f_1 = 0.1$, and $f_0 = 0.01$

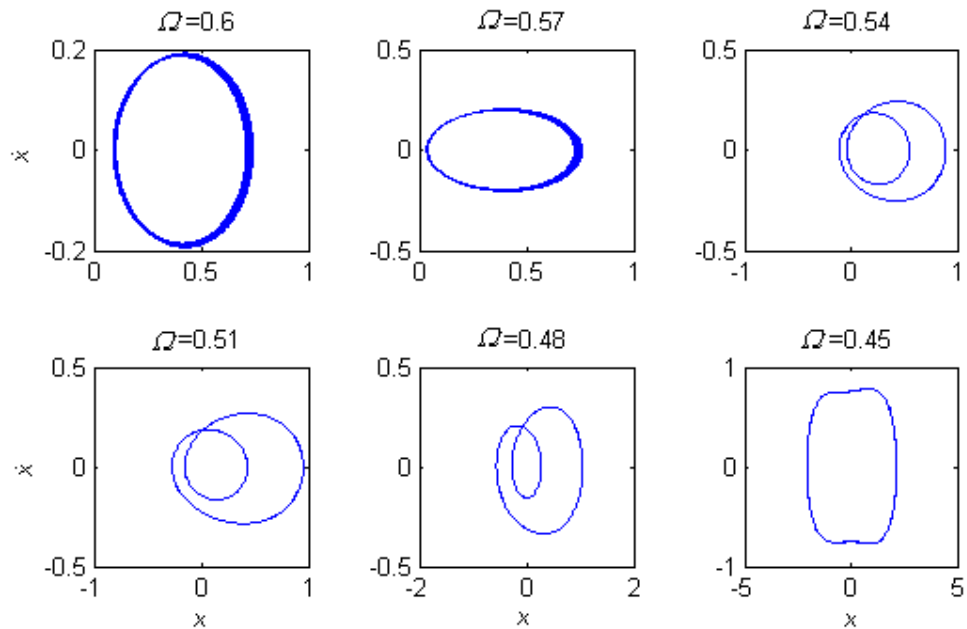


Figure A-3: Phase portrait of nonlinear vibration isolator for decreasing frequency, $\zeta = 0.025$, $\gamma = 0.0783$, $f_1 = 0.1$, and $f_0 = 0.01$

The total harmonic distortion for a static preload f_0 of 0.2 and the same other parameter values as previously used is shown in Figure A-4. The graph is plotted with a logarithmic y axis, since the peak is bigger than 200% and the other features are not visible otherwise. The peak in the THD corresponds to a local peak in the harmonic amplitude A_1 from the time domain simulation at a frequency of 0.3 which can be seen in Figure 5-3. The phase portraits at these frequencies are shown in Figure A-5 where the appearance of an additional loop is visible in the range where the THD has a high value. The time histories for three different frequencies in this range are shown in Figure A-6. The existence of the other harmonic can be seen here as well from the two peaks in each cycle.

There are also differences in the THD of the oscillator for increasing and decreasing frequency at a non-dimensional frequency of about .46 and .58. There is a jump-up and then jump-down in the FRC while frequency is increasing or decreasing. However, these jumps happen at different frequencies in the two cases. The amplitude follows different branches of the FRC for the increasing and decreasing frequencies in the two ranges mentioned. For detailed discussion on the jump up and jump down and the multiple amplitude of harmonic response one may refer to reference [80].

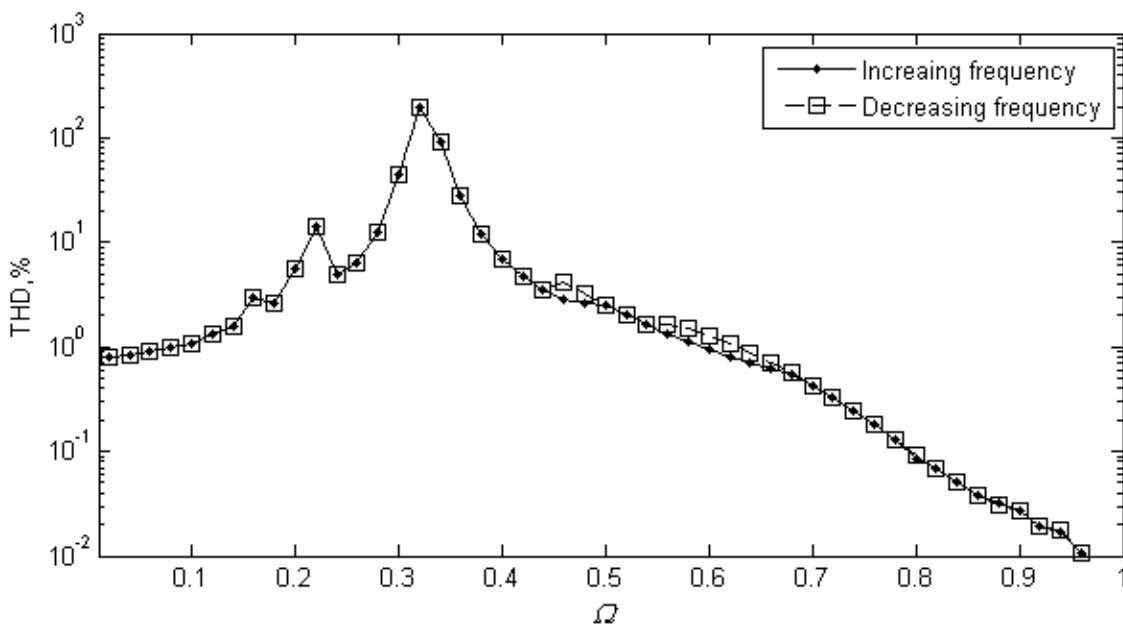


Figure A-4: Total harmonic distortion as a function of non-dimensional frequency for $\zeta = 0.025$, $\gamma = 0.0783$, $f_1 = 0.1$, and $f_0 = 0.2$

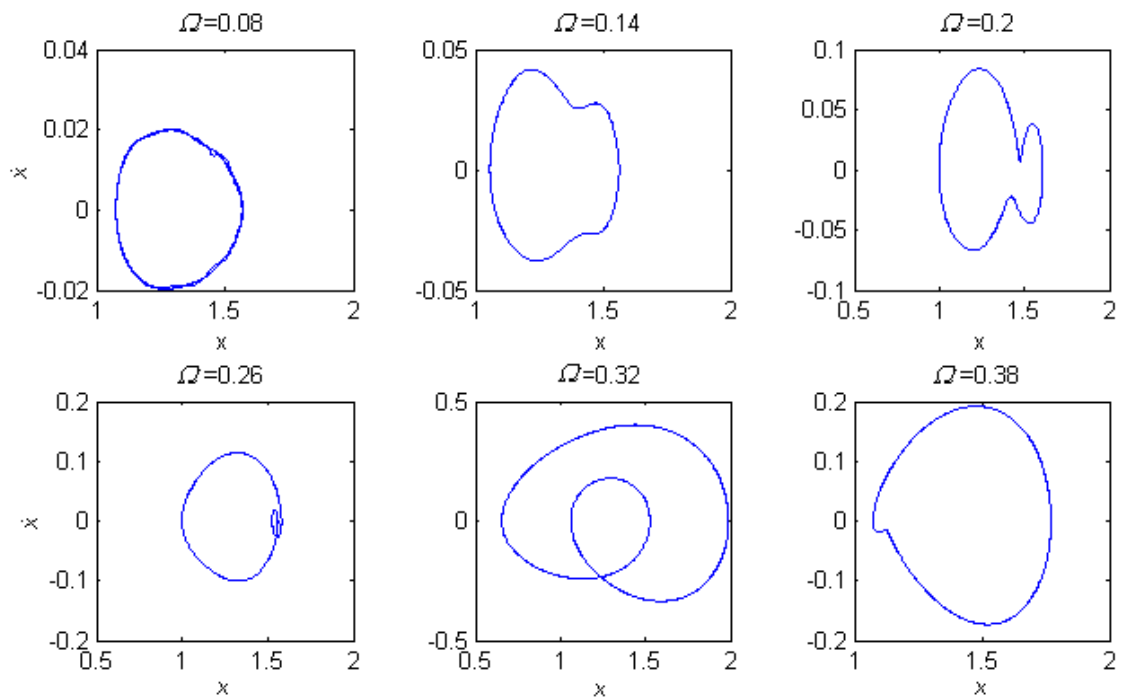


Figure A-5: Phase portrait of nonlinear vibration isolator for increasing frequency, $\zeta = 0.025$, $\gamma = 0.0783$, $f_1 = 0.1$, and $f_0 = 0.2$

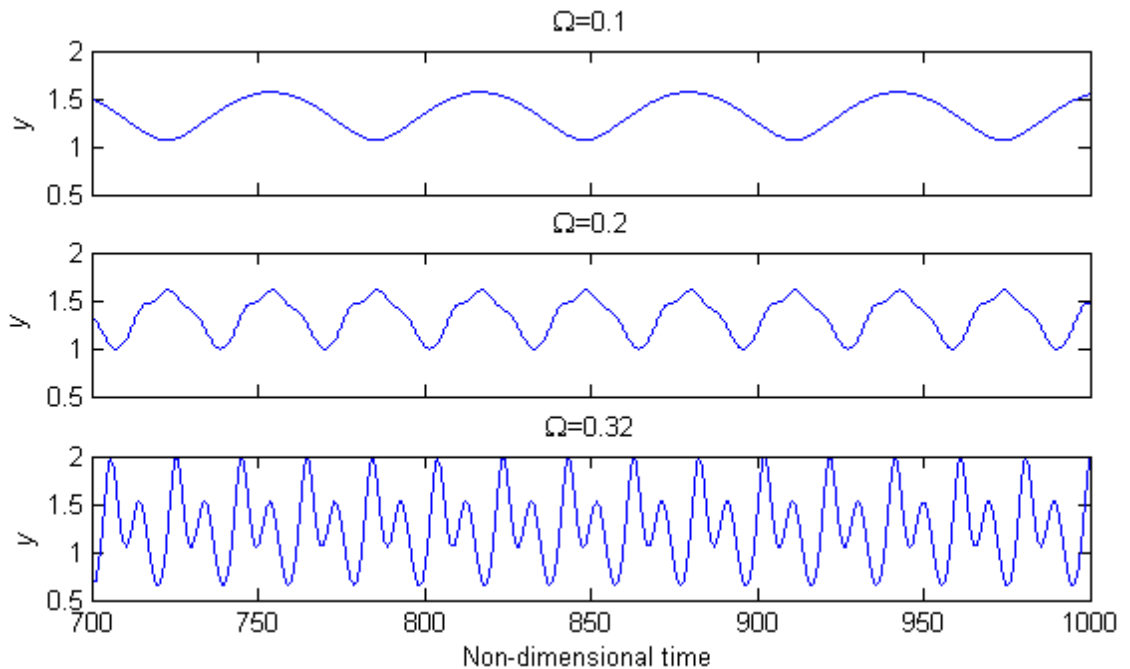


Figure A-6: Time history of nonlinear vibration isolator for different non-dimensional frequencies, $\zeta = 0.025$, $\gamma = 0.0783$, $f_1 = 0.1$, and $f_0 = 0.2$

The total harmonic distortion for f_0 equal to 0.5 is shown in Figure A-7. The same characteristics can be seen in this case as the previous one. There is a peak with very high amplitude just before the resonance frequency which corresponds here to the local peak in harmonic amplitude A_1 and is visible in time domain results of Figure 5-3. The difference here is that there are three branches in the THD curve here which are shown by a circle in Figure A-7. The third branch corresponds to the resonance branch in the FRC of harmonic amplitude A_1 in Figure 5-3 that is covered neither in sweeping frequency up nor down. To make the mass oscillate at this frequency, appropriate initial conditions must be chosen. Since there are three stable branches for the response of the oscillator, there are three branches of the THD accordingly in this range.

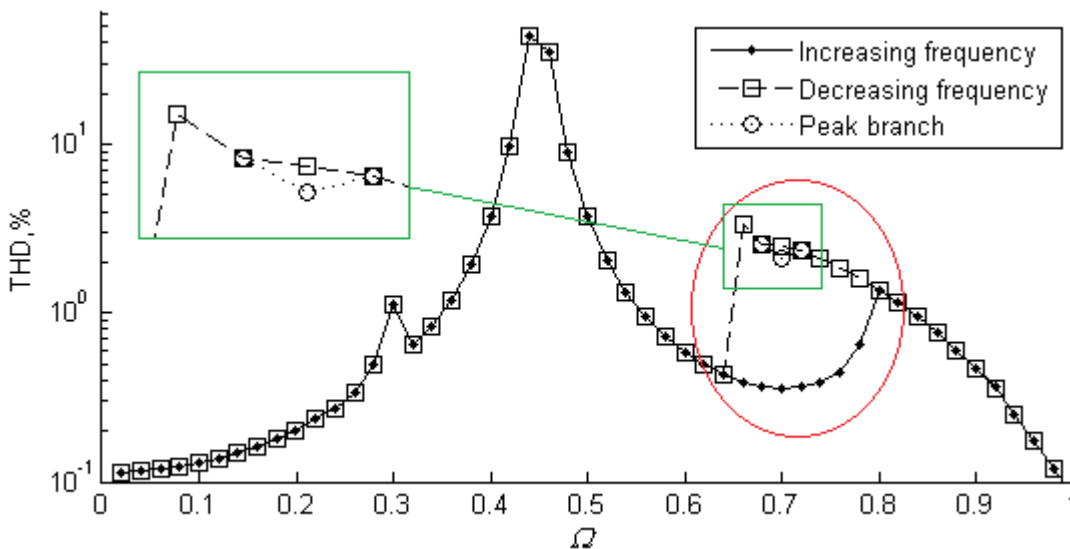


Figure A-7: Total harmonic distortion as a function of non-dimensional frequency for $\zeta = 0.025$, $\gamma = 0.0783$, $f_1 = 0.1$, and $f_0 = 0.5$

For a static preload of 0.95, the maximum of the THD drops to 25% at a non-dimensional frequency of 0.56. The FRC of response is of the softening type. The THD of this case is shown in Figure A-8. There is only one jump frequency while sweeping up or down the frequency. Jump-up happens at a non-dimensional frequency of 1 and jump-down occurs about 0.9. As expected, the two curves of the THD are different between these frequencies.

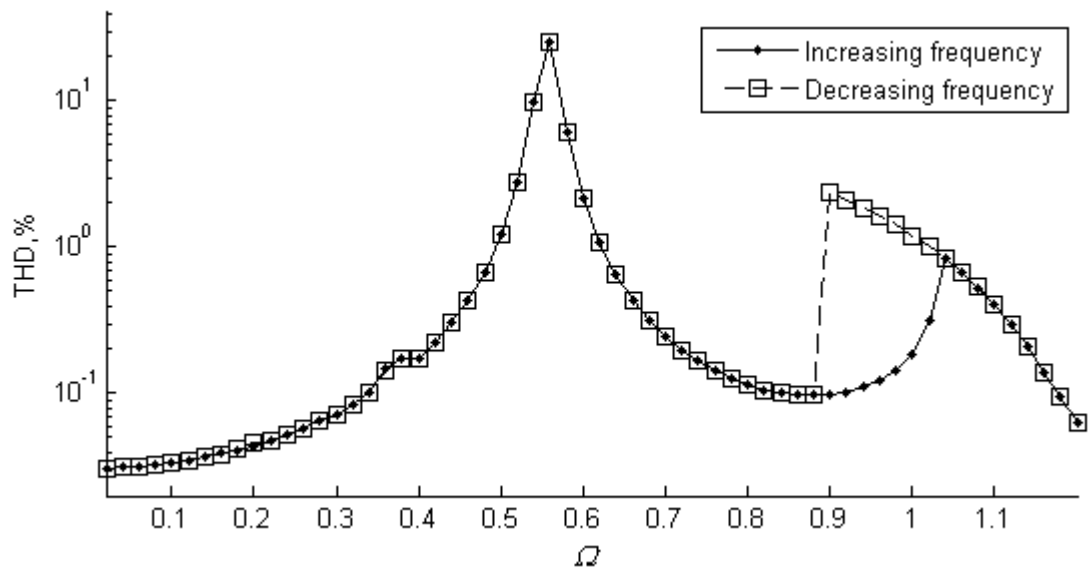


Figure A-8: Total harmonic distortion as a function of non-dimensional frequency for $\zeta = 0.025$, $\gamma = 0.0783$, $f_1 = 0.1$, and $f_0 = 0.95$

References

1. Rivin, E.I., *Passive vibration isolation*. 2003, New York: ASME Press. xv, 426 p.
2. Den Hartog, J.P., *Mechanical vibrations*. 4th ed. 1956, New York ; London: McGraw-Hill Book Company. xi, 436 p.
3. Carrella, A., M.J. Brennan, and T.P. Waters, *Static analysis of a passive vibration isolator with quasi-zero-stiffness characteristic*. *Journal of Sound and Vibration*, 2007. **301**(3-5): p. 678-689.
4. Carrella, A., M.J. Brennan, and T.P. Waters, *Optimization of a quasi-zero-stiffness isolator*. *Journal of Mechanical Science and Technology*, 2007. **21**(6): p. 946-949.
5. Carrella, A., M.J. Brennan, and T.P. Waters, *Demonstrator to show the effects of negative stiffness on the natural frequency of a simple oscillator*. *Proceedings of the Institution of Mechanical Engineers Part C-Journal of Mechanical Engineering Science*, 2008. **222**(7): p. 1189-1192.
6. Carrella, A., et al., *Force and displacement transmissibility of a nonlinear isolator with high-static-low-dynamic-stiffness*. *International Journal of Mechanical Sciences*, 2012. **55**(1): p. 22-29.
7. Carrella, A., et al., *On the design of a high-static-low-dynamic stiffness isolator using linear mechanical springs and magnets*. *Journal of Sound and Vibration*, 2008. **315**(3): p. 712-720.
8. Ibrahim, R.A., *Recent advances in nonlinear passive vibration isolators*. *Journal of Sound and Vibration*, 2008. **314**(3-5): p. 371-452.
9. Alabuzhev, P., et al., *Vibration protecting and measuring systems with quasi-zero stiffness*. *Applications of vibration series*. 1989, New York ; London: Hemisphere Publishing Co., Taylor & Francis Group. ix, 100 p.
10. Platus, D.L., *Negative Stiffness-Mechanism Vibration Isolation Systems*. *Vibration Control in Microelectronics, Optics, and Metrology*, 1992. **1619**: p. 44-54.
11. Platus, D.L., *Negative-stiffness-mechanism vibration isolation systems*. *Optomechanical Engineering and Vibration Control*, 1999. **3786**: p. 98-105.
12. Platus, D.L. and D.K. Ferry, *Negative-stiffness vibration isolation improves reliability of nanoinstrumentation*. *Laser Focus World*, 2007. **43**(10): p. 107-109.

13. Ahn, H.J., *Performance limit of a passive vertical isolator using a negative stiffness mechanism*. Journal of Mechanical Science and Technology, 2008. **22**(12): p. 2357-2364.
14. Winterflood, J. and D.G. Blair, *A long-period vertical vibration isolator for gravitational wave detection*. Physics Letters A, 1998. **243**(1-2): p. 1-6.
15. Park, S.T. and T.T. Luu, *Techniques for optimizing parameters of negative stiffness*. Proceedings of the Institution of Mechanical Engineers Part C-Journal of Mechanical Engineering Science, 2007. **221**(5): p. 505-511.
16. Carrella, A., et al., *On the force transmissibility of a vibration isolator with quasi-zero-stiffness*. Journal of Sound and Vibration, 2009. **322**(4-5): p. 707-717.
17. Kovacic, I., M.J. Brennan, and T.P. Waters, *A study of a nonlinear vibration isolator with a quasi-zero stiffness characteristic*. Journal of Sound and Vibration, 2008. **315**(3): p. 700-711.
18. Beccaria, M., et al., *Extending the VIRGO gravitational wave detection band down to a few Hz: metal blade springs and magnetic antisprings*. Nuclear Instruments and Methods in Physics Research Section A: Accelerators, Spectrometers, Detectors and Associated Equipment, 1997. **394**(3): p. 397-408.
19. Bertolini, A., et al., *Seismic noise filters, vertical resonance frequency reduction with geometric anti-springs: a feasibility study*. Nuclear Instruments and Methods in Physics Research Section A: Accelerators, Spectrometers, Detectors and Associated Equipment, 1999. **435**(3): p. 475-483.
20. Thomsen, J.J., *Vibrations and stability : advanced theory, analysis, and tools*. 2nd ed. 2003, Berlin ; New York: Springer. xxi, 404 p.
21. Winterflood, J., T. Barber, and D.G. Blair, *Using Euler buckling springs for vibration isolation*. Classical and Quantum Gravity, 2002(7): p. 1639.
22. Winterflood, J., D.G. Blair, and B. Slagmolen, *High performance vibration isolation using springs in Euler column buckling mode*. Physics Letters A, 2002. **300**(2-3): p. 122-130.
23. Winterflood, J., T.A. Barber, and D.G. Blair, *Mathematical analysis of an Euler spring vibration isolator*. Physics Letters A, 2002. **300**(2-3): p. 131-139.
24. Lee, C.M., V.N. Goverdovskiy, and A.I. Temnikov. *Multipurpose model for parametrical synthesis of the elastic elements with torsion "negative" stiffness*. in *Science and Technology, 2001. KORUS '01. Proceedings. The Fifth Russian-Korean International Symposium on*. 2001.

25. Lee, C.M., V.N. Goverdovskiy, and A.I. Temnikov, *Design of springs with "negative" stiffness to improve vehicle driver vibration isolation*. Journal of Sound and Vibration, 2007. **302**(4-5): p. 865-874.
26. Lee, C.M., V.N. Goverdovskiy, and S.B. Samoilenko, *Prediction of non-chaotic motion of the elastic system with small stiffness*. Journal of Sound and Vibration, 2004. **272**(3-5): p. 643-655.
27. Lee, C.M. and V.N. Goverdovskiy, *Alternative vibration protecting systems for men-operators of transport machines: modern level and prospects*. Journal of Sound and Vibration, 2002. **249**(4): p. 635-647.
28. Cella, G., et al., *Monolithic geometric anti-spring blades*. Nuclear Instruments and Methods in Physics Research Section A: Accelerators, Spectrometers, Detectors and Associated Equipment, 2005. **540**(2-3): p. 502-519.
29. Virgin, L.N. and R.B. Davis, *Vibration isolation using buckled struts*. Journal of Sound and Vibration, 2003. **260**(5): p. 965-973.
30. Shoup, T.E., *Shock and Vibration Isolation Using a Nonlinear Elastic Suspension*. Aiaa Journal, 1971. **9**(8): p. 1643-&.
31. Shoup, T.E. and G.E. Simmonds, *An Adjustable Spring Rate Suspension System*. Aiaa Journal, 1977. **15**(6): p. 865-866.
32. Plaut, R.H., J.E. Sidbury, and L.N. Virgin, *Analysis of buckled and pre-bent fixed-end columns used as vibration isolators*. Journal of Sound and Vibration, 2005. **283**(3-5): p. 1216-1228.
33. Plaut, R.H., et al., *Vibration isolation using buckled or pre-bent columns - Part 1: Two-dimensional motions of horizontal rigid bar*. Journal of Sound and Vibration, 2008. **310**(1-2): p. 409-420.
34. El-Kafrawy, A.E., A. Kandil, and A. Omar, *Vibration isolation of a symmetric and asymmetric rigid bar using struts subject to axial static and dynamic excitation*. Proceedings of the Institution of Mechanical Engineers, Part C: Journal of Mechanical Engineering Science, 2011. **225**(2): p. 334-346.
35. Jeffers, A.E., R.H. Plaut, and L.N. Virgin, *Vibration isolation using buckled or pre-bent columns - Part 2: Three-dimensional motions of horizontal rigid plate*. Journal of Sound and Vibration, 2008. **310**(1-2): p. 421-432.
36. El-Kafrawy, et al., *Vibration isolation of a symmetric rigid plate using struts under static and dynamic axial excitation*. Vol. 6. 2010, Heidelberg, ALLEMAGNE: Springer. 11.

37. Frisch-Fay, R., *Flexible bars*. 1962, London: Butterworths. 228p.
38. Bisshopp, K.E. and D.C. Drucker, *Large Deflection of Cantilever Beams*. Quarterly of Applied Mathematics, 1945. **3**, No. 3: p. 272-275.
39. Conway, H.D., *XCIV. The large deflection of simply supported beams*. Philosophical Magazine Series 7, 1947. **38**(287): p. 905 - 911.
40. Gospodnetic, D., *Deflection curve of a simply supported beam*. Transactions of the ASME, Journal of Applied Mechanics, 1959. **26**(4): p. 675-676.
41. Sundara Raja Iyengar, K.T. and S.K. Lakshmana Rao, *Large deflections of simply supported beams*. Journal of the Franklin Institute, 1955. **259**(6): p. 523-528.
42. Wang, T.M., S.L. Lee, and O.C. Zienkiewicz, *A numerical analysis of large deflections of beams*. International Journal of Mechanical Sciences, 1961. **3**(3): p. 219-228.
43. Wang, T.M., *Nonlinear bending of beams with concentrated loads*. Journal of the Franklin Institute, 1968. **285**(5): p. 386-390.
44. Wang, T.M., *Non-linear bending of beams with uniformly distributed loads*. International Journal of Non-Linear Mechanics, 1969. **4**(4): p. 389-395.
45. Belendez, T., C. Neipp, and A. Belendez, *Large and small deflections of a cantilever beam*. European Journal of Physics, 2002. **23**(3): p. 371-379.
46. Ferry, J.D., *Viscoelastic properties of polymers*. 3d ed. 1980, New York: Wiley. xxiv, 641 p.
47. Gent, A.N. and American Chemical Society. Rubber Division., *Engineering with rubber : how to design rubber components*. 2nd ed. 2001, Munich ; Cincinnati: Hanser. 365 p.
48. McCallion, H. and D.M. Davies, *Behaviour of Rubber in Compression under Dynamic Conditions*. Proceedings of the Institution of Mechanical Engineers, 1955. **169**(1): p. 1125-1140.
49. Shaska, K., R. Ibrahim, and R. Gibson, *Influence of excitation amplitude on the characteristics of nonlinear butyl rubber isolators*. Nonlinear Dynamics, 2007. **47**(1): p. 83-104.
50. Harris, J. and A. Stevenson, *On the Role of Nonlinearity in the Dynamic Behavior of Rubber Components*. Rubber Chemistry and Technology, 1986. **59**(5): p. 740-764.
51. Jones, D.I.G., *Handbook of viscoelastic vibration damping*. 2001, Chichester ; New York: J. Wiley. xvii, 391 p.

52. Lee, N.K., et al. *Design of engine mount using finite element method and optimization technique*. in *Proceedings of the 1998 SAE International Congress & Exposition, February 23, 1998 - February 26, 1998*. 1998. Detroit, MI, USA: SAE.
53. Richards, C.M. and R. Singh, *Characterization of rubber isolator nonlinearities in the context of single- and multi-degree-of-freedom experimental systems*. *Journal of Sound and Vibration*, 2001. **247**(5): p. 807-834.
54. Kim, S. and R. Singh, *Multi-dimensional characterization of vibration isolators over a wide range of frequencies*. *Journal of Sound and Vibration*, 2001. **245**(5): p. 877-913.
55. Zhang, J. and C.M. Richards, *Parameter identification of analytical and experimental rubber isolators represented by Maxwell models*. *Mechanical Systems and Signal Processing*, 2007. **21**(7): p. 2814-2832.
56. Nayfeh, A.H. and D.T. Mook, *Nonlinear oscillations*. Pure and applied mathematics. 1979, New York: Wiley. xiv, 704 p.
57. Hayashi, C., *Nonlinear oscillations in physical systems*. [Rev. and enl. ed. 1964, New York,; McGraw-Hill. xii, 392 p.
58. Kirk, C.L., *Non-Linear Random Vibration Isolators*. *Journal of Sound and Vibration*, 1988. **124**(1): p. 157-182.
59. Ravindra, B. and A.K. Mallik, *Performance of Nonlinear Vibration Isolators under Harmonic Excitation*. *Journal of Sound and Vibration*, 1994. **170**(3): p. 325-337.
60. Lu Z. Q. , Y.T.J., Brennan M. J. , Liu Z. G. , Li X. H., *On the dynamic behaviour of a specially configured non-linear isolator subject to random excitation*, in *7th European Nonlinear Dynamics Conference (ENOC 2011)*, G.R.a.F.R. D. Bernardini, Editor 2011: Rome, Italy.
61. Milovanovic, Z., I. Kovacic, and M.J. Brennan, *On the Displacement Transmissibility of a Base Excited Viscously Damped Nonlinear Vibration Isolator*. *Journal of Vibration and Acoustics-Transactions of the Asme*, 2009. **131**(5).
62. Le, T.D. and K.K. Ahn, *A vibration isolation system in low frequency excitation region using negative stiffness structure for vehicle seat*. *Journal of Sound and Vibration*, 2011. **330**(26): p. 6311-6335.
63. Thompson, J.M.T., *Instabilities and catastrophes in science and engineering*. 1982, Chichester West Sussex ; New York: Wiley. xvi, 226 p.
64. Thompson, J.M.T. and G.W. Hunt, *Elastic instability phenomena*. 1984, Chichester ; New York: Wiley. xii, 209 p.

65. Bonello, P., et al., *Designs for an adaptive tuned vibration absorber with variable shape stiffness element*. Proceedings of the Royal Society A: Mathematical, Physical and Engineering Science, 2005. **461**(2064): p. 3955-3976.
66. Bonello, P., M.J. Brennan, and S.J. Elliott, *The design of an adaptive tuned vibration absorber with a variable shape stiffness element*, 2004, University of Southampton, Institute of Sound and Vibration Research, (ISVR Technical Memorandum,(941)): Southampton, UK.
67. Brennan, M.J., et al., *The "click" mechanism in dipteran flight: if it exists, then what effect does it have?* Journal of Theoretical Biology, 2003. **224**(2): p. 205-213.
68. Chen, W.-F. and T. Atsuta, *Theory of beam-columns*. J Ross Publishing classics. 2008, Ft. Lauderdale, FL: J. Ross Pub.
69. Gere, J.M. and S. Timoshenko, *Mechanics of materials*. 3rd ed. PWS-Kent series in engineering. 1990, Boston: PWS-Kent Pub. Co. xviii, 807 p.
70. Fazekas, G.A., *A note on the bending of euler beams*. Journal of engineering education, 1967. **57**(5): p. 393,394.
71. Bazant, Z.P. and L. Cedolin, *Stability of structures : elastic, inelastic, fracture, and damage theories*. The Oxford engineering science series 26. 1991, New York: Oxford University Press. xxiv, 984 p.
72. Timoshenko, S., *History of strength of materials : with a brief account of the history of theory of elasticity and theory of structures*. 1953, New York: McGraw-Hill. 452 p.
73. Timoshenko, S., *Theory of elastic stability*. 2d ed. Engineering societies monographs. 1961, New York,: McGraw-Hill. 541 p.
74. Yan, B., et al., *Characteristics of distributed parameter isolators*. Journal of Sound and Vibration, 2009. **320**(3): p. 516-526.
75. Fahy, F. and J. Walker, *Advanced applications in acoustics, noise, and vibration*. 2004, London ; New York: Spon Press. xiii, 640 p.
76. Blevins, R.D., *Formulas for natural frequency and mode shape*. 1984, Malabar, Fla.: R.E. Krieger. xi, 492 p.
77. Bonello, P., M.J. Brennan, and S.J. Elliott, *Vibration control using an adaptive tuned vibration absorber with a variable curvature stiffness element*. Smart Materials and Structures, 2005. **14**(5): p. 1055.
78. ANSYS, Inc., *Theory Reference: ANSYS Release 14.0*. 2011: ANSYS Incorporated.

79. Petrone, F., M. Lacagnina, and M. Scionti, *Dynamic characterization of elastomers and identification with rheological models*. Journal of Sound and Vibration, 2004. **271**(1–2): p. 339-363.
80. Kovacic, I., M.J. Brennan, and B. Lineton, *On the resonance response of an asymmetric Duffing oscillator*. International Journal of Non-Linear Mechanics, 2008. **43**(9): p. 858-867.
81. Kovacic, I., M.J. Brennan, and B. Lineton, *Effect of a static force on the dynamic behaviour of a harmonically excited quasi-zero stiffness system*. Journal of Sound and Vibration, 2009. **325**(4-5): p. 870-883.
82. Kovacic, I. and M.J. Brennan, *The Duffing equation : nonlinear oscillators and their phenomena*. 2011, Chichester, West Sussex, U.K. ; Hoboken, N.J.: Wiley. xvi, 369 p.
83. Szemplinska-kapcia, W. and J. Bajkowski, *The 1/2 Subharmonic Resonance and Its Transition to Chaotic Motion in a Nonlinear Oscillator*. International Journal of Non-Linear Mechanics, 1986. **21**(5): p. 401-419.
84. Bollen, M.H.J. and I.Y.-H. Gu, *Signal processing of power quality disturbances*. IEEE Press series on power engineering. 2006, Hoboken, NJ: Wiley-Interscience. xx, 861 p.
85. Shmilovitz, D., *On the definition of total harmonic distortion and its effect on measurement interpretation*. Ieee Transactions on Power Delivery, 2005. **20**(1): p. 526-528.
86. Ueda, Y., *Explosion of strange attractors exhibited by Duffing's equation*. Annals of the New York Academy of Sciences, 1980. **357**(1): p. 422-434.